

2017

# Development of Fuel Electrodes for Reversible Solid Oxide Fuel Cell Applications

Addo, Paul

---

Addo, P. (2017). Development of Fuel Electrodes for Reversible Solid Oxide Fuel Cell Applications (Doctoral thesis, University of Calgary, Calgary, Canada). Retrieved from <https://prism.ucalgary.ca>. doi:10.11575/PRISM/25678

<http://hdl.handle.net/11023/3735>

*Downloaded from PRISM Repository, University of Calgary*

UNIVERSITY OF CALGARY

Development of Fuel Electrodes for Reversible Solid Oxide Fuel Cell Applications

by

Paul Kwesi Addo

A THESIS

SUBMITTED TO THE FACULTY OF GRADUATE STUDIES  
IN PARTIAL FULFILMENT OF THE REQUIREMENTS FOR THE  
DEGREE OF DOCTOR OF PHILOSOPHY

GRADUATE PROGRAM IN CHEMISTRY

CALGARY, ALBERTA

APRIL, 2017

© Paul Kwesi Addo 2017



## Abstract

The stability, sulfur tolerance, and electrochemical performance of Ni-YSZ (yttria-stabilized zirconia) composites and single phase  $\text{La}_{0.3}\text{M}_{0.7}\text{Fe}_{0.7}\text{Cr}_{0.3}\text{O}_{3-\delta}$  ( $\text{M} = \text{Sr}, \text{Ca}, (\text{LMFCr})$ ) perovskites, for use as fuel electrodes for reversible solid oxide fuel cell (RSOFC) applications, were investigated in detail. RSOFCs are electrochemical devices that can be operated in both the solid oxide fuel cell (SOFC) and solid oxide electrolysis cell (SOEC) modes. Although Ni-YSZ is the most common fuel electrode for RSOFC applications, it is prone to sulfur poisoning in ppm  $\text{H}_2\text{S}$  levels at operating temperatures  $> 650$  °C, thereby decreasing the rate of the hydrogen oxidation/reduction reaction (HOR/HER).

It is shown that, at  $\leq 650$  °C, exposure of Ni-YSZ to  $\leq 10$  ppm  $\text{H}_2\text{S}$  unexpectedly enhanced the HOR activity, while at higher temperatures, conventional Ni poisoning was seen. It was concluded that the activation behaviour at  $\leq 650$  °C was due to the formation of a catalytic Ni-S species (e.g.,  $\text{Ni}_3\text{S}_2$ ) at the triple phase boundary where the HOR/HER occurs. The sulfur tolerance of LCFCr electrodes was also investigated in  $\text{H}_2 + \text{low ppm H}_2\text{S}$ , with LCFCr showing the inverse behavior of Ni/YSZ. At  $> 700$  °C, exposure of LCFCr to  $\leq 10$  ppm  $\text{H}_2\text{S}$  activated the HOR/HER, while deactivation was seen at  $\leq 700$  °C. It was concluded that exposure of LCFCr to  $\text{H}_2\text{S}$  at higher temperatures led to an increase in the density of surface  $\text{FeO}_2$  terminated species, the proposed active site for the HOR/HER.

The LSFCr materials were also shown, for the first time, to be very active (comparable or better than other oxide materials (e.g.,  $\text{La}_{1-x}\text{Sr}_x\text{Cr}_{1-y}\text{Mn}_y\text{O}_{3-\delta}$ )) and stable electrocatalysts in  $\text{CO}/\text{CO}_2$  gas environments in both the SOFC and SOEC reaction directions at 600-800 °C. LSFCr was shown to be structurally stable in pure  $\text{CO}_2$  and 70%  $\text{CO}_2$ :30%  $\text{CO}$  mixtures at 800 °C, with no major impurities detected. Also, extensive electrochemical characterization, based on

both 2-electrode and 3-electrode full and half cell configurations, showed that LSFCr was more active as an electrocatalyst for the reduction of CO<sub>2</sub> than for the oxidation of CO. Furthermore, it was found that the surface interaction of CO<sub>2</sub> with LSFCr (adsorption, dissociation, electron transfer) was the slowest step in the reaction, relative to oxide ion transport processes.

## Acknowledgements

First, I would like to express my sincere appreciation and thanks to my supervisor, Dr. Viola Birss, for her support, inspiration, and continuous guidance over the course of my Ph.D. studies. Dr. Birss is an excellent teacher and researcher who has given me a very solid foundation in the field of electrochemistry, electrocatalysis and fuel cell systems for my future career. The many discussions related to my experimental results and the valuable input and advice on my thesis drafts are also much appreciated.

I would also like to thank my Ph.D. committee members, Dr. Venkatraman Thangadurai and Dr. Robert Marriott, for their constructive advice throughout the years. Also, I would like to thank Dr. Yujun Shi and Dr. Thierry Pagnier for being part of my examination committee and providing constructive advice on my thesis.

A big thank you also goes to members of the Birss group, especially the solid oxide fuel cell sub-group members, for their useful discussions and comments on my research. My sincere thanks go to Drs. Lisa Deleebeeck, Scott Paulson, Min Chen, and Aligul Buyukaksoy for their guidance and advice during my studies. Also, thank you to Dr. Anand Singh, Dr. Ehab El Sawy, Dr Kalpana Singh, and Robert Mayall for input on the editing of my thesis. I would like to express a special thanks to Beatriz Molero-Sanchez for her support and valuable discussions over the years.

Special thanks to my collaborators who made many helpful contributions to my Ph.D. thesis. Thanks to Dr. Stephen Skinner and Dr. Andrea Cavallaro (Imperial Collage London) for their help and contributions to the LEIS experiments and the interpretation of the results, and to Drs. Maxim Shishkin and Tom Ziegler (University of Calgary) for the DFT study of the effect of H<sub>2</sub>S on Ni-YSZ anodes. Also, I would like to express my gratitude to Drs. Aligul Buyukaksoy and

Ali Ahsen (Gebze Technical University) for their valuable XPS results. I would also like to thank Dr. David Avila-Brande (Universidad Complutense de Madrid) for the HRTEM micrographs shown in this thesis. Lastly, to Dr. Suresh Mulmi and Dr. Hala Handal, thank you very much for the help with the XRD and TGA experiments.

I would like to thank Dr. Michael Schoel for assistance with the SEM imaging and the EDX analysis shown in this thesis. Thank you also to Dr. Hebert Molero and Samuel Aquino for the very helpful XPS and AES analysis of the Ni-YSZ samples. I would also like to thank Mark Toonen, Andy Read, and Edward Cairns for help with the construction and repair of my experimental setup during my studies. I am also very grateful to the Department of Chemistry administration staff members, in particular Bonnie King, Janice Crawford, and Sarah Boschman, for all their help throughout the years. I would also like to thank the NSERC Solid Oxide Fuel Cells Canada (SOFCC) Strategic Research Network, Alberta Innovate Technology Futures (AITF), Carbon Management Canada (CMC), and the University of Calgary for financial support.

My deepest gratitude goes to my lovely wife, Anita Asameni, for her unconditional love and support throughout my studies and for being a caring mother to our beautiful children, Elijah and Lydia. I am also very thankful to my parents, my siblings, Bright Gomez, and James Addo for all their prayers and support throughout the years.

## **Dedication**

To my wife, Anita and our children, Elijah and Lydia and to my mother and my siblings.

## Table of Contents

Abstract.....	ii
Acknowledgements.....	iv
Dedication.....	vi
Table of Contents.....	vii
List of Tables.....	xi
List of Figures and Illustrations.....	xii
List of Symbols.....	xx
List of Abbreviations.....	xxi
Epigraph.....	xxiii
CHAPTER ONE: INTRODUCTION.....	1
1.1 Project background.....	1
1.2 Research objectives.....	5
1.3 Thesis organization.....	6
CHAPTER TWO: RELEVANT BACKGROUND.....	9
2.1 Reversible solid oxide fuel cells (RSOFCs).....	9
2.1.1 Operating principles of RSOFCs.....	11
2.2 Thermodynamics of RSOFCs.....	13
2.2.1 Modes of SOEC operation.....	16
2.2.2 Round-trip efficiency of RSOFCs.....	17
2.3 Materials for reversible solid oxide fuel cells.....	18
2.3.1 Fuel electrodes.....	19
2.3.1.1 Metal-based electrodes.....	19
2.3.1.2 Fluorite-based metal oxide fuel electrodes.....	20
2.3.1.3 Perovskite-based metal oxide fuel electrodes.....	20
2.3.2 Electrolytes.....	22
2.3.3 Oxygen electrodes.....	23
2.4 Application of RSOFCs for fuel production.....	24
2.4.1 H <sub>2</sub> O and CO <sub>2</sub> electrolysis in RSOFCs.....	24
2.4.2 Co-electrolysis of H <sub>2</sub> O+CO <sub>2</sub> in RSOFCs.....	25
2.4.3 Methane production in RSOFCs.....	27
2.5 Effect of H <sub>2</sub> S on RSOFC fuel electrodes.....	28
2.5.1 Effect of H <sub>2</sub> S on Ni-YSZ fuel electrode.....	28
2.5.2 Approaches used to develop sulfur tolerant fuel electrodes.....	30
2.6 Methods used to investigate SOFC and RSOFC electrodes and cell performance.....	32
2.6.1 Electrochemical methods.....	32
2.6.2 Electrochemical impedance spectroscopy (EIS).....	34
2.6.2 Cyclic voltammetry.....	36
2.7 Non-electrochemical methods used in this thesis work.....	37
CHAPTER THREE: EXPERIMENTAL METHODS.....	39
3.1 Material synthesis and preparation.....	39
3.1.1 Synthesis of La <sub>0.3</sub> M <sub>0.7</sub> Fe <sub>0.7</sub> Cr <sub>0.3</sub> O <sub>3-δ</sub> (M = Sr, Ca) perovskites.....	39

3.1.2 Preparation of screen printing organic carrier .....	39
3.1.3 NiO and Ytria stabilized zirconia (YSZ) powders .....	40
3.2 Cell fabrication .....	40
3.2.1 Ni-YSZ half and full cell fabrication.....	40
3.2.1.1 Fabrication of 3-electrode Ni-YSZ half cells .....	40
3.2.1.2 Fabrication of Ni-YSZ/YSZ/LSM-YSZ full cells .....	42
3.2.2 Fabrication of $\text{La}_{0.3}\text{M}_{0.7}\text{Fe}_{0.7}\text{Cr}_{0.3}\text{O}_{3-\delta}$ (M = Sr, Ca) half and full cells.....	42
3.2.2.1 Symmetrical $\text{La}_{0.3}\text{M}_{0.7}\text{Fe}_{0.7}\text{Cr}_{0.3}\text{O}_{3-\delta}$ (M = Sr, Ca, LMFCr)-based full cell fabrication .....	42
3.2.2.2 Fabrication of 2-and 3-electrode $\text{La}_{0.3}\text{M}_{0.7}\text{Fe}_{0.7}\text{Cr}_{0.3}\text{O}_{3-\delta}$ (M = Sr, Ca)-based half cells .....	44
3.2.3 Fabrication of LFCr-based thin film cells.....	45
3.2.4 Gases used for stability and electrochemical testing.....	46
3.3 Electrochemical cell testing .....	46
3.3.1 Electrochemical testing of Ni-YSZ half and full cells .....	46
3.3.2 Electrochemical testing of symmetrical $\text{La}_{0.3}\text{M}_{0.7}\text{Fe}_{0.7}\text{Cr}_{0.3}\text{O}_{3-\delta}$ (M = Sr, Ca)-based full and half cells.....	48
3.3.2.1 Testing of LMFCr-based 2-electrode half and full cells.....	48
3.3.2.2 3-Electrode LSFCr-based half cell testing.....	49
3.3.2.3 Electrochemical evaluation of Ni-YSZ and LMFCr-based cells.....	49
3.4 Material characterization methods.....	50
3.4.1 Powder X-ray diffraction (PXRD) .....	50
3.4.2 Fourier transform infrared (FTIR) spectroscopy .....	51
3.4.3 Thermogravimetric analysis (TGA) .....	51
3.4.4 Scanning electron microscopy/Energy dispersive X-ray spectroscopy (SEM/EDX) .....	52
3.4.5 High resolution transmission electron microscopy (HRTEM).....	52
3.4.6 Electron microprobe analysis .....	53
3.4.7 X-ray photoelectron spectroscopy (XPS).....	53
3.4.8 Auger electron spectroscopy (AES) .....	54
3.4.9 Low energy ion scattering spectroscopy (LEIS) .....	54

#### CHAPTER FOUR: ACTIVATION BEHAVIOR OF NI-YSZ FUEL ELECTRODE

(ANODE) IN LOW PPM $\text{H}_2\text{S}$ AT SUB- 600 °C .....	57
4.1 Introduction.....	57
4.2 Results and Discussion .....	59
4.2.1 Effect of $\text{H}_2\text{S}$ on 3-electrode Ni-YSZ half cell performance at 500-800 °C ...	59
4.2.2 Detailed electrochemical study of the activation of Ni-YSZ anode at 500 °C	63
4.2.3 Effect of $\text{H}_2\text{S}$ on Ni-YSZ anodes in 2-electrode full cell configuration at 500 °C .....	71
4.2.4 Understanding the $\text{H}_2\text{S}$ activation of Ni-YSZ anodes at < 600 °C .....	72
4.2.5 Density functional theory (DFT) analysis .....	83
4.3 Summary .....	85

<b>CHAPTER FIVE: PERFORMANCE AND SULFUR TOLERANCE OF</b>	
<b>LA<sub>0.3</sub>M<sub>0.7</sub>FE<sub>0.7</sub>CR<sub>0.3</sub>O<sub>3-Δ</sub> (M = SR, CA) SOLID OXIDE FUEL CELL ANODES ..86</b>	
5.1 Introduction.....	86
5.2 Results and Discussion .....	88
5.2.1 Performance of La <sub>0.3</sub> M <sub>0.7</sub> Fe <sub>0.7</sub> Cr <sub>0.3</sub> O <sub>3-δ</sub> (M = Sr, Ca) anodes in wet 30% H <sub>2</sub> /N <sub>2</sub> at 800 °C.....	88
5.2.2 Performance of LCFCr in H <sub>2</sub> /CO fuel mixtures at 800 °C.....	92
5.2.3 Chemical stability of LCFCr in H <sub>2</sub> S.....	95
5.2.4 Symmetrical LCFCr full cell studies in the presence or absence of H <sub>2</sub> S .....	97
5.2.5 Symmetrical half cell studies of LCFCr in the presence or absence of H <sub>2</sub> S in wet H <sub>2</sub> /N <sub>2</sub> .....	104
5.2.6 Understanding LCFCr activation and deactivation in H <sub>2</sub> S/H <sub>2</sub> environments.....	112
5.3 Summary.....	118
<b>CHAPTER SIX: STABILITY AND ELECTROCHEMICAL PERFORMANCE OF</b>	
<b>LA<sub>0.3</sub>SR<sub>0.7</sub>FE<sub>0.7</sub>CR<sub>0.3</sub>O<sub>3-Δ</sub> (LSFCr) REVERSIBLE SOFC ELECTRODES IN DRY CO<sub>2</sub>/CO ENVIRONMENTS .....</b>	
<b>120</b>	
6.1 Introduction.....	120
6.2 Results and Discussion .....	123
6.2.1 Chemical stability of LSFCr in pure CO <sub>2</sub> and CO <sub>2</sub> /CO atmospheres .....	123
6.2.1.1 Chemical stability of LSFCr in variable but dry pCO <sub>2</sub> (balance N <sub>2</sub> or He) .....	124
6.2.1.2 Chemical stability of LSFCr in dry CO <sub>2</sub> /CO mixtures .....	132
6.2.1.3 Chemical stability of LSFCr in dry CO/N <sub>2</sub> mixtures .....	135
6.2.2 Electrochemical performance of LSFCr in CO <sub>2</sub> and CO <sub>2</sub> /CO atmospheres .....	140
6.2.2.1 Performance of LSFCr-based RSOFC cell in dry CO <sub>2</sub> (balance N <sub>2</sub> ) .....	142
6.2.2.2 Performance of LSFCr RSOFC cell in dry CO <sub>2</sub> /CO gas mixtures .....	145
6.2.2.3 Stability of LSFCr-based RSOFC cells in dry CO/CO <sub>2</sub> mixtures .....	157
6.3 Summary.....	160
<b>CHAPTER SEVEN: THREE ELECTRODE HALF CELL STUDY OF</b>	
<b>LA<sub>0.3</sub>SR<sub>0.7</sub>FE<sub>0.7</sub>CR<sub>0.3</sub>O<sub>3-Δ</sub> (LSFCr) ELECTRODES IN CO<sub>2</sub>/CO ENVIRONMENTS .....</b>	
<b>162</b>	
7.1 Introduction.....	162
7.2 Results and Discussion .....	167
7.2.1 3-electrode half cell configurations .....	167
7.2.2 Validation of 3-electrode half cell data .....	167
7.2.3 LSFCr in 100% dry CO <sub>2</sub> using 3-electrode half cell.....	170
7.2.4 LSFCr in 30% CO <sub>2</sub> :30% CO (balance N <sub>2</sub> ) in using 3-electrode half cells .....	174
7.2.5 Performance of LSFCr WE in fixed CO content (balance CO <sub>2</sub> ).....	179
7.2.6 Effect of more extreme cathodic polarization of LSFCr WE on CO <sub>2</sub> reduction.....	180
7.3 Summary.....	183
<b>CHAPTER EIGHT: CONCLUSIONS AND SUGGESTED FUTURE WORK .....</b>	
<b>185</b>	
8.1 Main conclusions of this thesis work.....	185
8.2 Suggestions for future work.....	188

REFERENCES .....	190
APPENDIX.....	200

## List of Tables

Table 4.1 Resistance values* obtained by fitting the OCP impedance data (Figure 4.3 **) to the equivalent circuit shown in Figure 4.3a. ....	66
Table 5.1 Circuit element values* obtained by fitting the results in Figure 5.2** to the equivalent circuit model in Figure 5.1c .....	90
Table 5.2 Resistance values* obtained by fitting the impedance data in Figure 5.12** to the $R_s(R1CPE1)(R2CPE2)$ equivalent circuit model (Figure 5.1c) .....	107
Table 5.3 Calculated activation energies obtained from Figure 5.13 .....	110
Table 6.1 Elemental content from SEM-EDX analysis of the various regions of the SEM image in Figure 6.13 for LSF <sub>Cr</sub> , exposed to 30% CO:70% N <sub>2</sub> for 6 h at 800 °C.....	140
Table 7.1 Fitted parameters* from Figure 7.3a** using the $R_s(R1CPE1)(R2CPE2)(R3CPE3)$ equivalent circuit model (Figure 7.3c).....	171
Table 7.2 Fitted parameters* from Figure 7.5a** using the $R_s(R1CPE1)(R2CPE2)$ equivalent circuit model (Figure 7.5c).....	176
Table 7.3 Fitted parameters* from Figure 7.8a** using the $R_s(R1CPE1)(R2CPE2)$ equivalent circuit model (Figure 7.3c).....	182

## List of Figures and Illustrations

Figure 1.1 Schematic showing the estimated renewable energy share of global electricity production in 2015. Percentages do not add up internally due to rounding <sup>3</sup> . .....	2
Figure 1.2 Graphs showing (a) the world total energy consumption (quadrillion Btu) by energy source from 1990 to 2012 and a projection from 2012 to 2040. In (a) the dotted lines for coal and renewables show the projected effects of the U.S. Clean Power Plan, and (b) the world energy-related CO <sub>2</sub> emission (billion metric tons) by fuel type from 1990 to 2012 and a projection from 2012 to 2040 <sup>4</sup> . .....	3
Figure 2.1 Typical relationship between cell voltage and current for various state-of-the-art water electrolysis cells. $E_{th,water}$ and $E_{th,steam}$ are the thermoneutral voltages for water and steam electrolysis, respectively, while $E_{rev}$ is the reversible potential for water electrolysis at standard conditions <sup>33</sup> . .....	10
Figure 2.2 Schematic of a RSOFC <sup>30</sup> . .....	11
Figure 2.3 Energy (kJ/mol)-temperature profile for H <sub>2</sub> O and CO <sub>2</sub> <sup>60</sup> . .....	15
Figure 2.4 Representative current-voltage plot for a RSOFC operated in H <sub>2</sub> /H <sub>2</sub> O <sup>61</sup> . .....	16
Figure 2.5 Comparison of reversible solid oxide cell (ReSOC) technology to other energy storage systems as a function of investment cost per kWh per cycle and maximum discharge hours. Efficiency is denoted by the colors from purple to blue. Electricity arbitrage is possible for technologies that run at high efficiency, which are placed in the upper left part of the graph <sup>62</sup> . .....	18
Figure 2.6 Schematic of power output versus time for SOFCs with Ni-YSZ cermet anode, showing effect of sulfur poisoning <sup>159</sup> . .....	30
Figure 2.7 Representative impedance plots for a simulated simple RC circuit showing (a) the Nyquist plot, (b) impedance magnitude vs. frequency Bode plot, and (c) phase angle vs. frequency Bode plot. ....	36
Figure 3.1 Schematic of the Ni-YSZ-based 3-electrode half cell configuration. ....	41
Figure 3.2 Schematic of the 2-electrode full cell configuration. ....	42
Figure 3.3 Schematic of the LMFCr-based symmetrical full cell configuration. ....	43
Figure 3.4 Schematic of the LMFCr-based (a) 3-electrode and (b) 2-electrode half cell configurations. ....	45
Figure 3.5 Simplified schematic of the half cell test configuration. ....	47
Figure 3.6 Photo of the FCSH-V3 cell holder (Materials Mate, Italy). ....	48

Figure 4.1 Potentiostatic study of the effect of 5 ppm H<sub>2</sub>S exposure and removal on Ni-YSZ electrode as a function of temperature in humidified H<sub>2</sub>, showing the i-t plots at a 250 mV anode overpotential monitored at 50 °C increments from (a) 750-650 °C and (b) 600 -500°C. The 1 and 3 h times of exposure to 5 ppm H<sub>2</sub>S are marked. .... 60

Figure 4.2 Effect of cell thermal history on Ni-YSZ anode response to H<sub>2</sub>S exposure. Percentage change in H<sub>2</sub> oxidation current seen at Ni-YSZ anodes upon introduction of 5 ppm H<sub>2</sub>S in humidified H<sub>2</sub> for data acquired (a) from 800 °C down to 500 °C for Cell 1, (b) from 500°C up to 800 °C for Cell 2, and (c) a comparison plot showing the % i vs. temperature plot. A positive percentage change in current indicates H<sub>2</sub>S activation of the Ni anode, while negative changes indicate anode poisoning by H<sub>2</sub>S. .... 62

Figure 4.3 Response of Ni-YSZ anode (in 3-electrode cell) to H<sub>2</sub>S at the open circuit potential at 500 °C. (a) An example of Ni-YSZ anode impedance response during three cycles of 5 ppm H<sub>2</sub>S addition and removal, as seen in Figure 4.3b showing (i) before exposure to H<sub>2</sub>S, (ii) in 5 ppm H<sub>2</sub>S, and (iii) following removal of H<sub>2</sub>S and partial recovery in H<sub>2</sub>. (b) Resistances obtained from fitting the Nyquist plots to the equivalent circuit (Figure 4.3a) during the 75 h of three cycles of 5 ppm H<sub>2</sub>S addition and removal... 64

Figure 4.4 (a) i-t transients during introduction and removal of 5 ppm H<sub>2</sub>S in humidified H<sub>2</sub> at variable anodic overpotentials (50-250 mV) at 500 °C, and (b) the percent current increase versus time plots for the data in (a)..... 67

Figure 4.5 Cyclic voltammetry response of Ni-YSZ anode (Cell 3) with/without H<sub>2</sub>S. (a) Cyclic voltammetry ( $\pm$  250 mV at 5 mV/s) in humidified H<sub>2</sub> and after the addition of 5 ppm H<sub>2</sub>S at 500 °C and (b) the corresponding Tafel plots..... 70

Figure 4.6 Response of 2-electrode full cell (FC1) showing the i-t response during the introduction and removal of 5 ppm H<sub>2</sub>S in humidified H<sub>2</sub> at a 0.1 V cell potential (vs. OCP) at 500 °C..... 72

Figure 4.7 *Ex situ* XRD pattern for a Ni-YSZ anode after several days of electrochemical testing (OCP and polarized) in the presence of 5 ppm H<sub>2</sub>S added to humidified H<sub>2</sub> at 500 °C..... 75

Figure 4.8 SEM-EDX analysis of a Ni-YSZ anode after several days of electrochemical testing (OCP and polarized) at 500 °C in the presence of 5 ppm H<sub>2</sub>S added to H<sub>2</sub>. The “X” mark on the SEM image shows one of the locations where the EDX analysis was carried out. .... 76

Figure 4.9 XPS analysis of Ni-YSZ anode surface, after removal of the porous Ni current collector, following electrochemical studies at 500 °C and at an anode overpotential of 250 mV in 5 ppm H<sub>2</sub>S in humidified H<sub>2</sub> (half cell cooled down in H<sub>2</sub>). Deconvolution (156-175 eV) of the XPS pattern confirms the presence of sulfur (S2p) in the form of sulfate (169.9 and 171.1 eV), and sulfide (162.6 and 163.8 eV) on the sample surface. .... 77

Figure 4.10 Auger electron spectroscopy (AES) analysis of the Ni-YSZ cermet after exposure to 5 ppm H <sub>2</sub> S at 500 °C for 72 h and then rapidly cooled to room temperature showing (a) SEM image and AES elemental mapping for (b) Ni, (c) S, (d) Zr, (e) the combined Ni (green) and Zr (blue) maps, and (f) the combined Ni (green), S (yellow) and Zr (blue) elemental maps.....	79
Figure 4.11 LEIS <sup>4</sup> He <sup>+</sup> surface analysis of Ni-YSZ anode exposed to 10 ppm H <sub>2</sub> S added to humidified H <sub>2</sub> at 500 °C for 72 h, showing the spectrum for (a) the initial scan before any sputtering, (b) scan 4 after sputter removal of several layers, and (c) scan 40 after more sputtering to reach the underlying bulk composition. ....	81
Figure 4.12 LEIS depth-profile analysis of Ni-YSZ anode exposed to 10 ppm H <sub>2</sub> S added to humidified H <sub>2</sub> at 500 °C for 72 h showing (a) the Ni and Y+Zr profiles, and (b) the O and S profiles. ....	82
Figure 4.13 LEIS depth-profile analysis of a Ni foil exposed to 10 ppm H <sub>2</sub> S at humidified H <sub>2</sub> at 500 °C for 72 h showing (a) the Ni profile and (b) the O and S profiles. ....	83
Figure 5.1 OCP impedance data for symmetrical full cell based on La <sub>0.3</sub> M <sub>0.7</sub> Fe <sub>0.7</sub> Cr <sub>0.3</sub> O <sub>3-δ</sub> (M = Sr, Ca) electrodes, at 800 °C, showing (a) the Nyquist and (b) the Bode plots, all in wet 30% H <sub>2</sub> /N <sub>2</sub> gas mixtures at the fuel electrode and with air exposure at the oxygen electrode, and (c) equivalent circuit used for data fitting. ....	89
Figure 5.2 OCP impedance data for symmetrical full cell based on La <sub>0.3</sub> Ca <sub>0.7</sub> Fe <sub>0.7</sub> Cr <sub>0.3</sub> O <sub>3-δ</sub> (LCFCr) electrodes at 800 °C and showing (a) the Nyquist and (b) the Bode plots, all in wet 30% H <sub>2</sub> /N <sub>2</sub> gas mixtures at the fuel electrode and with air or O <sub>2</sub> exposure at the oxygen electrode. ....	90
Figure 5.3 Performance plot for symmetrical full cell based on La <sub>0.3</sub> M <sub>0.7</sub> Fe <sub>0.7</sub> Cr <sub>0.3</sub> O <sub>3-δ</sub> (M = Sr, Ca) electrodes and operated at 800 °C, all in wet 30% H <sub>2</sub> /N <sub>2</sub> gas mixture at the fuel electrode and with air exposure at the oxygen electrode. ....	92
Figure 5.4 OCP impedance data for symmetrical full cell based on two LCFCr electrodes at 800 °C, showing (a) the Nyquist and (b) the Bode plots, all in wet 30% H <sub>2</sub> /N <sub>2</sub> , 15% H <sub>2</sub> :15% CO, or 30% CO gas mixtures at the fuel electrode and with air exposure at the oxygen electrode. ....	93
Figure 5.5 (a) Performance plot for symmetrical full cell, based on LCFCr electrodes, operated at 800 °C in wet 30% H <sub>2</sub> /N <sub>2</sub> , 15% H <sub>2</sub> :15% CO, or 30% CO gas mixtures at the fuel electrode and with air exposure at the oxygen electrode, and (b) the ASR-i plots (derived from the i-V plot in (a)) for wet 30% H <sub>2</sub> /N <sub>2</sub> .....	95
Figure 5.6 <i>Ex situ</i> XRD patterns showing the chemical stability of La <sub>0.3</sub> Ca <sub>0.7</sub> Fe <sub>0.7</sub> Cr <sub>0.3</sub> O <sub>3-δ</sub> (LCFCr) powder (i) as-prepared, and (ii) after exposure to 30 ppm H <sub>2</sub> S/N <sub>2</sub> atmosphere with a 24 h dwell time at 800 °C. The sample in (ii) was heated and cooled at a ramp rate of 5 °C/min in H <sub>2</sub> S/N <sub>2</sub> atmosphere.....	96

Figure 5.7 OCP and polarized EIS response for symmetrical, 2-electrode full cell, based on LCFCr electrodes at 800 °C, with humidified 30% H<sub>2</sub>/N<sub>2</sub> (with or without 9 ppm H<sub>2</sub>S) fed to the fuel electrode and air fed to the oxygen electrode, showing the Nyquist plots acquired at (a) the OCP, (b) at 0.1 V less than the cell voltage at open circuit, and (c) at 0.3 V less than the cell voltage at open circuit. .... 98

Figure 5.8 OCP and polarized EIS data obtained from symmetrical full cell based on two LCFCr electrodes at 800-650 °C, with wet 30% H<sub>2</sub>/N<sub>2</sub>, with or without 9 ppm H<sub>2</sub>S, fed to the fuel electrode and air fed to the oxygen electrode, showing the R<sub>p</sub> vs E plots at (a) 800 °C, (b) 750 °C, (c) 700 °C, and (d) 650 °C. .... 99

Figure 5.9 EIS response from symmetrical full cells based on LCFCr electrodes at 800-650 °C, with wet 30% H<sub>2</sub>/N<sub>2</sub>, with or without 9 ppm H<sub>2</sub>S, fed to the fuel electrode and air fed to the oxygen electrode, showing (a) the % R<sub>p</sub> change at the OCP, 0.1 V, and 0.3 V vs. the OCP, and (b) R<sub>p</sub> at 0.3 V vs. the OCP. Negative %R<sub>p</sub> values represent LCFCr activation, while positive values show deactivation. .... 100

Figure 5.10 Short term study of symmetrical full cells based on two LCFCr electrodes at 800 °C, with wet 30% H<sub>2</sub>/N<sub>2</sub>, with or without 9 ppm H<sub>2</sub>S, fed to the fuel electrode and air fed to the oxygen electrode, at a constant cell voltage of 0.3 V less than the cell OCP, showing (a) the current versus time (i-t) plot and the corresponding (b) Nyquist and (c) Bode plots. .... 102

Figure 5.11 i-t response of a symmetrical full cell, based on two LCFCr electrodes at 600 °C with wet 30% H<sub>2</sub>/N<sub>2</sub>, with or without 9 ppm H<sub>2</sub>S, fed to the fuel electrode and air fed to the oxygen electrode, at a constant cell voltage of 0.3 V less than the cell OCP. .... 103

Figure 5.12 OCP EIS response for symmetrical half cell based on LCFCr electrodes at 800-600 °C in wet 50% H<sub>2</sub>/N<sub>2</sub>, with or without 10 ppm H<sub>2</sub>S, at (a) 800 °C, (b) 750 °C, (c) 700 °C (d) 650 °C, and (e) 600 °C. .... 105

Figure 5.13 Arrhenius plots for the EIS-obtained R values for a symmetrical half cell based on two LCFCr electrodes at 800-600 °C in wet 50% H<sub>2</sub>/N<sub>2</sub>, with or without 10 ppm H<sub>2</sub>S. (a) high frequency resistance R<sub>1</sub>, (b) low frequency resistance R<sub>2</sub>, and (c) polarization resistance R<sub>p</sub>. .... 109

Figure 5.14 Short term potentiostatic study of a symmetrical half cell involving two LCFCr electrodes in humidified 50% H<sub>2</sub>/N<sub>2</sub>, with 10 ppm H<sub>2</sub>S exposure and removal, at 0.3-1.0 V cell bias at (a) 850-800 °C, (b) 750-600 °C, (c) % current density change vs. temperature at 0.3 V from 850-600 °C, and (d) % current density change vs. applied potential at 800 °C. .... 111

Figure 5.15 Electron microprobe WDX elemental mapping of the polished cross-section of a LCFCr fuel electrode, slowly cooled in humidified 30% H<sub>2</sub>/N<sub>2</sub> containing 9 ppm H<sub>2</sub>S to 30 °C, after several days of electrochemical testing of the cell, in the temperature range of 600-800 °C. .... 113

- Figure 5.16 XPS spectra of LCFCr thin film samples exposed to humidified 30% H<sub>2</sub>/N<sub>2</sub>, with or without 10 ppm H<sub>2</sub>S addition, at 800 °C for 2 h, showing the peaks for (a) La, (b) Ca, (c) Fe, and (d) Cr. All samples were quenched at 800 °C instead of cooling slowly to 30 °C..... 114
- Figure 5.17 XPS spectra of LCFCr thin film samples exposed to humidified 30% H<sub>2</sub>/N<sub>2</sub>, showing the peaks for (a) Fe at 600 °C, with or without H<sub>2</sub>S addition for 5 h, and (b) a comparison plot of the Fe peaks at 600 °C and 800 °C. All samples were slowly cooled from either 600 °C or 800 °C to 30 °C in humidified 30% H<sub>2</sub>/N<sub>2</sub> containing 10 ppm H<sub>2</sub>S. 115
- Figure 5.18 XPS spectra of LCFCr thin film samples exposed to humidified 50% H<sub>2</sub>/N<sub>2</sub>, with or without H<sub>2</sub>S addition, at 800 and 600 °C for 5 h, showing the S2p peak after exposure at (a) 600 °C and (b) 800 °C..... 116
- Figure 6.1 *Ex situ* XRD patterns showing the chemical stability of the LSFCr powder (i) as-prepared and (ii) after exposure to dry 100% CO<sub>2</sub> atmosphere with a 24 h dwell time at 800 °C. Sample (ii) was heated and cooled at a ramp rate of 5 °C/min in a 100% CO<sub>2</sub> atmosphere. The symbol used to identify the LSFCr perovskite peaks is (#). ..... 125
- Figure 6.2 (a) *In situ* XRD patterns of LSFCr powder in dry 100% CO<sub>2</sub> from 30-800 °C and (b) magnified XRD pattern showing the (110) peak. The symbol used to identify the LSFCr (perovskite) peaks is (#)..... 126
- Figure 6.3 TG profiles of LSFCr powder from 30-900 °C at 3 °C/min in (a) 60% CO<sub>2</sub> (balance N<sub>2</sub>) and air, (b) multiple heating/cooling cycles in 60% CO<sub>2</sub> (balance N<sub>2</sub>), (c) heating profile in 60% CO<sub>2</sub> (balance N<sub>2</sub>) to 800 °C with 1 hr holding at 600 and 800 °C, and (d) isothermal profile at 600 and 800 °C from Figure 6.3c..... 128
- Figure 6.4 (a) TGA profile of LSFCr powder in 20% O<sub>2</sub> and 20% CO<sub>2</sub> (both balance He) from 30-800 °C at a 5 °C/min ramp rate and (b) plot showing oxygen non-stoichiometry (δ)..... 130
- Figure 6.5 Room temperature FTIR transmittance spectra for a homogenous mixture of dried KBr and powder samples of (i) SrCO<sub>3</sub>, (ii) as-prepared LSFCr, and (iii) LSFCr exposed to dry CO<sub>2</sub> from 30-800 °C with a 24 h dwell time at 800 °C. Sample (iii) was heated and cooled at a ramp rate of 5 °C/min in a dry 100 % CO<sub>2</sub> atmosphere..... 131
- Figure 6.6 SEM images of LSFCr powder (a) as-prepared and (b) exposed to dry CO<sub>2</sub> from 30-800 °C with a 24 h dwell time at 800 °C. Sample (b) was heated and cooled at a ramp rate of 5 °C/min in the same gas atmosphere..... 132
- Figure 6.7 *Ex situ* XRD patterns, showing the chemical stability of the LSFCr powder (a) as-prepared (i), exposed to 90% CO<sub>2</sub>:10% CO<sub>2</sub> (ii), and (b) 70% CO<sub>2</sub>:30% CO atmosphere, all from 30-800 °C with a 24 h dwell time at 800 °C. All samples were heated and cooled at a ramp rate of 5 °C/min in the same gas atmosphere. The symbols used to identify the peaks are as follows: (#) LSFCr (perovskite) and (+) SrCO<sub>3</sub>..... 133

- Figure 6.8 SEM images of LSFCr powders (a) as-prepared and after exposure to (b) 10% 90% CO<sub>2</sub>:10% CO and (c) 70% CO<sub>2</sub>:30% CO, from 30-800 °C with a 24 h dwell time at 800 °C. All samples were heated and cooled at 5 °C/min in the same gas atmosphere..... 134
- Figure 6.9 HRTEM images recorded along [001]<sub>p</sub> zone axis (p refers to the cubic perovskite) for LSFCr powders (a) as-prepared (b) dry and pure CO<sub>2</sub>, and (c) 90% CO<sub>2</sub>:10% CO, from 30-800 °C with a 24 h dwell time at 800 °C. All samples were heated and cooled at a ramp rate of 5 °C/min in the same gas atmosphere..... 135
- Figure 6.10 *Ex situ* XRD patterns showing the stability of the La<sub>0.3</sub>Sr<sub>0.7</sub>Fe<sub>0.7</sub>Cr<sub>0.3</sub>O<sub>3-δ</sub> (LSFCr) powder exposed from 30-800 °C to (i)10% CO:90% N<sub>2</sub> held for 24 h at 800 °C (ii) 30% CO:70% N<sub>2</sub> held for 6 h at 800 °C, (iii) 30% CO:70% N<sub>2</sub> held for 24 h at 800 °C. All samples were heated and cooled at a ramp rate of 5 °C/min in the same gas atmosphere. The symbols used to identify the peaks are as follows: (#) LSFCr (perovskite); (Δ) LaSrFeO<sub>4</sub>-based phase (K<sub>2</sub>NiF<sub>4</sub>); and (O) α-Fe..... 136
- Figure 6.11 *Ex situ* XRD patterns showing the re-exposure of decomposed (i) Fig. 6.10 (ii) and (ii) Fig.6.10 (iii) LSFCr sample to air from 30-800 °C, with 24 h holding time at 800 °C. All samples were heated and cooled at a ramp rate of 5 °C/min in the air atmosphere. The symbols used to identify the peaks are as follows: (#) LSFCr (perovskite); (Δ) LaSrFeO<sub>4</sub>-based phase (K<sub>2</sub>NiF<sub>4</sub>); and (x) impurities..... 137
- Figure 6.12 SEM images of LSFCr powder exposed to (a) 10% CO:90% N<sub>2</sub> for 24 h at 800 °C, (b) 30% CO:70% N<sub>2</sub> for 6 h at 800 °C, (c) 30% CO:70% N<sub>2</sub> for 24 h at 800 °C, and (d) exposure of the Fig. 6.12b sample to air for 24 h at 800 °C. All samples were heated and cooled at a ramp rate of 5 °C/min in the same gas atmosphere..... 138
- Figure 6.13 SEM image of LSFCr powder exposed to 30% CO:70% N<sub>2</sub> held for 6 h at 800 °C showing the four regions analyzed by EDX. .... 139
- Figure 6.14 A cross-sectional SEM image of the LSFCr/GDC/YSZ/GDC/LSFCr symmetrical RSOFC under study here, showing the fuel electrode and the oxygen electrode after electrochemical cell testing in CO<sub>2</sub>/CO atmospheres. Inset shows a higher magnification image of the fuel electrode of the cell..... 141
- Figure 6.15 OCP and polarized impedance data for symmetrical RSOFC with a configuration of LSFCr/GDC/YSZ/GDC/LSFCr, operated at 800 °C and showing (a) the Nyquist plot and (b) the phase angle Bode plot, in 100%, dry CO<sub>2</sub> at the fuel electrode and with air exposure at the oxygen electrode..... 143
- Figure 6.16 CV of the symmetrical LSFCr/GDC/YSZ/GDC/LSFCr full cell showing (a) the response in dry 100% CO<sub>2</sub>, 50% CO<sub>2</sub>:50% N<sub>2</sub>, and 10 % CO<sub>2</sub>:90% N<sub>2</sub> gas mixtures fed to the fuel electrode and with air exposure at the oxygen electrode at 800 °C, and (b) temperature studies of 100% CO<sub>2</sub> fed to the fuel electrode at 850, 800 and 750 °C and with air exposure at the oxygen electrode..... 145

Figure 6.17 OCP impedance data for symmetrical RSOFC with a configuration of LSFCr/GDC/YSZ/GDC/LSFCr, operated at 800 °C, and showing (a) the Nyquist and (b) the Bode plots, all in 90% CO<sub>2</sub>:10% CO and 70% CO<sub>2</sub>:30% CO gas mixtures at the fuel electrode and with air exposure at the oxygen electrode. .... 146

Figure 6.18 CV data obtained from symmetrical full cell with a configuration of LSFCr/GDC/YSZ/GDC/LSFCr, operated at 800 °C, showing (a) the CV plots acquired at 1 mV/s scan rate, and (b) the ASR-i plots (derived from the CV data in (a)), all in 90% CO<sub>2</sub>:10% CO and 70% CO<sub>2</sub>:30% CO gas mixtures at the fuel electrode and with air exposure at the oxygen electrode. .... 147

Figure 6.19 CVs (acquired at 1 mV/s) of the symmetrical LSFCr full cell, showing temperature studies at 850, 800 and 750 °C for 70% CO<sub>2</sub>:30% CO fed to the fuel electrode and air exposure to the oxygen electrode. .... 149

Figure 6.20 Temperature studies of the LSFCr/GDC/YSZ/GDC/LSFCr cell operated at 600-800 °C, showing (a) OCP EIS Nyquist response at 750-850 °C (b) OCP EIS Nyquist response at 600-700 °C, (c) phase angle Bode plot, and (d) activation energy plot of the EIS determined resistances, all in 70% CO<sub>2</sub>:30% CO gas mixture at the fuel electrode and air at the oxygen electrode. .... 151

Figure 6.21 Impedance response (at the open circuit potential) of a symmetrical LSFCr half cell tested in air at 800 °C, showing total R<sub>p</sub> of 0.50 Ω cm<sup>2</sup> for both electrodes. .... 152

Figure 6.22 Impedance response (at the open circuit potential) of a symmetrical GDC/YSZ/GDC cell, all in 90% CO<sub>2</sub>:10% CO at 800 °C, showing a total R<sub>p</sub> of 50 Ω cm<sup>2</sup> for both GDC electrodes. .... 154

Figure 6.23 OCP and polarized EIS response of the symmetrical LSFCr-based full cell, operated at 800 °C with 70% CO<sub>2</sub>:30% CO fed to the fuel electrode and air fed to the oxygen electrode, showing (a) the Nyquist and (b) the phase angle Bode plots (acquired at OCP, 0.2 V vs. OCP, and -0.2 V vs. OCP) and (c) the corresponding resistances obtained from the fitted Nyquist plots using the R<sub>s</sub>(R1CPE1)(R2CPE2) equivalent circuit model. .... 155

Figure 6.24 Polarization resistance (R<sub>p</sub>) of the symmetrical LSFCr full cell, operated at 800 °C with 90% CO<sub>2</sub>:10% CO, 70% CO<sub>2</sub>:30% CO, and 50% CO<sub>2</sub>:50% CO fed to the fuel electrode and air fed to the oxygen electrode. R<sub>p</sub> obtained at different fuel electrode potentials from the fitted Nyquist plots using the R<sub>s</sub>(R1CPE1)(R2CPE2) equivalent circuit model. .... 156

Figure 6.25 Medium term stability study of the symmetrical LSFCr-based RSOFC, tested for 133 h at 800 °C with 90% CO<sub>2</sub>:10% CO fed to the fuel electrode and air fed to the oxygen electrode, showing (a) the V-t plot at a -100 mA/cm<sup>2</sup> galvanostatic hold and (b) the corresponding Nyquist plots collected at the open circuit potential at 0, 20, 120 and 133 h. .... 157

Figure 6.26 Electron microprobe WDX elemental mapping of the polished cross-section of a LSFCr fuel electrode after several days of electrochemical testing of the cell CO <sub>2</sub> /CO atmospheres in the temperature range of 600-850 °C.....	159
Figure 7.1 Schematic of (a) the LSFCr 3-electrode half cell configuration used and (b) the electrochemical processes occurring at the gas/electrode/electrolyte interface during CO <sub>2</sub> reduction and CO oxidation. ....	166
Figure 7.2 (a) Impedance response (at the open circuit potential) of a LSFCr WE in a 3-electrode cell and the two LSFCr electrodes in the 2-electrode half cell, both tested in 70% CO <sub>2</sub> :30% CO at 800 °C, and (b) the equivalent circuit model used to fit the data in (a). ....	169
Figure 7.3 OCP and polarized (+100 mV and -100 mV) impedance response of LSFCr WE in 3-electrode half cell, operated at 800 °C in 100% CO <sub>2</sub> , showing (a) the Nyquist plots, (b) the phase angle Bode plots, and (c) the equivalent circuit model used to fit the data in (a). ....	171
Figure 7.4 Cyclic voltammetry data obtained for LSFCr WE in 3-electrode half cell, operated at 800 °C in pure CO <sub>2</sub> at 5 mV/s. ....	173
Figure 7.5 OCP and polarized (+100 mV and -100 mV) EIS response of the LSFCr WE in 3 electrode half cell experiment at 800 °C in 30% CO <sub>2</sub> :30% CO:40% N <sub>2</sub> , showing (a) the Nyquist plots, (b) the phase angle Bode plots, and (c) the equivalent circuit model used to fit the data in (a). ....	175
Figure 7.6 Cyclic voltammetry (CV) data obtained for LSFCr WE in 3-electrode half cell at 800 °C in 30% CO <sub>2</sub> :30% CO:40% N <sub>2</sub> at 1 mV/s. ....	177
Figure 7.7 OCP EIS response of LSFCr in 3-electrode half cell, operated at 800 °C in either 70% CO <sub>2</sub> :30% CO or 30% CO <sub>2</sub> :30% CO:40% N <sub>2</sub> environments. ....	180
Figure 7.8 OCP and negatively polarized EIS response of LSFCr WE in 3-electrode half cell, operated at 800 °C in 90% CO <sub>2</sub> :10% CO, showing (a) the Nyquist plots, (b) the phase angle Bode plots, and (c) the resistance vs. overpotential plot. ....	181

## List of Symbols

<b>Symbol</b>	<b>Definition</b>	<b>Unit</b>
$A$	Cross-sectional area	$cm^2$
$a$	Lattice constant	$\text{\AA}$
$C$	Capacitance	$F$
$E$	Potential	$V$
$E_a$	Activation energy	$eV$
$f$	Frequency	$Hz$
$F$	Faraday constant	$C/mol$
$\eta$	Efficiency	%
$R_s$	Series resistance	$\Omega cm^2$
$R_p$	Polarisation resistance	$\Omega cm^2$
$R$	Universal gas constant	$JK^{-1} mol^{-1}$
$T$	Temperature	$K^\circ C$
$TEC$	Thermal expansion coefficient	$K^{-1}$
$Z$	Impedance	$\Omega$
$Z'$	In-phase resistance	$\Omega$
$Z''$	Out-of-phase resistance	$\Omega$
$\theta$	Theta angle	<i>degrees</i>
$\rho$	Density	$g/cm^3$
$\omega$	Angular frequency	$rad/s$

## List of Abbreviations

ac	Alternating current
AES	Auger electron spectroscopy
AFC	Alkaline fuel cell
ASR	Area specific resistance
BV	Butler Volmer
CCS	Carbon capture and storage
CCU	Carbon conversion and utilization
CE	Counter electrode
CHP	Combined heat and power
COP	Conference of Parties
CPE	Constant phase element
CV	Cyclic voltammetry
dc	Direct current
DFT	Density functional theory
DME	Dimethyl ether
EDX	Energy dispersive X-ray spectroscopy
EIS	Electrochemical impedance spectroscopy
FC	Fuel cell
F-T	Fischer Tropsch
FRA	Frequency response analyzer
GDC	Gadolinium doped ceria
GGE	Gasoline gallon equivalent
HER	Hydrogen evolution reaction
HHV	High heating value
HOR	Hydrogen oxidation reaction
HRTEM	High resolution transmission electron microscopy
LCFCr	$\text{La}_{0.3}\text{Ca}_{0.7}\text{Fe}_{0.7}\text{Cr}_{0.3}\text{O}_{3-\delta}$
LEIS	Low energy ion scattering
LMFCr	$\text{La}_{0.3}\text{M}_{0.7}\text{Fe}_{0.7}\text{Cr}_{0.3}\text{O}_{3-\delta}$ (M = Ca, Sr)
LSCF	$\text{La}_{1-x}\text{Sr}_x\text{Co}_{1-y}\text{Fe}_y\text{O}_{3-\delta}$

LSCM	Strontium-manganese-doped lanthanum chromite
LSFCr	$\text{La}_{0.3}\text{Sr}_{0.7}\text{Fe}_{0.7}\text{Cr}_{0.3}\text{O}_{3-\delta}$
LSGM	$\text{La}_{0.8}\text{Sr}_{0.2}\text{Ga}_{0.8}\text{Mg}_{0.2}\text{O}_{3-\delta}$
LSM	$\text{La}_{(1-x)}\text{Sr}_x\text{MnO}_3$
MFC	Mass flow controller
MIEC	Mixed ionic and electronic conductor
NASA	National Aeronautics and Space Administration
Ni-YSZ	Nickel-ytria stabilized zirconia
OCP	Open circuit potential
PEMFC/PEM	Proton exchange membrane fuel cell
PXRD	Powder X-ray diffraction
RE	Reference electrode
RSOFCs	Reversible solid oxide fuel cells
SEM	Scanning electron microscopy
SDC	$\text{Ce}_{1-x}\text{Sm}_x\text{O}_{2-\delta}$
SRIM	Stopping and range of ions in matter
SOC	Solid oxide cell
SOEC	Solid oxide electrolysis cell
SOFC	Solid oxide fuel cell
TGA	Thermogravimetric analysis
TPB	Triple phase boundary
TPBL	Triple phase boundary length
TS	Tafel slope
WDX	Wavelength dispersive X-ray spectroscopy
WE	Working electrode
XRD	X-ray diffraction
XPS	X-ray photoelectron spectroscopy
YSZ	Ytria-stabilized zirconia

## Epigraph

“After climbing a great hill, one only finds that there are many more hills to climb.”

Mandela, Nelson. *Long Walk to Freedom: The Autobiography of Nelson Mandela*. Boston: Back Bay Books, 1995

## Chapter One: **Introduction**

### **1.1 Project background**

The increase in the world's energy demand, coupled with climate change issues, have led to efforts to reduce CO<sub>2</sub> emissions from fossil fuel consumption by incorporating renewable electrical energy sources, such as hydropower, wind and solar, into the energy sector<sup>1, 2</sup>. According to the Renewable Energy Network 21<sup>st</sup> Century (REN21) 2016 renewables report<sup>3</sup>, in 2015, renewable energy contributed about 23.7% (1,849 GW) to global electricity, showing an increase of 8% from 2014. Out of the 23.7% renewable power capacity in 2015, hydropower contributed about 16.6% (1064 GW), wind contributed 3.7% (433 GW), and solar photovoltaics (PV) contributed 1.2% (227 GW) (Figure 1.1). Further, the capacity of wind power increased from 59 GW in 2005 to 433 GW by the end of 2015, while solar photovoltaic (PV) global capacity increased from 5.1 GW in 2005 to 233 GW in 2015.

Some of the reasons for the rapid growth in renewables includes environmental concerns, improving price competitiveness of renewable technologies, policy initiatives, and the growing energy demand of developing and emerging economies<sup>3</sup>. However, energy production from solar and wind is intermittent, and thus electricity generated when these sources are readily available and demand is low must be efficiently stored for later use when energy is needed.

There are various types of electrical energy storage systems, each having different discharge times (seconds to hours) and storage capacity (kW to MW). The two areas gaining extensive research interest are batteries (Li-ion, redox-flow) and chemical storage (H<sub>2</sub>), using reversible fuel cells (electrolysers). With electrolyzers, surplus electrical energy is stored as chemical energy by the conversion of H<sub>2</sub>O and/or CO<sub>2</sub> to H<sub>2</sub> and/or CO. The two types of electrolyzers are low-temperature electrolysers (< 100 °C), such as proton exchange membrane

systems (PEM) and, alkaline electrolyzers, and high-temperature electrolyzers (> 500 °C), such as solid oxide electrolysis cells (SOECs).

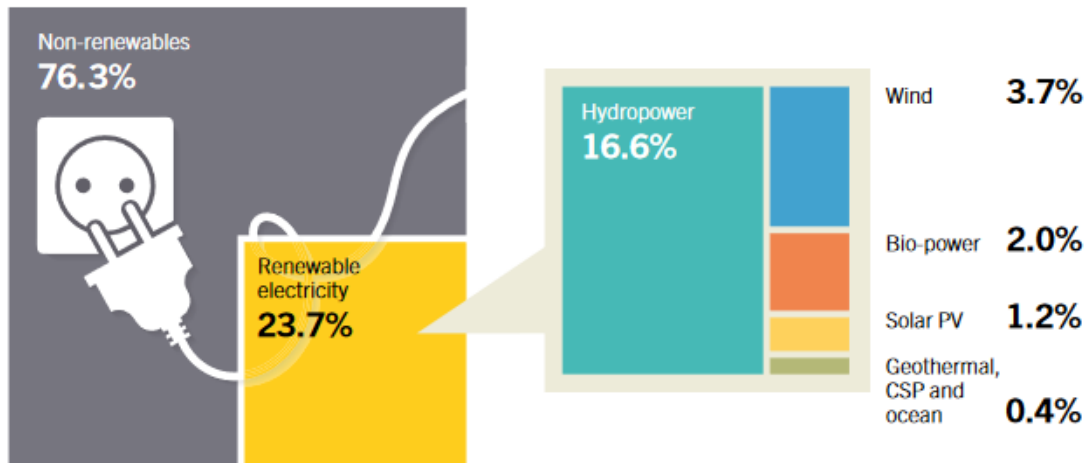


**Figure 1.1 Schematic showing the estimated renewable energy share of global electricity production in 2015. Percentages do not add up internally due to rounding<sup>3</sup>.**

Even though renewable energy (RE) generation has increased in the past few years and is being projected to increase further in the coming years, fossil fuel sources still continue to dominate our energy supply<sup>4</sup>. The International energy outlook 2016 report from the U.S. Energy Information Administration (May 2016)<sup>4</sup> projected that, up to 2040, the world's dependence on fossil fuels will continue to increase, as shown in Figure 1.2a. This is expected to lead to an increase in the world's energy CO<sub>2</sub> emissions (Figure 1.2b). If greenhouse gas (GHG) emissions are not controlled, by the end of the 21<sup>st</sup> century, it has been projected that the earth's temperature will be close to 5 °C higher than at present<sup>5, 6</sup>.

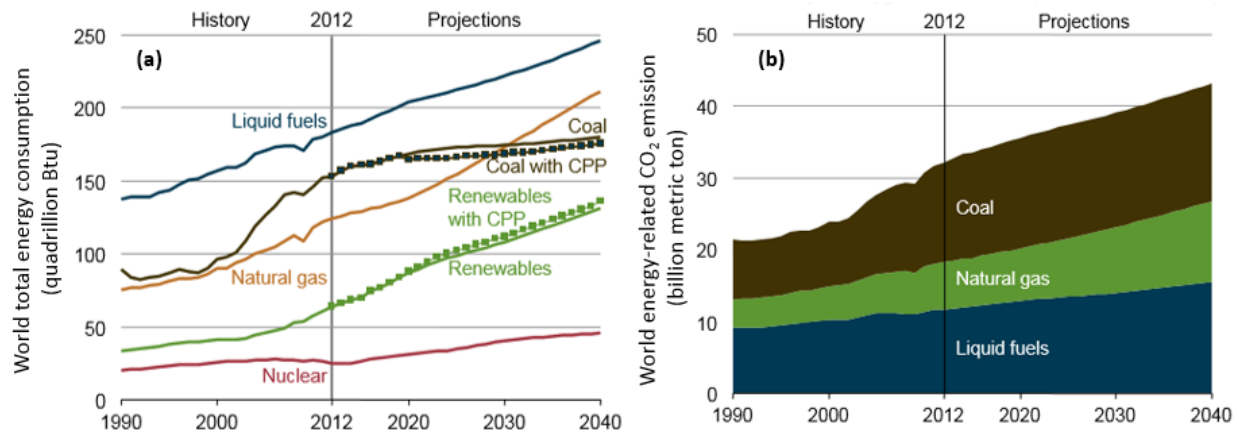


**Figure 1.2** Graphs showing (a) the world total energy consumption (quadrillion Btu) by energy source from 1990 to 2012 and a projection from 2012 to 2040. In (a) the dotted lines for coal and renewables show the projected effects of the U.S. Clean Power Plan, and (b) the world energy-related CO<sub>2</sub> emission (billion metric tons) by fuel type from 1990 to 2012 and a projection from 2012 to 2040<sup>4</sup>.

Therefore, it is critical to mitigate CO<sub>2</sub> emissions to minimize the predicted increase in the earth's temperature. Some of the strategies being adopted include carbon capture and storage (CCS) and carbon conversion and utilization (CCU). Briefly, in CCS, CO<sub>2</sub> is captured by pre-combustion, post-combustion, or oxy-fuel methods and the captured CO<sub>2</sub> is then compressed and transported for either geological or ocean storage. To meet the Paris Conference of Parties (COP 21, 2015) agreement climate goals of limiting the earth temperature increase to < 2 °C, an acceleration of CCS development and deployment is very important<sup>7</sup>. Currently, there are 21 large-scale CCS projects in operation or construction, with a combined CO<sub>2</sub> capture capacity of about 40 million tons annually<sup>7</sup>. It has been reported that, in order to meet the 2 °C target, an estimated 4,000 million tons of CO<sub>2</sub> need to be captured and stored in 2040<sup>7, 8</sup>. However, one of the main challenges of CCS technology is that it requires large capital investment, therefore hindering its rapid implementation<sup>9</sup>.

In CCU, the captured CO<sub>2</sub> is either utilized directly in, for example, enhanced oil recovery (EOR), or is used as a feedstock to produce useful marketable chemicals, such as methanol, ethanol or urea<sup>10, 11</sup>. The four main approaches used for CO<sub>2</sub> conversion to higher value products are chemical conversion, mineralization, biological conversion, and electrochemical conversion<sup>11</sup>. In electrochemical conversion, extensive research is being carried out to convert CO<sub>2</sub> to fuel at either low or high operating temperatures. The low-temperature (<100 °C) conversion of CO<sub>2</sub> has been attempted in aqueous, organic, or ionic liquid solvents, typically using metal-based catalysts (Cu, Au, Sn, Pd etc.), producing H<sub>2</sub>, CO, formic acid, methanol, ethanol etc.<sup>12, 13</sup>. However, these reactions are very slow, requiring high overpotentials, and are also not selective<sup>13, 14</sup>.

For these reasons, research is also focused on high temperature (HT) electrolysis systems, particularly reversible solid oxide fuel cells (RSOFCs). RSOFCs are single units that can run in both the electrolysis mode (solid oxide electrolysis cell (SOEC)) and the electricity generation mode (solid oxide fuel cell (SOFC)) at high temperatures (600-950 °C). RSOFCs are very efficient and have both thermodynamic and kinetic advantages over the low temperature systems. RSOFCs can be used for the electrolysis of H<sub>2</sub>O to H<sub>2</sub>, CO<sub>2</sub> to CO, or the co-electrolysis of H<sub>2</sub>O+CO<sub>2</sub> to syngas (H<sub>2</sub>+CO) and CH<sub>4</sub><sup>15-17</sup>. The syngas can then be used as a feedstock for the Fischer-Tropsch process to produce synthetic fuels.

Solid oxide cells for the electrolysis of H<sub>2</sub>O and the co-electrolysis of CO<sub>2</sub>/H<sub>2</sub>O were first employed by NASA in the 1960s to produce O<sub>2</sub> for life support and propulsion in submarines and spacecraft<sup>18-22</sup>. The HOT ELLY project in Germany in 1975 was the first SOEC project that was not related to space exploration<sup>23</sup>. This project focused on H<sub>2</sub> production through water electrolysis. Throughout the 1980s and 1990s, less research was carried out in the area of

SOECs until the late 1990s, when the concept of solid oxide electrolysis cells (SOECs) for the production of H<sub>2</sub> or syngas gained more attention.

Most of the RSOFC research reported in the literature is focused on Ni-YSZ (yttria stabilized zirconia) composite fuel electrodes, where fuel is either oxidized (at the SOFC Ni-YSZ anode) or reduced (at the SOEC Ni-YSZ cathode), a YSZ electrolyte separator, and a lanthanum strontium manganite (LSM) oxygen electrode for the reduction of O<sub>2</sub> (SOFC cathode) or oxidation of O<sup>2-</sup> (SOEC anode). While Ni-YSZ/YSZ/LSM RSOFC systems ('/' represents a solid-solid interface), operated at 800°C-1000 °C, are efficient, Ni-YSZ is susceptible to sulfur poisoning and coking, which significantly lowers cell performance<sup>24-26</sup>. Ni coarsening is another major issue during long term operation of RSOFCs, leading to degradation of the cell via loss of the triple phase boundary (TPB), the region at which the redox reaction occurs<sup>26</sup>.

Many of these SOFC and SOEC problems can be minimized by employing Ni-free catalysts. This has led to extensive research on the synthesis and electrochemical characterization of redox-stable metal oxides, such as perovskites, e.g., La<sub>0.75</sub>Sr<sub>0.25</sub>Cr<sub>0.5</sub>Mn<sub>0.5</sub>O<sub>3-δ</sub> (LSCM), which exhibit good performance and durability in both the SOFC and SOEC modes<sup>27</sup>.

## 1.2 Research objectives

The primary objectives of this thesis are to develop stable and active electrocatalysts for use as fuel electrodes in reversible solid oxide fuel cells (RSOFCs), with a particular emphasis on CO<sub>2</sub>/CO reactions and determining the effect of low levels of H<sub>2</sub>S in the fuel stream on electrode performance. The early part of the work was focused on Ni-YSZ fuel electrodes, then moved toward mixed ionic and electronic conducting perovskite oxides, specifically La<sub>0.3</sub>M<sub>0.7</sub>Fe<sub>0.7</sub>Cr<sub>0.3</sub>O<sub>3-δ</sub> (M = Sr, Ca). The specific objectives of this research are:

- To compare and understand H<sub>2</sub>S interactions with conventional Ni-YSZ fuel electrodes and La<sub>0.3</sub>M<sub>0.7</sub>Fe<sub>0.7</sub>Cr<sub>0.3</sub>O<sub>3-δ</sub> (M = Sr, Ca) perovskites at 500-800 °C in a humidified H<sub>2</sub> gas stream.
- To determine the activity and stability of La<sub>0.3</sub>Sr<sub>0.7</sub>Fe<sub>0.7</sub>Cr<sub>0.3</sub>O<sub>3-δ</sub> during CO<sub>2</sub> reduction and CO oxidation in pure CO<sub>2</sub> and mixed CO<sub>2</sub>/CO gas environments.
- To better understand CO<sub>2</sub> reduction and CO oxidation at La<sub>0.3</sub>Sr<sub>0.7</sub>Fe<sub>0.7</sub>Cr<sub>0.3</sub>O<sub>3-δ</sub> using advanced electrochemical methods.

### 1.3 Thesis organization

This thesis is divided into 8 chapters. Chapter 1 provides an overview of the use of reversible fuel cell technology as a conversion device to store surplus electrical energy (electricity) as chemical energy through the electrolysis of water and/or CO<sub>2</sub> to H<sub>2</sub> and/or CO. This is also relevant to the storage of renewable energy when demand is low and the conversion of H<sub>2</sub> and/or CO to electricity when demand is high. Chapter 1 also discusses the thesis objectives and organization.

Chapter 2 contains a literature review of reversible solid oxide fuel cells (RSOFCs), operated in either the fuel cell or electrolysis mode. The thermodynamics, material challenges, and stability of RSOFCs are reviewed. Also, Chapter 2 discusses the advances made in the synthesis of new materials, with emphasis on perovskites for RSOFC development. The experimental and methods used in this thesis are described in Chapter 3.

The thesis research results are given in Chapters 4 to 7. Each of the results chapters has a short introduction, results and discussion section, and a summary section. Chapters 4 and 5 are focused on the sulfur tolerance of conventional Ni-YSZ fuel electrodes and a

$\text{La}_{0.3}\text{Ca}_{0.7}\text{Fe}_{0.7}\text{Cr}_{0.3}\text{O}_{3-\delta}$  (LCFCr) perovskite electrode in  $\leq 10$  ppm  $\text{H}_2\text{S}$  at 500-850 °C. Chapters 6 and 7 discuss the stability, performance and electrochemical processes at  $\text{La}_{0.3}\text{Sr}_{0.7}\text{Fe}_{0.7}\text{Cr}_{0.3}\text{O}_{3-\delta}$  (LSFCr) during  $\text{CO}_2$  electrolysis and CO oxidation over a temperature range of 650-800 °C.

Specifically, Chapter 4 discusses the behavior of Ni-YSZ anodes (fuel electrodes) towards hydrogen oxidation in the presence of low ppm levels of  $\text{H}_2\text{S}$ , especially at sub-600 °C. This work involved a joint effort between a previous M.Sc. student, Lisa Deleebeeck, and a collaboration with Drs. Tom Ziegler and Maxim Shishkin (University of Calgary) and Drs. Stephen Skinner and Andrea Cavallaro (Imperial College, London). The majority of the data shown in this chapter were collected by P. Addo, with some results from L. Deleebeeck used for comparison. The results shown in Chapter 4 have been published (L. Deleebeeck, M. Shishkin, P. Addo, S. Paulson, H. Molero, T. Ziegler and V. Birss, *Activation of  $\text{H}_2$  oxidation at sulphur-exposed Ni surfaces under low-temperature SOFC conditions*, Physical Chemistry Chemical Physics, 2014. **16**(20): p. 9383-9393).

Chapter 5 gives a comparison of the electrochemical performance of  $\text{La}_{0.3}\text{Sr}_{0.7}\text{Fe}_{0.7}\text{Cr}_{0.3}\text{O}_{3-\delta}$  (LSFCr) and  $\text{La}_{0.3}\text{Ca}_{0.7}\text{Fe}_{0.7}\text{Cr}_{0.3}\text{O}_{3-\delta}$  (LCFCr) towards the hydrogen oxidation reaction (HOR) and, for the first time, examines the sulfur tolerance of  $\text{La}_{0.3}\text{Ca}_{0.7}\text{Fe}_{0.7}\text{Cr}_{0.3}\text{O}_{3-\delta}$  in low ppm levels of  $\text{H}_2\text{S}$  in the temperature range of 600-850 °C. Some of the text and figures in Chapter 5 have been published (P. K. Addo, B. Molero-Sánchez, A. Buyukaksoy, S. Paulson and V. Birss, *Sulfur tolerance of  $\text{La}_{0.3}\text{M}_{0.7}\text{Fe}_{0.7}\text{Cr}_{0.3}\text{O}_{3-\delta}$  ( $M = \text{Sr}, \text{Ca}$ ) solid oxide fuel cell anodes*, ECS Transactions, 2015. **66**: p. 219-228), with the majority of the data and text shown in this chapter collected by P. Addo.

The first part of Chapter 6 involves the characterization of LSFCr using various analytical techniques to establish its chemical stability in dry  $\text{CO}_2$  and  $\text{CO}_2/\text{CO}$  before being used

as an electrode for symmetrical RSOFC development. The chapter also examines the electrochemical performance and stability of a symmetrical LSFcr full cell towards CO<sub>2</sub> electrolysis and CO oxidation. Some of the text and figures have been published (P. K. Addo, B. Molero-Sanchez, M. Chen, S. Paulson and V. Birss, *CO/CO<sub>2</sub> study of high performance La<sub>0.3</sub>Sr<sub>0.7</sub>Fe<sub>0.7</sub>Cr<sub>0.3</sub>O<sub>3-δ</sub>-reversible SOFC electrodes*, Fuel Cells, 2015. **15**(5): p. 689-696), with the data and text shown in this chapter having been collected by P. Addo.

Chapter 7 seeks to understand the various electrochemical processes associated with CO<sub>2</sub> reduction and CO<sub>2</sub> oxidation in a LSFcr-based 3-electrode half cell (electrolyte-supported), operated in pure CO<sub>2</sub> and in a range of CO<sub>2</sub>:CO mixtures. Some of the text and figures have been published (B. Molero, P. Addo, A. Buyukaksoy, and V. Birss, *Electrochemistry of La<sub>0.3</sub>Sr<sub>0.7</sub>Fe<sub>0.7</sub>Cr<sub>0.3</sub>O<sub>3</sub> as an oxygen and fuel electrode for RSOFCs*, Faraday Discussions, 2015. **182**: p.159-175), while the data and text shown in this chapter having been collected by P. Addo.

Finally, Chapter 8 summarizes the main conclusions of Chapters 4-7 and discusses some possible future work.

## Chapter Two: **Relevant Background**

### **2.1 Reversible solid oxide fuel cells (RSOFCs)**

RSOFCs are high temperature ( $> 600$  °C) electrochemical devices that can run in both the SOFC and solid oxide electrolysis (SOEC) modes<sup>16, 28-30</sup>. In the SOFC mode, fuels, such as H<sub>2</sub>, natural gas, hydrocarbons, or syngas can be electrochemically converted (with air at the cathode) to electricity and heat. Research in the area of RSOFCs is progressing steadily due to knowledge transfer from SOFC technology. SOFCs are robust, quiet and reliable systems for highly efficient (ca. 90 %) combined electricity and heat production<sup>31</sup>.

However, when excess electricity is available from other sources, such as hydro, wind, and solar, a RSOFC can be operated in the SOEC mode, to convert the excess electricity (electrical energy) into chemical energy. This occurs through the electrolysis of H<sub>2</sub>O to H<sub>2</sub> and O<sub>2</sub>, or by the co-electrolysis of CO<sub>2</sub>/H<sub>2</sub>O to form H<sub>2</sub>/CO-rich gases, known as synthesis gas (syngas) at the cathode, and O<sub>2</sub> again at the anode<sup>16, 29</sup>. Syngas is the building block for producing synthetic hydrocarbon fuels through the Fischer-Tropsch process<sup>16, 29</sup>. Therefore, the co-electrolysis of H<sub>2</sub>O and CO<sub>2</sub> is an attractive approach to producing CO<sub>2</sub>-neutral synthetic hydrocarbon fuels<sup>32</sup> while simultaneously storing renewable energy.

High temperature electrolysis cells ( $> 600$  °C), such as SOECs, have numerous advantages over low temperature electrolysis systems ( $< 100$  °C), such as alkaline and proton exchange membrane (PEM) electrolyzers. Figure 2.1 compares the performance of an SOEC to PEM and alkaline water electrolyzers. It can be seen that high current densities (faster reaction kinetics) are observed for SOECs at lower applied potentials (0.8-1.3 V) than in alkaline and PEM electrolyzers, which require higher potentials and are thus less efficient<sup>33</sup>.

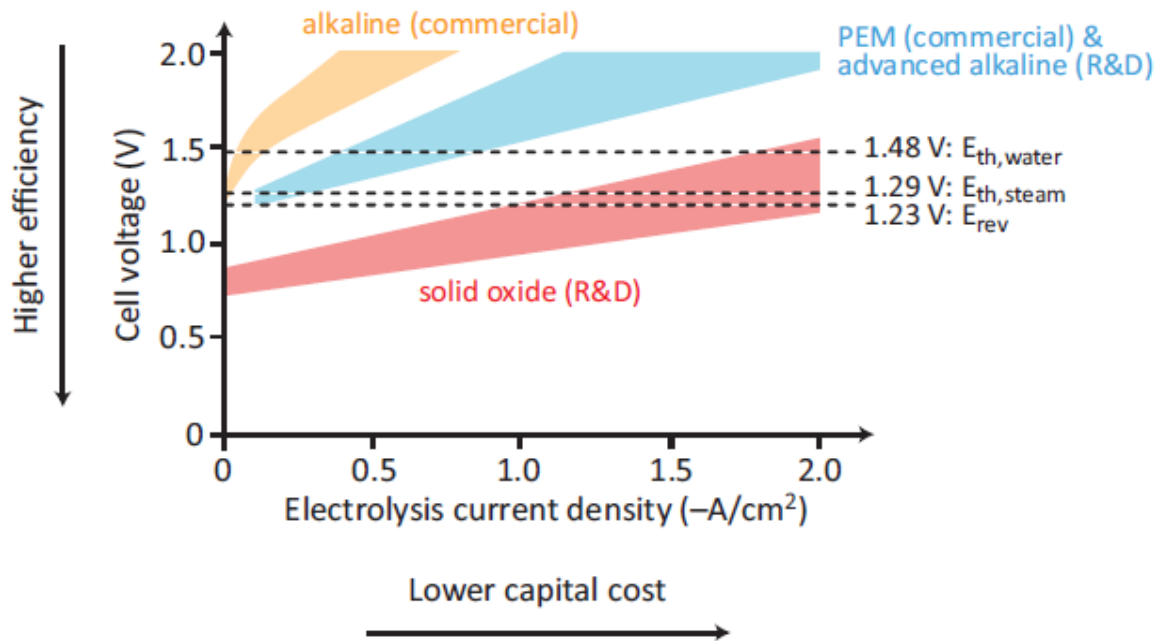


**Figure 2.1 Typical relationship between cell voltage and current for various state-of-the-art water electrolysis cells.  $E_{th,water}$  and  $E_{th,steam}$  are the thermoneutral voltages for water and steam electrolysis, respectively, while  $E_{rev}$  is the reversible potential for water electrolysis at standard conditions<sup>33</sup>.**

In the past few years, extensive research has been carried out on characterizing and testing electrode and electrolyte materials for steam electrolysis<sup>23, 34-36</sup>, CO<sub>2</sub> electrolysis<sup>36-40</sup>, and the co-electrolysis of both H<sub>2</sub>O and CO<sub>2</sub> to produce syngas in SOECs<sup>41-44</sup>. The best performing Ni-YSZ-based SOEC reported in the literature exhibited a current density of 6 A/cm<sup>2</sup> during steam electrolysis at 800 °C and a cell voltage of 1.67 V<sup>45</sup>. In comparison, Jensen *et al.* reported a current density of 3.6 A/cm<sup>2</sup> at 950 °C for a Ni-YSZ-based SOEC during steam electrolysis<sup>36</sup>, while a current density of 1.5 A/cm<sup>2</sup> was obtained at a cell voltage of 1.29 V during CO<sub>2</sub> electrolysis at 950 °C.

### 2.1.1 Operating principles of RSOFCs

As can be seen in Figure 2.2, a RSOFC is made up of a fuel electrode, an electrolyte, and an oxygen electrode. The reactions occurring at the oxygen and fuel electrodes during operation of the RSOFCs in either the SOFC (power generation) or SOEC (electrolysis) mode are shown in Reactions 2.1-2.3. In the SOFC mode,  $O_2$  is reduced to the oxide ion ( $O^{2-}$ ) at the cathode (oxygen electrode). The  $O^{2-}$  ion is then transported through a dense electrolyte to the anode (fuel electrode), where  $H_2$  and/or  $CO$  are oxidized to  $H_2O$  and  $CO_2$ , respectively, producing electricity and heat. In the SOEC (electrolysis) mode, the reverse processes occur, where  $H_2O$  and  $CO_2$  are reduced to  $H_2$  and  $CO$  at the cathode (fuel electrode), producing an oxide ion which is transported through the electrolyte to the anode (oxygen electrode), where  $O^{2-}$  is then oxidized to  $O_2$ .

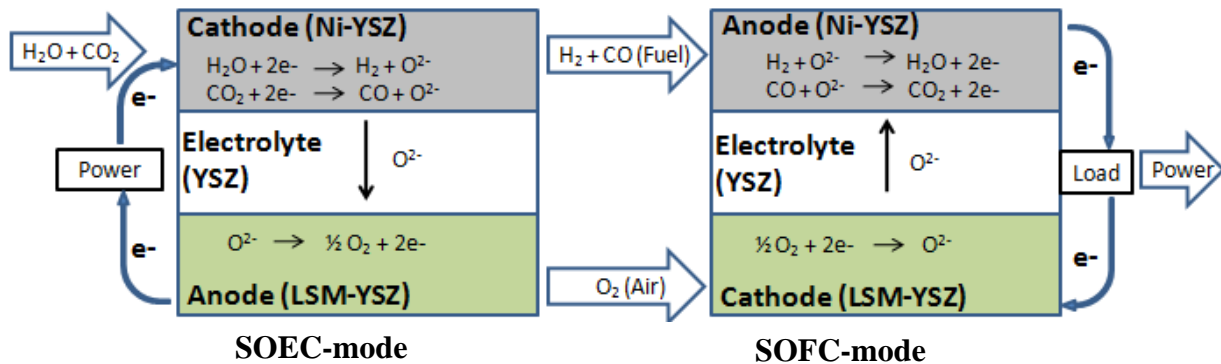
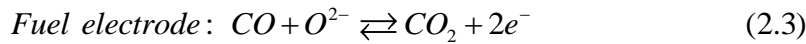
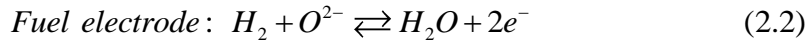
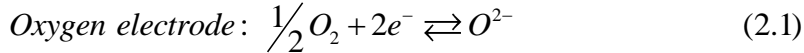


Figure 2.2 Schematic of a RSOFC<sup>30</sup>.

While asymmetrical mixed ionic and electronic conducting (MIEC) based RSOFCs have been examined in a number of studies in the literature<sup>15</sup>, the concept of symmetrical RSOFCs, where the same material is used as both the fuel and oxygen electrode<sup>16, 46-48</sup>, is a relatively new topic of investigation. This approach is meant to minimize the fabrication steps involved in developing the RSOFC, also making it possible to easily regenerate the fuel electrode after coking or sulfur poisoning, by flowing air or steam into the fuel electrode chamber<sup>16, 49</sup>. The electrode material for use in a symmetrical RSOFC must be stable in both oxygen and fuel environments. Also, it must be catalytically active for the reactions occurring at both the oxygen electrode (O<sub>2</sub> reduction and evolution reactions) and the fuel electrode (H<sub>2</sub> and/or CO oxidation and H<sub>2</sub>O and/or CO<sub>2</sub> reduction).

There are only a few studies focussed on developing symmetrical RSOFCs for the electrolysis of H<sub>2</sub>O or CO<sub>2</sub> in these high temperature devices. Examples of electrode materials that have been reported to be good candidates for symmetrical cell fabrication are La<sub>0.3</sub>Sr<sub>0.7</sub>Fe<sub>0.7</sub>Ti<sub>0.3</sub>O<sub>3- $\delta$</sub> <sup>50</sup>, Sr<sub>2</sub>Fe<sub>1.5</sub>Mo<sub>0.5</sub>O<sub>6</sub><sup>51</sup>, La<sub>0.6</sub>Sr<sub>0.4</sub>Fe<sub>0.9</sub>Ni<sub>0.1</sub>O<sub>3- $\delta$</sub> <sup>52</sup>, La<sub>0.75</sub>Sr<sub>0.25</sub>Cr<sub>0.5</sub>Mn<sub>0.5</sub>O<sub>3- $\delta$</sub> <sup>53</sup>, La<sub>0.7</sub>Ca<sub>0.3</sub>CrO<sub>3- $\delta$</sub> <sup>54</sup>, and La<sub>4</sub>Sr<sub>8</sub>Ti<sub>12-x</sub>Fe<sub>x</sub>O<sub>3- $\delta$</sub> <sup>49</sup>. Parallel work by our group has shown that La<sub>0.3</sub>M<sub>0.7</sub>Fe<sub>0.7</sub>Cr<sub>0.3</sub>O<sub>3- $\delta$</sub>  (LMFCr, M = Sr, Ca) exhibits excellent electrochemical performance as an oxygen electrode<sup>38, 46, 55-57</sup> and thus the performance of La<sub>0.3</sub>M<sub>0.7</sub>Fe<sub>0.7</sub>Cr<sub>0.3</sub>O<sub>3- $\delta$</sub>  (M = Sr, Ca) as a symmetrical RSOFC fuel electrode, operated in H<sub>2</sub>/H<sub>2</sub>O and CO/CO<sub>2</sub> atmospheres, is the focus of Chapters 5-7 of this thesis.

## 2.2 Thermodynamics of RSOFCs

At constant temperature and pressure, the maximum electrical work ( $W_{\text{elec, max}}$ ) that can be done by a fuel cell at standard states is related to the free energy change ( $\Delta G^\circ$ ) and thermodynamic reversible cell potential ( $E^\circ_{\text{cell}}$ ), using Equation 2.4<sup>58</sup>.

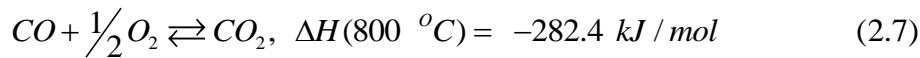
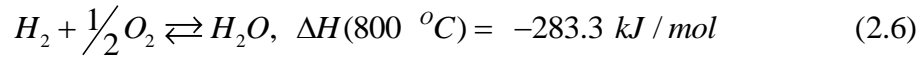
$$\Delta G^\circ = -W_{\text{elect, max}} = -nFE^\circ_{\text{cell}} \quad (2.4)$$

where  $n$  is the number of electrons transferred during the electrochemical reaction,  $F$  is the Faraday constant (96485 C/mol), and ( $E^\circ_{\text{cell}}$ ) is defined as:

$$E^\circ_{\text{cell}} = E^\circ_{r,c} - E^\circ_{r,a} \quad (2.5)$$

where the subscript  $c$  and  $a$  represents the reversible potential of the cathode and anode reactions, respectively<sup>59</sup>.

Using the Nernst equation, ( $E^\circ_{\text{cell}}$ ) can be related to the concentration of the reactants and products of the electrochemical reaction<sup>58</sup>. Therefore, for a  $H_2/O_2$  and  $CO/O_2$  fuel cell (Reactions 2.6-2.7), the reversible potential ( $E_r$ ) can be calculated using the Nernst Equations 2.8-2.9<sup>58</sup>,



$$E_r = E^\circ_{\text{cell}} + \frac{RT}{2F} \ln \frac{[P_{H_2} P_{O_2}^{1/2}]}{[P_{H_2O}]} \quad (2.8)$$

$$E_r = E^\circ_{\text{cell}} + \frac{RT}{2F} \ln \frac{[P_{CO} P_{O_2}^{1/2}]}{[P_{CO_2}]} \quad (2.9)$$

where  $R$  is the gas constant (8.314 J/K mol),  $T$  is temperature (K), and the number of electrons transferred is 2.

$E_r$  is the maximum potential that can be obtained during the spontaneous oxidation of  $H_2$  and  $CO$  (SOFC mode), while in the SOEC mode,  $E_r$  is the minimum potential (electrical energy) required for the decomposition of  $H_2O$  and  $CO_2$ . In the SOFC mode, the forward reactions (Reactions 2.3-2.4) are exothermic, while the backward reactions (SOEC mode) are endothermic. Therefore, in the SOEC mode, the total energy requirement for the decomposition of  $H_2O$  or  $CO_2$  is equivalent to the enthalpy of the reaction ( $\Delta H$ ), shown in Equation 2.10,

$$\Delta H = \Delta G + T\Delta S \quad (2.10)$$

where  $\Delta G$  is the electrical energy requirement and the heat requirement ( $Q$ ) is  $T\Delta S$ .

Figure 2.3 shows that the electrical demand ( $\Delta G$ , or  $E$ ) in an SOEC decreases while the heat demand ( $Q$  or  $T\Delta S$ ) increases with increasing operating temperature for both  $H_2O$  and  $CO_2$  electrolysis. Therefore, from the thermodynamic standpoint, the electrolysis of  $H_2O$  and  $CO_2$  at high temperatures ( $> 600$  °C) is more advantageous than at low temperatures ( $< 100$  °C) because the electrical energy demand for  $H_2O$  electrolysis decreases from 1.23 V at 25 °C to ca. 1 V at 800 °C, while for  $CO_2$  electrolysis, the electrical demand decreases from 1.33 V at 25 °C to ca. 1 V at 800 °C. Also, at high temperatures, part of the total energy required for the electrolysis process can be supplied as thermal energy via internal resistivity losses within the cell itself (especially at high current densities) or by direct external heat input (at low current densities)<sup>36</sup>. The external heat could be obtained from geothermal sources, industrial or nuclear facilities.

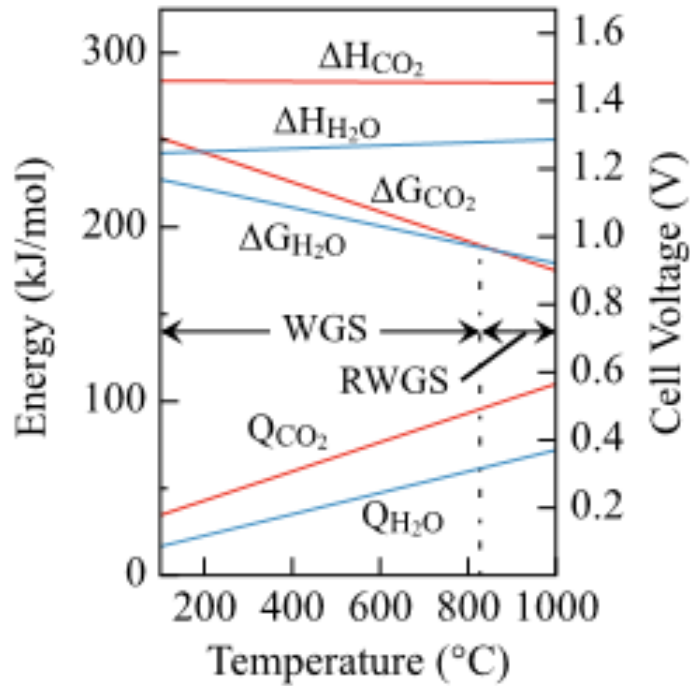


**Figure 2.3 Energy (kJ/mol)-temperature profile for H<sub>2</sub>O and CO<sub>2</sub><sup>60</sup>.**

A parameter or term commonly used in the SOEC mode is the thermoneutral potential ( $E_{th}$ ), expressed as:

$$E_{th} = \frac{\Delta H}{nF} \quad (2.11)$$

The thermoneutral potential is the potential at which the heat required for the electrolysis reaction is equal to the Joule heat generated in the electrolysis cell<sup>17, 33</sup>. The thermoneutral potential ( $E_{th}$ ) for steam and CO<sub>2</sub> at 800 °C is about 1.29 V and 1.48 V, respectively<sup>17</sup>.

The heat consumed/generated ( $Q$ ) by an isothermal RSOFC cell can be quantified by using the thermoneutral potential ( $E_{th}$ ) (Equation (2.12) and referred to in Figure 2.4)<sup>61</sup>,

$$Q = i(E_{cell} - E_{th}) \quad (2.12)$$

where  $i$  is current density and the operating potential of the RSOFC is  $E_{cell}$ . When  $Q < 0$ , net heat will be generated by the RSOFC cell<sup>61</sup>. Figure 2.4 presents a typical potential (V)-current density

(i) plot for a RSOFC cell operated in a  $H_2/H_2O$  atmosphere, showing the various regions where heat is generated or consumed<sup>61</sup>.

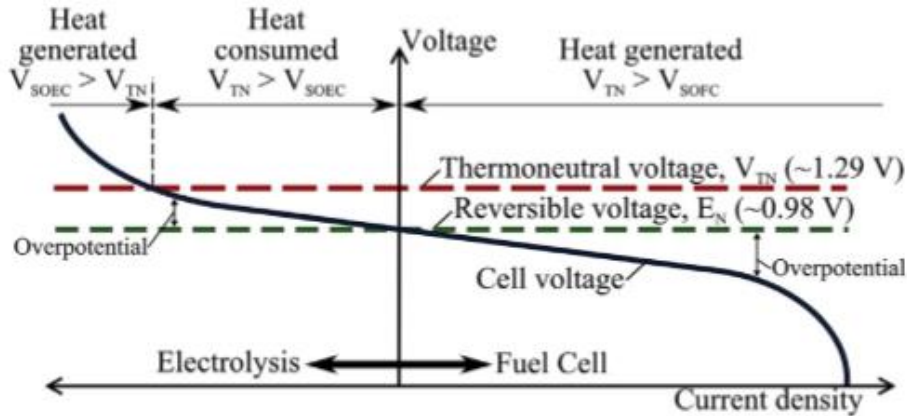


**Figure 2.4** Representative current-voltage plot for a RSOFC operated in  $H_2/H_2O$ <sup>61</sup>.

### 2.2.1 Modes of SOEC operation

Based on Figure 2.4, the three modes of operation of an RSOFC, in the SOEC mode, are endothermic, thermoneutral and exothermic<sup>15</sup>. The thermoneutral mode is when the cell is operated at the thermoneutral potential, where the heat consumption and generation are equal. This is the ideal mode of operation because the electrolysis reaction is self-sustaining and there is no need for the addition or removal of heat. In the endothermal mode, the cell is operated at a potential below the thermoneutral potential, and therefore external heat must be supplied to the cell to sustain the electrolysis reaction<sup>15</sup>. As the current density in the endothermal mode is low, the internal heat generated by the cell is too low to meet the heat demand of the cell. The exothermal mode of operation is when the cell is operated at a potential above the thermoneutral potential. As the current density in this mode is high and the Joule heat generated is greater than the heat consumption of the cell, the excess heat generated must be removed for efficient operation of the SOEC cell.

### 2.2.2 Round-trip efficiency of RSOFCs

The round-trip efficiency ( $\eta_{RT}$ ) of a reversible SOFC is defined as the quotient of the net energy generated in the SOFC mode (discharging) and the total energy supplied in the SOEC mode (charging)<sup>17, 61, 62</sup>. The ideal round-trip efficiency, not considering the auxiliary power required by the balance-of-plant (BOP) components, is given as<sup>17, 61</sup>.

$$\eta_{RT} = \frac{V_{SOFC}Q_{SOFC}}{V_{SOEC}Q_{SOEC}} \quad (2.13)$$

where V is the operating potential of the cell and Q is the charge supplied or consumed. Equation 2.13 can be simplified to Equation 2.14, if 100 % coulombic efficiency is assumed<sup>17</sup>.

$$\eta_{RT} = \frac{V_{SOFC}}{V_{SOEC}} \quad (2.14)$$

Therefore, to achieve a high round-trip efficiency,  $V_{SOFC}$  and  $V_{SOEC}$  should be as similar as possible<sup>17</sup>. Thus, operating the RSOFC cell at low overpotentials in both the SOFC and SOEC modes is necessary to achieve a high round-trip efficiency<sup>17, 61</sup>.

Figure 2.5 shows that RSOFCs can achieve a round-trip efficiency of > 70% at a low storage cost, which is comparable to pumped hydro and much better than most other technologies<sup>62</sup>. Jensen *et al.*<sup>62</sup> reported that RSOFCs can be used for large-scale electricity storage when combined with sub-surface storage of CO<sub>2</sub> and CH<sub>4</sub>. They proposed that a round-trip efficiency > 70% could be obtained at an estimated storage cost of about 3 ¢/kWh<sup>62</sup>.

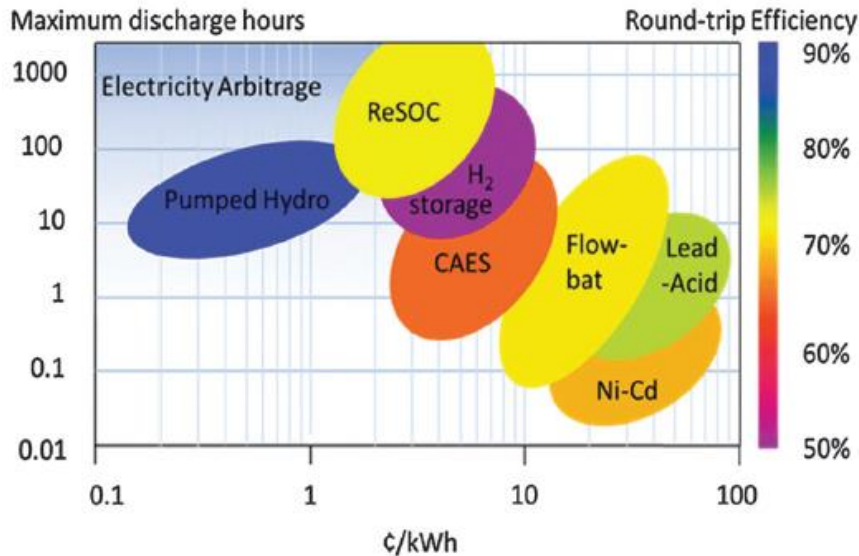


**Figure 2.5 Comparison of reversible solid oxide cell (ReSOC) technology to other energy storage systems as a function of investment cost per kWh per cycle and maximum discharge hours. Efficiency is denoted by the colors from purple to blue. Electricity arbitrage is possible for technologies that run at high efficiency, which are placed in the upper left part of the graph<sup>62</sup>.**

### 2.3 Materials for reversible solid oxide fuel cells

Both the fuel and oxygen electrodes used in RSOFCs must have a high ionic and electronic conductivity ( $> 0.1 \text{ S/cm}$ ), should be chemically compatible with all components of the cell, and must be catalytically active for the electrochemical reactions<sup>16, 60</sup>. The electrolyte must be dense with a high ionic conductivity ( $> 0.1 \text{ S/cm}$ ) at a given operating temperature. Also, the electrolyte must be stable in both oxidizing and reducing atmospheres and must be compatible with all other components of the cell<sup>16, 60</sup>.

### 2.3.1 Fuel electrodes

#### 2.3.1.1 Metal-based electrodes

Ni-yttria stabilized zirconia (YSZ) cermets are the conventional fuel electrodes used in RSOFCs because they show excellent electrochemical performance in both the SOFC and SOEC modes<sup>15, 40, 60, 63, 64</sup>. Ni-YSZ has been employed for the oxidation of various reactants, such as H<sub>2</sub>, CO, CH<sub>4</sub>, and for the electrolysis of H<sub>2</sub>O, CO<sub>2</sub> and co-electrolysis of H<sub>2</sub>O/CO<sub>2</sub>. However, Ni-YSZ fuel electrodes are prone to performance degradation in both the SOFC and SOEC modes. Some of the challenges of Ni-YSZ electrodes include sulfur poisoning, coke formation, redox instability, Ni coarsening, and silica segregation<sup>24-26, 65-74</sup>.

Other types of metal-based fuel electrodes that have been operated in H<sub>2</sub>/H<sub>2</sub>O and/or CO/CO<sub>2</sub> atmospheres include Cu-YSZ<sup>75</sup>, Pt-YSZ<sup>76, 77</sup> and Ni-Fe bimetallic metals<sup>78-84</sup>. Buyukaksoy *et al.* studied the performance of a symmetrical cell consisting of YSZ infiltrated into a porous Pt electrodes and operated in H<sub>2</sub>/H<sub>2</sub>O environments and reported a polarization resistance of 0.35 Ω cm<sup>2</sup> at 800 °C<sup>76</sup>. Tao *et al.* showed that the performance of Pt-YSZ cermet electrodes during CO<sub>2</sub> electrolysis was better than Pt electrodes<sup>77, 85</sup>. Kim *et al.* reported that a Cu-YSZ fuel electrode performed slightly better than Ni-YSZ for the electrolysis of H<sub>2</sub>O because of the open microstructure of Cu-YSZ and the higher electrical conductivity of Cu<sup>86</sup>, while Ni-Fe electrodes have been reported to be more active for the electrolysis of CO<sub>2</sub> and H<sub>2</sub>O than Ni alone<sup>79, 84, 87</sup>. It was also observed that the addition of a small amount of Fe could stabilize fine Ni particles by suppressing Ni particle growth<sup>79</sup>. A study by Wang *et al.* showed that the electrolysis current density at 1.6 V for Ni-Fe (9:1) and Ni electrodes, operated in 50% CO<sub>2</sub>:1% CO/Ar at 800 °C, were 1.84 A/cm<sup>2</sup> and 0.76 A/cm<sup>2</sup>, respectively<sup>79</sup>.

Even though these metal-based electrodes (Cu, Pt, Ni-Fe) have been shown to have good activity for H<sub>2</sub>/H<sub>2</sub>O and CO/CO<sub>2</sub> reactions, they are still susceptible to some of the drawbacks of Ni-YSZ electrodes. Therefore, one area of active research is the synthesis and development of other high performance, electrochemically stable, sulfur and coke tolerant fuel electrode materials<sup>15</sup>. Unlike metal-and metal-composite based electrodes, which require a high active triple phase boundary length (TPBL), the use of mixed ion and electron conducting (MIEC) perovskite or fluorite-based metal oxides as fuel electrodes for RSOFCS is advantageous. These materials do not rely on the length of the TPB, but rather, their entire surface is active towards the electrochemical reaction.

#### 2.3.1.2 Fluorite-based metal oxide fuel electrodes

The most common type of fluorite-based fuel electrodes for use in RSOFCS include ceria and doped ceria, where Ce is in the +3/+4 oxidation state. Ceria was first shown in 1964 to be catalytically active towards H<sub>2</sub> and CO oxidation under SOFC operating conditions<sup>88, 89</sup>. Doped ceria, such as Gd<sub>x</sub>Ce<sub>1-x</sub>O<sub>2-δ</sub> (GDC), has been investigated for the electrolysis of H<sub>2</sub>O and CO<sub>2</sub><sup>39, 90</sup>. Other types of ceria-based electrodes that have been reported to have catalytic activity towards H<sub>2</sub>/H<sub>2</sub>O reactions are Mo-doped CeO<sub>2</sub> nano-material (nCMO)<sup>91</sup> and Ce<sub>0.8</sub>Y<sub>0.1</sub>Mn<sub>0.1</sub>O<sub>2-δ</sub> (10CYMO)<sup>92</sup>, with a polarization resistance of 0.25 Ω cm<sup>2</sup> observed for 10CYMO electrode in wet H<sub>2</sub> at 800 °C<sup>92</sup>.

#### 2.3.1.3 Perovskite-based metal oxide fuel electrodes

Perovskites have a chemical formula of ABO<sub>3</sub>, where A and B are cations with different sizes (the A-site cation is larger than the B-site cation) and O is an oxygen anion<sup>93, 94</sup>. The A and

B-site cations are 12-fold and 6-fold coordinated with the O anion, respectively. The A-sites are occupied by divalent cations (alkaline earth metals) or trivalent cations (such as lanthanides), while the B-sites are usually occupied by transition metals and lanthanide cations with 3+ and/or 4+ oxidation states<sup>88</sup>. Doping the A- and B-sites of the structure with aliovalent metals influences the properties of the perovskites<sup>88</sup>. Doping the A-site can lead to the formation of oxygen vacancies which, in turn, improves the ionic conductivity of the material. Typically, B-site doping with transition metals, such as Fe, Cr, Co, and Mn, leads to improvement in the chemical stability and catalytic properties of the perovskite<sup>88</sup>.

Chen *et al.*<sup>46</sup> showed that doping the B-site of  $\text{La}_{1-x}\text{Sr}_x\text{FeO}_{3-\delta}$  (LSF) with Cr led to structural stability in reducing atmosphere. Some of the common perovskites used as fuel electrodes are  $\text{La}_{1-x}\text{Sr}_x\text{Cr}_{1-y}\text{Mn}_y\text{O}_{3-\delta}$  (LSCM)<sup>95-107</sup>,  $\text{La}_{1-x}\text{Sr}_x\text{TiO}_{3-\delta}$  (LST)<sup>108-113</sup> and  $\text{La}_{1-x}\text{Sr}_x\text{Fe}_{1-y}\text{Cr}_y\text{O}_{3-\delta}$  (LSFCr)<sup>38, 46, 47, 55, 114-119</sup>. LSCM has exhibited good performance for  $\text{H}_2/\text{H}_2\text{O}$  and  $\text{CO}/\text{CO}_2$  reactions<sup>96, 100-105, 107</sup>. However, most of the studies have involved combining the LSCM material with  $\text{Gd}_x\text{Ce}_{1-x}\text{O}_{2-\delta}$  (GDC) and other types of co-catalysts to increase the performance of the electrode.

The  $\text{La}_{1-x}\text{Sr}_x\text{Fe}_{1-y}\text{Cr}_y\text{O}_{3-\delta}$  (LSFCr)-based perovskite has been reported to be a very good oxygen electrode for SOFC applications, also being structurally stable down to a  $\text{pO}_2$  of  $10^{-21}$  atm<sup>46, 116</sup>. At a  $\text{pO}_2$  below  $10^{-21}$  atm, LSFCr decomposes, forming a  $\text{LaSrFeO}_4$ -based Ruddlesden-Popper phase and  $\alpha\text{-Fe}$ <sup>46</sup>, although the perovskite phase can be recovered after treating the decomposed powder in air<sup>46</sup>. However, there is no detailed study of the chemical stability and the electrochemical performance of LSFCr in  $\text{CO}_2$  and  $\text{CO}_2/\text{CO}$  atmospheres, which is the topic of the work described in Chapters 6 and 7 of this thesis. It has also been reported by our group that the Ca-analog of LSFCr ( $\text{La}_{0.3}\text{Ca}_{0.7}\text{Fe}_{0.7}\text{Cr}_{0.3}\text{O}_{3-\delta}$ , LCFCr) can be used as an active

and stable oxygen electrode<sup>55-57, 120</sup>. Chapter 5 covers off the behavior of LCFCr as a fuel electrode in humidified H<sub>2</sub> environments.

### 2.3.2 Electrolytes

Yttria stabilized zirconia (YSZ) is the most common electrolyte used for RSOFC applications. YSZ is structurally stable in both oxidizing and reducing atmospheres and exhibits good ionic conductivity (0.01 S/cm at high temperature (800 °C))<sup>15, 60</sup>. However, at intermediate temperatures (< 700 °C) the ionic conductivity is low<sup>60</sup>. Also, YSZ electrolyte has been reported to react at high temperatures (> 900 °C) with perovskite-based electrodes, leading to the formation of secondary phases, such as SrZrO<sub>3</sub>, La<sub>2</sub>Zr<sub>2</sub>O<sub>7</sub>, and CaZrO<sub>3</sub>, thereby degrading the performance of the electrode<sup>121-124</sup>. To prevent the formation of these secondary phases, ceria-based buffer layers are applied between the electrodes and the YSZ electrolyte<sup>125, 126</sup>.

The other common types of electrolytes used in RSOFCs are ceria-based (Gd<sub>x</sub>Ce<sub>1-x</sub>O<sub>2-δ</sub> (GDC)) and lanthanum gallate-based (La<sub>0.8</sub>Sr<sub>0.2</sub>Ga<sub>0.8</sub>Mg<sub>0.2</sub>O<sub>3-δ</sub> (LSGM))<sup>15, 16, 60</sup>. These electrolytes have a higher ionic conductivity (0.1 S/cm at 800 °C) than YSZ and therefore can be used at intermediate temperatures. One issue with ceria-based electrolytes is their instability under reducing atmospheres at the operating temperature of RSOFC. Under reducing environments, there is partial reduction of ceria from Ce<sup>4+</sup> to Ce<sup>3+</sup>, leading to the introduction of some electronic conductivity as well as mechanical stability issues<sup>15, 16, 60</sup>. It has been reported that the partial reduction of ceria-based electrolyte caused the current efficiency to decrease during H<sub>2</sub>O electrolysis, while in the SOFC mode, the reduction of the electrolyte led to a decrease in the power output<sup>60</sup>.

Similar to the ceria-based electrolytes, LSGM shows pure ionic conductivity in oxidizing conditions, but under reducing conditions, LSGM exhibits some electronic conductivity due to the partial reduction of  $Ga^{3+}$  to  $Ga^{2+}$ . However, despite the partial reduction of the LSGM electrolyte, LSGM-based cells generally show better performance than YSZ-based cells at intermediate temperatures<sup>15, 60</sup>.

### 2.3.3 Oxygen electrodes

The most studied oxygen electrode material for RSOFC applications is  $La_{1-x}Sr_xMnO_3$  (LSM). LSM is an electronic conductor ( $> 300$  S/cm), which limits the oxygen reduction or evolution reactions to the triple phase boundary (TPB) region at the electrode/electrolyte interface. The performance of LSM-based oxygen electrodes can be increased by combining the LSM material with the electrolyte material, such as YSZ or GDC, to form a composite. The addition of the electrolyte leads to an increase in the ionic conductivity, thereby extending the TPB into the electrode. One major drawback of LSM composite oxygen electrodes is the delamination of the electrode from the electrolyte during oxygen evolution in the SOEC mode<sup>15, 60, 127</sup>.

Therefore, alternative high performing mixed ionic and electronic oxygen electrodes, such as  $La_{1-x}Sr_xCo_{y-1}Fe_yO_{3-\delta}$  (LSCF)<sup>15, 128-136</sup>,  $La_{1-x}Sr_xCu_yFe_{y-1}O_{3-\delta}$  (LSCuF)<sup>15, 137-139</sup>,  $La_{0.3}M_{0.7}Fe_{0.7}Cr_{0.3}O_{3-\delta}$  (M= Sr or Ca)<sup>46, 57, 119, 120</sup> are some of the materials currently being investigated.  $La_{0.3}M_{0.7}Fe_{0.7}Cr_{0.3}O_{3-\delta}$  (M= Sr or Ca) oxygen electrodes have been reported to show comparable performance to LSCF<sup>46, 55, 57, 119</sup>. The polarization resistance reported for  $La_{0.3}Sr_{0.7}Fe_{0.7}Cr_{0.3}O_{3-\delta}$  (LSFCr) and  $La_{0.3}Ca_{0.7}Fe_{0.7}Cr_{0.3}O_{3-\delta}$  (LCFCr) in air at 800 °C was between 0.1-0.3  $\Omega$  cm<sup>2</sup><sup>46, 55, 57, 119</sup>. Also, it has been reported that both LSFCr and LCFCr show better

performance for the oxygen evolution reaction (OER in SOEC mode) than for the oxygen reduction reaction (ORR in SOFC mode), with no delamination of LSFcr and LCFcr electrodes observed in either case<sup>55, 57</sup>.

## 2.4 Application of RSOFCS for fuel production

### 2.4.1 H<sub>2</sub>O and CO<sub>2</sub> electrolysis in RSOFCS

Reactions 2.1-2.3 show the electrolysis of H<sub>2</sub>O and CO<sub>2</sub> to produce H<sub>2</sub> and CO at the fuel electrode and O<sub>2</sub> at the oxygen electrode. Ebbesen *et al.* studied the oxidation of H<sub>2</sub> and the reduction of H<sub>2</sub>O using a Ni-YSZ fuel electrode<sup>64</sup>. It was shown that the reduction of H<sub>2</sub>O was slower than the oxidation of H<sub>2</sub> on the Ni-YSZ electrode. The slow kinetics of H<sub>2</sub>O reduction at low current densities was partly attributed to the cooling of the active electrode, due to the endothermic nature of the reaction. In comparison, the exothermic H<sub>2</sub> oxidation reaction led to heating of the active electrode, thereby leading to faster kinetics<sup>64</sup>.

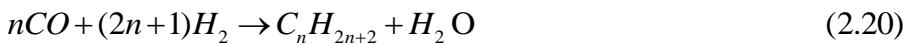
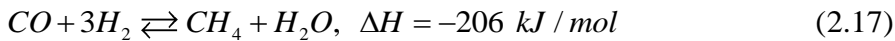
Various studies have shown that the performance of Ni-YSZ and La<sub>1-x</sub>Sr<sub>x</sub>Cr<sub>1-y</sub>Mn<sub>y</sub>O<sub>3-δ</sub> fuel electrodes towards H<sub>2</sub>O reduction and H<sub>2</sub> oxidation is better than CO<sub>2</sub> reduction and CO oxidation<sup>37, 43</sup>. A study by Graves *et al.*<sup>43</sup> reported a current density of about 1 A/cm<sup>2</sup> for the electrolysis of 50% H<sub>2</sub>O/H<sub>2</sub> and about 0.75 A/cm<sup>2</sup> for the electrolysis of 50% CO<sub>2</sub>/CO at 1.2 V and 850 °C, using a Ni-YSZ fuel electrode. Ni-YSZ fuel electrode can also catalyse the Reactions 2.15 and 2.16, leading to carbon deposition. Therefore, operating the Ni-YSZ fuel electrode at high temperatures and at high CO<sub>2</sub> utilization can promote carbon deposition and degrade the performance of the electrode.

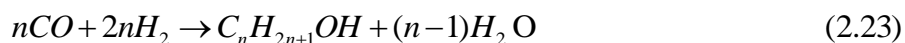


A study using  $\text{La}_{0.75}\text{Sr}_{0.25}\text{Cr}_{0.5}\text{Mn}_{0.5}\text{O}_{3-\delta}$  (LSCM) fuel electrodes for  $\text{H}_2\text{O}$  electrolysis showed that the current density increased from  $0.43 \text{ A/cm}^2$  in 20 %  $\text{H}_2\text{O}$  to  $0.59 \text{ A/cm}^2$  in 80 %  $\text{H}_2\text{O}$  at an applied electrolysis voltage of 1.6 V at  $850 \text{ }^\circ\text{C}$ <sup>140</sup>. A study by Graves *et al.*, based on Gd-doped  $\text{CeO}_2$  (GDC) nanoparticles coated on a Nb-doped  $\text{SrTiO}_3$  electrode (GDC-STN), showed that the  $\text{CO}_2/\text{CO}$  reaction had a higher activity than the  $\text{H}_2\text{O}/\text{H}_2$  reaction<sup>90</sup>. Cao *et al.*<sup>50</sup> reported the direct electrolysis of  $\text{CO}_2$  using a  $\text{La}_{0.3}\text{Sr}_{0.7}\text{Fe}_{0.7}\text{Ti}_{0.3}\text{O}_{3-\delta}$  (LSFT) electrode on either side of a symmetrical solid oxide electrolysis cell (SOEC). They showed that the LSFT electrode had a good activity for  $\text{CO}_2$  reduction at  $800 \text{ }^\circ\text{C}$ , giving a current density of  $0.52 \text{ A/cm}^2$  at an applied cell voltage of  $2.0 \text{ V}$ <sup>50</sup>.

#### 2.4.2 Co-electrolysis of $\text{H}_2\text{O}+\text{CO}_2$ in RSOFCS

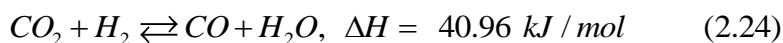
Co-electrolysis involves the simultaneous electrolysis of  $\text{H}_2\text{O}$  (Reaction 2.2) and  $\text{CO}_2$  (Reaction 2.3) to form synthesis gas ( $\text{CO}$  and  $\text{H}_2$ ) at the fuel electrode and  $\text{O}_2$  at the oxygen electrode (Reaction 2.1). The produced synthesis gas can be used directly or further processed chemically, through methanation (Reaction 2.17), methanol synthesis (Reaction 2.18), dimethyl ether (DME) synthesis (Reaction 2.19), or the Fischer Tropsch (F-T) process (Reactions 2.20-2.23)<sup>141, 142</sup>.





The F-T process involves the catalytic conversion of gas (CO+H<sub>2</sub>) to liquid, producing a crude blend of hydrocarbons, waxes and light refinery gases<sup>141</sup>. It has been reported that the syngas produced through co-electrolysis can be tailored to meet the required ratio of H<sub>2</sub>:CO needed for the F-T process<sup>141</sup>. Hartvigsen *et al.* reported the conversion of syngas produced through co-electrolysis of H<sub>2</sub>O/CO<sub>2</sub> to hydrocarbon fuels, based on the F-T process<sup>143</sup>. Becker *et al.* showed that the fuel production cost, based on a solid oxide electrolysis cell (SOEC)/F-T system model, ranged from 4.4 \$/GGE to 15 \$/ GGE (gasoline gallon equivalent) for an electricity price in the range of 0.02 \$ kW/h to 0.14 \$ kW/h<sup>144</sup>. This fuel production cost is still quite high when compare to the cost of crude oil. Therefore, it is important to develop a cost effective, reliable, and high performing SOEC system in order to accelerate the commercialization of SOECs for co-electrolysis reactions<sup>145</sup>.

Ni-YSZ fuel electrodes have been extensively investigated for CO<sub>2</sub>+H<sub>2</sub>O co-electrolysis<sup>32, 43, 63, 146, 147</sup>. Tao *at el.*<sup>147</sup> studied the durability of a Ni-YSZ fuel electrode for the co-electrolysis of 45% H<sub>2</sub>O:45% CO<sub>2</sub>:10% H<sub>2</sub> at current density of -1.5 or -2.0 A/cm<sup>2</sup> at 865 - 875 °C. They reported a gas conversion of 45% at -1.5 A/cm<sup>2</sup> and 60% at -2.0 A/cm<sup>2</sup> and showed that the cell could be operated for up to 700 h<sup>147</sup>. However, microstructural changes in the Ni-YSZ electrode close to the YSZ electrolyte led to performance degradation of the cell<sup>147</sup>. The mechanism of conversion of CO<sub>2</sub> to CO in co-electrolysis, especially using Ni-YSZ-based fuel electrodes, is not very clear in the literature<sup>145</sup>. There are studies<sup>41, 148, 149</sup> that claim that the CO produced during co-electrolysis is formed mainly through the reverse water gas shift reaction (Reaction 2.24), while others<sup>32, 43, 145</sup> have reported that CO<sub>2</sub> can be electrolyzed directly to CO during co-electrolysis.



Typically, the performance of Ni-YSZ electrodes during the co-electrolysis of steam+CO<sub>2</sub> is better than during CO<sub>2</sub> electrolysis<sup>43</sup>. Mass spectrometry measurements by Zhan *et al.*<sup>44</sup>, showed that, with increasing electrolysis current, the consumption of CO<sub>2</sub> and H<sub>2</sub>O increased, leading to an increase in the production of CO and H<sub>2</sub>. They reported a syngas production rate of 7 ml min<sup>-1</sup>cm<sup>-2</sup> when their Ni-YSZ-based cell was operated on 25% H<sub>2</sub>:25% CO<sub>2</sub>:50% H<sub>2</sub>O at 800 °C and 1.3 V.

*In situ* nano alloying of Pd on the surface a Ni-YSZ fuel electrode has been carried out for the co-electrolysis of H<sub>2</sub>O+CO<sub>2</sub> to syngas. It was reported that the Pd-Ni catalyst was selective for catalyzing the reverse water gas shift reaction, thereby increasing the CO<sub>2</sub> conversion rate<sup>150</sup>. Another material that has been investigated for co-electrolysis is LSCM<sup>96, 104</sup>. Xing *et al.*<sup>96</sup> studied the performance of LSCM, with or without the addition of Cu, for the co-electrolysis of CO<sub>2</sub>+H<sub>2</sub>O, showing that the LSCM-Cu electrode gave a better electrochemical performance than the LSCM material alone. It was also reported that co-electrolysis of H<sub>2</sub>O + CO<sub>2</sub> performed in a symmetrical cell based on a Sr<sub>2</sub>Fe<sub>1.5</sub>Mo<sub>0.5</sub>O<sub>6</sub> (SFM)-Sm<sub>0.2</sub>Ce<sub>0.8</sub>O<sub>1.9</sub> (SDC) electrode showed good electrochemical performance<sup>51</sup>. A current density of -734 mA/cm<sup>2</sup> at 1.3 V and a polarization resistance of 0.48 Ω cm<sup>2</sup> was obtained when the cell was operated at 850 °C<sup>51</sup>.

### 2.4.3 Methane production in RSOFCS

The co-electrolysis of H<sub>2</sub>O and CO<sub>2</sub> to methane is favourable at high pressure and low temperature<sup>144, 151</sup>. A thermodynamic analysis by Sun *et al.*<sup>151</sup>, based on 10% H<sub>2</sub>:25% CO<sub>2</sub>:65% H<sub>2</sub>O gas composition and 70% reactant utilization, showed that the CH<sub>4</sub> mole fraction in the

product increased as the temperature was decreased from 1000 to 600 °C at 35 atm. While at a constant temperature of 850 °C, the CH<sub>4</sub> mole fraction increased when the pressure was increased from 1-100 atm. Also, under high pressure or a high conversion of H<sub>2</sub>O/CO<sub>2</sub>, it has been reported that the Boudouard reactions (Reactions 2.15-2.16) can also occur, thereby depositing unwanted carbon within the Ni-YSZ fuel electrode<sup>151</sup>. Even though these studies have shown that methanation is favoured at high pressures, a study by Bierschenk *et al.* reported that about 10 % CH<sub>4</sub> can be generated by running a Ni-YSZ anode supported cell in 79% H<sub>2</sub> and 21% CO<sub>2</sub> at 600 °C and 1 atm<sup>17</sup>.

A study by Luo *et al.*<sup>152</sup> showed that the addition of H<sub>2</sub> to H<sub>2</sub>O/CO<sub>2</sub> led to a further increase in the rate of CH<sub>4</sub> production. The authors reported that the CH<sub>4</sub> production rate increased by less than 0.04% when the cell operating voltage varied from the open circuit voltage to 1.5 V without the addition of H<sub>2</sub>. However, with the addition of 20% H<sub>2</sub> to H<sub>2</sub>O/CO<sub>2</sub>, a 9.94% CH<sub>4</sub> yield was observed at 550 °C at an applied cell voltage of 1.5 V<sup>152</sup>.

## **2.5 Effect of H<sub>2</sub>S on RSOFC fuel electrodes**

### **2.5.1 Effect of H<sub>2</sub>S on Ni-YSZ fuel electrode**

As stated earlier, despite the excellent catalytic activity of Ni-YSZ fuel electrodes for H<sub>2</sub>/H<sub>2</sub>O and CO/CO<sub>2</sub> reactions, in the SOFC mode, they are susceptible to poisoning with low levels (1-100 ppm) of H<sub>2</sub>S exposure at operating temperatures (700-1000 °C)<sup>24, 153-156</sup>, thus negatively affecting the performance of the electrode. The two mechanisms of sulfur poisoning of Ni involve dissociative adsorption of sulfur (Reaction 2.25) and bulk nickel sulfide formation (Reactions 2.25-2.26)<sup>154</sup>. At high temperatures and low ppm of H<sub>2</sub>S, H<sub>2</sub>S readily dissociates to form a reversible sub-monolayer coverage of adsorbed sulfur (S<sub>ads</sub>) on the Ni surface<sup>24, 153-155</sup>,

blocking surface sites and causing irreversible surface reconstruction<sup>157</sup>, while the formation of bulk nickel sulfide species (Reactions 2.25-2.26) is favorable only at high H<sub>2</sub>S concentrations (> 500 ppm) and low temperatures (< 600 °C)<sup>154, 158</sup>.

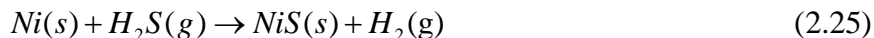
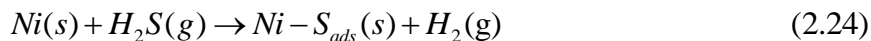
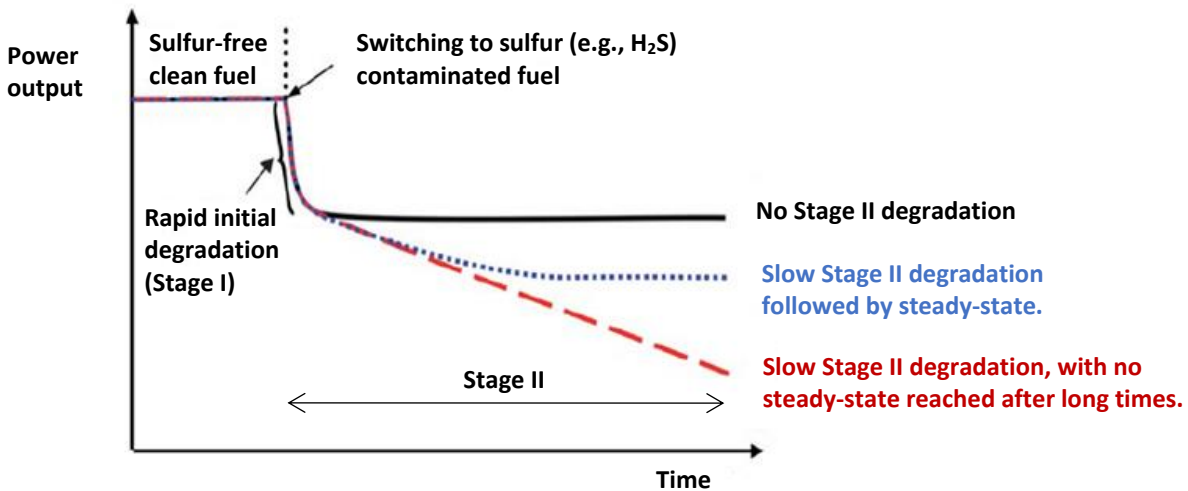


Figure 2.6 shows that there is a range of poisoning behavior observed for Ni-YSZ SOFC anodes upon exposure to low levels of H<sub>2</sub>S. An initial rapid drop in the power output (Stage I) is seen initially, which then leads to an increase in anode polarization resistance (Rp)<sup>159</sup>. Following this, various forms of Stage II behavior are seen, including where the cell either reaches a steady-state Rp after the initial drop without undergoing further degradation, or it shows slower degradation before reaching a steady-state, or, in some cases, Rp does not reach a steady-state at all. There is little understanding or agreement in the literature as to what causes Stage II poisoning, which can last for a very long time. Bulk sulfidation of Ni in Stage II seems unlikely, as this process is thermodynamically unfavorable<sup>159</sup>, especially when using only low ppm H<sub>2</sub>S and temperatures from 800-1000 °C.



**Figure 2.6 Schematic of power output versus time for SOFCs with Ni-YSZ cermet anode, showing effect of sulfur poisoning<sup>159</sup>.**

The effect of H<sub>2</sub>S on Ni-YSZ in the SOEC mode has not been extensively studied as yet. In one study of the long-term electrolysis of H<sub>2</sub>O and CO<sub>2</sub> using a Ni-YSZ electrode at 850 °C and 2.5 to 0.50 A/cm<sup>2</sup>, the cell degraded at a rate of 0.45 to 0.70 mV/h over the first few hundred hours, with a long-term degradation rate of between 0.003 and 0.032 mV/h seen when using as-received gases. The observed degradation was attributed to the presence of trace impurities, such as H<sub>2</sub>S, in the as-received gases. When the inlet gases were cleaned prior to the electrolysis studies, the degradation was completely eliminated<sup>73</sup>.

### **2.5.2 Approaches used to develop sulfur tolerant fuel electrodes**

There have been various approaches used to overcome the sulfur poisoning of Ni-YSZ fuel electrodes. One involves improving the sulfur tolerance of Ni-YSZ fuel electrode by the incorporation of foreign materials, such as CeO<sub>2</sub>, La<sub>2</sub>O<sub>3</sub>, Nb<sub>2</sub>O<sub>5</sub>, Sc<sub>2</sub>O<sub>3</sub>, Sn, and Sb, into the

electrode<sup>159-161</sup>. Unfortunately, most of these modified Ni-YSZ anodes still show sulfur poisoning in low ppm H<sub>2</sub>S<sup>159</sup>.

A second approach involves the fabrication of fuel electrode based on Ni-free conducting metal oxides, such as La<sub>1-x</sub>Sr<sub>x</sub>Cr<sub>1-y</sub>Mn<sub>y</sub>O<sub>3-δ</sub> (LSCM), Y-doped SrTiO<sub>3-δ</sub>, La<sub>1-x</sub>Sr<sub>x</sub>VO<sub>3-δ</sub> (LST), La<sub>1-x</sub>Sr<sub>x</sub>VO<sub>3-δ</sub> (LSV), Sr<sub>2</sub>Mg<sub>2-x</sub>Mo<sub>x</sub>O<sub>6-δ</sub> (SMMO), and La<sub>0.3</sub>M<sub>0.7</sub>Fe<sub>0.7</sub>Cr<sub>0.3</sub>O<sub>3-δ</sub> (M= Sr or Ca)<sup>56, 159</sup>. Most of these oxides have been claimed to be somewhat tolerant to sulfur exposure. For example, it has been shown that La<sub>0.3</sub>Sr<sub>0.7</sub>Fe<sub>0.7</sub>Cr<sub>0.3</sub>O<sub>3-δ</sub>, (LSFCr), operated on wet 50% H<sub>2</sub>/CO fuel containing 10 ppm H<sub>2</sub>S, exhibited only a small drop in cell potential, which recovered when H<sub>2</sub>S was removed<sup>46</sup>.

However, there are some conflicting reports about the sulfur tolerance of some of metal oxide anodes, especially LST. While some researchers reported that LST showed poisoning by H<sub>2</sub>S in the range of 26 to 1000 ppm<sup>159</sup>, others have reported no poisoning effects in 1000 ppm H<sub>2</sub>S, and rather, an enhancement effect in 5000 ppm H<sub>2</sub>S was observed<sup>162</sup>. For example, La<sub>0.3</sub>M<sub>0.7</sub>Fe<sub>0.7</sub>Cr<sub>0.3</sub>O<sub>3-δ</sub> (M= Sr or Ca) has been reported to be sulfur tolerant and showed enhancement of the hydrogen oxidation reaction rate in low ppm H<sub>2</sub>S environments at 800 °C<sup>56</sup>. Some of these SOFC sulfur-tolerant oxides, such as LSCM and LST, have also been employed for the electrolysis of H<sub>2</sub>O and CO<sub>2</sub> in the SOEC mode<sup>104, 163</sup>. However, their performance in the presence of sulfur containing impurities (e.g. H<sub>2</sub>S, SO<sub>2</sub>) during electrolysis has not been extensively studied as yet. To employ an RSOFC for CO<sub>2</sub> electrolysis, the CO<sub>2</sub> can be obtained from pre-combustion, oxyfuel combustion, or post-combustion sources. The CO<sub>2</sub> obtained from the post and oxyfuel combustion methods contains about 20-50 ppm of SO<sub>2</sub> as an impurity<sup>164</sup>, while CO<sub>2</sub> obtained from pre-combustion sources contains about 100 ppm of H<sub>2</sub>S+CO<sub>2</sub><sup>164</sup>.

These sulfur-containing impurities are could affect the performance of RSOFC fuel electrodes, as such needs to be investigated.

## **2.6 Methods used to investigate SOFC and RSOFC electrodes and cell performance**

### ***2.6.1 Electrochemical methods***

In reversible solid oxide fuel cells (RSOFCs), electrochemical reactions take place on the surface of the catalyst and/or at the triple phase boundary<sup>165-169</sup> and the performance can vary substantially, depending on the composition and microstructure of the electrolyte and the electrodes<sup>170</sup>. Thus, electrochemical performance measurements are critical to the assessment of new RSOFC materials, microstructures and cell designs. This can be done in numerous ways, including in 2-electrode full cells (the fuel and oxygen electrodes are in fuel and air/oxygen environments, respectively), 2- electrode half cell mode (both electrodes are exposed to the same gas environment), and 3-electrode methods, using either half or full cell designs. The advantage of 3-electrode methods, which involves the presence of a reference electrode, is that the reaction occurring at the working electrode (either in the fuel or air environment) can then be investigated independently, without interference from the reactions at the second (counter) electrode. However, carrying out 3-electrode work in high temperature fuel cells is known to be difficult<sup>171, 172</sup>.

Electrochemical characterization of RSOFCs (or SOFCs) can be performed by employing either direct (dc) or alternating (ac) electrical perturbation methods, both allowing the measurement of the electrode overpotential. The types of overpotentials associated with RSOFCs are activation ( $\eta_{act}$ ), ohmic ( $\eta_{ohm}$ ), and concentration ( $\eta_{conc}$ ). The total overpotential, obtained

from the i-V plot in Figure 2.4, is given by Equation 2.27. Therefore,  $E_{\text{cell}}$  in the SOFC ( $E_{\text{SOFC}}$ ) and SOEC ( $E_{\text{SOEC}}$ ) modes, as is represented by Equations 2.28 and 2.29 <sup>61</sup>.

$$\eta_{\text{total}} = \eta_{\text{act}} + \eta_{\text{ohm}} + \eta_{\text{conc}} \quad (2.27)$$

$$E_{\text{SOFC}} = E_{\text{rev}} - \eta_{\text{total}} \quad (2.28)$$

$$E_{\text{SOEC}} = E_{\text{rev}} + \eta_{\text{total}} \quad (2.29)$$

The activation overpotential ( $\eta_{\text{act}}$ ) is a complex function describing the charge transfer kinetics of an electrochemical reaction. In a performance plot (Figure 2.4),  $\eta_{\text{act}}$  is revealed most clearly at low current densities.  $\eta_{\text{act}}$  depends on the type of reactions occurring and the catalyst materials, electrode microstructure, reactant activities, electrolyte material, temperature and current density. The Butler-Volmer equation (Equation 2.30) is used to give a quantitative relationship between the current density and  $\eta_{\text{act}}$ . Usually, the charge transfer process is described by a parallel R-C circuit, where the time constant is given by  $RC$ <sup>173</sup>, where R and C are the resistance and capacitance, respectively.

$$i_{\text{net}} = i_o \left[ \exp\left(\frac{\alpha_a \eta F}{RT}\right) - \exp\left(\frac{-\alpha_c \eta F}{RT}\right) \right] \quad (2.30)$$

where  $i_{\text{net}}$  and  $i_o$  are the measured and exchange current densities, respectively,  $\eta$  is the overpotential,  $\alpha_a$  and  $\alpha_c$  are the anodic and cathodic transfer coefficients, respectively, and F and R are the Faraday and gas constants, respectively.

The ohmic overpotential ( $\eta_{\text{ohm}}$ ) arises from the resistance of RSOFC components. Bulk materials and interfaces between components cause resistance to electron flow and electrolyte materials and interfaces cause resistance to the transport of ions, which carry the current in the electrolyte phase. In RSOFCs, the main contributor to the ohmic overpotential is the electrolyte. Therefore, in an electrolyte-supported cell, the contribution of the electrolyte to the ohmic

resistance is significant compared to in electrode-supported cells<sup>173</sup>. The ohmic polarization can be described by a simple resistor without a parallel capacitance.

The concentration overpotential ( $\eta_{\text{conc}}$ ) describes the mass transport limitations associated with electrochemical processes in a RSOFC or SOFC. The  $\eta_{\text{conc}}$  component is observed predominantly at high current densities and is a function of the microstructure of both the fuel and oxygen electrodes, the partial pressure of the reactants, and the diffusion of the gases<sup>173</sup>.

### ***2.6.2 Electrochemical impedance spectroscopy (EIS)***

Alternating current (ac) methods apply a perturbation to the system in terms of an ac input current or voltage, and then the measured output voltage or current, respectively, is phase shifted from the input perturbation<sup>170, 174, 175</sup>. The most common technique used for ac measurements in electrochemistry is electrochemical impedance spectroscopy (EIS). EIS is a powerful method to characterize the various electrochemical processes occurring at the gas/electrode and electrode/electrolyte interfaces. In order to ensure that there is a linear relationship between the cell potential and current, small perturbations (< 50 mV) are used during impedance measurements<sup>170, 174, 176</sup>. Notably, EIS measurements can be carried out under OCP or polarized conditions<sup>170, 177</sup>.

Equivalent circuit modeling of EIS data is one method used to extract physically meaningful properties of the electrochemical system. This is done by modeling the impedance data in terms of an electrical circuit composed of passive elements, such as resistors (R), capacitors (C), inductors (L), and distributed elements such as constant phase elements (CPE) and Warburg elements ( $Z_w$ ). The Warburg element is used to represent the diffusion or mass transport impedance of the electrode or cell.

In general, the resistance of the electrolyte, along with the resistance of the electrical leads and electrical contacts, are described by a series resistance. Electrode interfaces are typically described by a resistor in parallel with a constant phase element (R/CPE)<sup>177</sup>. The CPE can represent the double layer capacitance of the electrode/electrolyte interface or the rapid change in redox state (i.e., the oxide vacancy concentration) of a metal oxide, termed a ‘pseudocapacitance’ or a ‘chemical capacitance’, while the R value is a charge transfer resistance.

A CPE value is used when the electrochemical interface or the metal oxide capacitor does not behave ideally. CPEs are used extensively in equivalent electrical circuits for the fitting of experimental impedance data. The CPE behavior is generally attributed to distributed surface reactivity, surface inhomogeneities, roughness or fractal geometries, electrode porosity, and to current and potential distributions associated with electrode geometry and morphology<sup>178</sup>.

The equation for a CPE is generally given<sup>177</sup> as:

$$Z_{CPE} = \frac{1}{CPE(i\omega)^n} \quad (2.31)$$

where  $\omega = 2\pi f$  is the angular frequency,  $i$  is the imaginary number, and  $n$  can have values from 0 to  $\pm 1$ . The CPE represent a circuit parameter with a limiting behavior as a capacitor for  $n = 1$ , a resistor for  $n = 0$ , and an inductor for  $n = -1$ <sup>178</sup>.

EIS data are usually represented in the form of a Nyquist or Bode plot, as shown in Figure 2.7. A Nyquist plot (Figure 2.7a) shows the imaginary impedance, which is indicative of the capacitive and inductive character of the cell, versus the real impedance (resistive component) of the cell, as the ac perturbation frequency is increased or decreased. In

comparison, a Bode plot show the impedance magnitude (Figure 2.7b) and phase angle (Figure 2.7c) as a function of frequency<sup>170, 177</sup>.

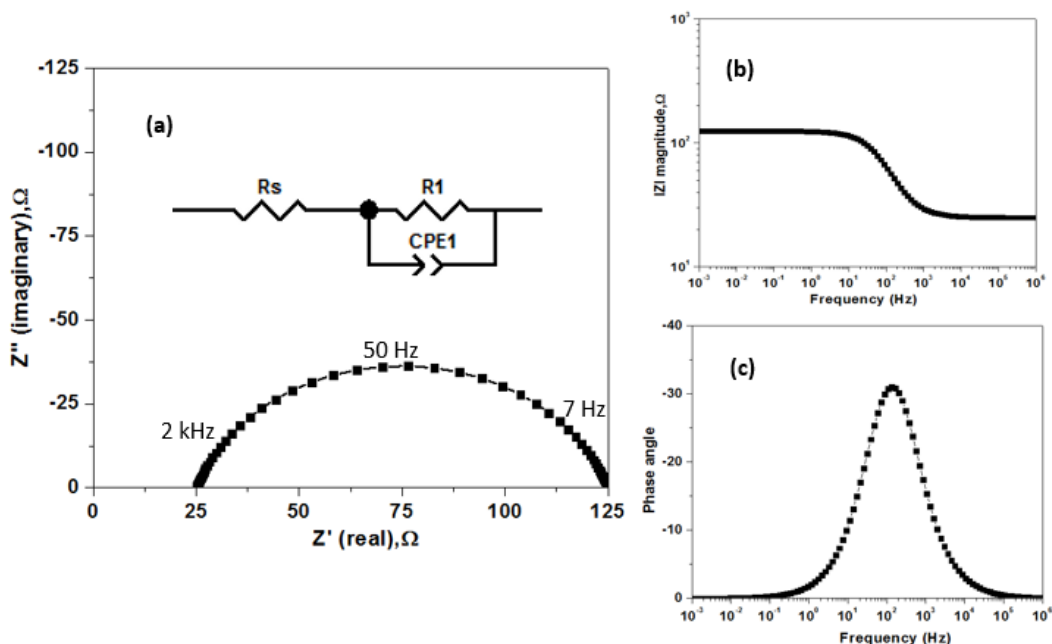


**Figure 2.7** Representative impedance plots for a simulated simple RC circuit showing (a) the Nyquist plot, (b) impedance magnitude vs. frequency Bode plot, and (c) phase angle vs. frequency Bode plot.

### 2.6.2 Cyclic voltammetry

Cyclic voltammetry (CV) involves measuring the current passed through the WE/electrolyte interface while the potential of the WE is varied vs. the reference electrode at a certain scan rate (typically mV/s). In activated controlled systems, Butler Volmer behaviour can be observed, as given by Equation 2.30<sup>88</sup>. The CVs are then analyzed in either the low or high field (low or high overpotential) modes, giving a linear and logarithmic relationship between current and overpotential, respectively. However, the CVs in the literature for many SOFC and RSOFC systems are linear in appearance, even at higher overpotentials when they should be

exponential, because they are often dominated by the series resistance, arising from the resistance of the electrolyte.

## **2.7 Non-electrochemical methods used in this thesis work**

As most of the characterization methods used in this work are relatively standard in fuel cell and materials related research, only a very brief overview of techniques used is given here. X-ray diffraction (XRD), which involves the diffraction of incident X-rays by the crystal planes of the material, was employed in this thesis for the phase identification of samples. As well, *ex situ* XRD analysis was used in Chapter 6 to initially assess the material crystal structure, with *in situ* XRD analysis then used to further understand the material behaviour under different gas atmospheres and temperatures.

Thermogravimetric analysis (TGA), which tracks the mass changes of a sample as a function of temperature in controlled gas atmospheres, was used to understand the chemical stability of the catalysts by tracking their mass changes in air and CO<sub>2</sub>/N<sub>2</sub> atmospheres from room temperature to 900 °C. Fourier transform infrared spectroscopy (FTIR), which involves measuring the infrared absorption or emission of a sample to determine the presence of certain types of chemical bonds, was used to probe the chemical stability of the perovskites in CO<sub>2</sub> atmospheres.

X-ray photoelectron spectroscopy (XPS) and Auger electron spectroscopy (AES) take advantage of the interaction of a solid sample with X-rays or electrons, respectively, and measuring the energy of the emitted surface (< 6 nm deep into the surface) electrons. Both techniques were used in this thesis work to determine the chemical composition of the surface region of the Ni-YSZ and the perovskites-based catalysts after exposure to low levels of H<sub>2</sub>S. In

both XPS and AES, the critical features that are tracked are the binding and kinetic energy, respectively, of emitted electrons in relation to their intensity.

Electron microprobe analysis (EMPA) was carried to establish the elemental composition of the samples, while scanning electron microscopy (SEM) and transmission electron microscopy (TEM) were used to determine the microstructure and morphology of powder samples and the electrochemical cells. Energy dispersive X-ray spectroscopy (EDX), a capability that is part of the SEM instruments, was employed for semi-quantification of the composition of powder and solid samples, including of sample cross-sections.

Low energy ion scattering (LEIS) is a highly sensitive surface technique that can provide resolved monolayer information about the surface composition<sup>179</sup>. The LEIS technique is based on the principle of classical momentum, where primary noble gas ions (e.g., He<sup>+</sup>, Ne<sup>+</sup>, and Ar<sup>+</sup>) of initial energies ranging from 0.5 to 10 keV strike surface atoms and the backscattered primary ions are analyzed, providing resolved monolayer information about the surface composition<sup>179</sup>.

## Chapter Three: **Experimental methods**

### **3.1 Material synthesis and preparation**

#### ***3.1.1 Synthesis of $\text{La}_{0.3}\text{M}_{0.7}\text{Fe}_{0.7}\text{Cr}_{0.3}\text{O}_{3-\delta}$ ( $\text{M} = \text{Sr}, \text{Ca}$ ) perovskites***

A glycine-nitrate combustion process was employed to prepare all of the  $\text{La}_{0.3}\text{M}_{0.7}\text{Fe}_{0.7}\text{Cr}_{0.3}\text{O}_{3-\delta}$  ( $\text{M} = \text{Sr}, \text{Ca}$ ) perovskite powders<sup>46, 120</sup>. Reagent grade  $\text{La}(\text{NO}_3)_2 \cdot 6\text{H}_2\text{O}$  (> 99.9%, Sigma-Aldrich),  $\text{Sr}(\text{NO}_3)_2$  (> 99.9%, Sigma-Aldrich),  $\text{Ca}(\text{NO}_3)_2 \cdot 4\text{H}_2\text{O}$  (> 99.9%, Sigma-Aldrich),  $\text{Fe}(\text{NO}_3)_3 \cdot 9\text{H}_2\text{O}$  (> 98%, Alfa Aesar),  $\text{Cr}(\text{NO}_3)_3 \cdot 9\text{H}_2\text{O}$  (98.5%, Alfa Aesar), and glycine (99.5%, Alfa Aesar) were dissolved in deionized water using metal proportions that were based on the desired stoichiometry of the  $\text{La}_{0.3}\text{Sr}_{0.7}\text{Fe}_{0.7}\text{Cr}_{0.3}\text{O}_{3-\delta}$  (LSFCr) and  $\text{La}_{0.3}\text{Ca}_{0.7}\text{Fe}_{0.7}\text{Cr}_{0.3}\text{O}_{3-\delta}$  (LCFCr) materials. A 2:1 mole ratio of glycine to the total metal cation content was used. Stirred solutions were slowly heated on a hot plate until auto-ignition and self-sustaining combustion occurred. The ash was subsequently pulverized and pre-calcined at 1200 °C for 2 h in air (conditions under which single phases are generated). The powders were then ball milled (high energy planetary ball mill, Pulverisette 5, Fritsch, Germany) in an isopropanol medium at a rotation speed of 300 rpm for 2 h using zirconia balls.

#### ***3.1.2 Preparation of screen printing organic carrier***

The organic carrier used for preparing both the  $\text{Gd}_{0.1}\text{Ce}_{0.9}\text{O}_{2-\delta}$  (GDC) and LMFCr slurries for use in screening printing on the solid electrolyte was prepared by mixing an ethyl cellulose (0.7 g) binder with a butyl benzyl phthalate (2 g) plasticizer in a mixed n-butanol (2 g) and terpinol (15 g) solvent. The solution was stirred at 70 °C for 1-2 h to achieve homogenous mixing of all components. This organic carrier composition was adopted from Dr. Min Chen (former member of the Birss group at University of Calgary).

### ***3.1.3 NiO and Yttria stabilized zirconia (YSZ) powders***

As received yttria stabilized zirconia (YSZ) (8 mol.%  $\text{Y}_2\text{O}_3$ , Tosoh TZ-8Y, Tosoh, Tokyo, Japan), NiO (99.9 %, Advanced Materials), and  $(\text{La}_{0.8}\text{Sr}_{0.2})_{0.98}\text{MnO}_3$  (LSM) (99.9%, Praxair, Woodinville; WA) powders were used to prepare the NiO-YSZ and LSM-YSZ slurries, used for fabricating the Ni-YSZ-based half and full cells, described in Section 3.2.

## **3.2 Cell fabrication**

### ***3.2.1 Ni-YSZ half and full cell fabrication***

This section describes the cell preparation used in Chapter 4 of this thesis.

#### **3.2.1.1 Fabrication of 3-electrode Ni-YSZ half cells**

Figure 3.1 shows the 3-electrode half cell geometry employed, consisting of a Ni-YSZ working electrode (WE) placed symmetrically to a Ni-YSZ counter electrode (CE) on the other side of a 1 mm thick (Tosoh) dense 8 mol.% YSZ (8YSZ) electrolyte disc with a 2.5 cm diameter. A Ni-YSZ reference electrode (RE) was located  $> 0.4$  cm from the CE on the CE side. Cells 1 and 2 were fabricated by painting the WE, CE and RE on a 1 mm thick (Tosoh) dense 8 mol.% YSZ (8YSZ) electrolyte disc with a ball milled 43:57 wt.% 8YSZ:NiO mixture containing terpinol/butanol. This was followed by oven-drying at 160 °C, adding a second layer of coarse particulate NiO paint to each electrode for electronic contact to the Ni sponge (Inco) current collector, oven drying, and then firing at 1300 °C for 2 h in air.

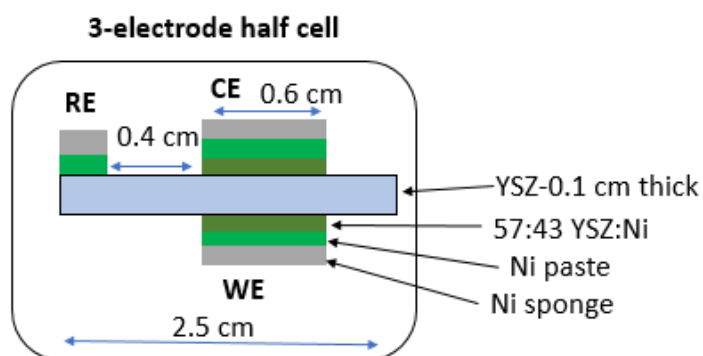


**Figure 3.1 Schematic of the Ni-YSZ-based 3-electrode half cell configuration.**

Other 3-electrode half cells (Cell 3) were prepared using infiltration methods. First, a YSZ scaffold was produced, consisting of a slurry of 8YSZ (Tosoh) with 9 wt. % graphite pore former (< 325 mesh, Sigma-Aldrich) suspended in ethanol, ethyl cellulose, and polyvinyl butyrol and then ball milled together. This mixture was spray-coated onto a 1 mm thick (12 mm diameter) 8YSZ dense electrolyte disc (Tosoh) to form the WE. Both the CE and RE were prepared by painting a mixture of NiO-YSZ suspended in terpinol onto the opposite side of the YSZ electrolyte, after which the cell was oven dried at 150 °C for 30 min. Then, a current collecting paste, consisting of NiO and 4 wt. % graphite suspended in terpinol, was painted onto each electrode, followed by firing at 1250 °C for 2 h.

After sintering, Ni was infiltrated into the WE by pipetting a small amount of 3 M nickel nitrate ( $\text{Ni}(\text{NO}_3)_2 \cdot 6\text{H}_2\text{O}$ , Sigma-Aldrich), dissolved in methanol, onto the WE surface and oven-drying at 150 °C and then at 300 °C for 15 min each. The pipetting and drying stages were repeated 20 times to give a ~ 13 wt. % Ni content infiltrated into the YSZ scaffold of the WE.

### 3.2.1.2 Fabrication of Ni-YSZ/YSZ/LSM-YSZ full cells

The full cells (FC1, Figure 3.2)) were fabricated by screen printing the NiO-YSZ anode (50:50 wt. % 8YSZ:NiO slurry containing terpinol) on the surface of a 0.1 cm thick (2.5 cm diameter) dense YSZ electrolyte disc. After screen printing, the cell was dried in air and fired at 1300 °C for 2 h. A second layer of NiO paste was then painted onto the NiO-YSZ surface. The cathode was prepared by screen printing a  $(\text{La}_{0.8}\text{Sr}_{0.2})_{0.98}\text{MnO}_3$  (LSM):YSZ terpinol based slurry on the opposite side of the dense electrolyte and then fired at 1150 °C for 2 h. After firing, a thin layer of Pt was applied onto the LSM-YSZ layer to serve as a current collector.

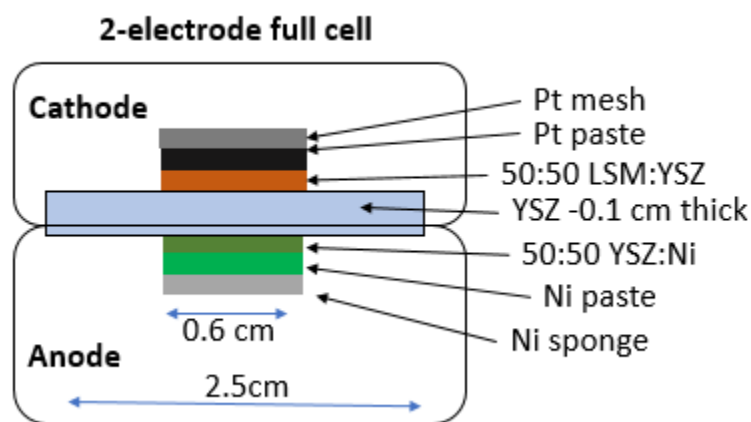


**Figure 3.2 Schematic of the 2-electrode full cell configuration.**

### 3.2.2 Fabrication of $\text{La}_{0.3}\text{M}_{0.7}\text{Fe}_{0.7}\text{Cr}_{0.3}\text{O}_{3-\delta}$ ( $M = \text{Sr}, \text{Ca}$ ) half and full cells

This section describes the cell fabrication methods used to obtain the results given in Chapters 5, 6 and 7.

#### 3.2.2.1 Symmetrical $\text{La}_{0.3}\text{M}_{0.7}\text{Fe}_{0.7}\text{Cr}_{0.3}\text{O}_{3-\delta}$ ( $M = \text{Sr}, \text{Ca}, \text{LMFCr}$ )-based full cell fabrication

Figure 3.3 shows the symmetrical LMFCr/doped ceria layer/yttria-stabilized zirconia (YSZ)/doped ceria/LMFCr full cells investigated in Chapters 5 and 6. To prepared the cells,

$\text{La}_{0.3}\text{M}_{0.7}\text{Fe}_{0.7}\text{Cr}_{0.3}\text{O}_{3-\delta}$  (M = Sr, Ca) powders mixed with organic carrier (described in Section 3.1.2) were ball milled at 200 rpm for about 1-2 h to prepare the  $\text{La}_{0.3}\text{M}_{0.7}\text{Fe}_{0.7}\text{Cr}_{0.3}\text{O}_{3-\delta}$  (M = Sr, Ca) slurry. The  $\text{La}_{0.3}\text{M}_{0.7}\text{Fe}_{0.7}\text{Cr}_{0.3}\text{O}_{3-\delta}$  (M = Sr, Ca) slurry was then screen-printed symmetrically onto both sides of a 300  $\mu\text{m}$  dense (2.5 cm diameter) YSZ electrolyte (Fuel Cells Materials) coated with a ca.10-30  $\mu\text{m}$  thick  $\text{Sm}_{0.2}\text{Ce}_{0.8}\text{O}_{2-\delta}$  (SDC) or  $\text{Gd}_{0.1}\text{Ce}_{0.9}\text{O}_{2-\delta}$  (GDC) buffer layer, followed by firing at 1100  $^{\circ}\text{C}$  for 2 h at a heating and cooling rate of 3  $^{\circ}\text{C}/\text{min}$ .

For the cells fabricated with a SDC buffer layer, custom-made YSZ electrolytes, with the SDC already screen-printed on it, were purchased from Fuel Cell Materials. The GDC buffer layers were prepared in-house by ball milling GDC powder (Fuel Cell Materials) with the organic carrier (Section 3.1.2) at 200 rpm for 1-2 h to form the slurry. The GDC slurry was then screen-printed onto both sides of a 300  $\mu\text{m}$  (2.5 cm diameter) YSZ electrolyte (Fuel Cell Materials) and fired at 1200  $^{\circ}\text{C}$  for 2 h at a heating and cooling rate of 5  $^{\circ}\text{C}/\text{min}$ .

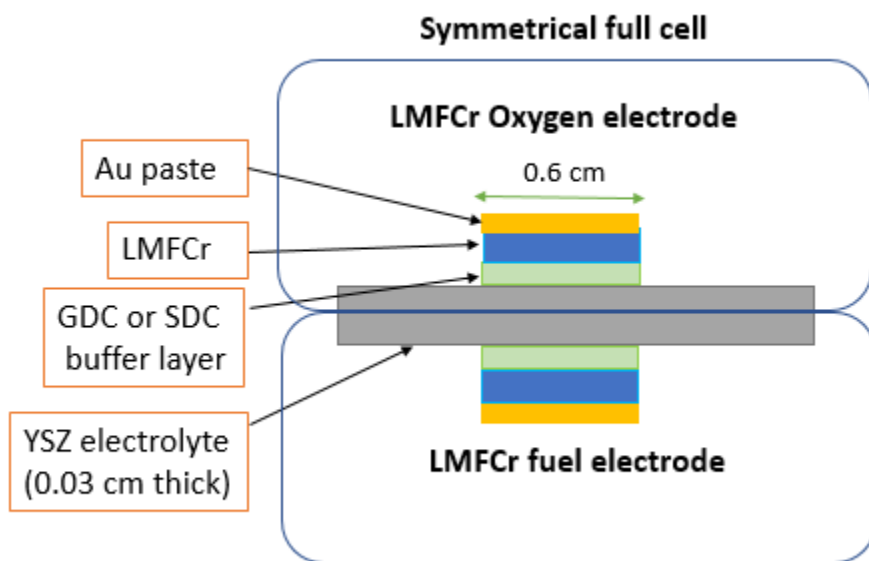


**Figure 3.3 Schematic of the LMFCr-based symmetrical full cell configuration.**

### 3.2.2.2 Fabrication of 2- and 3-electrode $\text{La}_{0.3}\text{M}_{0.7}\text{Fe}_{0.7}\text{Cr}_{0.3}\text{O}_{3-\delta}$ (M = Sr, Ca)-based half cells

To prepare the 3-electrode  $\text{La}_{0.3}\text{Sr}_{0.7}\text{Fe}_{0.7}\text{Cr}_{0.3}\text{O}_{3-\delta}$  (LSFCr) half cells (Figure 3.4a) investigated in Chapter 7, a GDC buffer layer was screen-printed onto both sides of a 300  $\mu\text{m}$  thick (2.5 cm diameter) dense YSZ electrolyte (Fuel Cell Materials) to serve as the working (WE), counter (CE), and reference (RE) electrodes. This was followed by firing at 1200 °C for 2 h at a heating and cooling rate of 5 °C/min. 30  $\mu\text{m}$  thick LSFCr working (WE) and counter (CE) electrodes were then screen-printed symmetrically onto both sides of the GDC buffer layer-coated YSZ discs. LSFCr was also used as the reference electrode (RE), screen-printed onto the same side of the YSZ as the working electrode (WE) and placed > 0.4 cm from the WE to prevent electrode geometry artifacts<sup>171, 172</sup>. The LSFCr electrodes were then fired at 1100 °C for 2 h at a heating and cooling rate of 5 °C/min.

For the 2-electrode LCFCr half cells (Figure 3.4b) study discussed in Chapter 5, the LCFCr slurry was symmetrically screen printed onto both sides of custom-made SDC buffer layer/YSZ discs (Fuel Cell Materials). The cells were then fired at 1100 °C for 2 h at a heating and cooling rate of 5 °C/min. As a control, symmetrical GDC/YSZ/GDC cells were also constructed by screen-printing and then tested in a 2-electrode half cell configuration (discussed in Chapter 6).

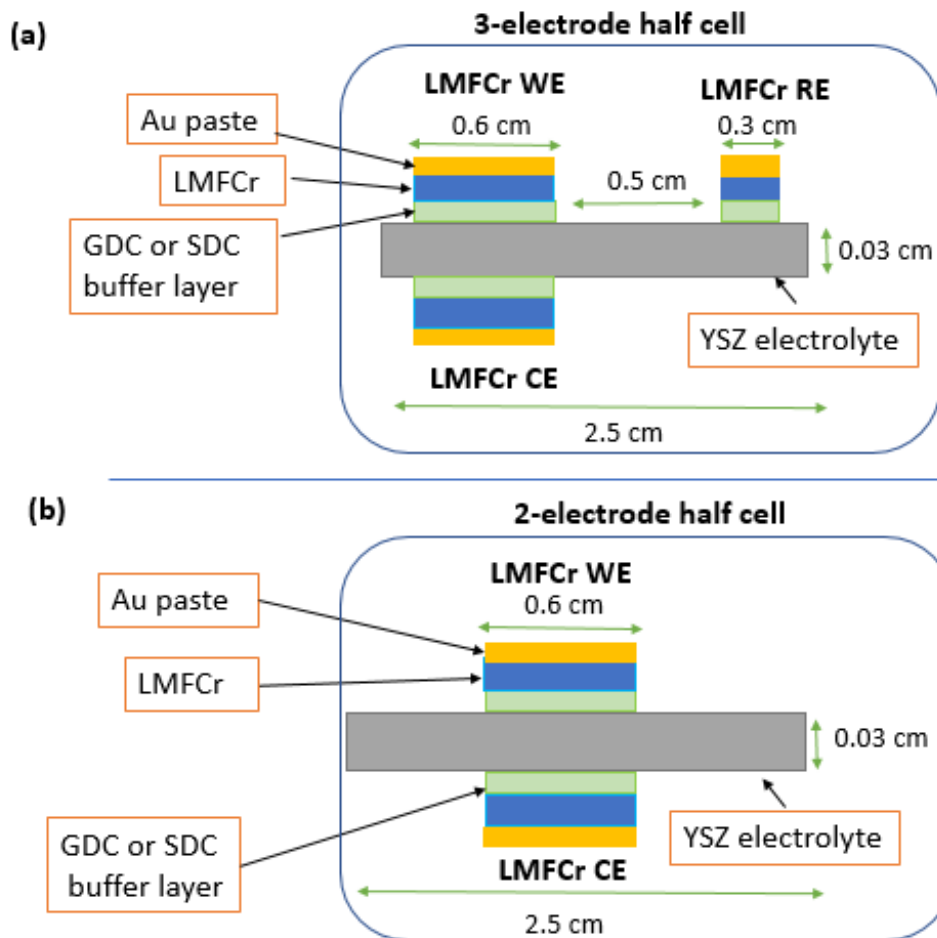


**Figure 3.4 Schematic of the LMFCr-based (a) 3-electrode and (b) 2-electrode half cell configurations.**

### 3.2.3 Fabrication of LCFCr-based thin film cells

The LCFCr thin film samples that were used for the XPS analysis, discussed in Chapter 5, were fabricated, by spin-coating a polymeric precursor solution of LCFCr onto a YSZ substrate at 2000 rpm for 30 s. 20 depositions were done to achieve a ca. 150  $\mu\text{m}$  thick LCFCr thin film on a 300  $\mu\text{m}$  YSZ disc (Fuel Cell Materials). After each deposition, the samples were heated at 100 and 250  $^{\circ}\text{C}$  for ca. 5 minutes before the next spin coating deposition was carried out.

The polymeric LCFCr solution was prepared by dissolving stoichiometric amounts of lanthanum (III) nitrate hexahydrate, calcium (II) nitrate tetrahydrate, iron (III) nitrate nonahydrate and chromium (III) nitrate nonahydrate salts in water and ethylene glycol, followed by stirring at 80 °C to allow for polymerization to take place<sup>180</sup>. The thin film samples were first fired at 800 °C in air to form the perovskite phase before the H<sub>2</sub>S exposure study was carried out.

### ***3.2.4 Gases used for stability and electrochemical testing***

The compressed gases used in this thesis for stability and electrochemical testing were air, O<sub>2</sub> (> 99.5%), H<sub>2</sub> (> 99.95%), N<sub>2</sub> (> 99.998%), CO<sub>2</sub> (99.8%), CO (> 99.5%), 30 ppm H<sub>2</sub>S (balance H<sub>2</sub>), and 52 ppm H<sub>2</sub>S (balance N<sub>2</sub>). All gases were purchased from Praxair, Calgary.

## **3.3 Electrochemical cell testing**

### ***3.3.1 Electrochemical testing of Ni-YSZ half and full cells***

Half cells were assembled in a single chamber cell holder using Ni sponge contacts (Inco), with the WE and CE coated with NiO paste during half cell loading to improve this contact. All components were held together via compression in a quartz tube half cell holder (Figure 3.5). Full cells were assembled in a cell holder (similar to Figure 3.5) using Ni sponge contacts (Inco), with the anode coated with Ni paste during cell loading to improve the contact. The cathode was painted with Pt paste and Pt gauze was used as the contact. For full cell testing, a glass sealant (Type 613, Aremco Products, USA) was used to isolate the fuel and O<sub>2</sub> sides from each other.

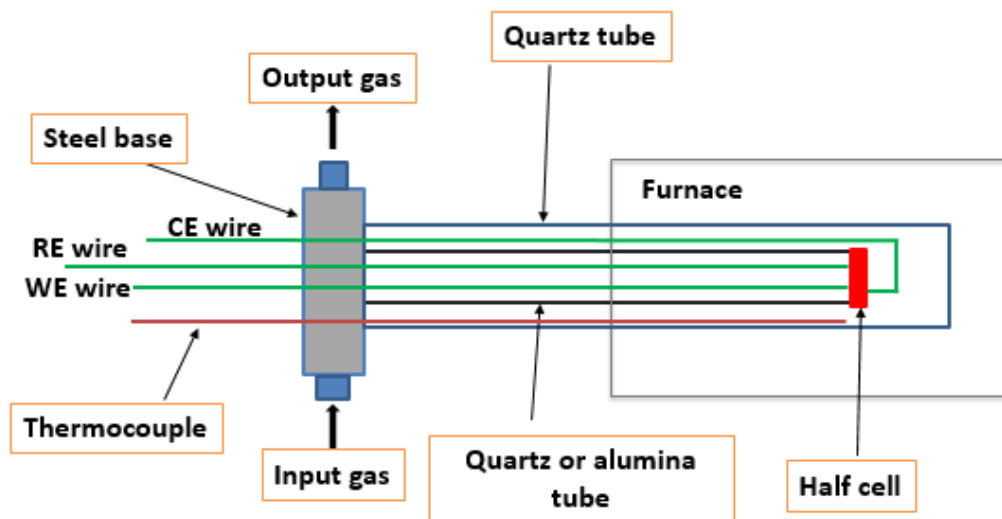


**Figure 3.5 Simplified schematic of the half cell test configuration.**

All cells were ramped to 800 °C in air (5 °C/min), after which N<sub>2</sub> was introduced for ~ 15 min (only to the anode chamber in the full cell study). At 800 °C, NiO was reduced to Ni in humidified 23.9 ml/min H<sub>2</sub> (3% H<sub>2</sub>O) + 2.5 ml/min N<sub>2</sub> for 30 min. The cell was then ramped down to the operating temperature in this reducing atmosphere. After equilibration for several hours, the electrochemical evaluation of painted Ni-YSZ half cells was initiated in 3% H<sub>2</sub>O 95:5 H<sub>2</sub>:N<sub>2</sub> (with or without 52.8 ppm H<sub>2</sub>S in the N<sub>2</sub> stream), resulting in a 5 ppm H<sub>2</sub>S in humidified H<sub>2</sub> composition. The fuel was introduced to all sides of the cell, but the gas flow (~ 25 ml/ min) was directed at the WE so that the response to H<sub>2</sub>S exposure would coincide with changes in gas composition. Infiltrated cells (Cell 3) were exposed to 8.56 ml/min H<sub>2</sub> (3% H<sub>2</sub>O) and 2 ml/min N<sub>2</sub> (with and without 52.8 ppm H<sub>2</sub>S), giving a ratio of 81:19 H<sub>2</sub>:N<sub>2</sub> (10 ppm H<sub>2</sub>S).

### 3.3.2 Electrochemical testing of symmetrical $\text{La}_{0.3}\text{M}_{0.7}\text{Fe}_{0.7}\text{Cr}_{0.3}\text{O}_{3-\delta}$ ( $\text{M} = \text{Sr}, \text{Ca}$ )-based full and half cells

#### 3.3.2.1 Testing of LMFCr-based 2-electrode half and full cells

Au paste (C 5729, Heraeus Inc. Germany) was painted on the  $\text{La}_{0.3}\text{M}_{0.7}\text{Fe}_{0.7}\text{Cr}_{0.3}\text{O}_{3-\delta}$  ( $\text{M} = \text{Sr}, \text{Ca}$ , (LMFCr)) layers on both sides of the YSZ electrolyte to serve as the current collector and Pt wires were used as the electrical leads. The cells were fixed in a FCSH-V3 cell holder (Materials Mate, Italy, Figure 3.6) for determining their electrochemical properties in various gas atmospheres over a temperature range of 600-850 °C. For full cell testing, a glass sealant (Type 613, Aremco Products, USA) was used to isolate the fuel and  $\text{O}_2$  sides from each other.

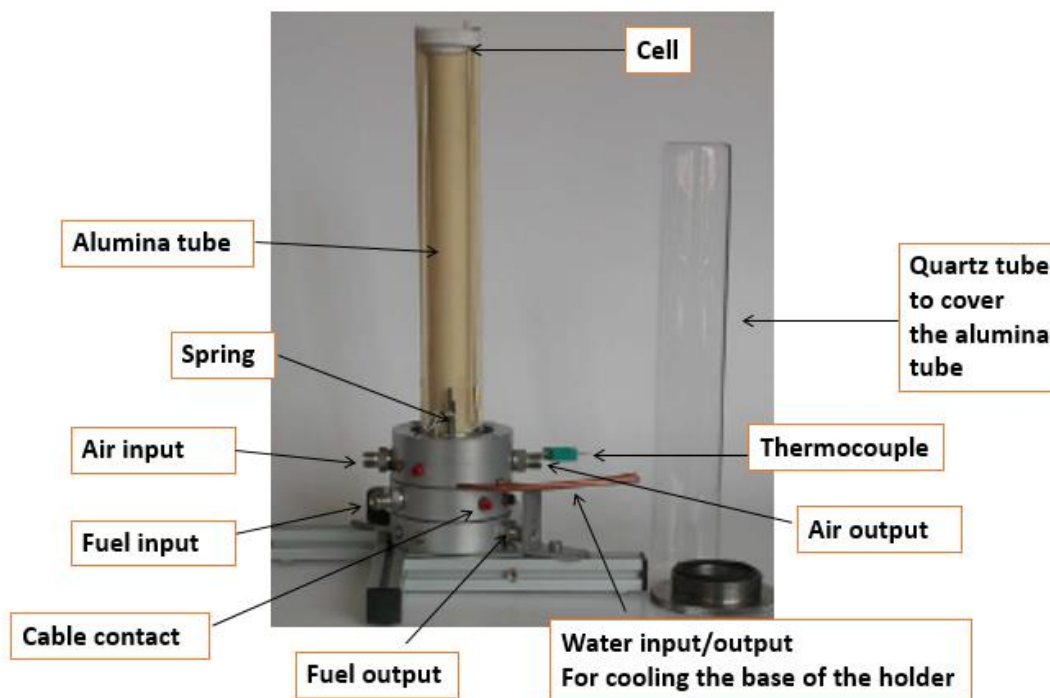


**Figure 3.6** Photo of the FCSH-V3 cell holder (Materials Mate, Italy).

The total flow rates were 25 ml/min and 40 ml/min at the fuel and oxygen electrodes, respectively. The total flow rate used for half cell testing was 50 ml/min to ensure that both of

the electrodes were exposed to the same environment. In Chapter 5, the gases used for electrochemical testing were humidified H<sub>2</sub>/N<sub>2</sub> (with or without 10 ppm H<sub>2</sub>S) and air. Chapter 6 mainly focused on using air, 20-100% CO<sub>2</sub>, 70-100% CO<sub>2</sub>:0-30% CO and 10-30% CO:70-90% N<sub>2</sub> gas mixtures for stability and electrochemical testing.

### 3.3.2.2 3-Electrode LSFCr-based half cell testing

Au paste (C 5729, Heraeus Inc. Germany) was painted on the WE, CE and RE surfaces to serve as the current collector. The electrochemical measurements to evaluate the cell performance were performed using 3-electrode methods in a range of dry gas atmospheres (air, 70-100% CO<sub>2</sub> and 30-100% CO<sub>2</sub>:0-30% CO), with a total flow rate of 50 ml/min.

### 3.3.2.3 Electrochemical evaluation of Ni-YSZ and LMFCr-based cells

Electrochemical impedance spectroscopy (EIS), cyclic voltammetry (CV), and potentiostatic and galvanostatic techniques were used for the electrochemical evaluation of the Ni-YSZ and LMFCr half and full cells, operated in various atmospheres at 500-850 °C. The EIS data were collected under open circuit and polarized conditions using an ac amplitude of 10-50 mV in the frequency range of 0.01 to 60 kHz and using a Solartron 1287/1255 potentiostat/galvanostat/impedance analyser. ZPlot software (Scribner Associates Inc.) was used to run the EIS experiments, while ZView software (Scribner Associates Inc.) was used to fit and analyze the EIS data, with the chi-squared values obtained from the equivalent circuit fitting of the data shown in this thesis being  $\leq 10^{-4}$ .

The CV and potentiostatic/galvanostatic measurements were performed using a Solartron 1287 interface, with control and data collection handled by Corrware software (Scribner

Associates Inc.) and CView software (Scribner Associates Inc.) employed for data analysis. For the 3-electrode half cell study discussed in Chapter 7, the CV measurements (sweep rates from 1-5 mV/s) were between -0.7 V and 0.7 V vs. the RE.

### **3.4 Material characterization methods**

#### **3.4.1 Powder X-ray diffraction (PXRD)**

Two instruments were used for the PXRD analysis, a Bruker D8 powder X-ray diffractometer and a Rigaku Multiflex X-ray diffractometer. Both instruments were operated at 40 kV and 40 mA, using a Cu target material. The PXRD data were acquired between 10 and 80 2-theta ( $2\theta$ ) values at a scan width of  $0.02^\circ$  and a counting time of 6 s. The PXRD analysis of the Ni-YSZ sample was carried out after several days of electrochemical testing of the cell in humidified  $H_2/N_2$ , with or without the addition of 10 ppm  $H_2S$ .

*Ex situ* PXRD was used for phase identification and determination of the chemical stability of the synthesized  $La_{0.3}M_{0.7}Fe_{0.7}Cr_{0.3}O_{3-\delta}$  ( $M = Sr, Ca, (LMFCr)$ ) powders in air, 20-100%  $CO_2$ , 70-100%  $CO_2$ :0-30%  $CO$ , 10-30%  $CO$ :70-90%  $N_2$ , and 30 ppm  $H_2S$  (balance  $N_2$ ) mixtures at room temperature. The chemical stability tests of LMFCr powders were carried out in the various gas mixtures from room temperature to 800 °C with varying dwell time (6-24 h) at 800 °C, before cooling down to room temperature in the same gas atmosphere.

*In situ* high temperature XRD analysis was carried out to further study the chemical stability of  $La_{0.3}Sr_{0.7}Fe_{0.7}Cr_{0.3}O_{3-\delta}$  (LSFCr) in  $CO_2$  environments, using the Bruker D8 Powder X-ray diffractometer with a high temperature stage (Anton Paar XRK 900). The LSFCr powder in the presence of  $CO_2$  was heated at 5 °C/min and the XRD data were collected at 30, 400, 600, and 800 °C for 30 min.

### ***3.4.2 Fourier transform infrared (FTIR) spectroscopy***

FTIR spectroscopy analysis was carried out on as-prepared LSFCr powder exposed to dry 100% CO<sub>2</sub> from 30-800 °C, with a 24 h dwell time at 800 °C, before cooling to 30 °C in CO<sub>2</sub>. The LSFCr sample was heated and cooled at a ramp rate of 5 °C/min in the CO<sub>2</sub> atmosphere.

The FTIR measurements were recorded in transmittance mode using a Varian Model FTS 7000 FTIR spectrophotometer, equipped with a DTGS detector. Small amounts of the LSFCr powder (20-25 mg), after exposure to CO<sub>2</sub>, were thoroughly mixed with pre-dried KBr powder by grinding. The experiment was performed in the frequency range of 4000-400 cm<sup>-1</sup> at a resolution of 4 cm<sup>-1</sup>, with 100 scans of data accumulation. Before running the samples, the instrument was calibrated by running a blank test, involving pure, dried, KBr powder placed on an aluminium holder after degassing in vacuum for 25 min at room temperature<sup>6</sup>. The blank test ensured the removal of atmospheric CO<sub>2</sub> that may have adsorbed on the samples<sup>6</sup>.

### ***3.4.3 Thermogravimetric analysis (TGA)***

The TG analysis was carried out to understand the thermal behavior, CO<sub>2</sub> stability, and the oxygen non-stoichiometry of the LSFCr material, as discussed in Chapter 6. The weight change of the LSFCr powder (20-50 mg), placed in an alumina crucible, was determined as a function of temperature using a Mettler-Toledo (HT-1600) instrument. The TGA experiments were carried out from room temperature to 900 °C at a rate of 3 °C/min or 5 °C/min in either air or 60% CO<sub>2</sub> (balance N<sub>2</sub>), with some isothermal measurements made at 600 and 800 °C in 60% CO<sub>2</sub> (balance N<sub>2</sub>).

#### ***3.4.4 Scanning electron microscopy/Energy dispersive X-ray spectroscopy (SEM/EDX)***

SEM/EDX analysis was carried out to determine the morphology, microstructure, and chemical composition of Ni-YSZ samples (Chapter 4), LSFCr powders exposed to various gas atmospheres (Chapter 6) and LSFCr cells (Chapter 6), using a Philips/FEI X23 ESEM, (Microscopy and Imaging Facility, Health Sciences, University of Calgary). The samples were usually sputter-coated with a thin layer of Pd-Au to avoid any charge build-up during SEM analysis. The SEM was operated at a working distance of ca. 10 mm and accelerating voltages in the range of 10-20 kV. EDX analyses were carried out to determine the elemental composition of the samples.

#### ***3.4.5 High resolution transmission electron microscopy (HRTEM)***

The high resolution transmission electron microscopy (HRTEM) analysis was carried out through a collaboration with Dr. Davide Avila-Brandé (Department of Inorganic Chemistry, Universidad Complutense, Madrid, Spain). The analysis was carried out on as-prepared LSFCr powder and on LSFCr powders exposed to 100% CO<sub>2</sub>, 90% CO<sub>2</sub>:10% CO, and 70% CO<sub>2</sub>:30% CO and from 30-800 °C, with a 24 h dwell time at 800 °C. All of the samples were heated and cooled at a ramp rate of 5 °C/min in the same gas atmosphere.

For the HRTEM analysis, the LSFCr powders were ground in n-butyl alcohol and ultrasonically dispersed. A few drops of the resulting suspension were deposited on a carbon-coated grid. HRTEM was performed using a JEOL JEM 3000F microscope (Universidad Complutense, Madrid, Spain) operating at 300 kV (double tilt,  $\pm 20^\circ$ , point resolution 0.17 nm), fitted with an X-ray energy dispersive spectroscopy (EDX) microanalysis system (OXFORD INCA) and an ENFINA spectrometer with an energy resolution of 1.3 eV. The atomic ratio of

the metals was determined by EDX, which showed good agreement between the analytical and nominal compositions in all of the crystals.

#### ***3.4.6 Electron microprobe analysis***

For elemental mapping, a JEOL JXA-8200 electron microprobe, employing five wavelength dispersive spectrometer (WDS) channels, was used for the elemental mapping of the LCFCr/GDC/YSZ/GDC/LCFCr cells (Chapter 5) after electrochemical testing in humidified 30% H<sub>2</sub>/N<sub>2</sub>, with or without the addition of ca.10 ppm H<sub>2</sub>S. Also, elemental mapping was carried out of a LSFcr-based symmetrical full cell (Chapter 6) after several days of testing in 70-100% CO<sub>2</sub>:0-30% CO atmospheres, at 600-850 °C. The samples were polished to very fine grades and then carbon-coated before the electron microprobe analysis.

#### ***3.4.7 X-ray photoelectron spectroscopy (XPS)***

XPS analysis was performed on Ni-YSZ anodes after electrochemical testing in 5 ppm H<sub>2</sub>S in H<sub>2</sub> at 500 °C. The XPS spectra were collected using a monochromatic Al source (1486.60 eV) on a PHI VersaProbe 5000 instrument (Catalyst Surface Science Laboratory, Department of Chemical and Petroleum Engineering, University of Calgary) with a 25 W X-ray beam (~100 μm dia). Charge compensation was achieved with low energy Ar<sup>+</sup> ions and an electron flood gun. The XPS data were processed using MultiPak software (Physical Electronics).

The XPS analysis of the LCFCr thin film samples, exposed to 30-50% humidified H<sub>2</sub>, with or without the addition of 10 ppm H<sub>2</sub>S, for varying lengths of time at 600 °C and 800 °C, was carried out by our collaborator, Dr. Ali Ahsen (Dr. Osturk's group, Turkey). The analysis was performed in a UHV chamber, which has a base pressure of 1.0x10<sup>-10</sup> torr. The chamber was

equipped with a conventional X-Ray source (Al K $\alpha$  and Mg K $\alpha$ ) and Phoibos 150 charged particle analyzer. The La3d, Ca2p, Cr2p, Fe 2p and S2p peaks were fit with a Voight function after subtracting the polynomial background functions.

#### ***3.4.8 Auger electron spectroscopy (AES)***

Auger electron spectroscopy (AES) analysis was performed on a rapidly cooled Ni-YSZ cermet that had been exposed to 5 ppm H<sub>2</sub>S at 500 °C for 72 h, as discussed in Chapter 4. Auger spectra were collected using a multi-channel detector with a cylindrical mirror analyzer on a Phi 690 scanning Auger NanoProbe system (Catalyst Surface Science Laboratory, Department of Chemical and Petroleum Engineering, University of Calgary), using a field emission electron gun at 10 kV and 10 nA. A scintillator was used for secondary electron imaging. The stage supporting the sample was tilted at 75° to avoid any charging effects and the main chamber was maintained under vacuum at 3x10<sup>-10</sup> torr. Elemental maps were obtained by using a 35,000X magnification and monitoring the Auger signals for S (156 eV), Ni (849 eV) and Zr (1847 eV).

#### ***3.4.9 Low energy ion scattering spectroscopy (LEIS)***

To further understand the state of sulfur on H<sub>2</sub>S-exposed Ni-YSZ samples, we began a collaborative research effort with Dr. Stephen Skinner at Imperial College London (UK), who has access to a highly sensitive surface technique, low energy ion scattering spectroscopy (LEIS). For the LEIS analysis (performed by Dr Andrea Cavallaro), Ni-YSZ and Ni foil samples, exposed to humidified H<sub>2</sub> + 10 ppm H<sub>2</sub>S conditions at 500 °C for 72 h and rapidly quenched to room temperature, were investigated.

The LEIS experiments were performed using a Qtac<sup>100</sup> instrument (ION-TOF GmbH) at a base pressure of  $\sim 3 \times 10^{-10}$  mbar (which increases to the  $10^{-8}$  mbar range during the analysis due to the flux of noble gas). The instrument was fitted with a double toroidal energy analyzer (DTA), which collects the scattered ions at a scattering angle of  $145^\circ$  from all azimuth angles. The LEIS measurements were performed using a 3 keV He<sup>+</sup> primary ion beam and a 5 nA current directed perpendicularly to the target surface.

Due to the high detection efficiency of this analyzer–detector system and rastering of the ion beam across the sample surface (typically over  $0.75 \times 0.75$  mm<sup>2</sup>), the LEIS spectra were recorded with an ion dose as low as  $3.5 \times 10^{14}$  ions/cm<sup>2</sup>. The samples were analyzed without any cleaning step. Once the samples were introduced into the UHV chamber, the LEIS spectra were recorded and then followed by low-energy sputtering by 0.5 keV Ar<sup>+</sup> bombardment at  $59^\circ$  to remove the outer surface for the LEIS depth profile analysis. The sputtered area was  $1.5 \times 1.5$  mm<sup>2</sup> and the sputter time was 10 s with a 1 s pulse time. A  $1.6 \times 10^{14}$  ions/cm<sup>2</sup> Ar<sup>+</sup> ion dose was recorded. A SRIM (Stopping and Range of Ions in Matter) 2008 package was used to estimate the crater depth and the Ar sputtering rate of the LEIS depth profile analysis<sup>181</sup>.

### 3.5 Error Analysis

All mass flow controllers (MFCs, Alicat Scientific (MCS Series)) were calibrated using soap bubble movement in a 10 ml graduated pipette. To calculate the total flow rate in ml/min, the displacement time of the soap bubble over a specific volume was measured with a stopwatch<sup>88</sup>.<sup>182</sup>. The MFCs had a  $\pm 1\%$  error on the set temperature<sup>182</sup>.

XRD data collected from the Bruker D8 Advances instrument were calibrated before the measurements using a NIST corundum standard SRM 1976a to check for peak error due to the

instrument alignment<sup>6</sup>. It was adjusted to be within  $0.01^\circ$  for  $2\theta$  over the whole angular range. The errors in the TGA furnace temperature and balance of the Mettler Toledo thermal system TGA/DSC1 were  $\pm 0.5^\circ\text{C}$  and  $\pm 1\ \mu\text{g}$ , respectively.

The temperature of the furnace (Linderberg/Blue M\*) used for all of the electrochemical and stability tests had an error of  $\pm 3^\circ\text{C}$ . The temperature was measured by using a calibrated thermocouple (Chromel-Alumel Omega that has an error of  $\pm 1^\circ\text{C}$ ).

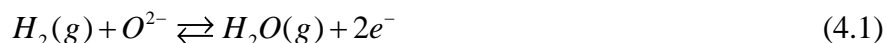
Calibration of the Solartron 1287/1255 potentiostat/galvanostat/impedance analyser with a dummy cell with a resistance of  $1.9\text{-}9.3\ \Omega$  and over a frequency range of  $1\text{-}10\ \text{Hz}$  gave an error of approximately  $0.1\%$  between the measured and true resistance value. The Varian 7000 FTIR spectrometer has an estimated error of  $\pm 2\ \text{cm}^{-1}$  over the full whole frequency range<sup>6</sup>.

## Chapter Four: **Activation behavior of Ni-YSZ fuel electrode (anode) in low ppm H<sub>2</sub>S at sub-600 °C**

This Chapter contains some data from a published paper (L. Deleebeeck, M. Shishkin, P. Addo, S. Paulson, H. Molero, T. Ziegler and V. Birss, *Activation of H<sub>2</sub> oxidation at sulphur-exposed Ni surfaces under low temperature SOFC conditions*, Physical Chemistry Chemical Physics, 2014, **16**(20): p. 9383-9393), reproduced by permission of the PCCP Owner Societies. Majority of the results and text shown are my contributions.

### **4.1 Introduction**

Previous work in our group and by others have shown that, even though Ni-yttria stabilized zirconia (YSZ) cermets have excellent properties as anodes in solid oxide fuel cells (SOFCs) for the oxidation of H<sub>2</sub> (Reaction 4.1), they tend to be poisoned by the presence of low levels of H<sub>2</sub>S at the operating temperature (800-1200 °C)<sup>177, 183-185</sup>. The poisoning effect of H<sub>2</sub>S on Ni-YSZ decreases the performance of the anode towards the hydrogen oxidation reaction (HOR) because of the adsorption of sulfur (S) on the surface of the Ni catalyst at the triple phase boundary (TPB), which decreases the number of active sites available for the HOR<sup>186</sup>.



Both experimental<sup>187</sup> and theoretical (density functional theory)<sup>157, 188</sup> work have suggested an inverse linear relationship between the surface coverage of S<sub>ads</sub> and adsorbed hydrogen (H<sub>ads</sub>) on Ni, such that the H<sub>ads</sub> coverage approaches zero as S<sub>ads</sub> approaches 100% coverage (one S<sub>ads</sub> for two surface Ni atoms). Also, it has been shown in the literature that the poisoning of Ni-YSZ anodes by low ppm H<sub>2</sub>S (ca. <100 ppm) increases as the operating temperature of the SOFCs is decreased (e.g., from 1100 to 700 °C) and as the concentration of H<sub>2</sub>S is increased<sup>184, 185, 189</sup>.

While there has been some work done on the performance Ni-YSZ anodes in ppm levels of H<sub>2</sub>S at temperatures of ca. 650 °C or below<sup>189, 190</sup>, there has been no systematic study carried

out down to 500 °C. This is presumably because it has been assumed that Ni-based anodes would be significantly deactivated by H<sub>2</sub>S under these conditions. One of the advantages of decreasing the operating temperature of SOFCs to sub 600 °C is minimization of the various degradation issues, such as oxidation of interconnects, Ni oxidation and related morphology changes, and coking, all of which negatively affect SOFCs at high temperature<sup>157, 191</sup>. Also, operating SOFCs at sub 600 °C allows the efficient use of infiltrated electrode nanomaterials to generate higher triple phase boundary (TPB) lengths with less sintering and stability issues that are typically observed at higher operating temperatures, e.g., at ca. > 750 °C<sup>157</sup>. Because of this increasing focus on SOFC operation at < 600 °C<sup>192, 193</sup>, the primary purpose of the present study was to rigorously determine the extent of sulfur poisoning of Ni-YSZ anodes in the presence of up to 10 ppm H<sub>2</sub>S in this lower temperature range<sup>156</sup>.

In this chapter, it is shown that there is an unexpected improved performance seen for the Ni-YSZ anode towards the oxidation of hydrogen at intermediate temperatures (500-600 °C) in the presence of 5-10 ppm H<sub>2</sub>S in humidified H<sub>2</sub>. These experiments were carried out using both three-electrode electrolyte-supported Ni/YSZ symmetrical half cells and a Ni-YSZ/YSZ/LSM (La<sub>1-x</sub>Sr<sub>x</sub>MnO<sub>3</sub>)-YSZ full cell. Based on detailed analytical characterization and density functional theory (DFT) modeling, it is proposed that the activation of the Ni-YSZ anode (fuel electrode) towards hydrogen oxidation (HOR) is due to the local formation of a thin layer of Ni-S species (e.g., Ni<sub>3</sub>S<sub>2</sub>) at the triple phase boundary (TPB). It is shown that the energy barrier for H<sub>2</sub> oxidation at the Ni<sub>3</sub>S<sub>2</sub>/YSZ interface is lower than at Ni/YSZ, thus explaining the results.

## 4.2 Results and Discussion

### 4.2.1 Effect of H<sub>2</sub>S on 3-electrode Ni-YSZ half cell performance at 500-800 °C

The hydrogen oxidation reaction (HOR) behavior of a 3 electrode Ni-YSZ half cell, with the fabrication details discussed in Chapter 3, was studied with or without the addition of 5 ppm H<sub>2</sub>S to humidified 97% H<sub>2</sub>/N<sub>2</sub> at 500-800 °C. Figure 4.1 shows the i-t plots of the cell operated in humidified H<sub>2</sub> with the addition and removal of 5 ppm H<sub>2</sub>S, acquired at a 250 mV anode overpotential with a 50 °C stepwise decrease from 800 to 500 °C. From Figure 4.1, it is seen that, as the temperature was decreased from 800 to 500 °C, the current density corresponding to the HOR activity decreased. As expected<sup>179, 180, 184</sup>, from 800 to 650 °C (Figure 4.1a), the addition of H<sub>2</sub>S to the humidified H<sub>2</sub> leads to poisoning (loss of current) of the Ni-YSZ electrode, while removal of H<sub>2</sub>S leads to a slow recovery of the current. As seen, the recovery process is slower than the poisoning step, which agrees with theoretical predictions<sup>194</sup>. Even though the recovery step is slower, the cell recovers slightly faster at 800 and 750 °C than at 700 °C and 650 °C. At 800 °C, as shown in Figure 4.1a, the cell completely recovers after ca. 8 h of removal of the H<sub>2</sub>S, indicating complete reversibility.

The behavior of the cell from 600-500 °C is shown in Figure 4.1b. At 600 °C, the addition of H<sub>2</sub>S leads to poisoning (loss of current). However, the extent of poisoning is smaller when compared to at > 650 °C and the cell completely recovers with the removal of H<sub>2</sub>S. This is interesting because the understanding in literature is that the extent of poisoning should increase as the temperature is lowered. Unexpectedly, at 550 and 500 °C, the addition of H<sub>2</sub>S leads to an increase in current density (activation), as can be seen in Figure 4.1b, and the cell completely recovers at 550 and 500 °C when H<sub>2</sub>S is removed.

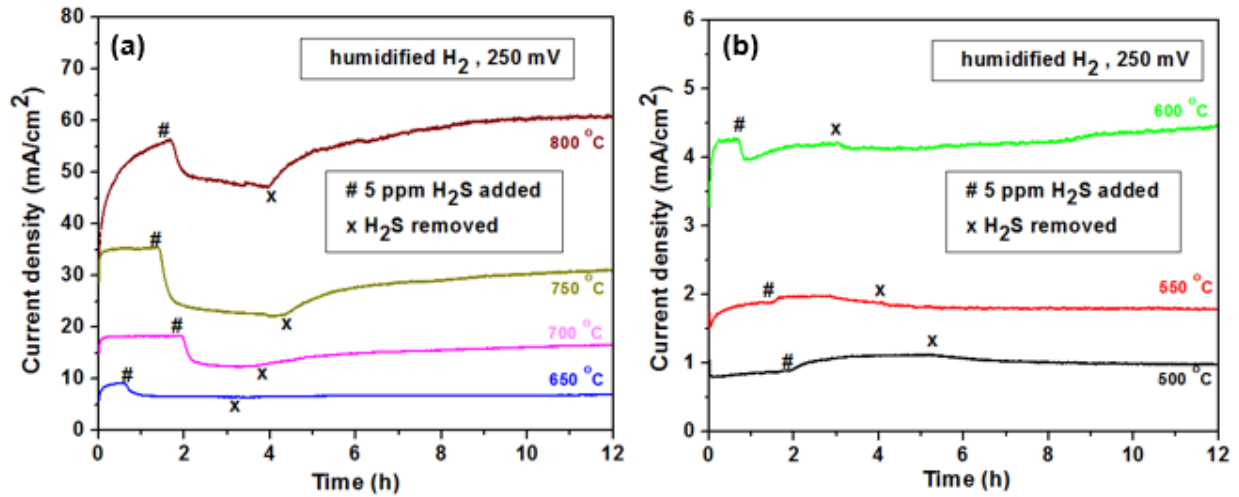


**Figure 4.1** Potentiostatic study of the effect of 5 ppm H<sub>2</sub>S exposure and removal on Ni-YSZ electrode as a function of temperature in humidified H<sub>2</sub>, showing the i-t plots at a 250 mV anode overpotential monitored at 50 °C increments from (a) 750-650 °C and (b) 600-500 °C. The 1 and 3 h times of exposure to 5 ppm H<sub>2</sub>S are marked.

For a clear comparison of the extent of poisoning or activation of the Ni-YSZ electrode when H<sub>2</sub>S is added to the H<sub>2</sub> gas stream, the i-t plots were converted to % i-t plots using equation 4.2.

$$\%i = \frac{(i_{t=0} - i_{t>0})}{i_{t=0}} \times 100 \quad (4.2)$$

where  $i_{t=0}$  is the current density at the onset of H<sub>2</sub>S exposure,  $i_{t>0}$  is the current density before the removal of H<sub>2</sub>S,  $t = 0$  is the H<sub>2</sub>S exposure onset time, and  $t > 0$  is the final time before removal of H<sub>2</sub>S. Also, the influence of thermal history on the extent of poisoning or activation of Ni-YSZ electrodes was studied. Different cells were investigated, where for Cell 1 (Figure 4.1), the initial H<sub>2</sub>S exposure was carried out at 800 °C before decreasing to 500 °C, whereas in Cell 2, the initial H<sub>2</sub>S exposure was 500 °C before increasing the temperature to 800 °C. The primary reason for

this study was to understand whether the effect of the activation observed at 500 °C could be seen at a higher temperature.

Figure 4.2 shows the percent current density change with respect to the thermal behavior/history of Cells 1 and 2 when H<sub>2</sub>S was added and removed. Figure 4.2a (Cell 1) shows the percent current density (% i-t) plots of only the part of the i-t plots in Figure 4.1 where H<sub>2</sub>S was added and removed. In Figures 4.2a and 4.2c, the percent loss of current density (extent of poisoning) of Cell 1 is seen to increase from 18% at 800 °C to 38% at 750 °C. From 750 °C to 650 °C, it decreases to 30%. At 600 °C, only a 10% current density loss is observed, showing a lower extent of poisoning. For Cell 1, the increase in current density (activation) with the introduction of H<sub>2</sub>S is observed at 550 °C and 500 °C. At 550 °C, the current density increased by 10%, while at 500 °C, a 22% increase in current is observed. For Cell 1, the 600 and 550 °C data (Figure 4.1b) likely reflect a transitional state where activation and deactivation behavior is intermingled.

The introduction of H<sub>2</sub>S first at 500 °C (Cell 2) after the reduction of the NiO-YSZ electrode at 800 °C in humidified H<sub>2</sub> is shown in Figures 4.2b and 4.2c. As seen in Figure 4.2c, the percent loss in current density (extent of poisoning) for Cell 2 from 700 to 800 °C is lower than that of Cell 1. Thus, the current density loss for Cell 2 is ca. 15-18% from 700-800 °C, whereas for Cell 1, the current density loss is between 18-38%. The current density increased by 22% at 500 °C for Cell 2, similar to Cell 1. As can be seen, in both Figure 4.2b and 4.2c, the % current density gain (activation) for Cell 2 extends from 500-650 °C, whereas for Cell 1, activation or enhancement of the HOR in the presence of H<sub>2</sub>S was only observed from 500-550 °C. The % current density gain for Cell 2 decreased slightly from 22% to 18% from 500-600 °C, and at 650 °C, the % current density gain is 5%. Therefore, for Cell 2, the activation/deactivation transition

temperature is likely between 600-650 °C, whereas for Cell 1, the transition temperature is between 550-600 °C. This shows that the activation effect observed at 500 °C can be extended to intermediate temperatures (600-650 °C) if the introduction of H<sub>2</sub>S to the cell is initially carried out at lower temperatures (500 °C) before going to higher temperatures (>700 °C).

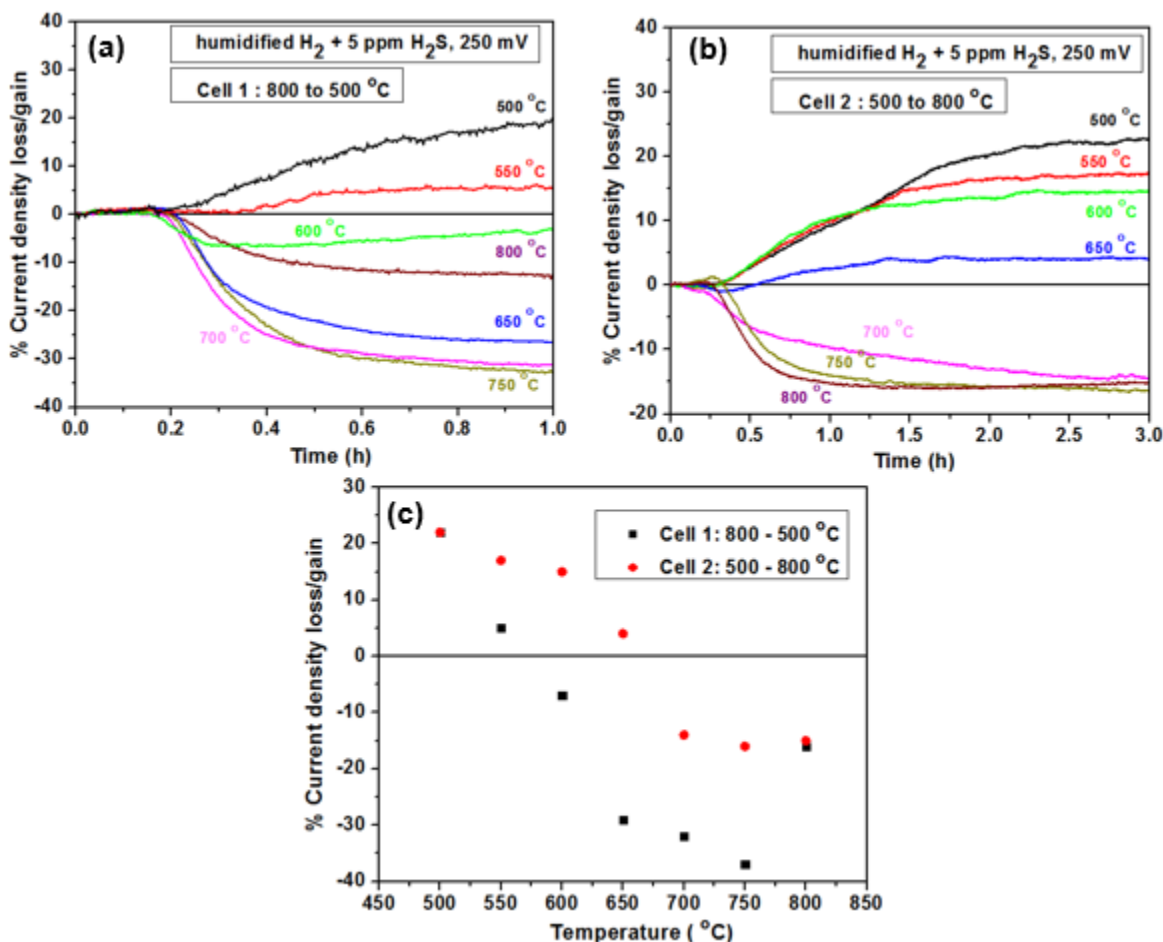


**Figure 4.2** Effect of cell thermal history on Ni-YSZ anode response to H<sub>2</sub>S exposure. Percentage change in H<sub>2</sub> oxidation current seen at Ni-YSZ anodes upon introduction of 5 ppm H<sub>2</sub>S in humidified H<sub>2</sub> for data acquired (a) from 800 °C down to 500 °C for Cell 1, (b) from 500 °C up to 800 °C for Cell 2, and (c) a comparison plot showing the % *i* vs. temperature plot. A positive percentage change in current indicates H<sub>2</sub>S activation of the Ni anode, while negative changes indicate anode poisoning by H<sub>2</sub>S.

These results therefore strongly suggest that a new surface species or state, which is catalytic towards H<sub>2</sub> oxidation, can be formed at the Ni-YSZ anode in H<sub>2</sub>S at low temperatures (500 °C). Once formed, its effects persist to higher operating temperatures (e.g., 600 °C) than when H<sub>2</sub>S exposures are carried out at higher temperatures first. This has important implications for the development of a sulfur tolerant cell that would be operated only at temperatures of 600 °C or lower, e.g., metal-supported SOFCs.

#### ***4.2.2 Detailed electrochemical study of the activation of Ni-YSZ anode at 500 °C***

To further understand the reaction mechanism associated with the activation of Ni-YSZ anodes in 5 ppm H<sub>2</sub>S at 500 °C, this section provides a more detailed electrochemical analysis vs. Section 4.2.1, based on both ac and dc techniques. The study was carried out with a 3-electrode Ni-YSZ cell kept solely at 500 °C, with or without H<sub>2</sub>S added to the humidified H<sub>2</sub> gas steam.

Figure 4.3 shows the open circuit electrochemical impedance spectroscopy (EIS) data acquired when exposing a Ni-YSZ fresh cell to 3 cycles of 5 ppm H<sub>2</sub>S addition and removal at 500 °C for 75 h. The inductive behavior at low frequencies (Figure 4.3a), seen as an inward curl at low frequencies, is likely due to further anode activation during long polarization times. Figure 4.3b shows the resistance vs. time plot, obtained by fitting the Nyquist plot to a R<sub>s</sub>(R1CPE1)(R2CPE2) equivalent circuit (Figure 4.3a). R<sub>s</sub> is the series resistance, which is mainly dominated by the electrolyte. R1CPE1 and R2CPE2 reflect the processes occurring at high and low frequencies, respectively, where R1 is the high frequency resistance, R2 is the low frequency resistance and R<sub>p</sub> is the polarization resistance (R1 + R2). The CPEs are constant phase elements and were converted to capacitance using Equation 4.3<sup>195</sup>:

$$C_i = \frac{(R_i Q_i)^{1/n_i}}{R_i} \quad (4.3)$$

where R is a resistance and Q is a constant phase element (CPE), representing a time-dependent capacitive element, and n is the associated parameter that indicates the similarity of Q to an ideal capacitor, for which n = 1.

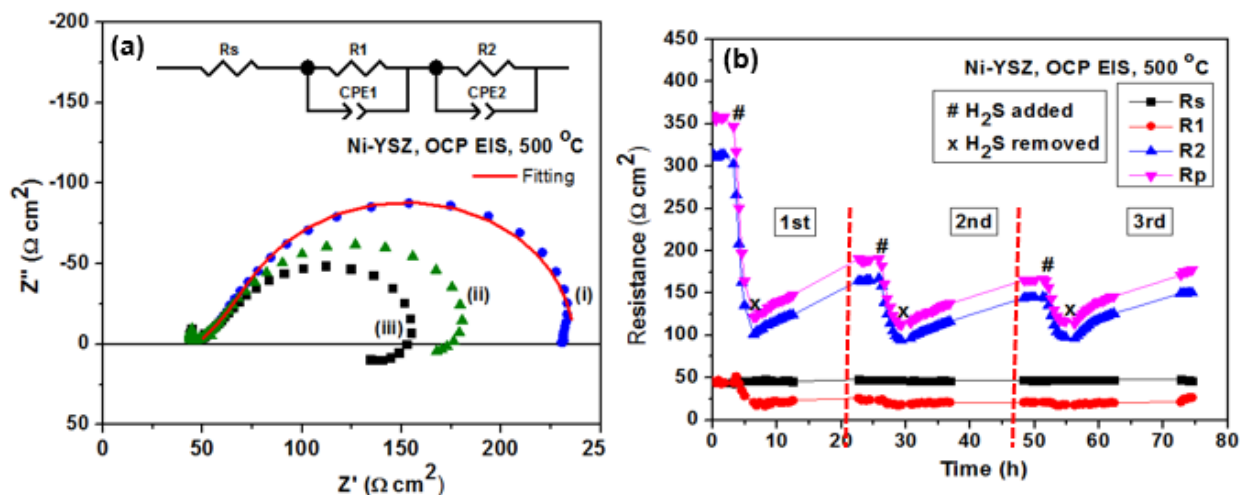


**Figure 4.3** Response of Ni-YSZ anode (in 3-electrode cell) to H<sub>2</sub>S at the open circuit potential at 500 °C. (a) An example of Ni-YSZ anode impedance response during three cycles of 5 ppm H<sub>2</sub>S addition and removal, as seen in Figure 4.3b showing (i) before exposure to H<sub>2</sub>S, (ii) in 5 ppm H<sub>2</sub>S, and (iii) following removal of H<sub>2</sub>S and partial recovery in H<sub>2</sub>. (b) Resistances obtained from fitting the Nyquist plots to the equivalent circuit (Figure 4.3a) during the 75 h of three cycles of 5 ppm H<sub>2</sub>S addition and removal.

From Figure 4.3b and Table 4.1, it is seen that the polarization resistance (Rp) decreases rapidly from 360 to 145 Ω cm<sup>2</sup> when 5 ppm H<sub>2</sub>S was added, while the series resistance (Rs) remains constant at ca. 47 Ω cm<sup>2</sup>. This shows the vast improvement in the anode activity that results when it is first exposed to H<sub>2</sub>S at 500 °C, resulting in a 60% decrease in Rp. Because Rp only very slowly recovers from 120 to 189 Ω cm<sup>2</sup> after H<sub>2</sub>S is removed in the first cycle, this significant activity improvement is still seen 24 h later, indicating that the anode remains activated for lengthy period of times, even after H<sub>2</sub>S is removed.

Table 4.1 shows a 41% and 30% decrease in  $R_p$  in the second and third cycles of  $H_2S$  addition/removal, respectively, indicating that this kinetically stable  $H_2S$ -activated state can be maintained for a 'fresh anode' for tens of hours. Also, it is observed that both the high ( $R_1$ ) and low ( $R_2$ ) frequency resistances decrease when  $H_2S$  is added to the humidified  $H_2$ . For a Ni-YSZ anode, the low frequency arc, seen at about 1 Hz, is ascribed to a gas conversion process which is caused by a stagnant layer of gas above the electrode surface<sup>196</sup>. The gas conversion impedance typically has an  $n$  value of 1 and a high capacitance ( $>1$  F/cm<sup>2</sup>) and is not temperature dependent<sup>196</sup>.

Therefore, to confirm that  $R_2$  is not due to gas conversion or mass transport limitations, temperature studies were carried out. It was observed that  $R_2$  decreased from ca. 150  $\Omega$  cm<sup>2</sup> at 500 °C to 5  $\Omega$  cm<sup>2</sup> at 800 °C and the low frequency capacitance ( $C_2$ ), calculated based on Equation 4.3, was 10<sup>-3</sup> F/cm<sup>2</sup> at 500 °C. Therefore, the results show that the low frequency arc is not due to gas conversion or mass transport limitations.

The effect of the anode overpotential on the catalytic effect of  $H_2S$  exposure on the HOR at Ni-YSZ anodes at 500 °C was also investigated. Figure 4.4 shows the  $i$ - $t$  plots of a Ni-YSZ anode at overpotentials of 50 to 250 mV with the addition and removal of 5 ppm  $H_2S$  at 500 °C. As expected, the current density increases as the overpotential is increased from 50 to 250 mV, with the addition of  $H_2S$  to  $H_2$  giving an enhancement of the hydrogen oxidation reaction at all overpotentials.

**Table 4.1 Resistance values\* obtained by fitting the OCP impedance data (Figure 4.3 \*\*) to the equivalent circuit shown in Figure 4.3a.**

Cycle	Time (h)	Gas	Rs ( $\Omega \text{ cm}^2$ )	R1 ( $\Omega \text{ cm}^2$ )	R2 ( $\Omega \text{ cm}^2$ )	Rp# ( $\Omega \text{ cm}^2$ )	%Rp loss
First	0	H <sub>2</sub>	44	45	315	360	60
	5	H <sub>2</sub> + H <sub>2</sub> S	46	27	117	144	
Second	24	H <sub>2</sub>	47	24	165	189	41
	29	H <sub>2</sub> + H <sub>2</sub> S	47	18	94	112	
Third	50	H <sub>2</sub>	47	21	145	166	30
	55	H <sub>2</sub> + H <sub>2</sub> S	47	18	98	116	
	74	H <sub>2</sub>	46	27	151	177	

\* R1 and R2 obtained from the high (ca. 100 Hz) and low (ca. 1 Hz) frequency arcs, respectively.

\*\* 3 electrode Ni-YSZ anode, operated at 500 °C in wet 97 % H<sub>2</sub>/N<sub>2</sub> with the addition and removal of H<sub>2</sub>S.

# Rp = R1 + R2. Rp values may not add up due to internal rounding

Figure 4.4b shows the corresponding percent current change plot for the addition and removal of H<sub>2</sub>S, obtained from the data in Figure 4.4a by using Equation 4.2. From Figure 4.4b, the addition of H<sub>2</sub>S leads to a 30% increase in current density at 50 mV, while a 20% and 22% increase in current density was obtained at a 100 and 250 mV anode overpotential, respectively. However, there is no clear trend seen in the magnitude of the activation of the Ni-YSZ anode towards the hydrogen oxidation reaction with overpotential. Even so, at low overpotentials (50 mV), a slightly higher % current density is seen when compared to the case at a 250 mV overpotential. Also, deactivation was slow in each case when H<sub>2</sub>S is removed at 500 °C, as seen in Figure 4.4b.

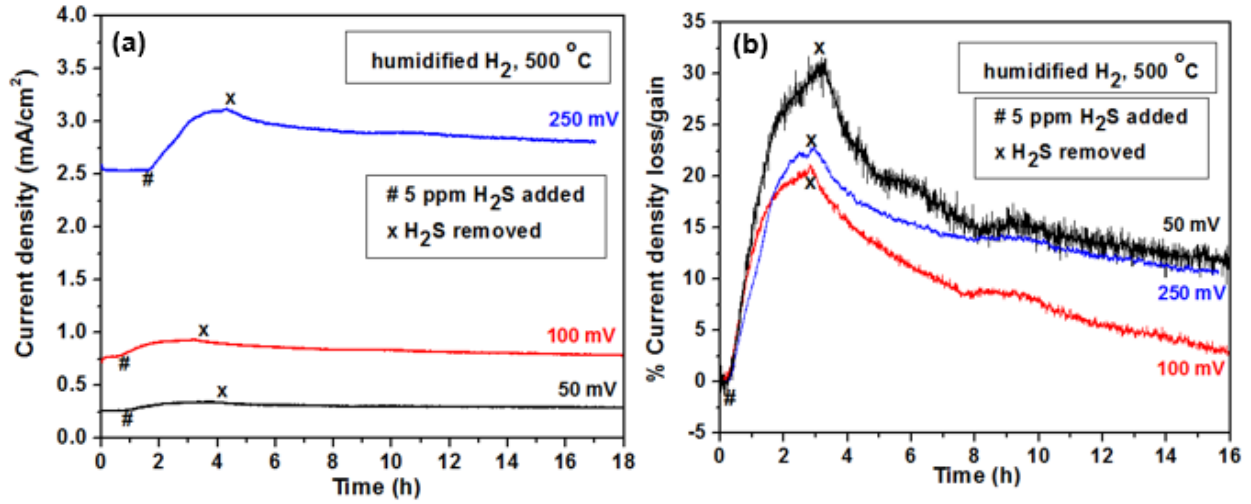


**Figure 4.4 (a) i-t transients during introduction and removal of 5 ppm H<sub>2</sub>S in humidified H<sub>2</sub> at variable anodic overpotentials (50-250 mV) at 500 °C, and (b) the percent current increase versus time plots for the data in (a).**

Cyclic voltammetry (CV) studies were also carried out in the 3-electrode cell to determine the effect of H<sub>2</sub>S on the hydrogen oxidation reaction (HOR) rate and mechanism. Using the Butler-Volmer relationship (Equation 4.4) and its simplified form (Equation 4.5)<sup>173</sup>, representing only the anodic/positive part of Equation 4.4, kinetic parameters, such as the exchange current density (*i*<sub>o</sub>), Tafel slope, and transfer coefficient ( $\alpha_a$ ), associated with the HOR process at 500 °C at a Ni-YSZ anode, were determined.

$$i_{net} = i_o \left[ \exp\left(\frac{\alpha_a \eta F}{RT}\right) - \exp\left(\frac{-\alpha_c \eta F}{RT}\right) \right] \quad (4.4)$$

$$\log i_{net} = \log i_o + \frac{\alpha_a F \eta}{2.303 RT} \quad (\text{at positive } \eta) \quad (4.5)$$

where *i*<sub>net</sub> and *i*<sub>o</sub> are the measured and exchange current densities, respectively,  $\eta$  is the overpotential,  $\alpha_a$  and  $\alpha_c$  are the anodic and cathodic transfer coefficients, respectively, and *F* and *R* are the Faraday and gas constants, respectively. Based on the Tafel slope (Equation 4.6), the  $\alpha$

values, which can be used to help identify the reaction mechanism and the slowest step, can be obtained.

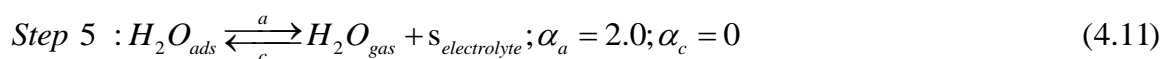
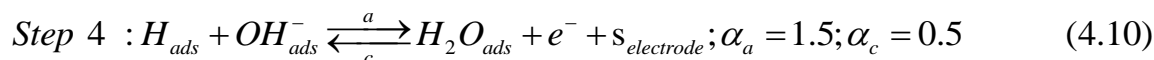
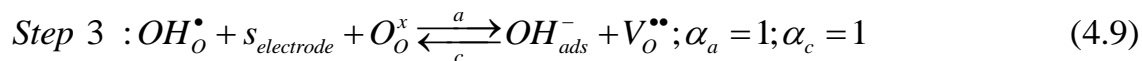
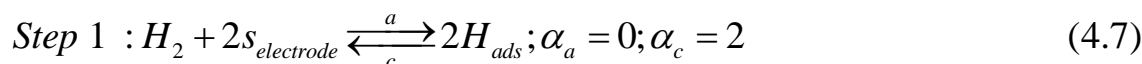
$$\text{Tafel slope} = \frac{2.303RT}{\alpha F} \quad (4.6)$$

The Tafel slope (mV/decade) is dependent on both temperature and the transfer coefficient ( $\alpha$ ). The calculated Tafel slopes at 25 and 500 °C for  $\alpha_a$  of 0.5, 1, 1.5 and 2.0 are shown in Table 4.2<sup>197</sup>. As can be seen, the Tafel slope decreases with increasing  $\alpha_a$  and increases with increasing temperature. An  $\alpha_a$  of 0.5 and 1.5 have been suggested to be associated with the rate limiting step being the first and second electron transfer process, respectively, while an  $\alpha_a$  of 1 indicates that a chemical step after a first electron step is rate limiting and an  $\alpha_a$  of 2 reflects a chemical step after a second electron step being rate limiting<sup>197</sup>.

**Table 4.2 Theoretical Tafel slope values using equation 4.6 for different  $\alpha$  values at 25 and 500 °C.**

$\alpha$	Tafel Slope (mV/decade)		Rate limiting step
	25 °C	500 °C	
0.5	118	306	First electron transfer
1.0	59	153	Chemical step
1.5	39	102	Second electron transfer
2.0	30	77	Chemical step

The proposed reaction mechanism for H<sub>2</sub> oxidation (Steps 1-5, forward reactions) and H<sub>2</sub>O reduction (Steps 5-1, backward reactions) at a Ni and Pt electrode at 800 °C, with predicted corresponding anodic ( $\alpha_a$ ) and cathodic ( $\alpha_c$ ) transfer coefficients, are as follows<sup>197, 198</sup>:



where a and c represents anodic and cathodic reactions, respectively, and  $O_o^x$ ,  $OH_o^\bullet$ ,  $OH_{\text{ads}}^-$  and  $H_2O_{\text{ads}}$  reflect oxide, hydroxyl, hydroxide and water species at the TPB.  $V_o^{\bullet\bullet}$  is an oxide vacancy within the electrolyte and  $s_{\text{electrode}}$  and  $s_{\text{electrolyte}}$  represent the surface vacancies on the electrode and electrolyte, respectively<sup>197</sup>.

Figure 4.5a shows the CV response of the Ni-YSZ anode in the 3-electrode cell, with or without  $H_2S$ , after  $iR$  correction using equation 4.12, where  $i$  is the measured current density and  $R_s$  is the series resistance from the impedance data. Higher current densities are seen throughout the full potential range ( $\pm 250$  mV) when humidified 5 ppm  $H_2S$  was added to the 95:5  $H_2:N_2$  gas mixture, compared to the CV currents seen in the absence of  $H_2S$ , all at 500 °C. This further confirms that ppm levels of  $H_2S$  increase the catalytic activity of the HOR at Ni-YSZ anodes.

$$E(iR \text{ corrected}) = E(\text{measured}) - iR_s \quad (4.12)$$

Figure 4.5b shows the Tafel plots, and using the high field approximation (100-250 mV). The observed Tafel slope (TS) is 155-160 mV/decade, which is close to the theoretical value of 153 mV/decade for  $\alpha_a = 1$  at 500 °C (Table 4.2). Based on the proposed reaction mechanism (Reactions 4.7-4.11) for the HOR, this suggests that a chemical process (probably Reaction 4.9)

following the first electron transfer step is rate limiting during hydrogen oxidation at Ni-YSZ in the presence or absence of H<sub>2</sub>S.

The extrapolated exchange current density is approximately a factor of two times higher in the presence versus absence of 5 ppm H<sub>2</sub>S, as seen in Table 4.3. A higher  $i_0$  when H<sub>2</sub>S is added to humidified H<sub>2</sub> indicates a better catalytic activity of the Ni-YSZ anode towards the HOR at 500 °C, as also seen in the results above.

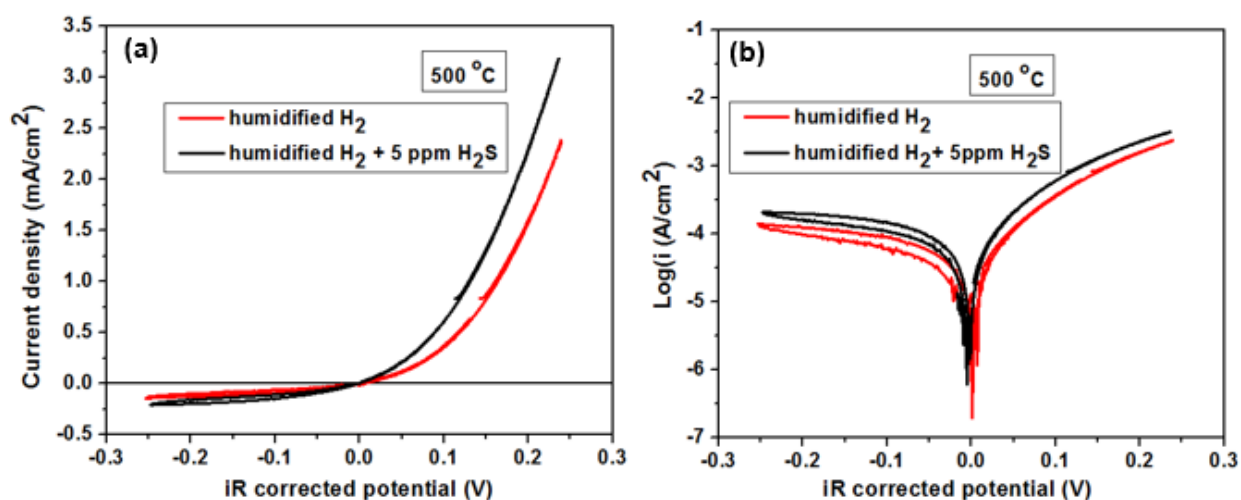


**Figure 4.5** Cyclic voltammetry response of Ni-YSZ anode (Cell 3) with/without H<sub>2</sub>S. (a) Cyclic voltammetry ( $\pm 250$  mV at 5 mV/s) in humidified H<sub>2</sub> and after the addition of 5 ppm H<sub>2</sub>S at 500 °C and (b) the corresponding Tafel plots.

**Table 4.3** Extrapolated kinetic parameters from Figure 4.5b.

Anodic Branch	Humidified H <sub>2</sub>	Humidified H <sub>2</sub> + 5 ppm H <sub>2</sub> S
$\alpha_a$	0.99	0.93
$i_0$ (mA/cm <sup>2</sup> )	0.09	0.15

Interestingly, from the CV in Figure 4.5, it can be seen that the cathodically polarized Ni-YSZ electrode (reduction of steam in humidified H<sub>2</sub>) also shows activation at 500 °C when ppm levels of H<sub>2</sub>S are introduced. This has a direct impact on solid oxide electrolysis cell (SOEC) applications, where it is known that exposure of Ni (now the cathode) to trace quantities of H<sub>2</sub>S can cause severe poisoning effects with prolonged operation at higher temperatures (800-850 °C). In fact, the operation of SOECs at temperatures down to ca. 600 °C is an area of significant interest in relation to minimizing cell degradation effects<sup>73</sup>, and thus the catalytic effect of H<sub>2</sub>S on Ni reported here under electrolysis conditions could be highly advantageous.

#### ***4.2.3 Effect of H<sub>2</sub>S on Ni-YSZ anodes in 2-electrode full cell configuration at 500 °C***

As discussed above, the activation of the hydrogen oxidation reaction in the presence of low ppm H<sub>2</sub>S (5-10 ppm) at 500 °C was very evident in the 3-electrode half cell studies discussed above. Therefore, it was important to show that this activation behavior is not only associated with half cells, but can also be observed in a full cell configuration. Therefore, in this study, a 2-electrode electrolyte-supported full cell, consisting of a Ni-YSZ anode, a YSZ electrolyte, and a LSM-YSZ cathode, was used.

Figure 4.6 shows the performance of such a full cell (Ni-YSZ/YSZ/LSM-YSZ) at 0.1 V vs. the OCP at 500 °C, with humidified 97% H<sub>2</sub>/N<sub>2</sub> fed to the anode and the cathode exposed to stagnant air. It is seen that the addition of 5 ppm H<sub>2</sub>S to humidified H<sub>2</sub> gives a rapid increase in current at 500 °C at constant potential, while the removal of H<sub>2</sub>S after the activation step results in a slow but steady decrease in current. These results demonstrate that both full cells and half cells exhibit an enhancement in the HOR rate in the presence of low ppm H<sub>2</sub>S at < 600 °C.

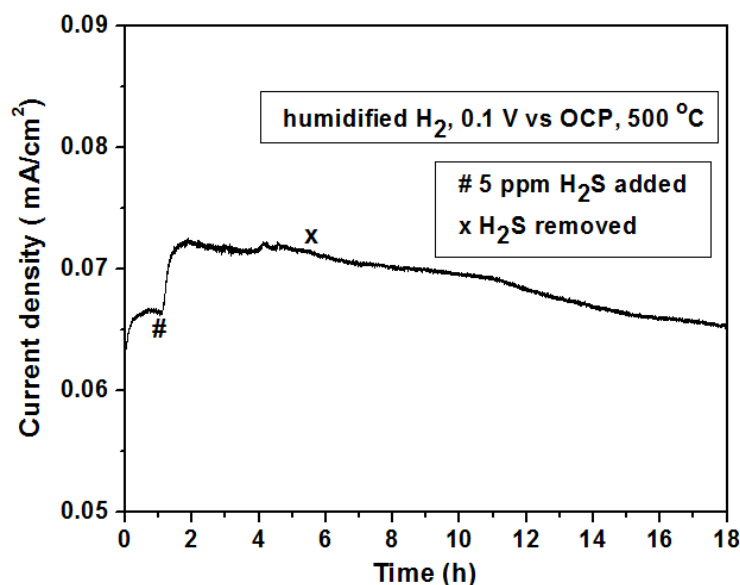


**Figure 4.6** Response of 2-electrode full cell (FC1) showing the *i-t* response during the introduction and removal of 5 ppm H<sub>2</sub>S in humidified H<sub>2</sub> at a 0.1 V cell potential (vs. OCP) at 500 °C.

#### 4.2.4 Understanding the H<sub>2</sub>S activation of Ni-YSZ anodes at < 600 °C

Electrochemically, it has been shown here that Ni-YSZ anodes are activated towards the hydrogen oxidation reaction in the presence of low ppm H<sub>2</sub>S at sub-600 °C. However, an important question relates to understanding which Ni and S species are present at the anode, especially at the TPB, during exposure of Ni-based anodes to low ppm H<sub>2</sub>S environments at temperatures below ca. 600 °C. Also, the electrochemical results rule out a simple saturated monolayer sulfur coverage at the Ni-YSZ electrolyte interface in this temperature range, which has been predicted to be highly inhibiting of the H<sub>2</sub> dissociation reaction. Earlier work by Grgicak *et al.*<sup>199, 200</sup> showed that bulk Ni sulfides (e.g. Ni<sub>3</sub>S<sub>2</sub>) are catalytic towards H<sub>2</sub> oxidation, enhancing rates by 1.3 and 1.6 times (at 800 and 950 °C, respectively) vs. those found for Ni-YSZ in pure H<sub>2</sub>. However, this catalytic effect of H<sub>2</sub>S at high temperatures is seen only at very

high H<sub>2</sub>S concentrations ( $\geq 5,000$  ppm H<sub>2</sub>S in H<sub>2</sub>), conditions required to retain the bulk Ni sulfide phases in a H<sub>2</sub> atmosphere.

In our work, bulk Ni<sub>3</sub>S<sub>2</sub> formation is not expected, but a thin layer can possibly form at the TPB. Published phase diagrams<sup>201-203</sup> also suggest that only a surface adsorbed sulfur phase (up to one monolayer coverage) is thermodynamically stable under our experimental conditions. However, the literature is not clear at which temperature/conditions a sulfur monolayer covered Ni surface state would transition to a bulk sulfide phase, and which intermediate phase would be formed during this transition.

As one possibility, the thermal history dependence of the H<sub>2</sub> oxidation activation behavior may suggest that a metastable, more sulfidized catalytic phase co-exists with the monolayer surface coverage, especially at H<sub>2</sub> depleted zones at the Ni-YSZ electrolyte interface. As H<sub>2</sub> is consumed by the oxidation process, the local increase in the H<sub>2</sub>S:H<sub>2</sub> ratio that results could potentially stabilize a thin Ni sulfide phase. It has also been proposed<sup>204</sup> that a relatively stable intermediate transition state between a simple sulfur monolayer on Ni and bulk Ni sulfide can exist under the conditions employed in this work, perhaps also related to high temperature re-ordering of the Ni-S surface, as reported in the literature. Therefore, it is possible that incipient Ni<sub>3</sub>S<sub>2</sub> formation in small amounts is occurring in our work, since we are observing the same catalytic effect of Ni<sub>3</sub>S<sub>2</sub> towards the HOR as reported by Grgicak *et al.*<sup>199, 200</sup>.

Minor quantities of bulk Ni sulfides have been detected on nickel-gadolinium-doped ceria (Ni-GDC) anodes<sup>202, 203, 205</sup>, even in low H<sub>2</sub>S environments. This is possibly because of local H<sub>2</sub> consumption during steam production, thus stabilizing a Ni sulfide phase. In other work, Ni-YSZ cermets, cooled down slowly from typical SOFC operating temperatures (600-800 °C) in 50 ppm H<sub>2</sub>S (in 1.5% H<sub>2</sub>O, 48.5% N<sub>2</sub>, and 50% H<sub>2</sub>), were shown to contain a number of bulk

Ni sulfides, including Ni<sub>3</sub>S<sub>4</sub>, β-NiS, and Ni<sub>3</sub>S<sub>2</sub>, as identified by Raman spectroscopy<sup>206, 207</sup>. However, these phases likely formed during cooling to temperatures well below 500 °C, as *in situ* Raman studies at 570 °C showed no evidence of any bulk Ni-sulfide phases.

However, an *in situ* Raman study by Thi *et al.*<sup>158</sup> showed that exposure of a Ni pellet to 300 ppm H<sub>2</sub>S/3% H<sub>2</sub>/Ar atmosphere at 500 °C led to the formation of Ni<sub>3</sub>S<sub>2</sub>. In contrast, at 800 °C, no nickel sulfide species were detected. Based on optical microscopy experiments, Thi *et al.*<sup>158</sup> reported that Ni<sub>3</sub>S<sub>2</sub> can be detected at 800 °C after its formation at lower temperature (ca. 500 °C). Also, they showed that exposure of a Ni-GDC (gadolinia doped ceria) pellet to 500 ppm H<sub>2</sub>S/3% H<sub>2</sub>/Ar atmosphere at 715 °C resulted in the formation of nickel sulfide crystals<sup>158</sup>. Even though Thi *et al.*<sup>158</sup> detected nickel sulfide at 500 °C, based on *in situ* Raman studies, Raman spectroscopy cannot easily detect the presence of a thin (few monolayer thick) Ni sulfide film, distributed in a porous Ni-YSZ anode, as is likely the case under our experiment conditions.

Thus, as very little published work has examined Ni-YSZ anodes after exposure to H<sub>2</sub>S under our experimental conditions, especially while taking all of the appropriate precautions during cool down, several *ex situ* analyses were carried out here in order to attempt to explain our results. This is because high temperature *in situ* verification of the sulfur surface speciation of Ni is very challenging to achieve. In this work, samples exposed to 5 ppm H<sub>2</sub>S (with or without electrochemical testing) for between days and several weeks, most typically at 500 °C, were rapidly cooled to room temperature in a pure H<sub>2</sub> environment.

Figure 4.7 shows the powder X-ray diffraction (PXRD) pattern for a Ni-YSZ anode after several days of electrochemical testing, with or without 5 ppm H<sub>2</sub>S in humidified H<sub>2</sub> at 500 °C, and then rapidly cooled down to room temperature to preserve any Ni-S phases formed at 500

°C. It is seen that only the peaks associated with Ni and YSZ are seen, indicating that there is no bulk Ni-S phase formed.

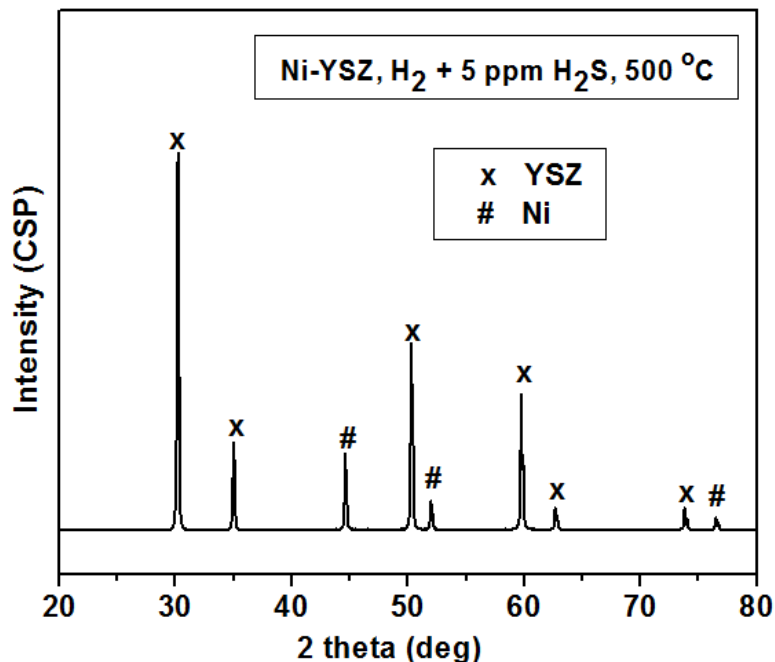


**Figure 4.7** *Ex situ* XRD pattern for a Ni-YSZ anode after several days of electrochemical testing (OCP and polarized) in the presence of 5 ppm H<sub>2</sub>S added to humidified H<sub>2</sub> at 500 °C.

Scanning electron microscopy (SEM) and energy dispersive X-ray (EDX) analysis of the sample shown in Figure 4.8 revealed no change in the Ni-YSZ composite structure or composition after several days of electrochemical testing at 500 °C in the presence of 5 ppm H<sub>2</sub>S added to humidified H<sub>2</sub>, again indicating the absence of any measurable amounts of bulk Ni sulfide species. This is unsurprising, as these techniques are bulk analysis methods, able to detect only micron scale layers or more of Ni sulfide on the Ni surface.

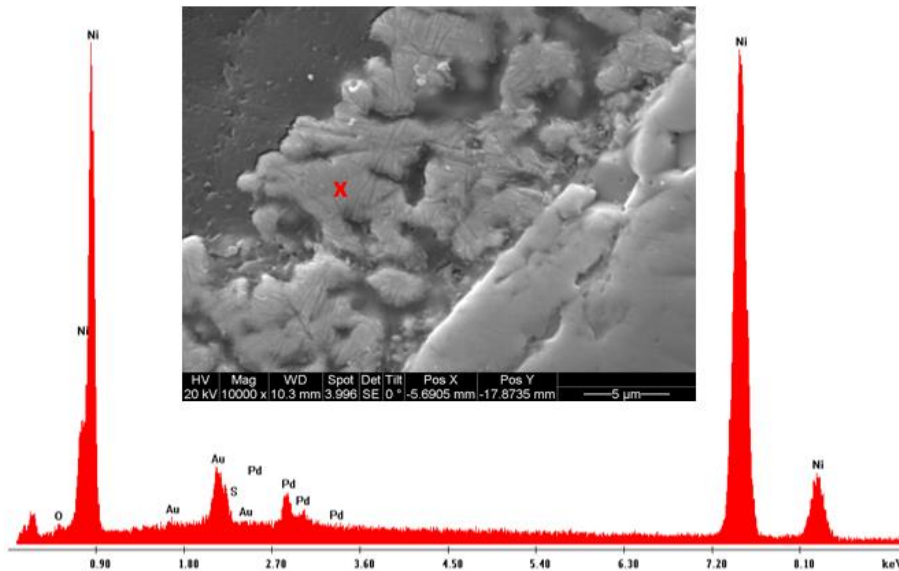
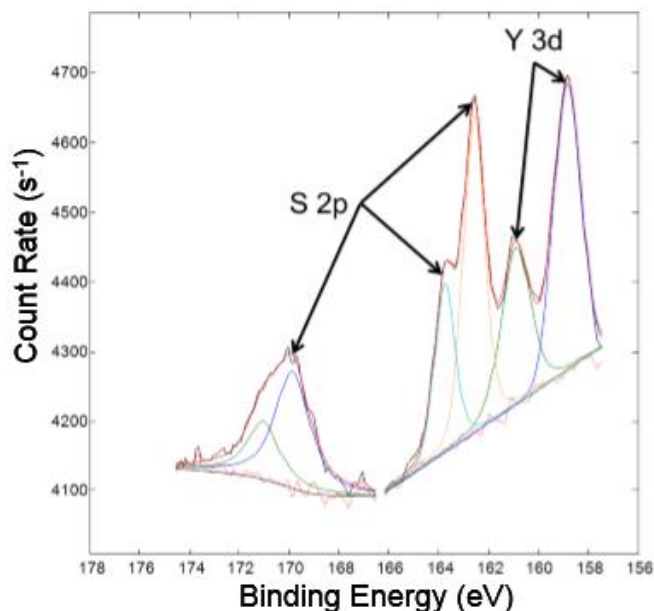


**Figure 4.8 SEM-EDX analysis of a Ni-YSZ anode after several days of electrochemical testing (OCP and polarized) at 500 °C in the presence of 5 ppm H<sub>2</sub>S added to H<sub>2</sub>. The “X” mark on the SEM image shows one of the locations where the EDX analysis was carried out.**

In comparison, X-ray photoelectron spectroscopy (XPS) results obtained for a Ni-YSZ anode surface following electrochemical studies at 500 °C at an anode overpotential of 250 mV in 5 ppm H<sub>2</sub>S in humidified H<sub>2</sub> (e.g., Figure 4.4) indicated the presence of sulfur. The detected sulfur (S2p) is in the form of a sulfate (169.9 and 171.1 eV) and sulfide (162.6 and 163.8 eV). The sulfate peak, seen at ca. 170 eV (Figure 4.9), is likely due to room temperature air oxidation of S or sulfide during sample transfer<sup>208</sup>. Analysis of the curve fits suggests that the sulfide:sulfate molecular ratio is 6:4, and that the total sulfur detected is ca. 3% of the Ni signal (with the signal coming from roughly 15-25 atomic layers into the Ni substrate).

Importantly, the higher intensity of the sulfide peaks relative to the sulfate peaks suggests that a certain portion of an underlying Ni sulfide layer survived the transfer to the XPS chamber. As care was taken to quickly cool the cells down in a pure H<sub>2</sub> atmosphere to minimize any

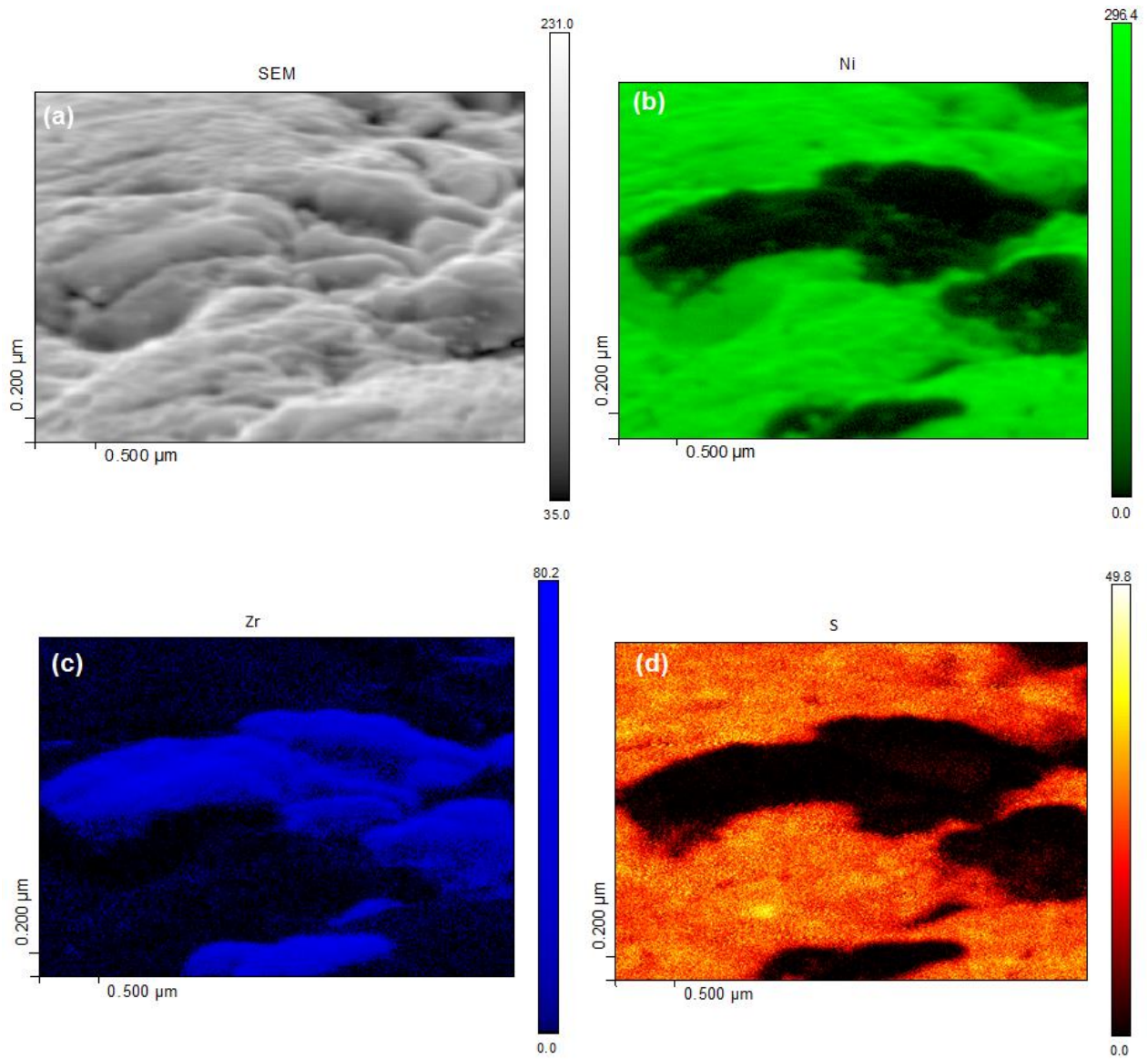
further interactions between Ni and H<sub>2</sub>S at 500 °C, these results argue for the presence of a thin layer of Ni sulfide under our experimental conditions (Figure 4.9). However, as the depth of analysis of XPS is 4-6 nm, it is not possible to conclude whether the detected sulfide is a monolayer film or some other near-surface sulfur state.



**Figure 4.9 XPS analysis of Ni-YSZ anode surface, after removal of the porous Ni current collector, following electrochemical studies at 500 °C and at an anode overpotential of 250 mV in 5 ppm H<sub>2</sub>S in humidified H<sub>2</sub> (half cell cooled down in H<sub>2</sub>). Deconvolution (156-175 eV) of the XPS pattern confirms the presence of sulfur (S2p) in the form of sulfate (169.9 and 171.1 eV), and sulfide (162.6 and 163.8 eV) on the sample surface.**

Auger Electron Spectroscopy analysis (AES) was also carried out on a Ni-YSZ sample exposed to 5 ppm H<sub>2</sub>S (balance in H<sub>2</sub>) for 72 h at 500 °C and then rapidly cooled to room temperature. Figure 4.10 shows the SEM image (Figure 4.10a) and the associated AES elemental map for Ni (Figure 4.10b), S (Figure 4.10c), Zr (Figure 4.10d), a combination of the Ni and Zr maps (Figure 4.10e), and a combination of the Ni, S and Zr maps (Figure 4.10f). Figure 4.10f

clearly shows that sulfur is present only on the Ni surface (and not on YSZ), although again, the exact thickness or quantity of the sulfur-containing surface species could not be determined.



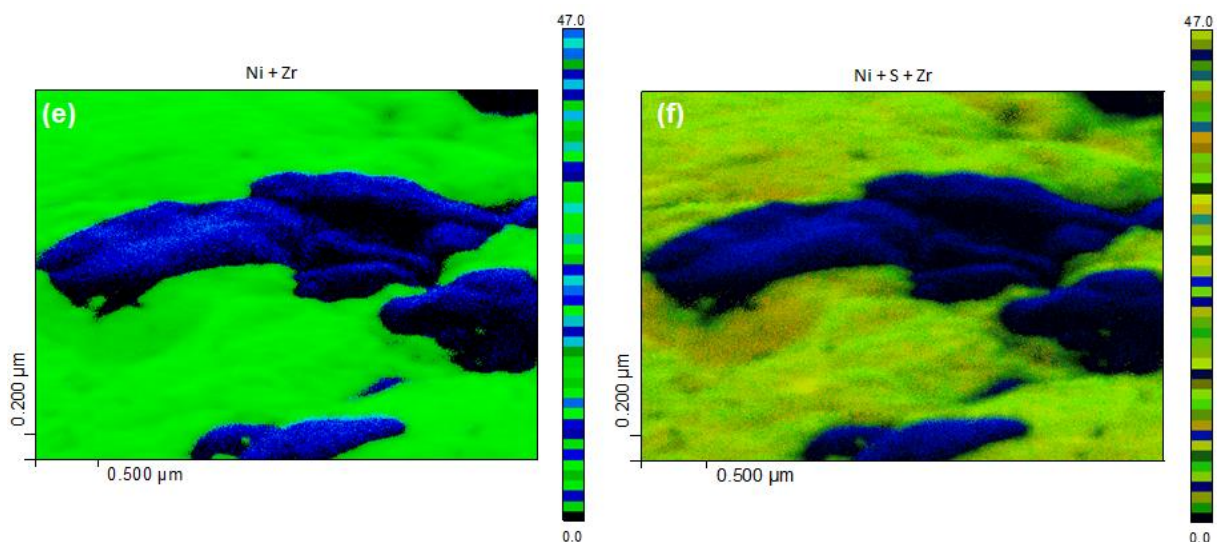


**Figure 4.10** Auger electron spectroscopy (AES) analysis of the Ni-YSZ cermet after exposure to 5 ppm H<sub>2</sub>S at 500 °C for 72 h and then rapidly cooled to room temperature showing (a) SEM image and AES elemental mapping for (b) Ni, (c) S, (d) Zr, (e) the combined Ni (green) and Zr (blue) maps, and (f) the combined Ni (green), S (yellow) and Zr (blue) elemental maps.

Since the results obtained from the XPS and AES analysis were limited and cannot provide monolayer level information, we began a collaborative research effort with Dr. Stephen Skinner's group at Imperial College London (UK), which has access to a highly sensitive surface technique, low energy ion scattering spectroscopy (LEIS). This instrument can, in theory, determine how deep sulfur penetrates into a Ni surface in 10 ppm H<sub>2</sub>S at temperatures below 600 °C through a monolayer by monolayer analysis.

The LEIS technique is based on the principle of classical momentum, where primary noble gas ions (e.g., He<sup>+</sup>, Ne<sup>+</sup>, and Ar<sup>+</sup>) of initial energies ranging from 0.5 to 10 keV strike surface atoms and the backscattered primary ions are analyzed, providing resolved information about the surface composition<sup>179, 209</sup>. For the LEIS analysis, both Ni-YSZ and Ni foil samples,

exposed to humidified H<sub>2</sub> and 10 ppm H<sub>2</sub>S conditions at 500 °C and rapidly quenched to room temperature, were investigated.

Figure 4.11 shows the LEIS spectra for the Ni-YSZ sample before (Scan 0 - Figure 4.11a) and after Ar sputtering (Figures 4.11b and 4.11c). The samples were analyzed as received without a cleaning step to remove any contaminants, such as carbon, from the surface. Usually, the cleaning or preparation step in a LEIS analysis involves oxygen<sup>181</sup>. Therefore, in order not to lose any S adsorbed on the surface in the form of SO<sub>2</sub>, this step was ignored.

As can be seen from the first/initial surface scan (Figure 4.11a), no peaks associated with Ni, S, O, Y or Zr were seen. This is because the Ni-YSZ surface is masked with contaminants, such as carbon, which has also been reported by others<sup>181</sup>. After removing (Ar sputtering) the first few surface layers, peaks corresponding to Ni, S, O, Y and Zr can clearly be seen in the spectrum in Figure 4.11b, with the heavier elements showing signals at higher energies (eV). The LEIS signals for S and Ni are observed at 1850 eV and 2300 eV, respectively. This spectrum shows the presence of S on the Ni-YSZ surface. Figure 4.11c shows the spectrum for the fortieth He LEIS scan after more sputtering to reveal the composition of the bulk. The intensity of the Ni, O, and Y+Zr peaks increased as the analysis proceeded deeper into the sample and the S peak could then no longer be observed.

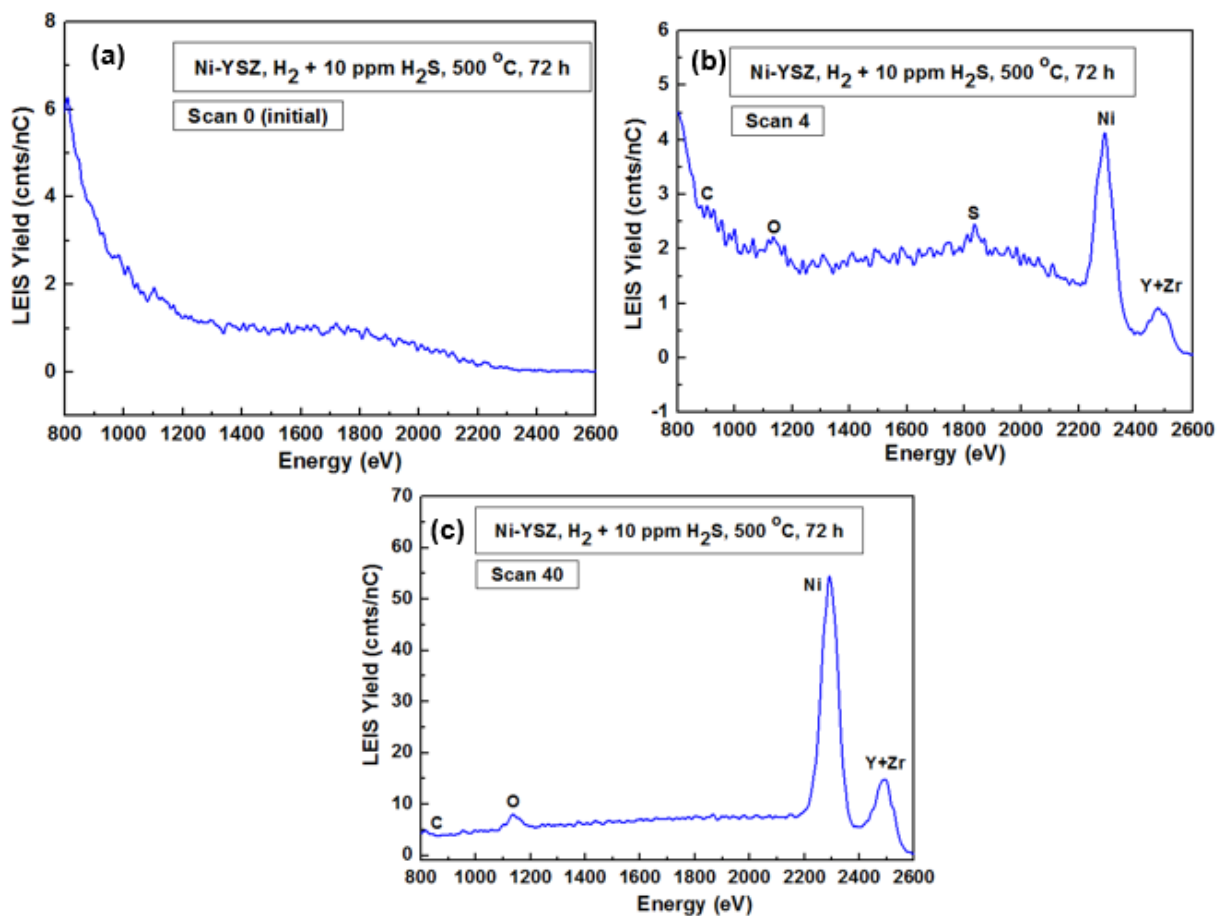


**Figure 4.11** LEIS  $^4\text{He}^+$  surface analysis of Ni-YSZ anode exposed to 10 ppm  $\text{H}_2\text{S}$  added to humidified  $\text{H}_2$  at 500 °C for 72 h, showing the spectrum for (a) the initial scan before any sputtering, (b) scan 4 after sputter removal of several layers, and (c) scan 40 after more sputtering to reach the underlying bulk composition.

To obtain a better understanding of the distribution of the various elements with depth, Figure 4.12 shows the LEIS depth profile analysis for the Ni-YSZ sample exposed to  $\text{H}_2\text{S}$ . Each data point in Figure 4.12 represents a He LEIS surface scan after sputtering a 1.5 x 1.5 mm area with 0.5 keV  $\text{Ar}^+$  at a  $1.6 \times 10^{14}$  ions/ $\text{cm}^2$  dose (See Chapter 3 for complete details of the LEIS analysis). From Figure 4.12a, it is seen that the Ni and Y+Zr peak intensity increases with depth, as expected. The intensity of O and S is very low, as shown in Figure 4.12b, with the signal for

O increasing with depth. However, the S signal is close to the background noise at all times, with no clear trend seen. This indicates that the amount of S adsorbed on the surface of the Ni-YSZ is very small. Also, because the Ni-YSZ sample was porous and rough, it is possible that this could have affected the S intensity.

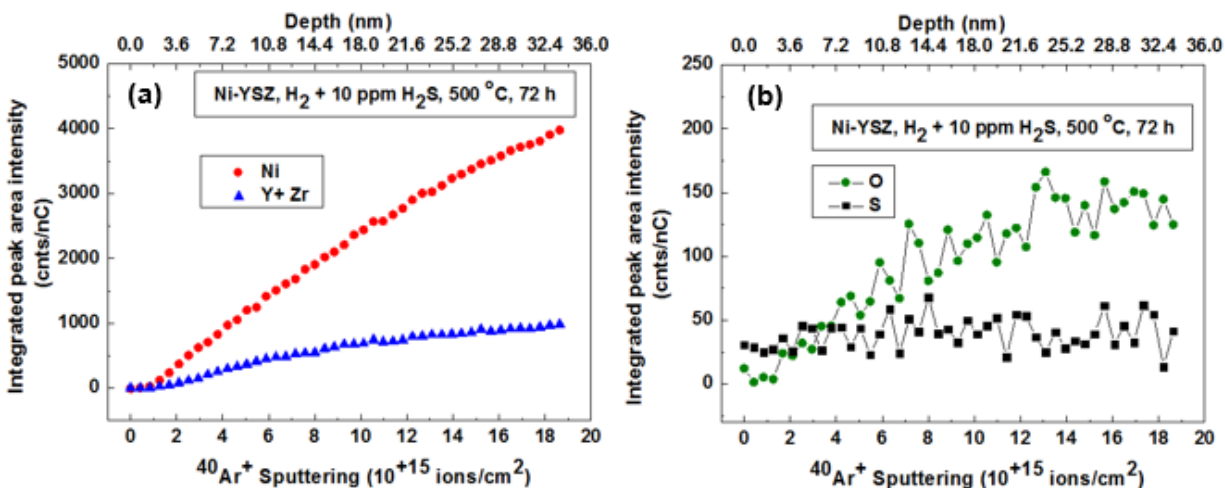


**Figure 4.12** LEIS depth-profile analysis of Ni-YSZ anode exposed to 10 ppm H $_2$ S added to humidified H $_2$  at 500 °C for 72 h showing (a) the Ni and Y+Zr profiles, and (b) the O and S profiles.

Therefore, a Ni-foil sample, which had much less or no porosity, exposed to the same experimental conditions as the porous Ni-YSZ sample, should show a higher intensity of S. Figure 4.13a shows that, for the Ni foil, the Ni signal intensity increases with sputtering to an estimated 18 nm into the sample before the Ni content starts to plateau. In Figure 4.13b, it is seen that both the S and O intensity increase rapidly to an estimated 3 nm depth before slowly decreasing with depth. These data show that any S present on the Ni foil surface is only in the outer few layers. The O signal followed the same trend as S, probably because the surface of the Ni foil was oxidized, forming sulfate, since the sample was exposed to air (as seen in the XPS

result, Figure 4.9). To the best of our knowledge, there is no prior literature where LEIS has been used to study the S poisoning of Ni-YSZ electrodes. However, LEIS has been used to study the segregation of impurities, such as oxides of Na, Si and Ca, on the surface of YSZ<sup>210</sup>. Also, LEIS has been employed to show that the surface and sub-surface chemical composition of various electrode materials, such as  $\text{GdBaCo}_2\text{O}_{5+\delta}$ <sup>211</sup>,  $\text{Pr}_{2-x}\text{La}_x\text{NiO}_{4+\delta}$ <sup>212</sup> and  $\text{NdGaO}_3$ <sup>181</sup>, was very different from the bulk, mainly due to segregation of cations onto the surface.

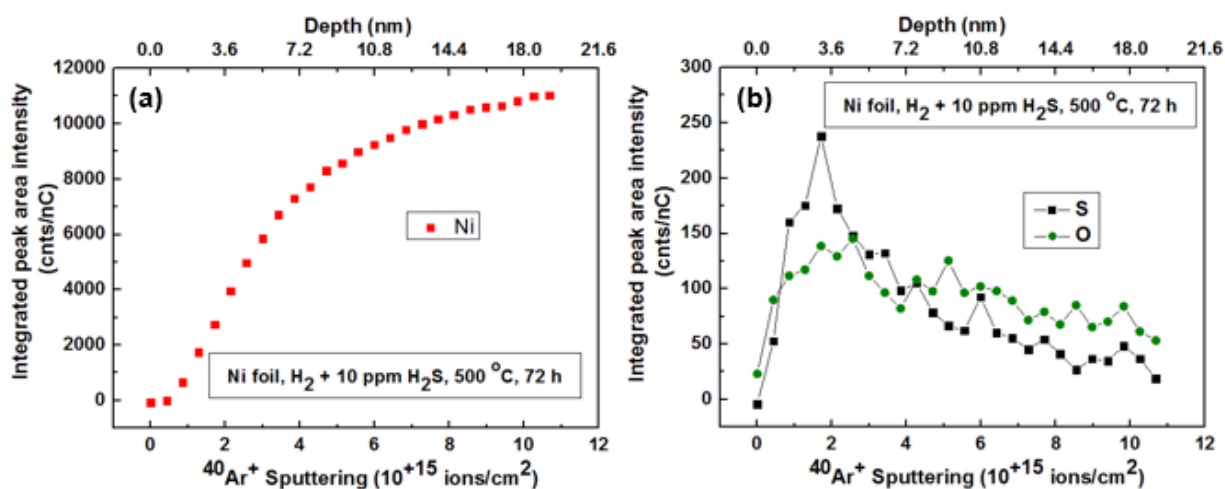


**Figure 4.13** LEIS depth-profile analysis of a Ni foil exposed to 10 ppm H<sub>2</sub>S at humidified H<sub>2</sub> at 500 °C for 72 h showing (a) the Ni profile and (b) the O and S profiles.

#### 4.2.5 Density functional theory (DFT) analysis

Based on the physical characterization results discussed above, especially the XPS and LEIS data, it appears that a thin surface layer of Ni-S (e.g., Ni<sub>3</sub>S<sub>2</sub>) is formed on Ni under our experimental conditions. To further confirm that Ni<sub>3</sub>S<sub>2</sub> is catalytically more active towards hydrogen oxidation reaction (HOR) than is Ni, a collaborative research effort was carried out with Dr. Tom Ziegler's group (University of Calgary) to employ DFT calculations to confirm

this assumption, because the catalytic effect of Ni<sub>3</sub>S<sub>2</sub> on H<sub>2</sub> oxidation is not well understood in the literature.

The DFT calculations showed that that hydrogen oxidation is more favorable at a Ni<sub>3</sub>S<sub>2</sub>/YSZ interface as compared to the respective pathways at the normal Ni/YSZ interface. A detailed analysis of the electronic and structural properties showed that the structural relaxation of the Ni<sub>3</sub>S<sub>2</sub>/YSZ interface is responsible for the very favorable energy pathway for hydrogen oxidation. It was shown that the pH<sub>2</sub>O, produced at Ni<sub>3</sub>S<sub>2</sub>/YSZ during H<sub>2</sub> oxidation, is significantly higher as compared to at the Ni/YSZ interface, indicating a higher activity of Ni<sub>3</sub>S<sub>2</sub>/YSZ as an HOR catalyst. The DFT calculations also suggested that the removal of interfacial O<sup>2-</sup> species (vacancy formation) during water formation at the Ni<sub>3</sub>S<sub>2</sub>/YSZ interface is more favorable than at Ni/YSZ, with structural relaxation of the Ni<sub>3</sub>S<sub>2</sub>/YSZ interface being responsible for a very favorable energy pathway for hydrogen oxidation.

These DFT predictions are consistent with the effect of the experimental history of the Ni-YSZ anode on the extent of H<sub>2</sub>S activation or poisoning, observed in Figure 4.2. It is possible that structural rearrangements of the Ni/Ni<sub>3</sub>S<sub>2</sub>/YSZ TPB region occur with H<sub>2</sub>S exposure, especially at lower temperatures. For example, it has been shown that short exposures of Ni to 1 ppm H<sub>2</sub>S at 700 °C can lead to enhanced metal sintering, and, at higher ppm H<sub>2</sub>S levels, can cause surface etching. Given the right conditions, advantageous restructuring of the TPB in H<sub>2</sub>S at lower temperatures may be at least partly responsible for the variability in the extent of activation seen between cells.

### 4.3 Summary

This work was the first to report that Ni-YSZ (yttria-stabilized zirconia) anodes can be activated at sub-600 °C in the presence of low ppm H<sub>2</sub>S (5-10 ppm) to enhance the hydrogen oxidation reaction (HOR)<sup>156</sup>, of great relevance to solid oxide fuel cells (SOFCs). Employing both direct (dc) and alternating (ac) current electrochemical techniques and both full cell and half cell studies, it was shown that H<sub>2</sub>S activation of Ni-YSZ anode towards the HOR is always seen at 500-550 °C. And based on the thermal history of the cell, the transition between activation and poisoning can either be at 550-600 °C or 600-650 °C, depending on whether the Ni-YSZ anode was first exposed to H<sub>2</sub>S at a higher temperature (800 °C) or lower temperature (500 °C).

To better understand what is causing the activation of the HOR at 500-600 °C, various *ex situ* bulk and surface characterization methods were used to examine H<sub>2</sub>S-exposed porous Ni-YSZ anodes and smooth Ni foils. From X-ray photoelectron spectroscopy (XPS) and low energy ion scattering (LEIS) analysis, it was suggested that a thin layer of Ni-S (e.g., Ni<sub>3</sub>S<sub>2</sub>) was forming at the triple phase boundary region and could be responsible for the activation behavior seen at low temperatures. Under our experimental conditions, bulk Ni<sub>3</sub>S<sub>2</sub> formation is not possible since bulk sulfide formation is favourable only at higher ppm of H<sub>2</sub>S (> 500 ppm) and lower temperatures (< 600 °C). However, at the right ratio of H<sub>2</sub>:H<sub>2</sub>S at the TPB, Ni sulfide species can be formed locally. Density functional theory (DFT) calculations confirmed this analysis, showing that the Ni<sub>3</sub>S<sub>2</sub>/YSZ interface lowers the activation barrier for the HOR in comparison to the Ni/YSZ interface.

## Chapter Five: **Performance and sulfur tolerance of $\text{La}_{0.3}\text{M}_{0.7}\text{Fe}_{0.7}\text{Cr}_{0.3}\text{O}_{3-\delta}$ (M = Sr, Ca) solid oxide fuel cell anodes**

This chapter contains some published data from P. K. Addo, B. Molero-Sánchez, A. Buyukaksoy, S. Paulson and V. Birss, *Sulfur tolerance of  $\text{La}_{0.3}\text{M}_{0.7}\text{Fe}_{0.7}\text{Cr}_{0.3}\text{O}_{3-\delta}$  (M = Sr, Ca) solid oxide fuel cell anodes*, ECS Transactions, 2015. **66**: p. 219-228).

### **5.1 Introduction**

In Chapter 4, it was shown that Ni-YSZ fuel electrodes (anodes), operated in the SOFC mode, are prone to sulfur poisoning at operating temperatures  $> 600/650$  °C, thereby degrading the performance of the hydrogen oxidation reaction (HOR). As a result, extensive research has been carried out to develop sulfur tolerant SOFC anode materials based on Ni-free conducting metal oxides, such as perovskites. For example,  $\text{La}_{0.75}\text{Sr}_{0.25}\text{Cr}_{0.5}\text{Mn}_{0.5}\text{O}_{3-\delta}$  (LSCM) has been reported to exhibit a comparable electrochemical performance for the HOR as seen at Ni-YSZ at 900 °C<sup>213</sup>.

However, LSCM has been shown to be less sulfur tolerant in fuels containing 10%  $\text{H}_2\text{S}$ <sup>214</sup>. Studies by Mukundan *et al.*<sup>162</sup> showed that  $\text{La}_{0.4}\text{Sr}_{0.6}\text{TiO}_{3-\delta}$  (LST) is a sulfur tolerant SOFC anode, as it did not exhibit any form of degradation in a 5000 ppm  $\text{H}_2\text{S} + \text{H}_2$  fuel. Studies by Haag *et al.*<sup>116</sup> showed that  $\text{LaSr}_2\text{Fe}_2\text{CrO}_{9-\delta}\text{-Gd}_{0.1}\text{Ce}_{0.9}\text{O}_{2-\delta}$  composite anodes, exposed to 22 ppm  $\text{H}_2\text{S}$ , exhibited only a slight decrease in performance relative to the response in  $\text{H}_2$ . Also,  $\text{La}_{0.3}\text{Sr}_{0.7}\text{Fe}_{0.7}\text{Cr}_{0.3}\text{O}_{3-\delta}$ , (LSFCr), operated on wet 50%  $\text{H}_2/\text{CO}$  fuel containing 10 ppm  $\text{H}_2\text{S}$ , showed only a small drop in cell potential, indicating very good stability as an anode in sulfur-containing environments<sup>46</sup>.

In contrast, several other perovskites have been reported to show an enhancement in the rate of hydrogen oxidation in the presence of  $\text{H}_2\text{S}$ , including  $\text{La}_{0.7}\text{Sr}_{0.3}\text{VO}_{3-\delta}$  (LSV)<sup>215</sup>,  $\text{Sm}_{0.95}\text{Ce}_{0.05}\text{Fe}_{0.97}\text{Ni}_{0.03}\text{O}_{3-\delta}$  (SCFN)<sup>216</sup>, and  $\text{Y}_{0.9}\text{Sr}_{0.1}\text{Cr}_{0.9}\text{Fe}_{0.1}\text{O}_{3-\delta}$  (YSCF)<sup>217</sup>. For LSV, the

observed enhancement was attributed to the formation of a conducting vanadium sulfide phase, replacing an insulating form ( $\text{Sr}_3\text{V}_2\text{O}_8$ )<sup>215</sup>, while for SCFN and YSCF, it was suggested that the active phase that forms in the presence of  $\text{H}_2\text{S}$  is probably  $\text{FeS}$ <sup>216, 217</sup>.

Previous and current studies in our group have explored the substitution of the A-site (M) in the mixed conducting perovskite,  $\text{La}_{0.3}\text{M}_{0.7}\text{Fe}_{0.7}\text{Cr}_{0.3}\text{O}_{3-\delta}$  (M = Sr, Ca), to form  $\text{La}_{0.3}\text{Sr}_{0.7}\text{Fe}_{0.7}\text{Cr}_{0.3}\text{O}_{3-\delta}$  (LSFCr) and  $\text{La}_{0.3}\text{Ca}_{0.7}\text{Fe}_{0.7}\text{Cr}_{0.3}\text{O}_{3-\delta}$  (LCFCr)<sup>46, 57</sup>, respectively. These perovskites have been successfully employed as both fuel and oxygen electrodes for solid oxide fuel cell (SOFC) and solid oxide electrolysis cell (SOEC) applications, using a YSZ (yttria stabilized zirconia) electrolyte covered with GDC (gadolinium doped ceria) buffer layers, as shown in Figure 3.3.

It has been reported previously that symmetrical SOFCs, based on the LSFCr perovskite, showed good tolerance to low ppm sulfur content in the fuel stream, exhibited excellent electrochemical activity towards  $\text{H}_2$  and CO oxidation, and were also active for the oxygen reduction reaction (ORR)<sup>46</sup>. More recently, it has also been demonstrated that LCFCr shows excellent catalytic properties for both the ORR and the oxygen evolution reaction (OER)<sup>57</sup>.

However, the performance of LCFCr as a fuel electrode has not been studied as yet. Therefore, in this work, LCFCr was examined as an anode in half cell and full cell studies in humidified  $\text{H}_2$  atmospheres, with or without  $\text{H}_2\text{S}$ , in comparison to the more well studied LSFCr perovskite, as well as with Ni-YSZ electrodes that were studied in depth in Chapter 4. The symmetrical full and half cells were constructed by screen-printing  $\text{La}_{0.3}\text{M}_{0.7}\text{Fe}_{0.7}\text{Cr}_{0.3}\text{O}_{3-\delta}$  (M = Sr, Ca) on a yttria-stabilized zirconia (YSZ) electrolyte, covered by a thin samaria-doped ceria (SDC) buffer layer. Electrochemical methods, involving both alternating (ac) and direct (dc)

techniques, were used in a symmetrical 2-electrode full and half cell configuration in H<sub>2</sub>, with or without the addition of 9 ppm H<sub>2</sub>S, all at 600-850 °C.

It is shown that LCFCr is a very good anode catalyst in H<sub>2</sub> fuel, with this mixed conducting perovskite material demonstrating enhanced catalytic activity when up to 10 ppm H<sub>2</sub>S was added to the H<sub>2</sub> fuel stream at operating temperatures > 700 °C, and anode poisoning occurring at temperatures below this. In contrast, in the Ni-YSZ study discussed in Chapter 4 exhibited the opposite effects, with an enhancement in the HOR activity observed in the presence of low ppm H<sub>2</sub>S at operating temperatures < 650 °C and poisoning at temperatures above this. It is suggested that the activation behaviour of LCFCr, observed at higher temperatures (> 700 °C), may be because exposure of LCFCr to H<sub>2</sub>S at higher temperatures led to an increase in the density of surface FeO<sub>2</sub> terminated species, which may be the preferred sites for the HOR/HER.

## 5.2 Results and Discussion

### 5.2.1 Performance of $La_{0.3}M_{0.7}Fe_{0.7}Cr_{0.3}O_{3-\delta}$ ( $M = Sr, Ca$ ) anodes in wet 30% H<sub>2</sub>/N<sub>2</sub> at 800 °C

To carry out a first stage comparison of the performance of the  $La_{0.3}Sr_{0.7}Fe_{0.7}Cr_{0.3}O_{3-\delta}$  (LSFCr) and  $La_{0.3}Ca_{0.7}Fe_{0.7}Cr_{0.3}O_{3-\delta}$  (LCFCr) perovskite materials in H<sub>2</sub> environments, impedance (EIS) and potentiodynamic techniques were employed. The Nyquist data, shown in Figure 5.1a, were fitted to a  $R_s(R1CPE1)(R2CPE2)$  equivalent circuit (Figure 5.1c), without the inclusion of a series inductor, even though inductive behavior was sometimes seen at high frequencies. An example of the good fits obtained of the EIS data to the selected equivalent circuit is shown in Figure 5.1c, giving a chi-squared value of < 10<sup>-4</sup>. It should be noted that all of the fits of the impedance data shown in this chapter gave similarly low chi-squared values.

From Figure 5.1a, a polarization resistance ( $R_p$ ) of 1.1 and 1.5  $\Omega \text{ cm}^2$  was obtained for LCFCr and LSFCr in 30% humidified  $\text{H}_2$  at 800  $^\circ\text{C}$ , respectively. This evaluation, which was repeated multiple times for different cells, shows that the performance of LCFCr is slightly better than LSFCr, as also seen for the oxygen evolution (OER) and reduction (ORR) reactions in parallel work from our group<sup>57</sup>. This is probably because the average thermal expansion coefficient (TEC) of LCFCr is  $12 \times 10^{-6} \text{ K}^{-1}$  at 25-1200  $^\circ\text{C}$ <sup>57</sup>, which is lower than the  $16 \times 10^{-6} \text{ K}^{-1}$  at 50-900  $^\circ\text{C}$  for LSFCr<sup>46</sup>. Therefore, LCFCr likely has a better interfacial contact with the GDC buffer layer, which has a TEC of ca.  $12 \times 10^{-6} \text{ K}^{-1}$ <sup>218, 219</sup>, leading to better cell performance overall. Despite this, the impedance response is quite similar for the two materials, with two time constants (R/CPE) seen in both cases. From the Bode plots (Figure 5.1b), the summit frequencies for the high (R1CPE1) and low (R2CPE2) are seen to be ca. 100 Hz and 0.1-1 Hz, respectively.

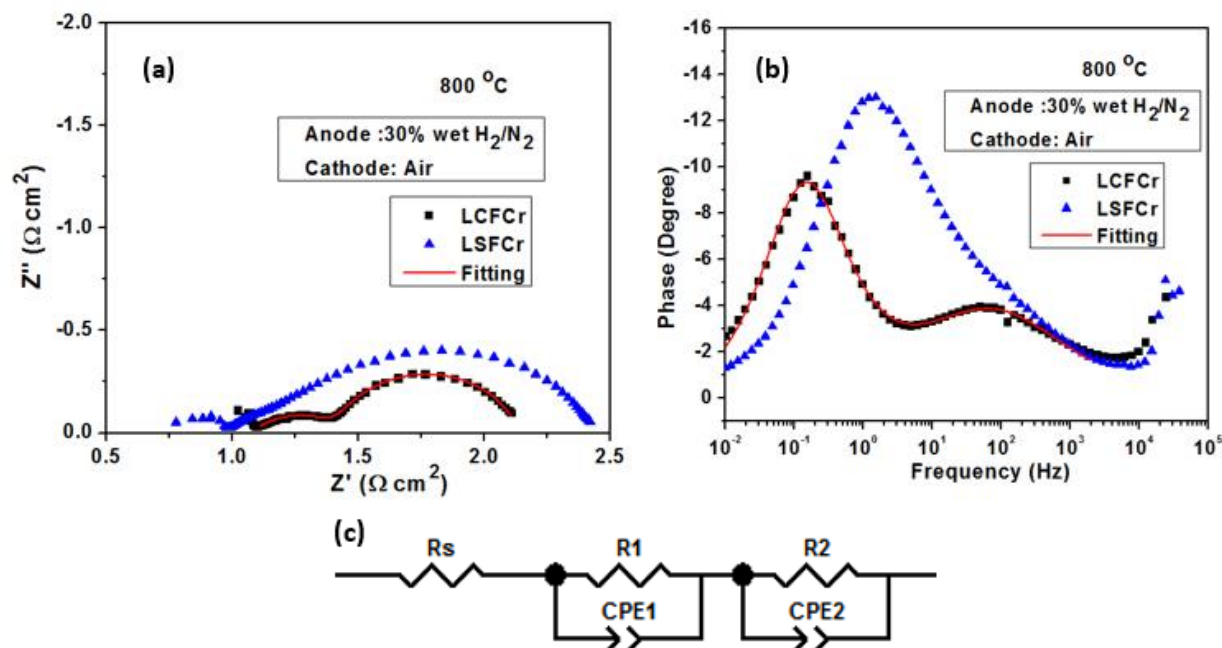


**Figure 5.1** OCP impedance data for symmetrical full cell based on  $\text{La}_{0.3}\text{M}_{0.7}\text{Fe}_{0.7}\text{Cr}_{0.3}\text{O}_{3-\delta}$  ( $\text{M} = \text{Sr}, \text{Ca}$ ) electrodes, at 800  $^\circ\text{C}$ , showing (a) the Nyquist and (b) the Bode plots, all in wet 30%  $\text{H}_2/\text{N}_2$  gas mixtures at the fuel electrode and with air exposure at the oxygen electrode, and (c) equivalent circuit used for data fitting.

To determine which of the arcs (R1CPE1 or R2CPE2) in Figure 5.1 relates to the oxygen (cathode) vs. fuel (anode) electrode, the cathode in the LCFCr full cell was fed with either air or pure oxygen. From Figure 5.2, it is clear that the high frequency (100 Hz) arc can be attributed to the cathode, since in pure O<sub>2</sub> (vs. air) the high frequency resistance (R1) decreased from 0.37 to 0.28 Ω cm<sup>2</sup>, while the low frequency resistance (R2) changed only slightly, as shown in Table 5.1.

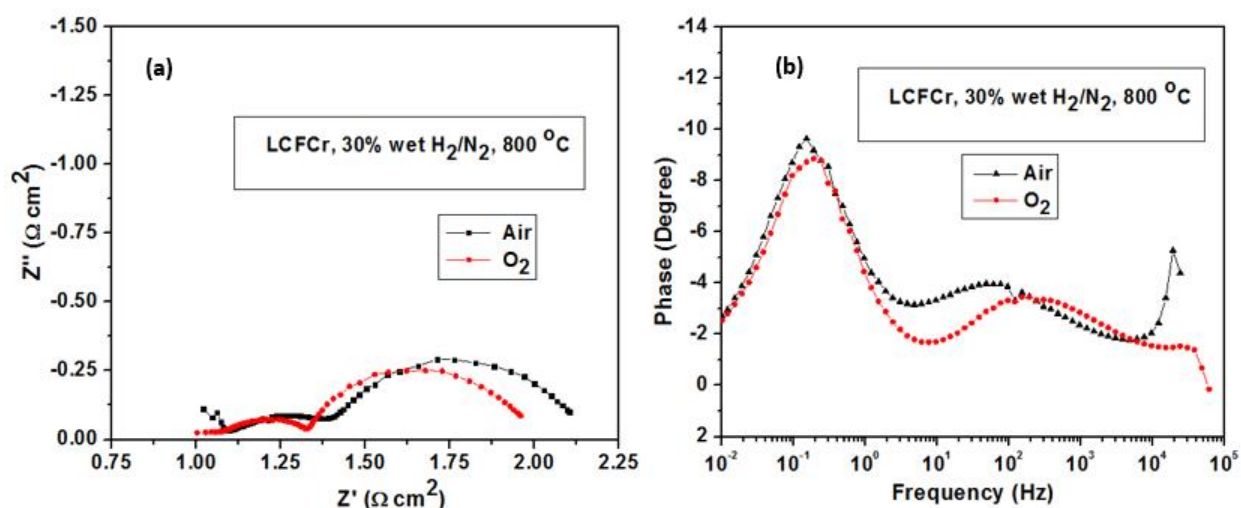


**Figure 5.2** OCP impedance data for symmetrical full cell based on La<sub>0.3</sub>Ca<sub>0.7</sub>Fe<sub>0.7</sub>Cr<sub>0.3</sub>O<sub>3-δ</sub> (LCFCr) electrodes at 800 °C and showing (a) the Nyquist and (b) the Bode plots, all in wet 30% H<sub>2</sub>/N<sub>2</sub> gas mixtures at the fuel electrode and with air or O<sub>2</sub> exposure at the oxygen electrode.

**Table 5.1** Circuit element values\* obtained by fitting the results in Figure 5.2\*\* to the equivalent circuit model in Figure 5.1c

Cathode gas	R <sub>s</sub> (Ω cm <sup>2</sup> )	R1 (Ω cm <sup>2</sup> )	R2 (Ω cm <sup>2</sup> )	R <sub>p</sub> (Ω cm <sup>2</sup> )
Air	1.1	0.37	0.68	1.1
O <sub>2</sub>	1.1	0.28	0.65	0.91

\* R1 and R2 obtained from the high (ca. 100 Hz) and low (ca. 0.1 Hz) frequency arcs, respectively.

\*\* Symmetrical fuel cell based on LCFCr electrodes, operated at 800 °C in wet 30% H<sub>2</sub>/N<sub>2</sub> gas mixtures at the fuel electrode and with air or O<sub>2</sub> exposure at the oxygen electrode.

# R<sub>p</sub> = R1 + R2

The resistance values were obtained by fitting the Nyquist plots in Figure 5.2a to the equivalent circuit model shown in Figure 5.1c.  $R_s$  is the series resistance,  $R_p$  is the polarization resistance ( $R_p = R_1 + R_2$ ), and  $(R_1CPE1)$  and  $(R_2CPE2)$  are the time constants at high (100 Hz) and low (0.5 Hz) frequencies, respectively. Therefore, the low frequency arc ( $R_2CPE2$ ) is due predominantly to contributions from the fuel electrode (anode), while the high frequency arc ( $R_1CPE1$ ) arises from the oxygen electrode (cathode), consistent with what has been reported in the literature for other mixed conducting perovskite systems, including LSFCr<sup>46, 115</sup>.

Direct current (dc) experiments were also carried out to evaluate the performance of the full cell, based on  $La_{0.3}M_{0.7}Fe_{0.7}Cr_{0.3}O_{3-\delta}$  ( $M = Sr, Ca$ ) at both the fuel electrode (anode) and oxygen electrode (cathode). Figure 5.3 shows the performance plots of LCFCr and LSFCr cells operated on humidified 30%  $H_2$  (balance  $N_2$ ) fed to the fuel electrode and the oxygen electrode exposed to air at 800 °C. The LCFCr cell shows a maximum current and power density of 270 mA/cm<sup>2</sup> and 140 mW/cm<sup>2</sup>, respectively, while the analogous values for the LSFCr cell are 255 mA/cm<sup>2</sup> and 135 mW/cm<sup>2</sup>, consistent with the impedance data in Figure 5.1.

A direct comparison of the performance of  $La_{0.3}M_{0.7}Fe_{0.7}Cr_{0.3}O_{3-\delta}$  ( $M = Sr, Ca$ ) to other perovskite materials reported in the literature is not possible, as the performance plots shown in this Chapter have not been iR corrected, while in the literature, some are corrected while others are not. Therefore, the performance plots in Figure 5.3 are affected by the resistance contribution from the YSZ electrolyte. Even so, the performance of these  $La_{0.3}M_{0.7}Fe_{0.7}Cr_{0.3}O_{3-\delta}$  ( $M = Sr, Ca$ )-based cells, especially of the Ca compound, is comparable, if not better than that of many other symmetrical cells (based on perovskite electrodes) reported in the literature. This includes  $La_4Sr_8Ti_{12-x}Fe_xO_{38-\delta}$  (LSTF), which showed power densities of 90-100 mW/cm<sup>2</sup> at 950 °C in humidified  $H_2$ <sup>49</sup>.

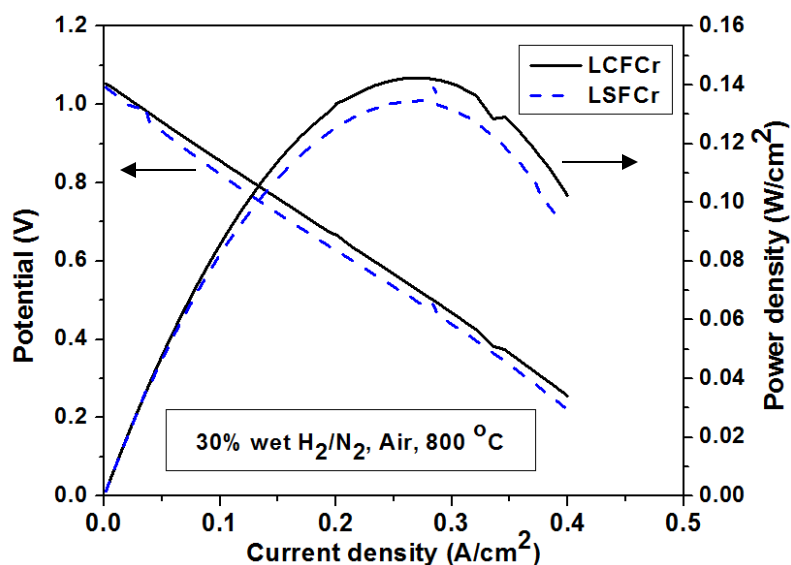


**Figure 5.3** Performance plot for symmetrical full cell based on  $\text{La}_{0.3}\text{M}_{0.7}\text{Fe}_{0.7}\text{Cr}_{0.3}\text{O}_{3-\delta}$  ( $\text{M} = \text{Sr}, \text{Ca}$ ) electrodes and operated at  $800\text{ }^\circ\text{C}$ , all in wet 30%  $\text{H}_2/\text{N}_2$  gas mixture at the fuel electrode and with air exposure at the oxygen electrode.

Therefore, due to the better performance of LCFCr in the  $\text{H}_2$  fuel environment, the rest of this chapter is focused on the LCFCr material as a SOFC fuel electrode (anode)<sup>56</sup>. Although LSFCr was shown to decompose (reversibly) in pure  $\text{H}_2$  atmospheres in our group's earlier work<sup>46</sup>, the LCFCr studies described in the rest of this chapter include experiments in  $\text{H}_2$  and in  $\text{CO}/\text{H}_2$  mixtures, although ppm levels of  $\text{H}_2\text{S}$  were added only to the  $\text{H}_2$  atmospheres. Notably, all of the experiments were carried out in 2-electrode full and half cell configurations, with LCFCr employed at both electrodes, as shown in Figures 3.3 and 3.4.

### 5.2.2 Performance of LCFCr in $\text{H}_2/\text{CO}$ fuel mixtures at $800\text{ }^\circ\text{C}$

The performance of the LCFCr fuel electrode was examined first in wet  $\text{H}_2$ ,  $\text{CO}$ , and in syngas ( $\text{H}_2+\text{CO}$ ) atmospheres, without any  $\text{H}_2\text{S}$  exposure, with air introduced to the LCFCr material at the other electrode. Figure 5.4a shows that the polarization resistance of the cell is

0.95  $\Omega \text{ cm}^2$  in  $\text{H}_2$ , which is slightly smaller than the  $R_p$  values obtained in the CO (1.1  $\Omega \text{ cm}^2$ ) and CO+ $\text{H}_2$  (1.0  $\Omega \text{ cm}^2$ ) atmospheres. This indicates that the material is only a somewhat better catalyst for  $\text{H}_2$  oxidation than it is for CO oxidation. A study by Bierschenk *et al.*<sup>115</sup>, showed that the total anode polarization resistance of a  $\text{LaSr}_2\text{Fe}_2\text{CrO}_{9-\delta}$ -based cell at 800 °C increased by 2 times by switching from pure  $\text{H}_2$  to pure CO. Others have also shown that the polarization resistance of a Ni-YSZ anode operated in CO increased by 2-10 times when compared to the performance in  $\text{H}_2$ <sup>115, 220, 221</sup>.

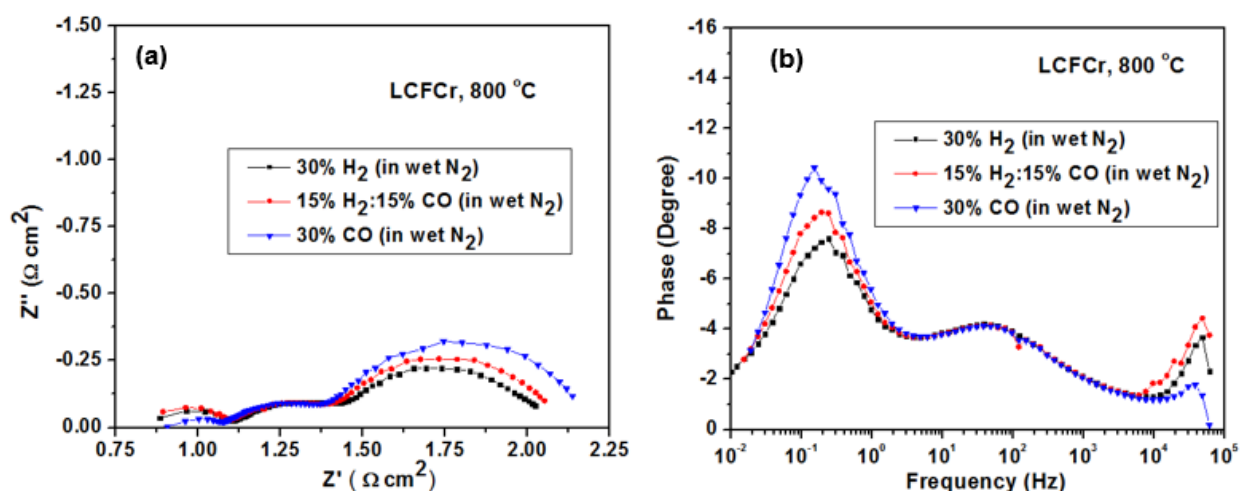


**Figure 5.4** OCP impedance data for symmetrical full cell based on two LCFCr electrodes at 800 °C, showing (a) the Nyquist and (b) the Bode plots, all in wet 30%  $\text{H}_2/\text{N}_2$ , 15%  $\text{H}_2$ :15% CO, or 30% CO gas mixtures at the fuel electrode and with air exposure at the oxygen electrode.

Overall, these results show that LCFCr is a very promising SOFC anode material that can be employed in a range of fuels, giving a very good performance in all cases. From the Nyquist (Figure 5.4a) and Bode (Figure 5.4b) plots, it is seen that it is the low frequency arc ( $R_2/\text{CPE}_2$ ) that is changing with changing fuel environments, again confirming that the low frequency arc is associated primarily with the anode.

The performance plot of the cell in these three gases is shown in Figure 5.5. The OCP in the three gases is seen to be ca. 1.06 V, which is very close to the theoretical value, indicating that the anode and cathode compartments are well sealed and that there is no gas leakage. As stated earlier, there is not much difference in the activity of the LCFCr material in H<sub>2</sub>, CO and H<sub>2</sub>+CO atmospheres, as supported here by these dc measurements. Even with the significant contribution here of the relatively thick YSZ electrolyte (300 μm) to the series resistance of these cells, the maximum power density is between 140 to 150 mW/cm<sup>2</sup> in these environments, while the maximum current density is in the range of 250-270 mA/cm<sup>2</sup>, all at 800 °C. The performance of this LCFCr symmetrical cell is higher than that reported by Ruiz-Morales *et al.*<sup>222</sup>, where they showed that a La<sub>0.7</sub>Ca<sub>0.3</sub>CrO<sub>3-δ</sub> (LCC)-based symmetrical cell, operated in H<sub>2</sub> at 950 °C, gave a power density of only ca. 100 mW/cm<sup>2</sup>. To better understand the total area specific resistance (ASR) associated with the cell when operated in wet 30% H<sub>2</sub> (balance N<sub>2</sub>), the i-V plot, shown in Figure 5.5a, was differentiated to give the ASR (ASR = dE/di) of the cell. From Figure 5.5b, it can be seen that the ASR decreased from ca. 2.05 to 1.90 Ω cm<sup>2</sup> from 0 A/cm<sup>2</sup> (OCP) to about 0.2 A/cm<sup>2</sup> and then increased to 2.3 Ω cm<sup>2</sup> at 0.4 A/cm<sup>2</sup>. The ASR value obtained at OCP for the LCFCr cell operated in wet 30% H<sub>2</sub> (balance N<sub>2</sub>) is in good agreement with the ASR value (ASR = R<sub>s</sub>+R<sub>p</sub>) obtained from the OCP impedance data shown in Figure 5.4.

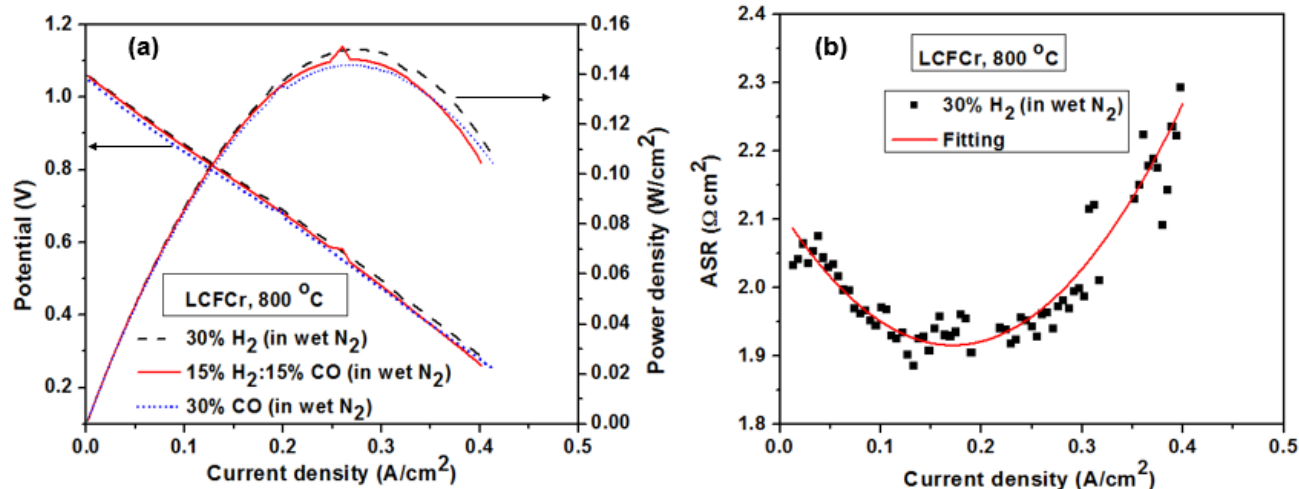


**Figure 5.5** (a) Performance plot for symmetrical full cell, based on LCFCr electrodes, operated at 800 °C in wet 30% H<sub>2</sub>/N<sub>2</sub>, 15% H<sub>2</sub>:15% CO, or 30% CO gas mixtures at the fuel electrode and with air exposure at the oxygen electrode, and (b) the ASR-i plot (derived from the i-V plot in (a)) for wet 30% H<sub>2</sub>/N<sub>2</sub>.

### 5.2.3 Chemical stability of LCFCr in H<sub>2</sub>S

Since this is the first time LCFCr has been demonstrated to be a catalytically active fuel electrode for H<sub>2</sub>/H<sub>2</sub>O and CO/CO<sub>2</sub> reactions, it was considered to be important to evaluate whether it can tolerate low ppm H<sub>2</sub>S levels at operating temperature of 600-850 °C, also in comparison with Ni-YSZ (Chapter 4). Figure 5.6 shows evidence for the chemical stability of LCFCr exposed to 30 ppm H<sub>2</sub>S (balance N<sub>2</sub>) from room temperature to 800 °C, with a 24 h holding time at 800 °C, and then cooled down to room temperature. From the X-ray diffraction (XRD) patterns, it can be seen that there are no detectable secondary phases formed, suggesting that LCFCr in the presence of H<sub>2</sub>S is stable.

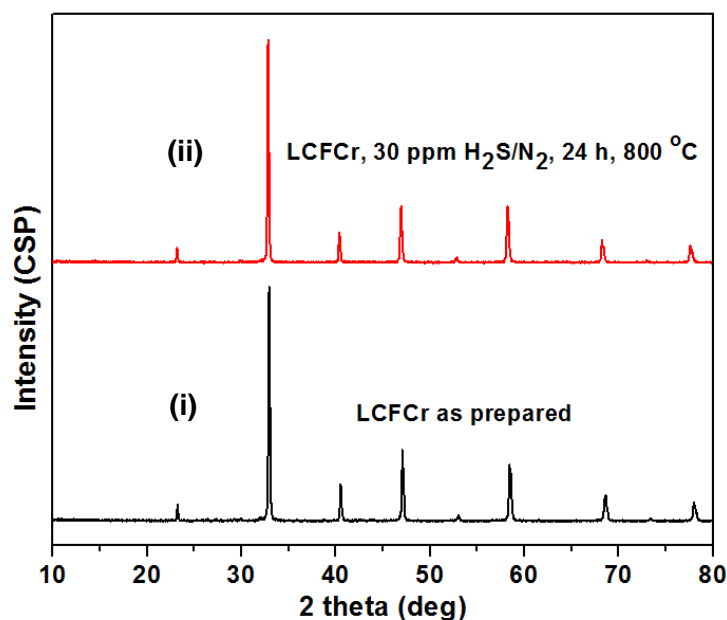


**Figure 5.6** *Ex situ* XRD patterns showing the chemical stability of  $\text{La}_{0.3}\text{Ca}_{0.7}\text{Fe}_{0.7}\text{Cr}_{0.3}\text{O}_{3-\delta}$  (LCFCr) powder (i) as-prepared, and (ii) after exposure to 30 ppm  $\text{H}_2\text{S}/\text{N}_2$  atmosphere with a 24 h dwell time at 800 °C. The sample in (ii) was heated and cooled at a ramp rate of 5 °C/min in  $\text{H}_2\text{S}/\text{N}_2$  atmosphere.

Other perovskites, such as  $\text{La}_{1-x}\text{Sr}_x\text{Cr}_{1-y}\text{Mn}_y\text{O}_{3-\delta}$  (LSCM), have also been shown to be chemically stable when exposed to 10 ppm  $\text{H}_2\text{S}$  at 800 °C for 24 h. However, when exposed to 30 ppm  $\text{H}_2\text{S}$  at 800 °C for 120 h, minor impurities, such as  $\text{La}_2\text{O}_2\text{S}$ , have been observed<sup>223</sup>. Zha *et al.*<sup>214</sup> investigated the sulfur tolerance of  $\text{La}_{0.75}\text{Sr}_{0.25}\text{Cr}_{1-x}\text{Mn}_x\text{O}_{3-\delta}$  ( $x = 0.4, 0.5, 0.6$ ) (LSCM) and showed that an increase in the Cr content led to a more sulfur tolerant LSCM material. However, exposure of LSCM to high  $\text{H}_2\text{S}$  content (10%) led to the formation of  $\text{MnS}$ ,  $\alpha\text{-MnOS}$ , and  $\text{La}_2\text{O}_2\text{S}$ , which decreased the performance of the cell<sup>214</sup>.

#### 5.2.4 Symmetrical LCFCr full cell studies in the presence or absence of H<sub>2</sub>S

Figure 5.7 shows the EIS data for a symmetrical LCFCr/SDC/YSZ/SDC/LCFCr full cell in humidified 30% H<sub>2</sub> (balance N<sub>2</sub>), with or without the addition of 9 ppm H<sub>2</sub>S, fed to the fuel electrode (anode) and air fed to the oxygen electrode, all at 800 °C. Figure 5.7a shows that, when 9 ppm H<sub>2</sub>S is added to humidified 30% H<sub>2</sub> under open circuit potential (OCP) conditions, the polarization resistance (R<sub>p</sub>) actually decreased slightly, from 1.0 to 0.96 Ω cm<sup>2</sup>, with no deactivation of the LCFCr seen at 800 °C. This slight decrease in the R<sub>p</sub> of the LCFCr-based cell at 800 °C is contrary to what was observed at Ni-YSZ, where at 800 °C, the addition of low ppm H<sub>2</sub>S led to deactivation of the cell (e.g., Figure 4.1). In comparison, any sulfur-induced performance enhancement behavior reported for other types of perovskites has been observed at much higher concentrations of H<sub>2</sub>S (1-5%)<sup>215-217</sup>.

Figures 5.7b and 5.7c show the polarized EIS results for the LCFCr-based cell under dc polarization in H<sub>2</sub>, with or without the addition of 9 ppm H<sub>2</sub>S, again at 800 °C. When the cell was polarized in the fuel cell mode to 0.1 V less than the full cell open circuit voltage (1.05 V), i.e., at a cell voltage of ca. 0.95 V (Figure 5.7b), R<sub>p</sub> decreased from 0.97 Ω cm<sup>2</sup> in H<sub>2</sub> to 0.90 Ω cm<sup>2</sup> in the presence of H<sub>2</sub>S. However, when the anode was polarized at 0.3 V (ca. 0.75 V cell voltage), R<sub>p</sub> decreased from 0.80 to 0.72 Ω cm<sup>2</sup> (Figure 5.7c). This indicates that the enhancement of the performance of LCFCr in H<sub>2</sub> in the presence of H<sub>2</sub>S improves further under bias, at least at 800 °C. It can be seen from the Nyquist plots (Figure 5.7) that the addition of H<sub>2</sub>S affects only the low frequency arc (R<sub>2</sub>CPE<sub>2</sub>), which as discussed earlier (Figure 5.2), is associated with the processes occurring at the LCFCr electrode exposed to the fuel (H<sub>2</sub>).

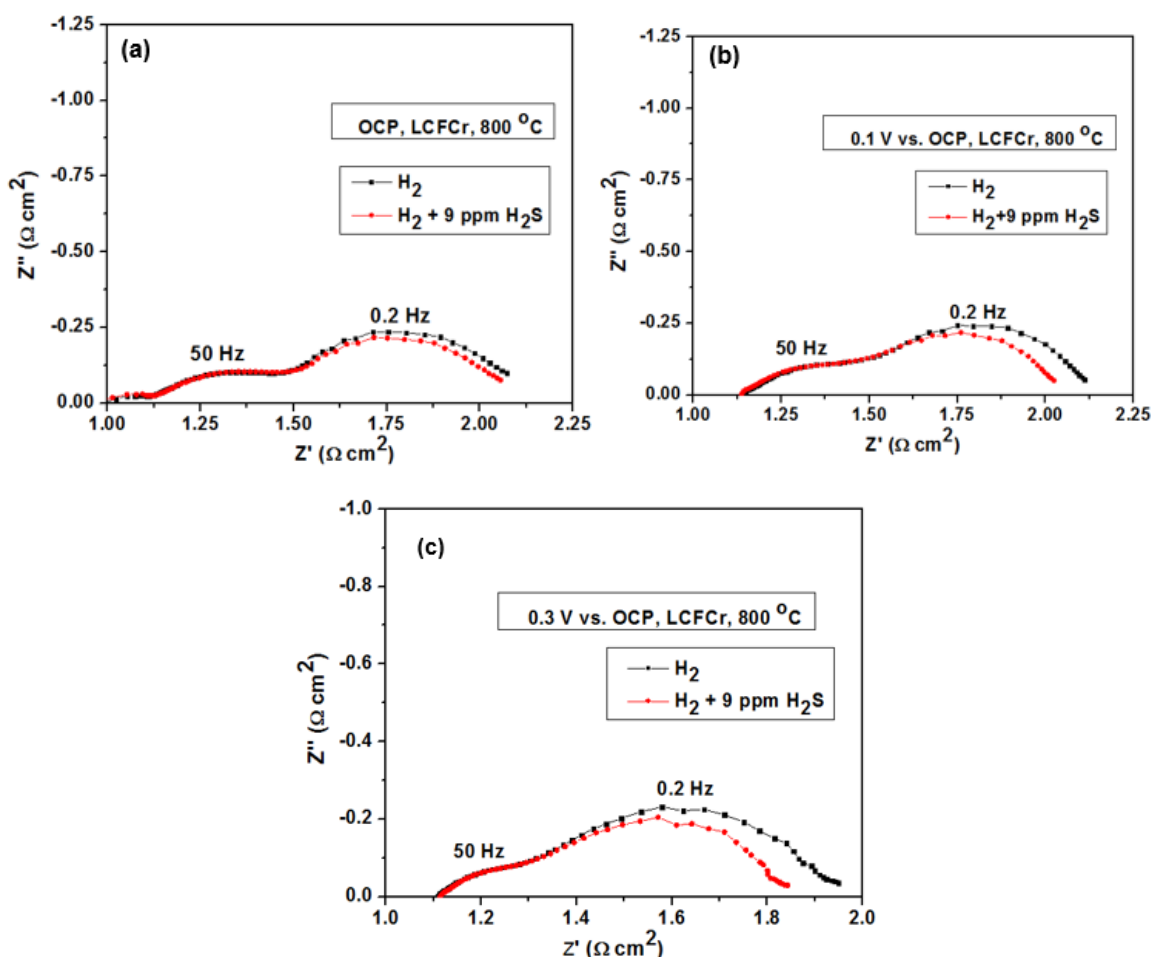


**Figure 5.7** OCP and polarized EIS response for symmetrical, 2-electrode full cell, based on LCFCr electrodes at 800 °C, with humidified 30% H<sub>2</sub>/N<sub>2</sub> (with or without 9 ppm H<sub>2</sub>S) fed to the fuel electrode and air fed to the oxygen electrode, showing the Nyquist plots acquired at (a) the OCP, (b) at 0.1 V less than the cell voltage at open circuit, and (c) at 0.3 V less than the cell voltage at open circuit.

Figure 5.8 shows the temperature dependence of the polarization resistance ( $R_p$ ) of the same type of symmetrical cells, fed with humidified 30% H<sub>2</sub>/N<sub>2</sub> and with the addition or removal of 9 ppm H<sub>2</sub>S at the fuel electrode (anode) and air fed to the oxygen electrode, from 800 to 650 °C.  $R_p$  was again obtained by fitting the Nyquist plots to the  $R_s(R_1CPE_1)(R_2CPE_2)$  equivalent circuit (Figure 5.1c). Figures 5.8a and 5.8b clearly show that exposure of LCFCr to low ppm H<sub>2</sub>S at 800 and 750 °C leads to activation towards the hydrogen oxidation reaction (HOR), contrary to

what was seen for Ni-YSZ anodes in Chapter 4, where anode poisoning was seen under the same conditions. However, Figures 5.8c and 5.8d show that the  $R_p$  values of the cell, exposed to  $H_2S$  under both OCP and polarized conditions at 700 and 650 °C, respectively, increase, indicating a decrease in the HOR rate at these temperatures, again opposite to what was seen for Ni-YSZ under analogous conditions (Figure 4.1).

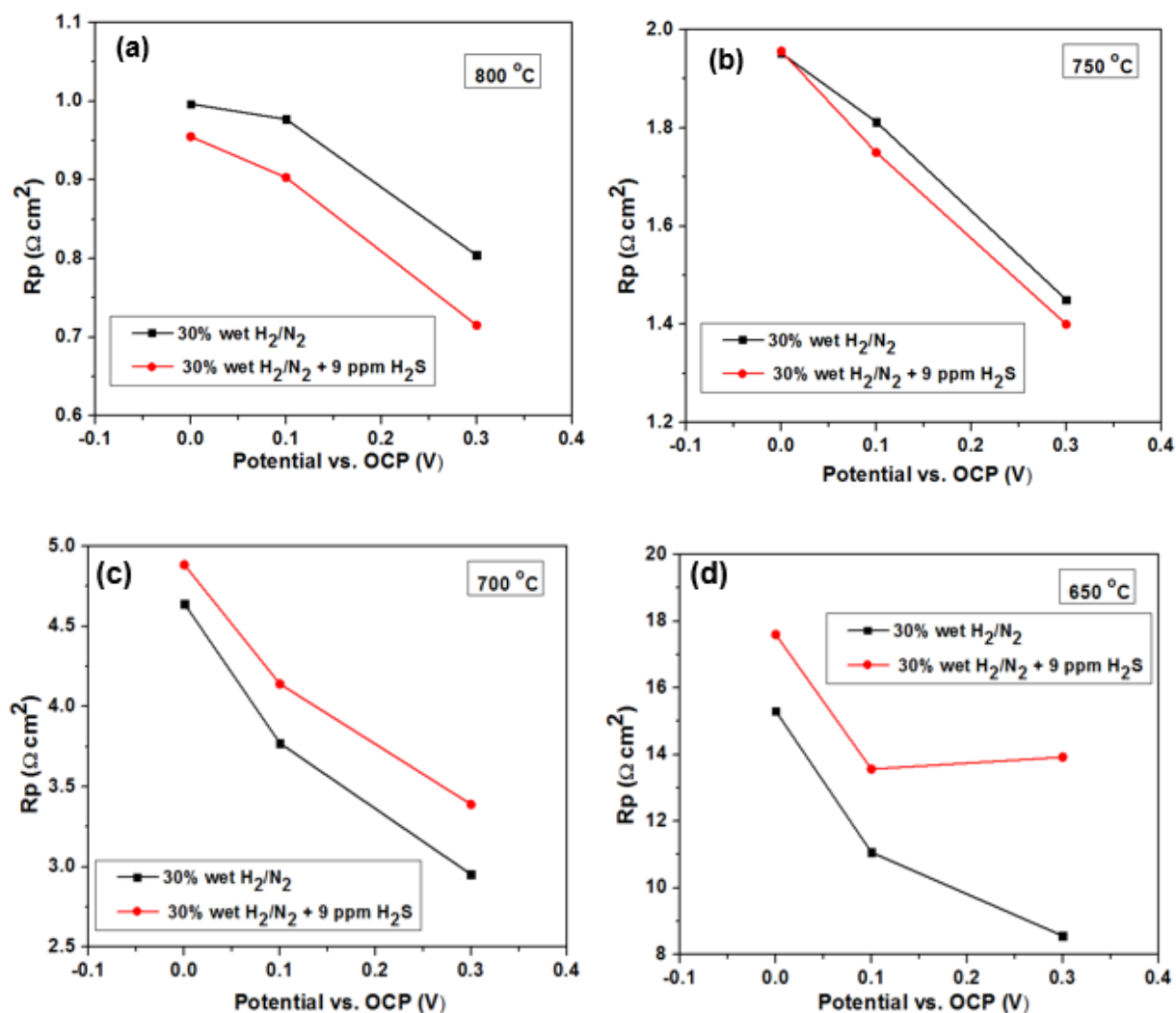
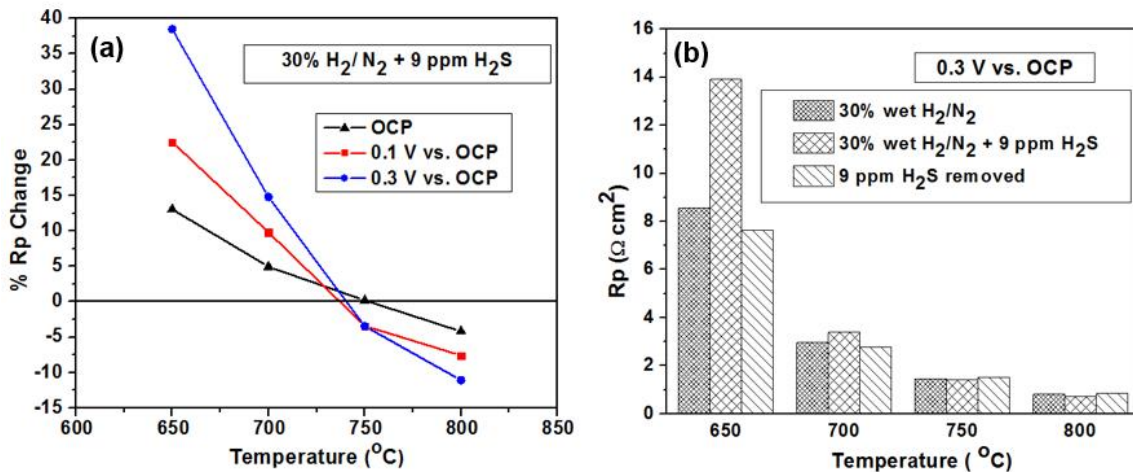


Figure 5.8 OCP and polarized EIS data obtained from symmetrical full cell based on two LCFCr electrodes at 800-650 °C, with wet 30%  $H_2/N_2$ , with or without 9 ppm  $H_2S$ , fed to the fuel electrode and air fed to the oxygen electrode, showing the  $R_p$  vs  $E$  plots at (a) 800 °C, (b) 750 °C, (c) 700 °C, and (d) 650 °C.

To better display the extent of activation and deactivation under OCP and polarized EIS conditions, the % Rp change was calculated, based on the Rp data in Figure 5.8 and using Equation 5.1.

$$\% Rp \text{ change} = \left[ \frac{Rp(H_2) - Rp(H_2S)}{Rp(H_2)} \right] \times 100 \quad (5.1)$$

where Rp(H<sub>2</sub>) is the Rp before the addition of H<sub>2</sub>S and Rp(H<sub>2</sub>S) is the Rp after the addition of H<sub>2</sub>S. Figure 5.9a shows that Rp decreased by 4% under OCP conditions and by 7% and 11% in the presence of H<sub>2</sub>S at 800 °C when the cell was polarized at 0.1 and 0.3 V less than the full cell open circuit voltage, respectively. At 750 °C, Rp decreased by 5% at both 0.1 and 0.3 V vs. OCP conditions, while at 700 °C, Rp increased from about 5% under OCP conditions to 15% at 0.3 V vs. the OCP. The deactivation is more clearly seen at 650 °C under both OCP and polarized conditions, with Rp increasing by 15% at the OCP, while at 0.1 and 0.3 V polarization, Rp increased by 25 and 40%, respectively.



**Figure 5.9** EIS response from symmetrical full cells based on LCFCr electrodes at 800-650 °C, with wet 30% H<sub>2</sub>/N<sub>2</sub>, with or without 9 ppm H<sub>2</sub>S, fed to the fuel electrode and air fed to the oxygen electrode, showing (a) the % Rp change at the OCP, 0.1 V, and 0.3 V vs. the OCP, and (b) Rp at 0.3 V vs. the OCP. Negative %Rp values represent LCFCr activation, while positive values show deactivation.

It is also important to note that the activation and deactivation behaviour observed for the LCFCr-based cell from 800 to 650 °C is completely reversible, as shown in Figure 5.9b. At 800 and 750 °C, while performance activation is observed in the presence of H<sub>2</sub>S, removal of H<sub>2</sub>S leads to the complete recovery of R<sub>p</sub>. Also, the deactivation observed at 700 and 650 °C is equally reversible, where the increase in R<sub>p</sub> seen at these temperatures recovers to its original value when H<sub>2</sub>S is removed from the H<sub>2</sub> gas stream.

To further study the performance of the LCFCr electrode towards H<sub>2</sub> oxidation in the presence or absence of 9 ppm H<sub>2</sub>S in wet 30% H<sub>2</sub>/N<sub>2</sub>, potentiostatic studies were carried out at 0.3 V less than the full cell OCP (i.e., at a 0.75 V cell voltage) at 800 °C. Figure 5.10a shows the i-t plot, with or without H<sub>2</sub>S addition. As can be seen, upon the addition of 9 ppm H<sub>2</sub>S to the H<sub>2</sub> fuel at 9 h, the current density increased from 145 mA/cm<sup>2</sup> to 155 mA/cm<sup>2</sup>, giving a 4.3% improvement in current density. After 2 h of removal of H<sub>2</sub>S from the H<sub>2</sub>/H<sub>2</sub>O stream, the current density decreased to 145 mA/cm<sup>2</sup>, identical to the value observed before H<sub>2</sub>S exposure.

It can also be seen in Figure 5.10a that the activation behaviour of LCFCr electrodes in the presence of low ppm H<sub>2</sub>S is very reproducible. For example, exposure of the cell to humidified H<sub>2</sub>/N<sub>2</sub> containing 9 ppm H<sub>2</sub>S for 4 h under OCP conditions and then re-running the potentiostatic study gave a current density of ca. 155 mA/cm<sup>2</sup>, while removal of the H<sub>2</sub>S led to a decrease in the current density, similar to what was observed in the first run. This shows that the enhancement is observed only in the presence of H<sub>2</sub>S and that the cell fully recovers in the absence of H<sub>2</sub>S, suggesting that no bulk sulfide phase forms but rather that only some type of surface species is generated.

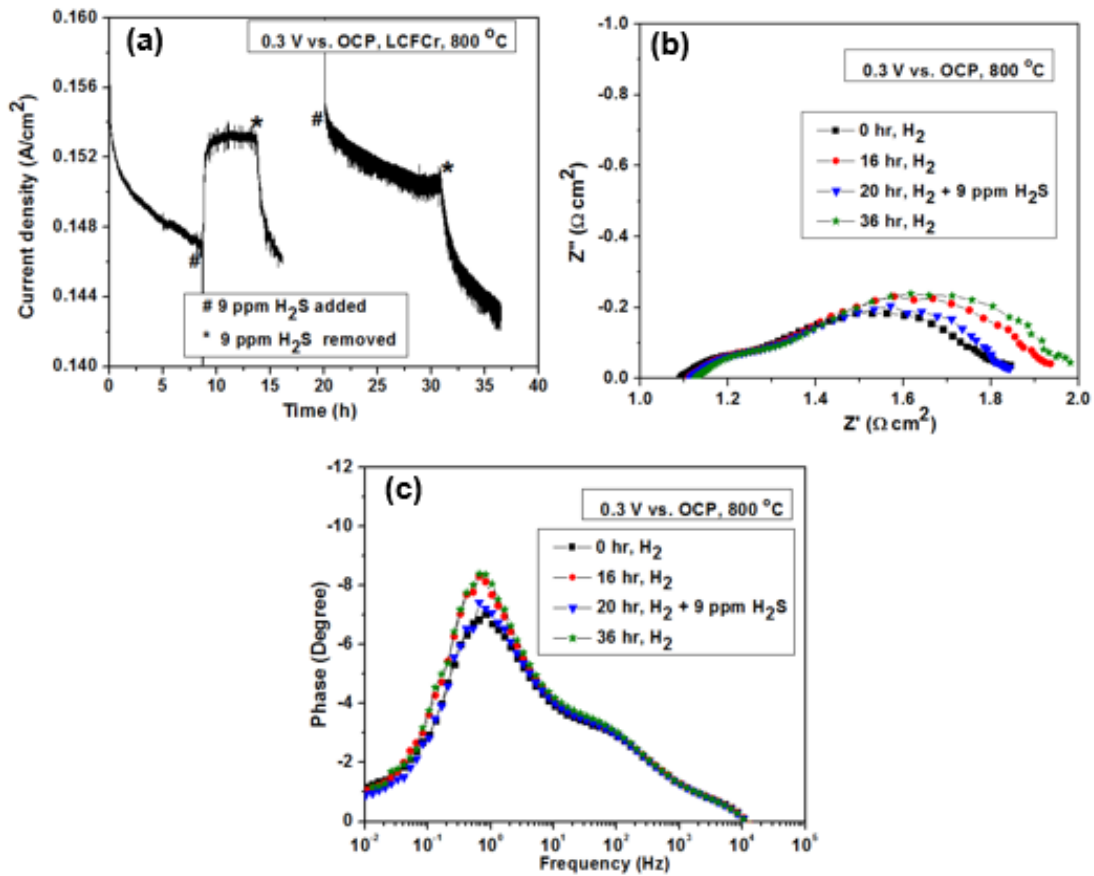


**Figure 5.10** Short term study of symmetrical full cells based on two LCFCr electrodes at 800 °C, with wet 30% H<sub>2</sub>/N<sub>2</sub>, with or without 9 ppm H<sub>2</sub>S, fed to the fuel electrode and air fed to the oxygen electrode, at a constant cell voltage of 0.3 V less than the cell OCP, showing (a) the current versus time (i-t) plot and the corresponding (b) Nyquist and (c) Bode plots.

Polarized impedance measurements were carried out at various times in the presence or absence of H<sub>2</sub>S in this potentiostatic study in wet 30% H<sub>2</sub>/N<sub>2</sub>, with Figures 5.10b and 5.10c showing the Nyquist and Bode plots, respectively. From the polarized (0.3 V vs. OCP) impedance data, the high frequency arc, which is dominated by the cathode process, only changed slightly, while the low frequency arc changed more noticeably during the addition and removal of H<sub>2</sub>S at 800 °C, as anticipated. By fitting the Nyquist plots (Figure 5.10c) to the equivalent circuit in Figure 5.1c, the high frequency resistance (R1) increased from 0.25 to 0.28

$\Omega \text{ cm}^2$  (ca. 10%), indicating a slight degradation of the oxygen electrode, after 36 h of testing. However, the low frequency resistance (R2) increased from 0.46 to 0.55  $\Omega \text{ cm}^2$  (by ca. 25%) after 36 h of the potentiostatic study, with or without the addition of 9 ppm  $\text{H}_2\text{S}$  to the  $\text{H}_2$  gas stream.

The i-t response of the full cell was also examined at 600 °C at 0.3 V polarization from the full cell OCP (i.e., at a cell voltage of 0.81 V) with the repeated addition and removal of 9 ppm  $\text{H}_2\text{S}$  (Figure 5.11). The addition of  $\text{H}_2\text{S}$  leads to a rapid decrease in the current density. However, the cell completely recovers with the removal of the  $\text{H}_2\text{S}$  from the  $\text{H}_2/\text{N}_2$  gas stream.

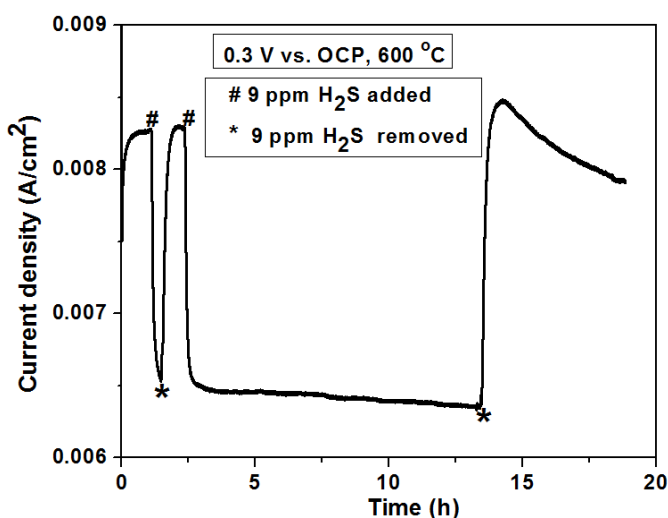


**Figure 5.11** i-t response of a symmetrical full cell, based on two LCFCr electrodes at 600 °C with wet 30%  $\text{H}_2/\text{N}_2$ , with or without 9 ppm  $\text{H}_2\text{S}$ , fed to the fuel electrode and air fed to the oxygen electrode, at a constant cell voltage of 0.3 V less than the cell OCP.

Overall, the results presented in Section 5.2.4 have shown that exposure of the LCFCr fuel electrode (in a symmetrical full cell configuration) to wet  $\text{H}_2/\text{N}_2 + 9 \text{ ppm } \text{H}_2\text{S}$  leads to an enhancement (activation) of the hydrogen oxidation reaction at  $> 700 \text{ }^\circ\text{C}$ , while at  $\leq 700 \text{ }^\circ\text{C}$ , the cell deactivated in the presence of  $\text{H}_2\text{S}$ . Also, both the impedance and potentiostatic results have

shown that the cells quickly and completely recover after either the activation or deactivation process when H<sub>2</sub>S is removed from the H<sub>2</sub> gas stream.

### ***5.2.5 Symmetrical half cell studies of LCFCr in the presence or absence of H<sub>2</sub>S in wet H<sub>2</sub>/N<sub>2</sub>***

To confirm that the activation and deactivation behaviour of LCFCr in ppm levels of H<sub>2</sub>S is not seen only in a symmetrical fuel cell study, half cell studies were also carried out. Figure 5.12 shows the Nyquist plots under OCP conditions for a 2-electrode half cell containing only the two LCFCr electrodes, with both electrodes exposed to wet 50% H<sub>2</sub>/N<sub>2</sub> in the presence or absence of 10 ppm H<sub>2</sub>S from 600 to 800 °C.

It is seen in Fig. 5.12 that the addition of H<sub>2</sub>S at 800 and 750 °C again leads to activation of the half cell, which equates to a decrease in the total R<sub>p</sub> (both electrodes). At below 750 °C, adding H<sub>2</sub>S caused the R<sub>p</sub> to increase, thus deactivating the cell (Figure 5.12b), similar to what was seen in the 2-electrode full cell studies described in Section 5.2.4. Table 5.2 shows the resistances obtained by fitting the data in Figure 5.12 to the R<sub>s</sub>(R1/CPE1) (R2/CPE2) equivalent circuit (Figure 5.1c), with both the high (R1) and low frequency (R2) resistances increasing with temperature. Based largely on the MIEC oxide literature<sup>224, 225</sup>, R1 is attributed to the oxide ion charge transfer process at the electrode/electrolyte interface, while R2 is related to the H<sub>2</sub> adsorption/desorption and electron transfer reactions.

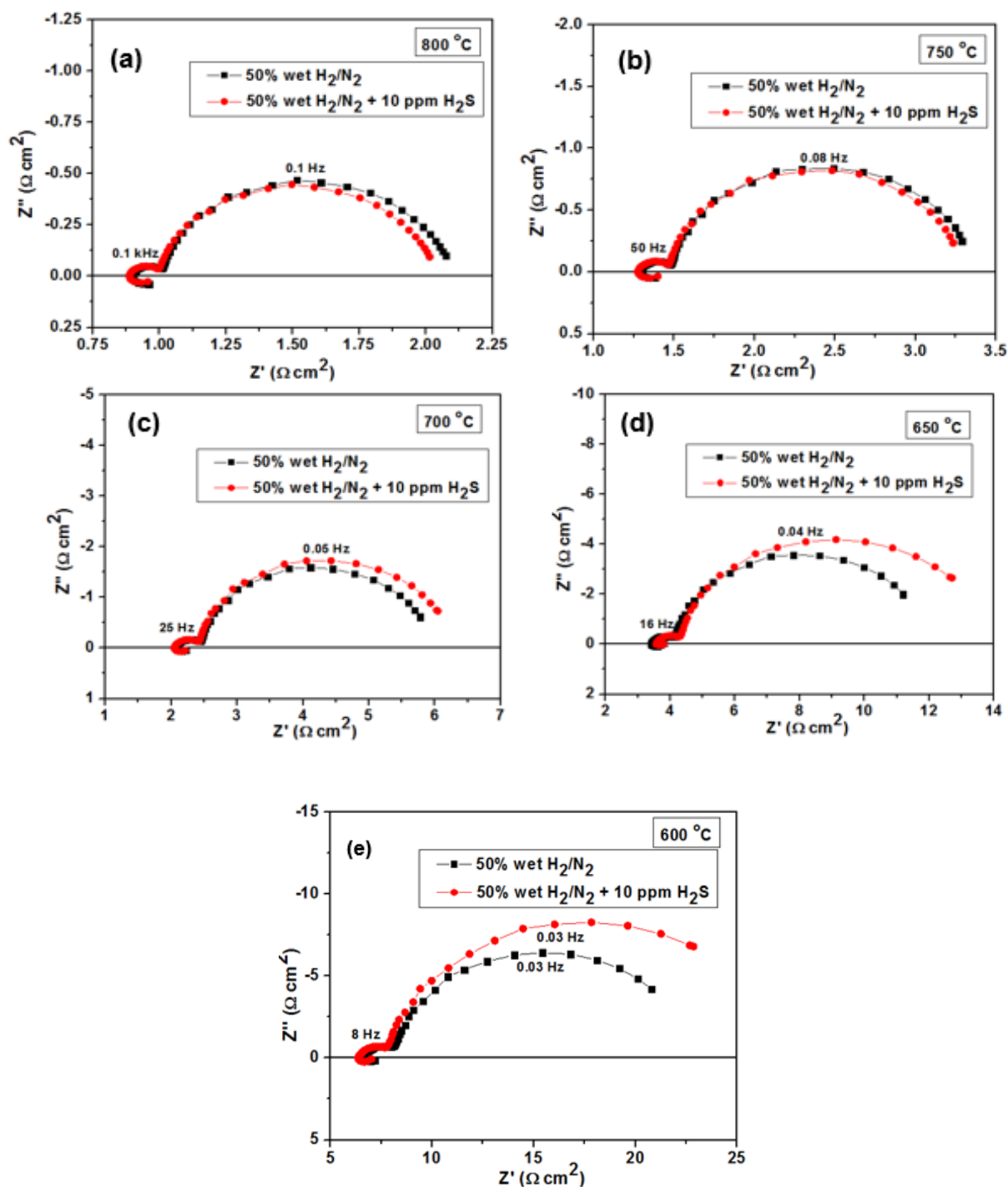


Figure 5.12 OCP EIS response for symmetrical half cell based on LFCr electrodes at 800-600 °C in wet 50%  $H_2/N_2$ , with or without 10 ppm  $H_2S$ , at (a) 800 °C, (b) 750 °C, (c) 700 °C (d) 650 °C, and (e) 600 °C.

In the previous full cell study, discussed in Section 5.2.1, the high frequency arc was shown to be due to the oxygen processes occurring at the air cathode and thus it would have overlapped with the high frequency arc seen in Figure 5.12. In this half cell study, it can be seen that R1 (part of the fuel reactions) is smaller than the low frequency resistance (R2), which is related to the surface processes associated with the hydrogen oxidation (HOR)/hydrogen evolution (HER) reaction.

From Table 5.2, it is seen that R1 does not change at any temperature with the addition of H<sub>2</sub>S, consistent with it being due to an underlying interface, whereas R2 does. At 800 and 750 °C, where performance activation is observed in 10 ppm H<sub>2</sub>S, R2 decreased slightly from 1.1 to 1.0 Ω cm<sup>2</sup> (ca. 10%) at 800 °C and from 1.9 to 1.8 Ω cm<sup>2</sup> at 750 °C with the addition of H<sub>2</sub>S to the H<sub>2</sub> stream. At 700, 650, and 600 °C, R2 increased with the addition of H<sub>2</sub>S. The largest R<sub>p</sub> change is observed at 600 °C, where it increased from 17 Ω cm<sup>2</sup> in the absence of H<sub>2</sub>S to 21 Ω cm<sup>2</sup> with the addition of H<sub>2</sub>S, giving a 19% change in R<sub>p</sub>.

Direct comparison of the %R<sub>p</sub> values between the half (Figure 5.12, Table 5.2) and full cell (Figure 5.9) results cannot be made because of the different experiment conditions employed in these two experiments. In the full cell study, 30% humidified H<sub>2</sub>/N<sub>2</sub> + 9 ppm H<sub>2</sub>S was used, compared to 50% humidified H<sub>2</sub>/N<sub>2</sub> + 10 ppm H<sub>2</sub>S in the half cell study. However, qualitatively, in both cases, the presence of low ppm H<sub>2</sub>S enhances the performance of the HOR/HER at LCFCr at > 750 °C, while at < 750 °C, a drop in performance is observed.

**Table 5.2 Resistance values\* obtained by fitting the impedance data in Figure 5. 12\*\* to the Rs(R1CPE1)(R2CPE2) equivalent circuit model (Figure 5.1c)**

T (°C)	Atmosphere	Rs ( $\Omega \text{ cm}^2$ )	R1 ( $\Omega \text{ cm}^2$ )	R2 ( $\Omega \text{ cm}^2$ )	Rp <sup>#</sup> ( $\Omega \text{ cm}^2$ )	% Rp change <sup>##</sup>
800	H <sub>2</sub>	0.90	0.11	1.1	1.2	-8.3
	H <sub>2</sub> + 10 ppm H <sub>2</sub> S	0.89	0.11	1.0	1.1	
750	H <sub>2</sub>	1.3	0.20	1.9	2.1	-4.8
	H <sub>2</sub> + 10 ppm H <sub>2</sub> S	1.3	0.20	1.8	2.0	
700	H <sub>2</sub>	2.1	0.39	3.5	3.9	+7.1
	H <sub>2</sub> + 10 ppm H <sub>2</sub> S	2.1	0.39	3.8	4.2	
650	H <sub>2</sub>	3.4	0.73	7.8	8.6	+14
	H <sub>2</sub> + 10 ppm H <sub>2</sub> S	3.6	0.75	9.3	10	
600	H <sub>2</sub>	6.6	1.6	15	17	+19
	H <sub>2</sub> + 10 ppm H <sub>2</sub> S	6.4	1.5	19	21	

\* R1 and R2 obtained from the high (ca. 100 Hz) and low (ca. 1 Hz) frequency arcs, respectively.  
 \*\* Symmetrical half cell based on LCFCr electrodes, operated at 800-600 °C, in wet 50% H<sub>2</sub>/N<sub>2</sub>, w/wo H<sub>2</sub>S present.

# Rp = R1 + R2. Rp values may not add up due to internal rounding.

## %Rp change calculated using Equation 5.1. Negative and positive %Rp values indicate activation and deactivation of the cell, respectively.

Figure 5.13 shows the Arrhenius plots of the resistances shown in Table 5.2. The calculated activation energies for the high frequency resistance (R1) (Figure 5.13a), low frequency resistance (R2) (Figure 5.13b), and the polarization resistance (Rp) (Figure 5.13c) are shown in Table 5.3. It is seen that the activation energy related to R1 (Ea (R1)) does not change with the addition of H<sub>2</sub>S to the H<sub>2</sub> gas stream and is 102 kJ/mol and 101 kJ/mol in the absence and presence of 9 ppm H<sub>2</sub>S in the H<sub>2</sub> stream, respectively. This shows that the presence of H<sub>2</sub>S

does not affect the slowest step associated with the oxide ion charge transfer process at the electrode/electrolyte interface, which is not surprising, considering that this a buried interface. Also, this further confirms the assignment of the high frequency arc to process occurring at the electrode/electrolyte interface<sup>55</sup>.

The low frequency resistance activation energy ( $E_a$  (R2)) for the LCFCr electrode in the absence of H<sub>2</sub>S is 105 kJ/mol, whereas in the presence of H<sub>2</sub>S, a higher activation energy of 116 kJ/mol is observed. As discussed earlier, the low frequency resistance (R2) is due to surface processes, such as H<sub>2</sub> adsorption, dissociation, and charge transfer at the gas/electrode interface. Thus, the addition of H<sub>2</sub>S is expected to alter one or more of these steps. It is possible that, at below 750 °C when deactivation is seen, H<sub>2</sub>S simply blocks some of the active sites required for the HOR, which would not change the  $E_a$  value. Finally, as seen in Table 5.3, the value obtained for  $E_a$  (R<sub>p</sub>) is similar to the  $E_a$  (R2) value, because the contribution of R2 to R<sub>p</sub> is dominant.

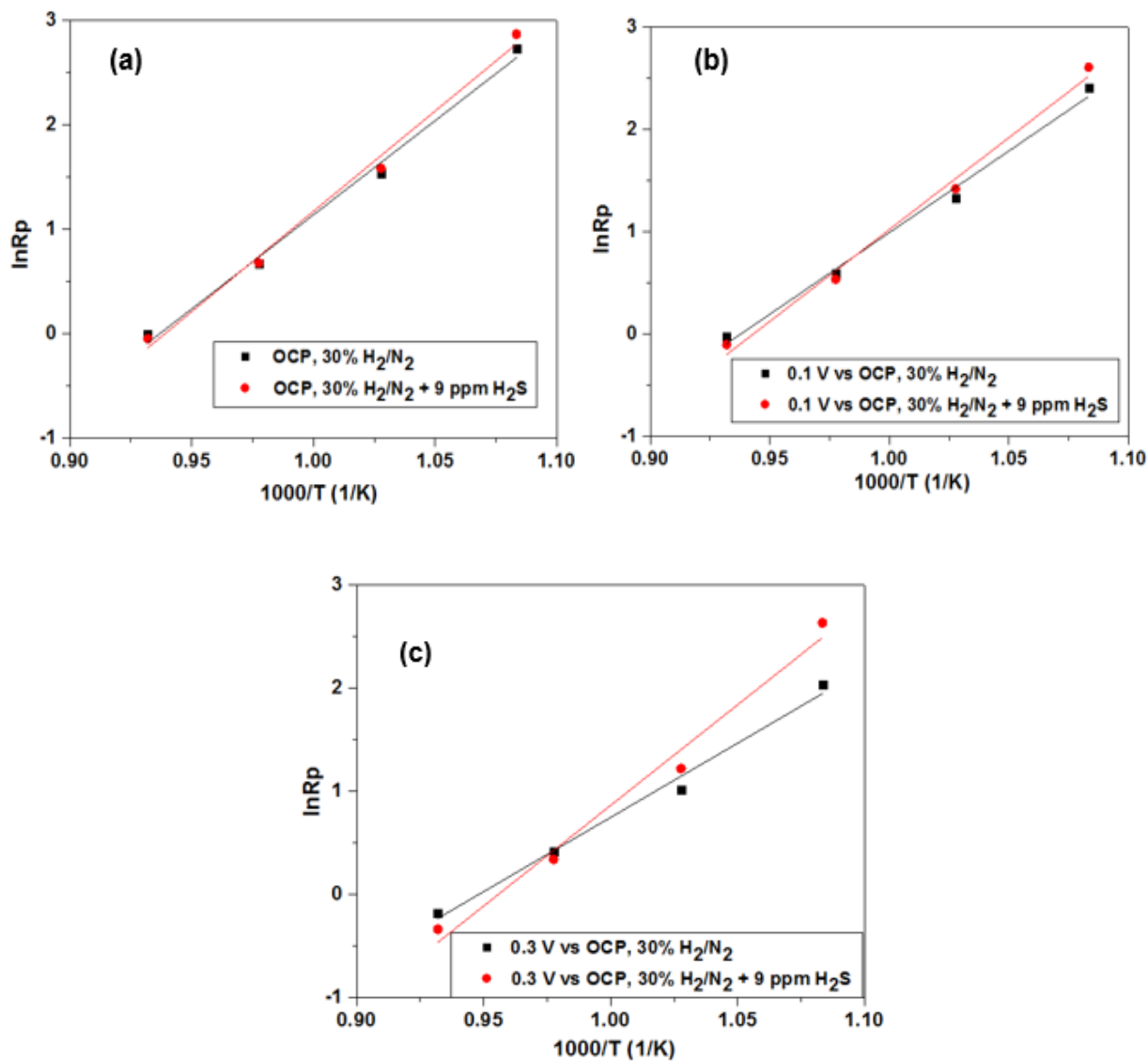


**Figure 5.13** Arrhenius plots for the EIS-obtained R values for a symmetrical half cell based on two LCFCr electrodes at 800-600 °C in wet 50% H<sub>2</sub>/N<sub>2</sub>, with or without 10 ppm H<sub>2</sub>S. (a) high frequency resistance R1, (b) low frequency resistance R2, and (c) polarization resistance R<sub>p</sub>.

**Table 5.3 Calculated activation energies obtained from Figure 5.13**

Atmosphere	Activation energy (kJ/mol)		
	R1*	R2*	Rp <sup>#</sup>
50% H <sub>2</sub> /N <sub>2</sub>	102	105	105
50% H <sub>2</sub> /N <sub>2</sub> + 9 ppm H <sub>2</sub> S	101	116	115

\* R1 and R2 obtained from the high (ca. 100 Hz) and low (ca. 1 Hz) frequency arcs, respectively.

The i-t plots for the symmetrical LSF<sub>Cr</sub> half cell are shown in Figure 5.14 for temperatures between 600 to 850 °C. Figure 5.14 shows that, when a 0.3-1 V bias (the potential difference between the working (WE) and the counter (CE) electrodes) is applied in the half cell at 750-850 °C, the current density increases when H<sub>2</sub>S is added. Similar to what was seen from the impedance data (Figure 5.12), at below 750 °C, deactivation of the cell is observed (decrease in current density) with the addition of H<sub>2</sub>S.

Again, as was also seen in the full cell study (Section 5.2.4), the activation or deactivation observed in the presence of H<sub>2</sub>S is fully recoverable when H<sub>2</sub>S is removed from the gas stream. Figure 5.14c shows the percent current density change at each temperature, calculated from Figures 5.14a and 5.14b. The enhancement in the % current density decreases slightly with decreasing temperature. Thus, at 850 °C, the % i gain is 2%, while it is only 1% at 750 °C. Figure 5.14c shows that, at < 750 °C, a significant % i loss is observed, with the current density decreasing by 5% and 32% at 700 °C and 600 °C, respectively.

The effect of the magnitude of the applied bias between the WE and CE on the activation behavior (at 800 °C) is shown in Figure 5.14d. As the potential difference between the WE and CE was increased from 0.3 V to 1 V, the percent current change increased from 0.5% to 2.5%. This shows that the activation of LCF<sub>Cr</sub> in the presence of H<sub>2</sub>S is being influenced by the

applied potential, whereas for the Ni-YSZ anode discussed in Chapter 4, there was no clear trend in the percent current change with H<sub>2</sub>S exposure at varying applied anodic overpotentials.

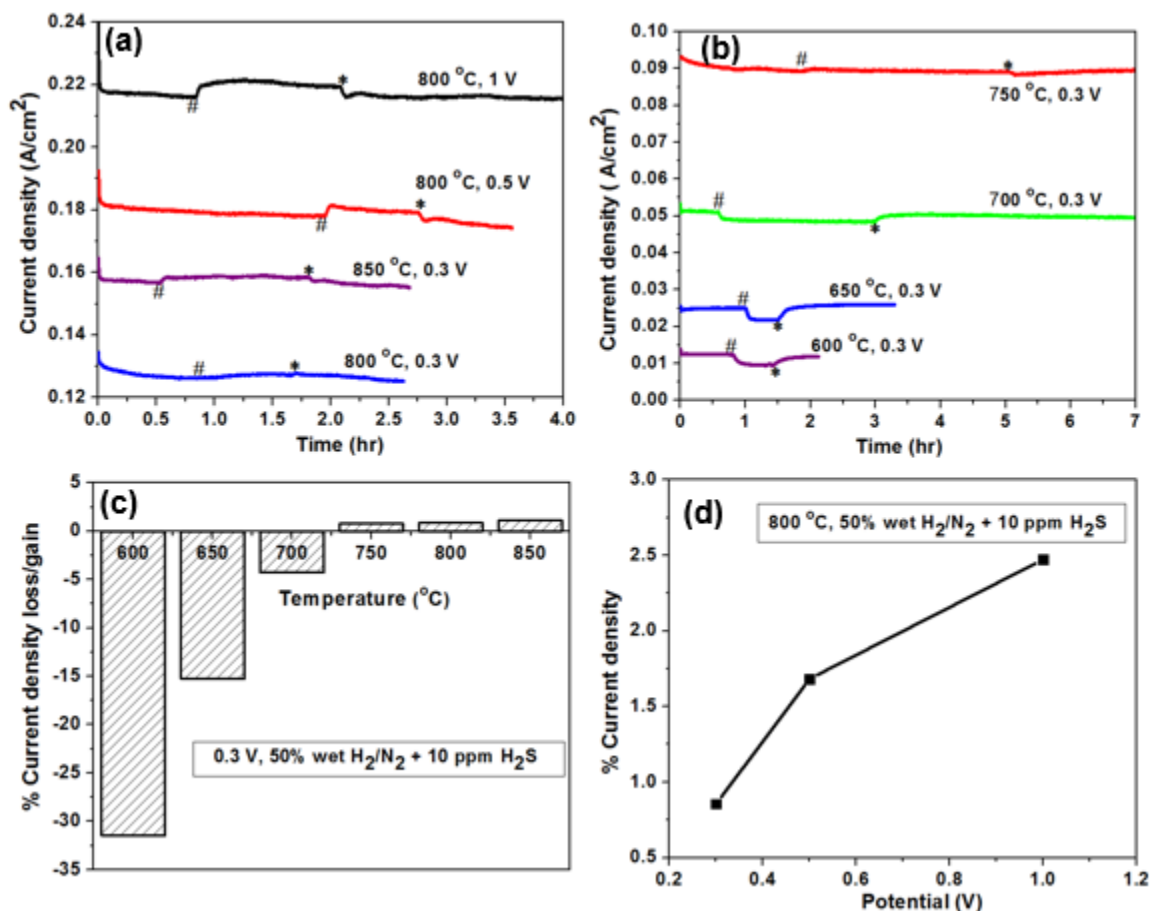


**Figure 5.14** Short term potentiostatic study of a symmetrical half cell involving two LCFCr electrodes in humidified 50% H<sub>2</sub>/N<sub>2</sub>, with 10 ppm H<sub>2</sub>S exposure and removal, at 0.3-1.0 V cell bias at (a) 850-800 °C, (b) 750-600 °C, (c) % current density change vs. temperature at 0.3 V from 850-600 °C, and (d) % current density change vs. applied potential at 800 °C.

A possible explanation for the LCFCr behavior, which is a mixed ionic and electronic conductor, is that the applied overpotential changes the LCFCr surface properties through an increase or decrease in the concentration of oxygen vacancies (i.e., a change in the oxidation states of surface Fe and Cr ions). For example, it has been reported that the surface concentration

of  $\text{Ce}^{3+}/\text{Ce}^{4+}$  on a doped ceria electrode influences the rate of the hydrogen oxidation/steam reduction reactions<sup>226</sup>.

### ***5.2.6 Understanding LCFCr activation and deactivation in $\text{H}_2\text{S}/\text{H}_2$ environments***

To attempt to understand the interesting effect of  $\text{H}_2\text{S}$  on the performance of the LCFCr fuel electrode, an electron microprobe wavelength-dispersive X-ray spectroscopy (WDX) elemental map was collected from a symmetrical full cell (Section 5.2.4). This experiment was carried out on a cell that had been electrochemically tested for several days in humidified 30%  $\text{H}_2/\text{N}_2$ , with or without the addition of 9 ppm  $\text{H}_2\text{S}$ , in the temperature range of 600-800 °C and then slowly cooled to 30 °C in humidified 30%  $\text{H}_2/\text{N}_2$  containing 9 ppm  $\text{H}_2\text{S}$ . Figure 5.15 shows the backscattered electron (BSE) image of the cell and the WDX maps of Ce, La, Ca, Fe, Cr, and S. It can be seen from Figure 5.15 that La, Ca, Fe, and Cr are distributed evenly throughout the electrode, with sulfur seen only in the LCFCr phase, and with no sulfur observed in the ceria buffer layer or in the Au current collector. This shows that  $\text{H}_2\text{S}$  adsorbs or reacts with the LCFCr material in some way, affecting the HOR in different ways at various temperatures, as was discussed above.

X-ray photoelectron spectroscopy (XPS) was also used to further understand the activation behaviour seen at 800 °C and the deactivation at 600 °C when LCFCr was exposed to 10 ppm  $\text{H}_2\text{S}$  in humidified  $\text{H}_2$ . These experiments were carried out on a thin film (150  $\mu\text{m}$  thick) of LCFCr, spin-coated onto a YSZ substrate to facilitate the XPS analysis, thus eliminating the effect of surface porosity and roughness effects.

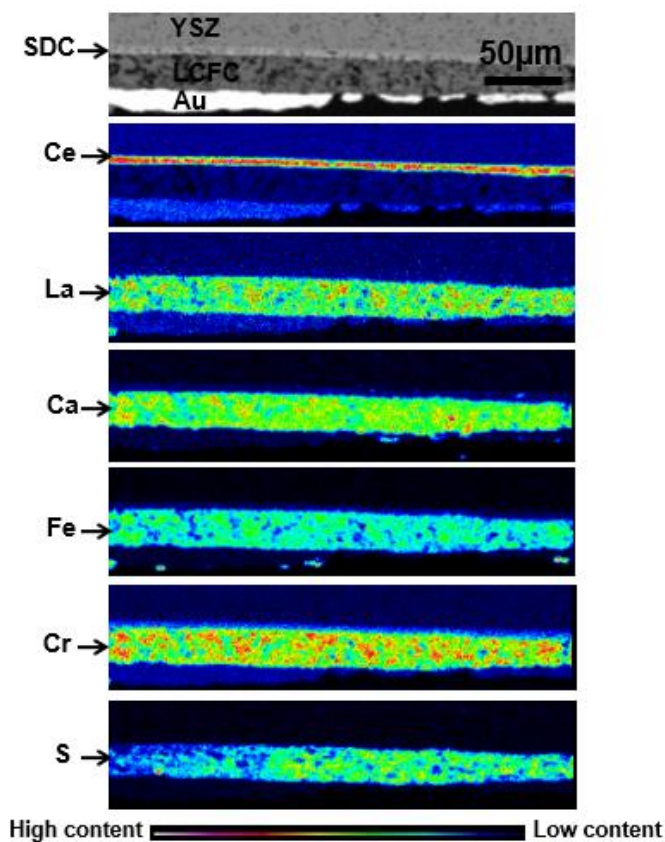


**Figure 5.15** Electron microprobe WDX elemental mapping of the polished cross-section of a LCFCr fuel electrode, slowly cooled in humidified 30%  $H_2/N_2$  containing 9 ppm  $H_2S$  to 30 °C, after several days of electrochemical testing of the cell, in the temperature range of 600-800 °C.

Figure 5.16 shows the XPS spectra for samples ramped in humidified 30%  $H_2/N_2$  from 30 to 800 °C, with a 2 h holding time at 800 °C, in either humidified 30%  $H_2/N_2$  or humidified 30%  $H_2/N_2$  + 9 ppm  $H_2S$ . After 2 h of exposure time, the samples were quenched by sliding them out from the hot zone of a tube furnace (800 °C) to the edge of the quartz tube, which had a temperature of ca. 150 °C. Also, for comparison, other samples were cooled in the same gas atmosphere to room temperature instead of being quenched at 800 °C.

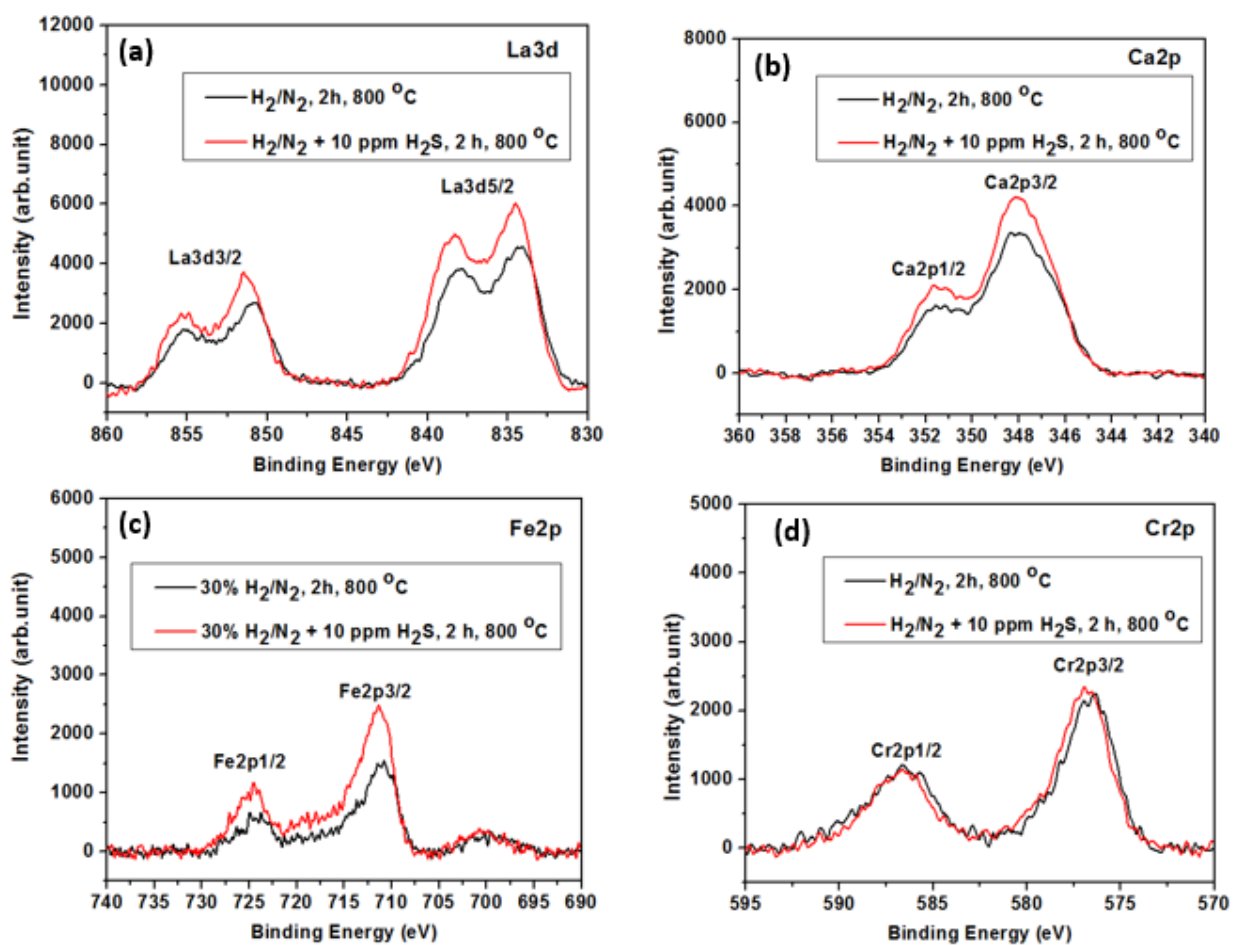


**Figure 5.16** XPS spectra of LFCr thin film samples exposed to humidified 30%  $\text{H}_2/\text{N}_2$ , with or without 10 ppm  $\text{H}_2\text{S}$  addition, at 800 °C for 2 h, showing the peaks for (a) La, (b) Ca, (c) Fe, and (d) Cr. All samples were quenched at 800 °C instead of cooling slowly to 30 °C.

The XPS spectra in Figure 5.16 show that, with the addition of  $\text{H}_2\text{S}$  at 800 °C, the peak intensity of La, Ca and Fe increases, whereas the Cr peak did not change. This suggests that  $\text{H}_2\text{S}$  may influence the amount of La, Ca and Fe at the perovskite surface (ca. 4-6 nm). It has been reported that Fe sites are more favourable for S adsorption than are Cr sites<sup>227, 228</sup>, so this could explain why the Cr peaks of the LFCr thin film sample remained the same in the presence or absence of  $\text{H}_2\text{S}$ . No S peak was detected on any of the quenched samples studied here.

Therefore, in subsequent experiments, the samples were cooled in the same gas environment to room temperature and the holding time at 800 °C or 600 °C was increased from 2 h to 5 h.

The XPS analysis of the cooled samples is shown in Figure 5.17. Figure 5.17a shows the Fe2p spectra for LCFCr-thin film samples exposed to humidified 30% H<sub>2</sub>/N<sub>2</sub> in the presence or absence of H<sub>2</sub>S from 30 °C to 600 °C, with a holding time of 5 h at 600 °C, and then cooled to room temperature in the same gas atmosphere. From Figure 5.17, the addition of H<sub>2</sub>S leads to a higher Fe2p peak intensity at 600 °C, which is the same trend observed for the quenched sample at 800 °C (Figure 5.16c).

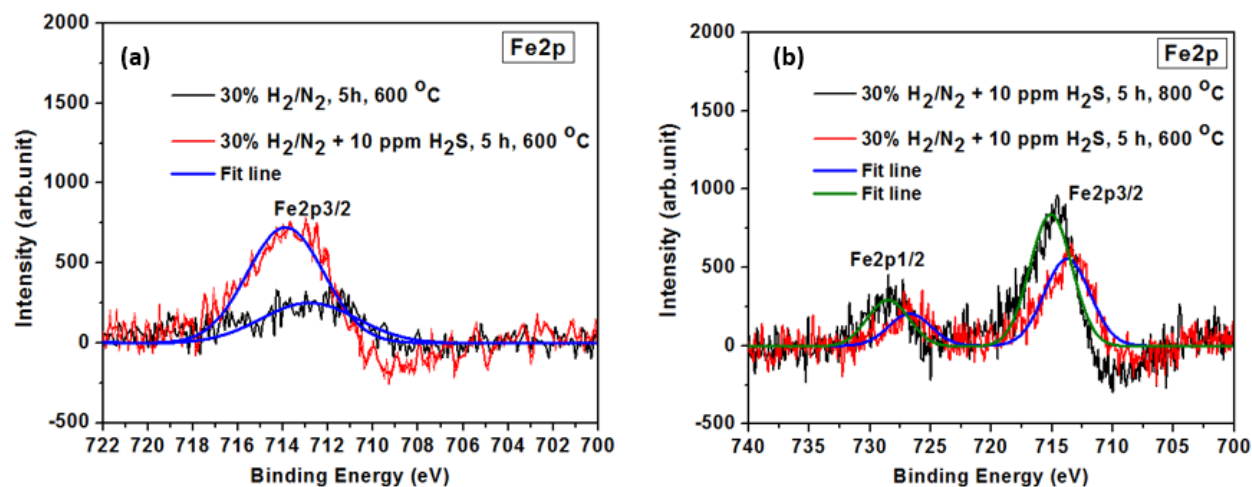


**Figure 5.17** XPS spectra of LCFCr thin film samples exposed to humidified 30% H<sub>2</sub>/N<sub>2</sub>, showing the peaks for (a) Fe at 600 °C, with or without H<sub>2</sub>S addition for 5 h, and (b) a comparison plot of the Fe peaks at 600 °C and 800 °C. All samples were slowly cooled from either 600 °C or 800 °C to 30 °C in humidified 30% H<sub>2</sub>/N<sub>2</sub> containing 10 ppm H<sub>2</sub>S.

Figure 5.17b shows a comparison of the Fe peaks obtained for samples exposed to humidified 30% H<sub>2</sub>/N<sub>2</sub> plus 10 ppm H<sub>2</sub>S at 600 and 800 °C. The Fe peaks at 800 °C are shifted by about 2.5 eV to a higher binding energy and the peak intensity is higher when compared to

the peaks at 600 °C. This is because, at higher temperatures (800 °C), the surface and sub-surface composition of the LCFCr could be different than at lower temperatures.

Figure 5.18 shows the S2p XPS spectra for the LCFCr-thin film samples, ramped from either 30 °C to 600 °C (Figure 5.18a) or 800 °C (Figure 5.18b) in either humidified 30% H<sub>2</sub>/N<sub>2</sub> or 30% H<sub>2</sub>/N<sub>2</sub> + 10 ppm H<sub>2</sub>S, with a 5 h hold at the testing temperature before cooling down to 30 °C in the same gas atmosphere. As expected, no sulfur peak was detected on the samples that were not exposed to H<sub>2</sub>S at either 600 or 800 °C (Figure 5.18), while the samples exposed to humidified 30% H<sub>2</sub>/N<sub>2</sub> + 10 ppm H<sub>2</sub>S showed S2p peak. Based on the deconvolution of the S2p in Chapter 4 (Figure 4.9), the detected sulfur (S2p) here is in the form of a sulfate (169-172 eV), with no sulfide peak (162-163 eV) detected on the surface of the LCFCr sample. Unlike the quenched samples (Figure 5.16), these samples showed the presence of a sulfur peak for the samples treated at 600 °C (Figure 5.18a) and 800 °C (Figure 5.18b), indicating that H<sub>2</sub>S probably interacts with the LCFCr material under these conditions.

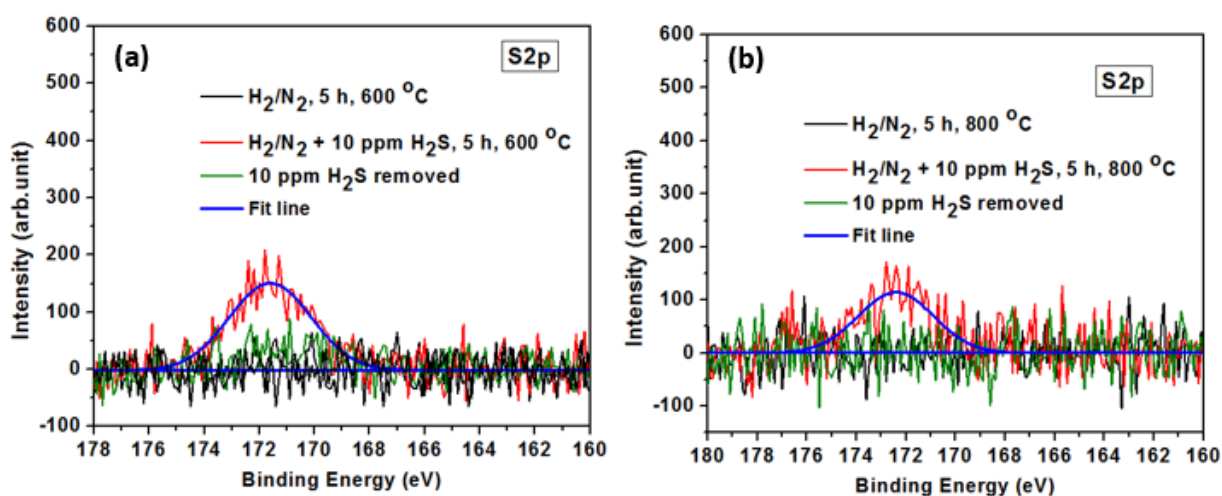


**Figure 5.18** XPS spectra of LCFCr thin film samples exposed to humidified 50% H<sub>2</sub>/N<sub>2</sub>, with or without H<sub>2</sub>S addition, at 800 and 600 °C for 5 h, showing the S2p peak after exposure at (a) 600 °C and (b) 800 °C.

Furthermore, to determine whether any sulfur adsorbed on the LCFCr material after exposure to H<sub>2</sub>S can be completely removed, XPS analysis was carried out on samples ramped to 600 °C or 800 °C, held for 5 h in humidified 30% H<sub>2</sub>/N<sub>2</sub> + 10 ppm H<sub>2</sub>S and then cooled to 30 °C in humidified 30% H<sub>2</sub>/N<sub>2</sub>. and samples that were cooled down in humidified 30% H<sub>2</sub>/N<sub>2</sub>.

When the samples were cooled down to 30 °C in H<sub>2</sub> after 5 h of H<sub>2</sub>S exposure at either 600 °C or 800 °C, no S2p peak was detected. This shows the complete removal of any form of sulfur species on the LCFCr surface, suggesting that no bulk sulfide species were formed, as these would be harder or slower to remove. This agrees with the electrochemical data (Figures 5.9 and 5.14), where complete recovery of the performance of the LCFCr cell was quickly observed after removal of H<sub>2</sub>S from the humidified H<sub>2</sub>/N<sub>2</sub> gas stream.

A density functional theory (DFT) study by Walker *et al.*<sup>227</sup>, focused on the effect of H<sub>2</sub>S on Sr<sub>2</sub>Fe<sub>1.5</sub>Mo<sub>0.5</sub>O<sub>6-δ</sub> (SFMO) anodes, showed that at low temperatures (ca. 600 °C), Fe-O-Fe terminated surfaces are prone to conversion to Fe-S-Fe (Reaction 5.2) in low ppm H<sub>2</sub>S environments (< 20 ppm). At high temperatures (ca. 800 °C), higher ppm H<sub>2</sub>S contents (80-100 ppm) are required to promote Reaction 5.2. Here, it is suggested that, since only 10 ppm H<sub>2</sub>S was used, more surface Fe-O-Fe terminated groups on LCFCr could be converted to Fe-S-Fe at ≤ 700 °C than at > 700 °C, thereby decreasing the number of active sites available for the hydrogen oxidation reaction (HOR, (Reaction 5.3)) and leading to activity deactivation,



where V<sub>o</sub><sup>\*\*</sup> is an oxygen vacancy in the LCFCr surface.

It has also been reported that, at low temperatures, FeO<sub>2</sub>-terminated surfaces are prone to sulfur poisoning, hindering surface oxygen vacancy formation, which is required for the HOR

<sup>227</sup>. However, it has been shown that the Fe-S-Fe species can be converted back to Fe- $V_o^{\bullet\bullet}$ -Fe (Reaction 5.4) in the presence of a H<sub>2</sub> gas stream. Therefore, the complete recovery of the electrochemical performance of the cell after deactivation at  $\leq 700$  °C in the presence of H<sub>2</sub>S could be because Reaction 5.4 occurs when H<sub>2</sub>S is removed from the H<sub>2</sub> gas stream.



Overall, it is proposed here that, since Cr sites are not very favourable for S adsorption <sup>227, 228</sup>, the Fe-sites, which are favourable for S adsorption <sup>227, 228</sup> and also active for the hydrogen oxidation reaction, could be responsible for the electrochemical activation seen at  $> 700$  °C or the deactivation observed at  $\leq 700$  °C. Based on these preliminary XPS data, there are probably more terminated Fe-O-Fe species at the surface of LCFCr in the presence of H<sub>2</sub>S at 800 °C, which have not been converted to Fe-S-Fe, compared to at 600 °C, providing more active sites for the HOR (Reaction 5.3) at 800 °C.

### 5.3 Summary

This chapter is focussed on determining the activity of several mixed conducting perovskite oxides, particularly La<sub>0.3</sub>Sr<sub>0.7</sub>Fe<sub>0.7</sub>Cr<sub>0.3</sub>O<sub>3- $\delta$</sub>  (LSFCr) and La<sub>0.3</sub>Ca<sub>0.7</sub>Fe<sub>0.7</sub>Cr<sub>0.3</sub>O<sub>3- $\delta$</sub>  (LCFCr) <sup>46, 57</sup> in half cell and full cell configurations in humidified H<sub>2</sub> environments, with and without ppm levels of H<sub>2</sub>S, all at 600-800 °C. It was found that LCFCr is the more active fuel electrode catalyst, consistent with parallel work showing that LCFCr is also the better air cathode material <sup>55</sup> and thus the majority of this chapter was focussed on the effect of H<sub>2</sub>S on the LCFCr fuel electrode.

It was demonstrated by X-ray diffraction that LCFCr, exposed to 30 ppm H<sub>2</sub>S/N<sub>2</sub> at 800 °C for 24 h, did not show the formation of any secondary phases, indicating that the LCFCr

material is structurally stable in low ppm H<sub>2</sub>S environments. In a symmetrical full cell study, both the OCP and polarized impedance data showed that, at > 700 °C, the addition of 9 ppm H<sub>2</sub>S to the cell led to an enhancement (activation) of the hydrogen oxidation reaction (HOR), while at ≤ 700 °C, the cell deactivated in the presence of H<sub>2</sub>S. In either of these modes, the cell was quickly and fully recovered when H<sub>2</sub>S was removed. In the two electrode half cell studies, the cell was fed with humidified 50% H<sub>2</sub>/N<sub>2</sub>, with or without 10 ppm H<sub>2</sub>S, again showing the same trends with H<sub>2</sub>S exposure. For example, at 800 °C, the addition of 10 ppm H<sub>2</sub>S to the half cell led to a 8% decrease in the polarization resistance (R<sub>p</sub>), while at 600 °C, R<sub>p</sub> increased by 19%.

To better understand the interactions of LCFCr with H<sub>2</sub>S, elemental mapping using electron probe analysis as well as X-ray photoelectron spectroscopy were used. The electron probe analysis showed that sulfur was detected only on the LCFCr phase, with no sulfur observed in the ceria buffer layer or the Au current collector. The XPS analysis showed that H<sub>2</sub>S exposure led to an increase in the density of surface FeO<sub>2</sub> terminated species, required for the hydrogen oxidation reaction (HOR), relative to the case at 600 °C, also supported by a density functional theory (DFT) calculation reported in literature for Sr<sub>2</sub>Fe<sub>1.5</sub>Mo<sub>0.5</sub>O<sub>6-δ</sub> (SFMO) anodes<sup>227</sup>. The deactivation of LCFCr at ≤ 700 °C could be due to the interaction of H<sub>2</sub>S with surface FeO<sub>2</sub>-terminated species, forming surface Fe-S-Fe species, thereby reducing the number of active sites available for the HOR<sup>227</sup>.

## Chapter Six: **Stability and electrochemical performance of $\text{La}_{0.3}\text{Sr}_{0.7}\text{Fe}_{0.7}\text{Cr}_{0.3}\text{O}_{3-\delta}$ (LSFCr) reversible SOFC electrodes in dry $\text{CO}_2/\text{CO}$ environments**

This Chapter contains some data from a published paper (P. K. Addo, B. Molero-Sanchez, M. Chen, S. Paulson and V. Birss, *CO/CO<sub>2</sub> study of high performance  $\text{La}_{0.3}\text{Sr}_{0.7}\text{Fe}_{0.7}\text{Cr}_{0.3}\text{O}_{3-\delta}$  - reversible SOFC electrodes*, Fuel Cells, 2015. **15**(5): p. 689-696)

### **6.1 Introduction**

As discussed in Chapter 1, the concept of carbon capture and utilization (CCU) is gaining worldwide attention as one of the approaches to mitigating climate change<sup>9</sup>. In CCU, waste  $\text{CO}_2$  is used as a feedstock for both chemical and fuel production<sup>9</sup>. Therefore, there is great interest in the development of solid oxide electrolysis cells (SOECs) that can reduce  $\text{CO}_2$  to  $\text{CO}$ , or  $\text{CO}_2/\text{steam}$  to  $\text{CO}/\text{H}_2$  (syngas) at the cathode, while releasing pure oxygen at the anode. In the reverse mode, oxygen and fuel (e.g.,  $\text{CO}/\text{H}_2$ ) react at each electrode, generating electricity and heat in a solid oxide fuel cell (SOFC). Reversible solid oxide fuel cells (RSOFCs) are devices that can be operated in both the SOEC and SOFC modes, all at high temperatures (600-950 °C). The present study, with its focus on  $\text{CO}_2/\text{CO}$  reactions at  $\text{La}_{0.3}\text{M}_{0.7}\text{Fe}_{0.7}\text{Cr}_{0.3}\text{O}_{3-\delta}$  (M = Sr, Ca, (LMFCr)) electrodes, thus has direct relevance to the development of RSOFCs.

The use of solid oxide cells (SOCs) for  $\text{CO}_2$  electrolysis was first demonstrated by NASA in their Mars missions, where a symmetrical cell, based on Pt or Pt/YSZ (yttria-stabilized zirconia) electrodes, was used to convert  $\text{CO}_2$  to  $\text{CO}$  at the cathode (fuel electrode) and  $\text{O}_2$  at the anode (oxygen electrode)<sup>19-22</sup>. As discussed in Chapter 2, most of the SOECs used for  $\text{CO}_2$  electrolysis reported in the literature have been based on a Ni-YSZ composite fuel electrode, a YSZ electrolyte, and a lanthanum strontium manganite (LSM) oxygen electrode. Ni-YSZ fuel electrodes have shown good electrochemical performance for  $\text{CO}_2$  reduction, although there are

some concerns related to their stability due to Ni oxidation and coke formation in pure CO<sub>2</sub> and CO<sub>2</sub>/CO atmospheres.

Due to these stability issues associated with Ni-YSZ, research has increasingly focused on the development of new materials for CO<sub>2</sub>/CO interconversion. Examples of electrodes used for this purpose include perovskites, such as La<sub>1-x</sub>Sr<sub>x</sub>Cr<sub>1-y</sub>Mn<sub>y</sub>O<sub>3-δ</sub> (LSCM)<sup>96, 100, 102-104</sup>. A perovskite-based fuel electrode, such as LSCM-Gd<sub>x</sub>Ce<sub>1-x</sub>O<sub>2-δ</sub>, has shown Rp values of only ca. 1.0 Ω cm<sup>2</sup> at 850 °C in 90% CO<sub>2</sub>:10% CO<sup>102, 103</sup>. Also, LSCM infiltrated into a YSZ scaffold together with 0.5 wt. % Pd supported on 5 wt. % Ce<sub>0.48</sub>Zr<sub>0.48</sub>Y<sub>0.04</sub>O<sub>2</sub> and operated on 90% CO<sub>2</sub>:10% CO at 800 °C, showed cathodic currents as large as 1.8 A/cm<sup>2</sup> during CO<sub>2</sub> reduction at an applied cell voltage of 1.4 V<sup>27</sup>.

Another promising family of perovskites, which has been used mainly as SOFC fuel anodes, is the ferrite analogue of LSCM, La<sub>0.3</sub>Sr<sub>0.7</sub>Fe<sub>0.7</sub>Cr<sub>0.3</sub>O<sub>3-δ</sub> (LSFCr). As discussed in Chapter 5 and also reported by others, LSFCr is a very active anode for the oxidation of H<sub>2</sub> and CO<sup>46, 114, 116, 118, 119, 229, 230</sup>. However, there are only a few published studies in which LSFCr has been employed specifically for the electrolysis of CO<sub>2</sub>. For example, in a study by Bierschenk *et al.*<sup>115</sup> involving the operation of LSFCr in a H<sub>2</sub>/CO atmosphere, the focus was on SOFC operation only, not on CO<sub>2</sub> electrolysis. Therefore, the present work is unique in terms of its focus on the performance of LSFCr in both the SOFC and SOEC modes in CO/CO<sub>2</sub> atmospheres.

It has been reported previously that LSFCr is structurally stable down to a pO<sub>2</sub> of 10<sup>-21</sup> atm, below which it decomposes to secondary phases<sup>46, 119, 229</sup>. An extensive study by Chen *et al.* showed that the partial substitution of Cr into the B site of La<sub>0.3</sub>Sr<sub>0.7</sub>FeO<sub>3-δ</sub> (LSF) improved the structural stability of the material in reducing atmospheres (pO<sub>2</sub> 10<sup>-21</sup> atm)<sup>46</sup>. However, the

authors showed that long time exposure of LSFcr to a dry 10% H<sub>2</sub>/N<sub>2</sub> atmosphere at 800 °C led to the formation of a LaSrFeO<sub>4</sub>-based phase (K<sub>2</sub>NiF<sub>4</sub>-like Ruddlesden-Popper phase) and α-Fe. Also, an *in situ* neutron diffraction study by Haag *et al.* showed that, at 800 °C and a pO<sub>2</sub> of 10<sup>-21</sup> atm, LSFcr decomposes to LaCrO<sub>3</sub>, a spinel phase, and α-Fe<sup>229</sup>.

Although Haag *et al.*<sup>229</sup> used gas mixtures of air, Ar, CO<sub>2</sub>, 1% CO/Ar, and CO to obtain the required pO<sub>2</sub> during their neutron diffraction experiments, to the best of our knowledge, there has been no detailed study carried out regarding the stability of LSFcr perovskites in pure, dry CO<sub>2</sub> (pO<sub>2</sub> ~10<sup>-7</sup> atm at 800 °C), CO<sub>2</sub>/CO mixtures (pO<sub>2</sub> of 10<sup>-18</sup>-10<sup>-19</sup> atm at 800 °C) and CO (pO<sub>2</sub> > 10<sup>-23</sup> atm at 800 °C) environments. Therefore, to use this Sr-rich perovskite-based material as an electrode for CO<sub>2</sub>/CO reactions, it is critical to determine its stability in these atmospheres, especially in high pCO<sub>2</sub> from 30-800 °C to determine if any secondary phases are formed. This is because other types of perovskites, with alkaline earth metals (such as Sr, Ba) doped into the A-site, have been shown to form carbonate species in pure CO<sub>2</sub> atmosphere. For example, it has been reported that exposure of Ba<sub>0.5</sub>Sr<sub>0.5</sub>Co<sub>0.8</sub>Fe<sub>0.2</sub>O<sub>3-δ</sub> (BSCF)<sup>231</sup> and La<sub>0.6</sub>Sr<sub>0.4</sub>Co<sub>0.2</sub>Fe<sub>0.8</sub>O<sub>3-δ</sub> (LSCF)<sup>232</sup> to CO<sub>2</sub> led to the formation of carbonate species, which negatively affected the electrochemical performance of the electrode.

Therefore, the first part of this chapter reports, for the first time, a detailed study of the chemical stability of LSFcr when exposed to a range of different CO<sub>2</sub>/CO environments with a pO<sub>2</sub> ranging from 10<sup>-7</sup>-10<sup>-23</sup> atm. It is shown that, in 20-100% CO<sub>2</sub> (pO<sub>2</sub> ~10<sup>-7</sup> atm) from 30-800 °C, LSFcr remained structurally stable with no formation of bulk SrCO<sub>3</sub>, while exposure of LSFcr to 70% CO<sub>2</sub>:30% CO (pO<sub>2</sub> ~10<sup>-19</sup> atm) at 800 °C showed the formation of minor impurities. The second part of this chapter investigates the electrochemical performance of a symmetrical 2-electrode full cell, involving LSFcr as both the oxygen and fuel electrodes and

operated on CO<sub>2</sub>/CO gas mixtures fed to the fuel electrode and air exposure of the oxygen electrode. Specifically, it shown that the LSF<sub>Cr</sub>-based RSOFC, evaluated at 600-850 °C, exhibits a very good electrochemical performance during both the reduction of CO<sub>2</sub> (SOEC mode) and oxidation of CO (SOFC mode) at the fuel electrode.

## 6.2 Results and Discussion

### 6.2.1 Chemical stability of LSF<sub>Cr</sub> in pure CO<sub>2</sub> and CO<sub>2</sub>/CO atmospheres

The stability of the La<sub>0.3</sub>Sr<sub>0.7</sub>Fe<sub>0.7</sub>Cr<sub>0.3</sub>O<sub>3-δ</sub> (LSF<sub>Cr</sub>) powder at 30-900 °C in dry 20-100% CO<sub>2</sub> (balance N<sub>2</sub> or He, pO<sub>2</sub> of 10<sup>-5</sup> to 10<sup>-7</sup> atm at 800 °C), 90-70% CO<sub>2</sub>:10-30% CO (pO<sub>2</sub> of 10<sup>-18</sup> to 10<sup>-19</sup> atm at 800 °C), and 10-30% CO:90-70% N<sub>2</sub> (pO<sub>2</sub> ≥ 10<sup>-23</sup> atm at 800 °C) atmospheres was investigated in this work. The pO<sub>2</sub> values for the CO/CO<sub>2</sub> mixtures were calculated using Equations 6.1<sup>220</sup> and 6.2<sup>233</sup>.

$$\ln(pO_2)_{anode} = \frac{2\Delta G^o}{RT} + 2\ln\left(\frac{pCO_2}{pCO}\right) \quad (6.1)$$

$$\Delta G^o = -282.5 + 0.0866T \quad (6.2)$$

where  $\Delta G^o$  is the Gibbs free energy, R is the gas constant (8.314 J/mol.K), and T is temperature. The pO<sub>2</sub> of dry 20-100% CO<sub>2</sub> (balance N<sub>2</sub> or He) at ca. 800 °C was calculated by assuming that the CO<sub>2</sub> gas stream (balance N<sub>2</sub>) contained a very small amount of CO (0.01%), while for 10-30% CO (balance N<sub>2</sub>), it was assumed that the CO gas stream contained a very small amount of CO<sub>2</sub> (0.01%). These theoretical pO<sub>2</sub> values were found to be in good agreement with the experimental values, obtained from the open circuit potentials (OCPs) of full cells in which CO<sub>2</sub> or CO<sub>2</sub>/CO was fed to the fuel electrode and air to the oxygen electrode and then using Equation 6.3<sup>220</sup>, the pO<sub>2</sub> at the anode (fuel electrode) was determined. .

$$E = \frac{RT}{4F} + \ln \left( \frac{pO_{2(cathode)}}{pO_{2(anode)}} \right) \quad (6.3)$$

where  $pO_{2(cathode)}$  is the  $pO_2$  (0.21 atm for air) at the cathode under OCP conditions and  $pO_{2(anode)}$  is the  $pO_2$  at the anode.

The chemical stability study discussed here is based on results obtained from X-ray diffraction (XRD), Fourier transform infrared (FTIR) spectroscopy, thermogravimetric analysis (TGA), scanning electron microscopy (SEM), high resolution transmission electron microscopy (HRTEM), and energy dispersive X-ray spectroscopy (EDS).

#### 6.2.1.1 Chemical stability of LSFCr in variable but dry $pCO_2$ (balance $N_2$ or He)

Figure 6.1 shows the XRD patterns for the as-prepared LSFCr powder and after exposure of the powder to dry  $CO_2$  from 30 °C to 800 °C and then holding at 800 °C for 24 h before cooling to room temperature. It is seen that the powder remains as a single phase (perovskite) in the  $CO_2$  atmosphere for long exposure times. No peaks associated with the formation of any secondary phases, such as SrO or  $SrCO_3$ , are observed.

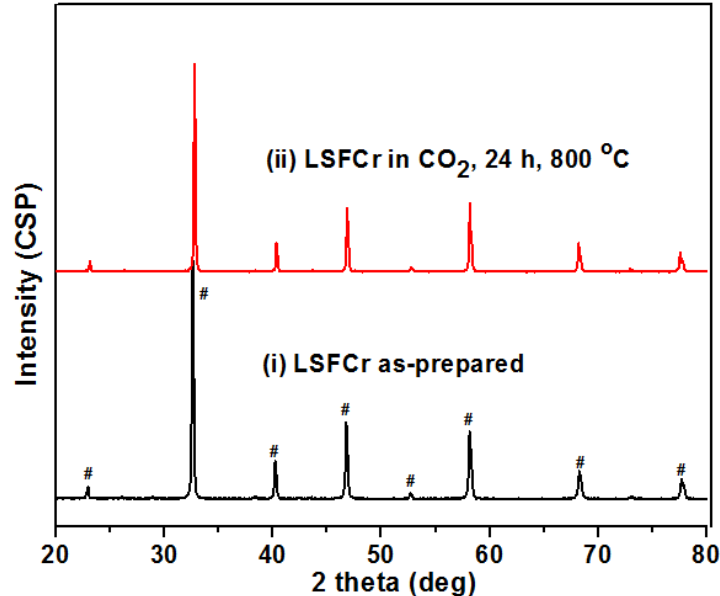


**Figure 6.1** *Ex situ* XRD patterns showing the chemical stability of the LSFCr powder (i) as-prepared and (ii) after exposure to dry 100% CO<sub>2</sub> atmosphere with a 24 h dwell time at 800 °C. Sample (ii) was heated and cooled at a ramp rate of 5 °C/min in a 100% CO<sub>2</sub> atmosphere. The symbol used to identify the LSFCr perovskite peaks is (#).

This is very promising because some studies of other perovskites, such as (LaSr)(CoFe)O<sub>3-δ</sub> with high Sr contents, used as oxygen separation membranes, showed the formation of SrCO<sub>3</sub> after long exposures to CO<sub>2</sub><sup>234</sup>. However, other oxygen membrane studies have shown that, even though CO<sub>2</sub> readily adsorbs onto the surface of (LaSr)(CoFe)O<sub>3-δ</sub>, it does not react and the adsorbed CO<sub>2</sub> can be desorbed by changing the sweeping gas. In other work, Benson *et al.*<sup>235</sup>, have shown that CO<sub>2</sub> enhances the surface exchange coefficient of O<sub>2</sub> at La<sub>0.6</sub>Sr<sub>0.4</sub>Co<sub>0.2</sub>Fe<sub>0.8</sub>O<sub>3-δ</sub> (LSCF).

Based on Lewis acid-base theory, the interaction between CO<sub>2</sub>, which serves as the acid, and the perovskite as a base, can be established<sup>236</sup>. Therefore, the acidity of the doping cations would be a good indicator of the CO<sub>2</sub> tolerance of a perovskite<sup>236</sup>. It is known that metal oxides with a higher acidity have a lower tendency to interact with CO<sub>2</sub><sup>237</sup>. Acidity trends of some

doping cations of perovskites have been reported in the literature<sup>237</sup>, showing the following sequence:  $\text{Nb}^{5+} > \text{Co}^{4+} > \text{Co}^{3+} > \text{Fe}^{3+} > \text{Co}^{2+} > \text{Fe}^{2+}$ . Although  $\text{Fe}^{4+}$  is not listed here, its acidity can be expected to be between that for  $\text{Co}^{4+}$  and  $\text{Co}^{3+}$ <sup>237</sup>. Therefore, considering the high Fe content (35 mol %) of LSFCr, which has been shown to be stable in higher valence states (+3, +4)<sup>119, 238</sup>, it is possible that the relative acidity of LSFCr is quite high, thus preventing any reaction with  $\text{CO}_2$  that could lead to the decomposition of LSFCr and the formation of  $\text{SrCO}_3$  over the temperature range of our studies. Also, previous studies have shown that, by doping the B-site of  $\text{La}_{0.3}\text{Sr}_{0.7}\text{Fe}_{0.7}\text{O}_{3-\delta}$  with Cr, there is an increase in the structural stability over a wide  $p\text{O}_2$  range ( $1\text{-}10^{-21}$  atm)<sup>46, 229</sup>.

To further prove that LSFCr is stable in dry  $\text{CO}_2$  and remains as a single phase without any detectable secondary phases, high temperature *in situ* XRD experiments were performed from 30 to 800 °C. As seen in Figure 6.2, the *in situ* high temperature XRD patterns show that the perovskite phase is stable, as observed at 30, 400, 600, and 800 °C in a  $\text{CO}_2$  atmosphere.

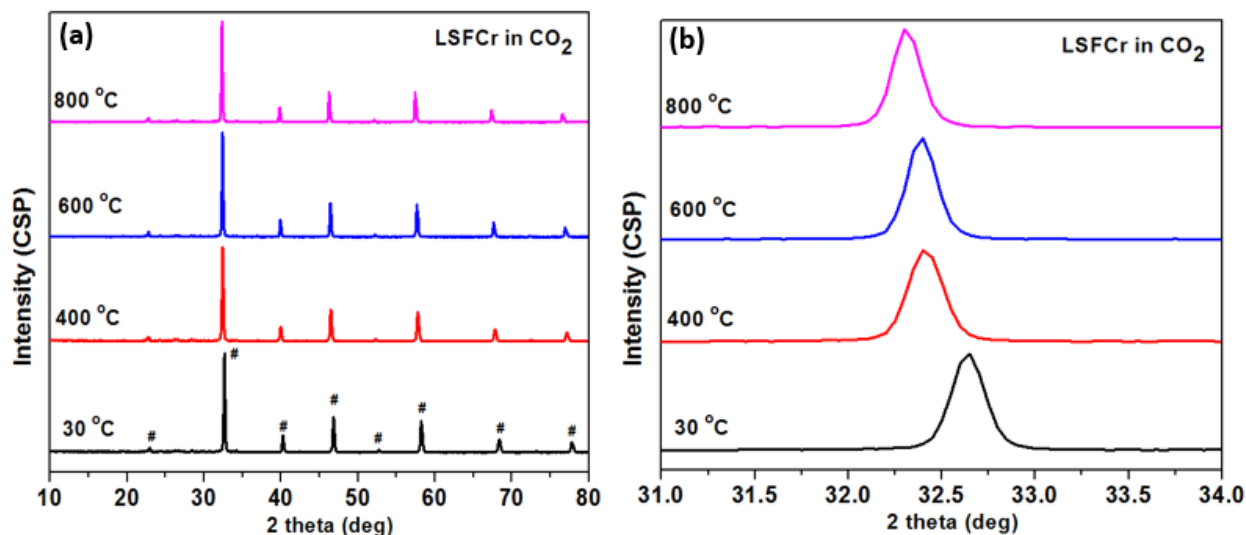


**Figure 6.2 (a) *In situ* XRD patterns of LSFCr powder in dry 100%  $\text{CO}_2$  from 30-800 °C and (b) magnified XRD pattern showing the (110) peak. The symbol used to identify the LSFCr (perovskite) peaks is (#).**

While the peaks shift to lower  $2\theta$  (degrees) with increasing temperature, as shown in Figure 6.2b for the (110) peak, this is fully expected due to the increase in the lattice constant parameters.

To further establish the chemical stability of the LSFCr material in the CO<sub>2</sub> environment, TG analysis was performed to determine the weight change of the powder upon heating and cooling from room temperature to 900 °C in CO<sub>2</sub>. Figure 6.3a shows the TG profile of the LSFCr powder in air and in 60% CO<sub>2</sub> (balance N<sub>2</sub>). The heating TGA profile in air was used as the baseline to show the weight change of the material with respect to temperature so that any weight change observed in CO<sub>2</sub> can be established correctly. As can be seen, there is no measurable weight loss of the powder in either air or CO<sub>2</sub> below 400 °C. At 400 °C, loss of lattice O<sup>2-</sup> begins as LSFCr is reduced, which is observed by weight loss in both air and CO<sub>2</sub>, as expected<sup>46</sup>. The larger weight loss observed in 60% CO<sub>2</sub> (balance N<sub>2</sub>) is due to the lower pO<sub>2</sub> (10<sup>-7</sup>atm) of CO<sub>2</sub> versus air (0.21 atm).

The TG analysis of the powder in CO<sub>2</sub> shows no weight gain in either the heating or cooling profiles, indicating that no SrCO<sub>3</sub> had formed, which agrees with the XRD analysis above. Various studies have shown that the onset temperature for carbonate formation is around 500 °C and a > 2% weight gain has been observed due to carbonate formation for other types of perovskites (for example, Ba<sub>0.95</sub>Ca<sub>0.05</sub>Co<sub>0.1</sub>Fe<sub>0.9</sub>O<sub>3- $\delta$</sub> , Sr<sub>1-x</sub>Ca<sub>x</sub>Fe<sub>0.5</sub>Co<sub>0.5</sub>O<sub>3- $\delta$</sub> , Ba<sub>0.5</sub>Sr<sub>0.5</sub>Ce<sub>1-x-y-z</sub>Zr<sub>x</sub>Gd<sub>y</sub>Y<sub>z</sub>O<sub>3- $\delta$</sub> , BaZr<sub>0.1</sub>Ce<sub>0.7</sub>Y<sub>0.1</sub>M<sub>0.1</sub>O<sub>3- $\delta$</sub>  (M = Fe, Ni, Co, Y and Yb), which are not stable in dry CO<sub>2</sub><sup>88, 239-241</sup>.

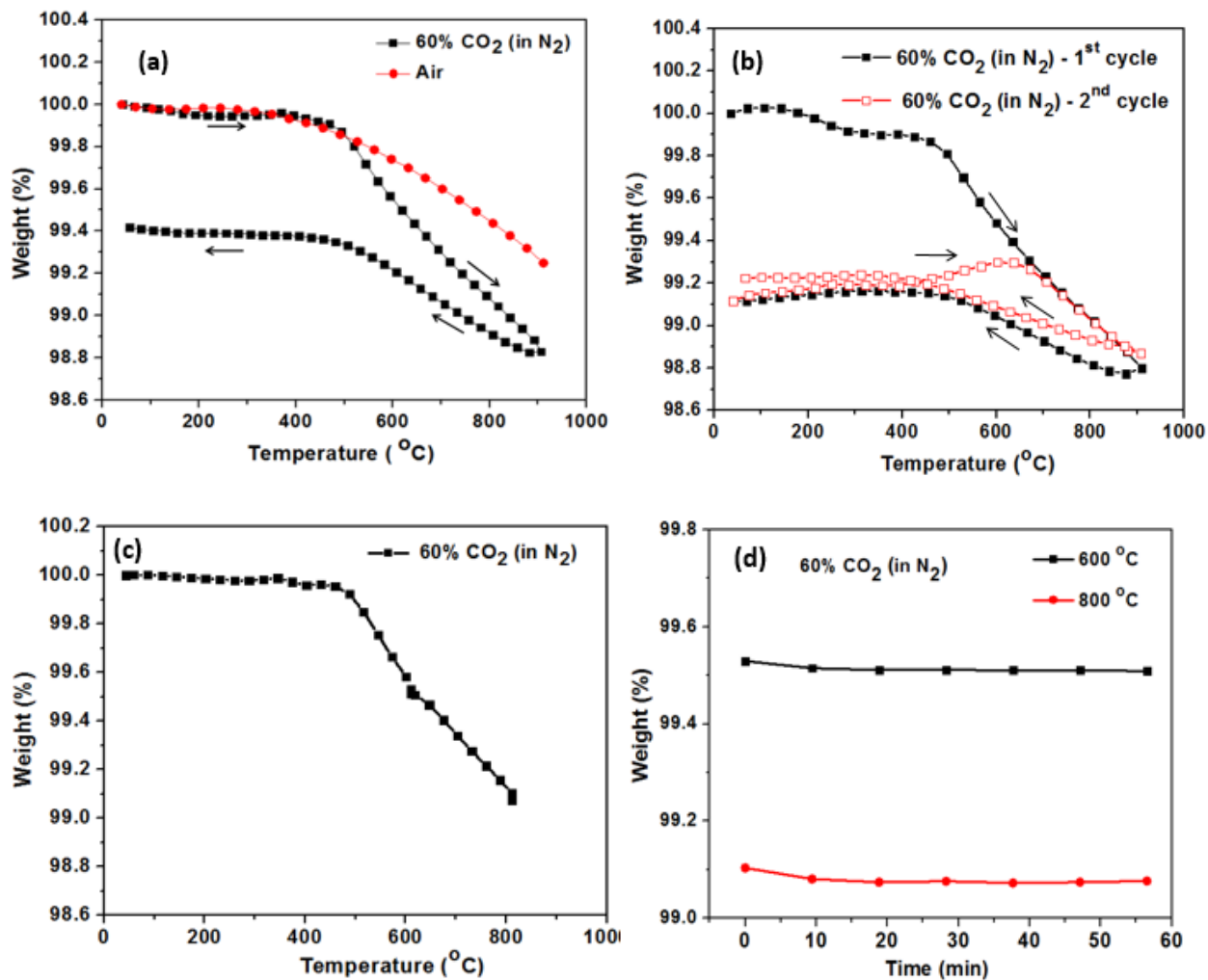


**Figure 6.3** TG profiles of LSFCr powder from 30-900 °C at 3 °C/min in (a) 60% CO<sub>2</sub> (balance N<sub>2</sub>) and air, (b) multiple heating/cooling cycles in 60% CO<sub>2</sub> (balance N<sub>2</sub>), (c) heating profile in 60% CO<sub>2</sub> (balance N<sub>2</sub>) to 800 °C with 1 hr holding at 600 and 800 °C, and (d) isothermal profile at 600 and 800 °C from Figure 6.3c.

In the cooling profile (from 900 to 30 °C) in CO<sub>2</sub> (Figure 6.3a), the weight did not return to its original value, indicating that the lattice oxygen that was lost from LSFCr during heating was not fully re-incorporated into the LSFCr structure during cooling. This is probably due to the lower pO<sub>2</sub> of the 60 % CO<sub>2</sub> gas (balance N<sub>2</sub>, pO<sub>2</sub> ~ 10<sup>-7</sup> atm) compared to air (0.21 atm), because

it has been reported that the weight change associated with LSFCr is reversible upon heating and cooling in air<sup>119</sup>.

To test the observation of incomplete weight recovery of LSFCr in CO<sub>2</sub> during cooling, two heating and cooling cycles of LSFCr in CO<sub>2</sub> were performed, as shown in Figure 6.3b. This shows that, during the first cycle, a similar profile was observed (as in Figure 6.3a), where incomplete recovery was observed during cooling at RT. However, during the second cycle, the LSFCr recovers to its initial weight of 99.2% during cooling at RT. Once LSFCr is equilibrated after the first cycle, subsequent cycles start at a lower percent weight loss, corresponding to an increase in the concentration of oxygen vacancies and a higher O<sub>2</sub> non-stoichiometry ( $\delta$ ). It can be seen from the second cycle that there is a slight increase in weight (0.1%) between 500-700 °C, probably due to the surface adsorption of some CO<sub>2</sub> on LSFCr, in relation to the increase in the concentration of oxygen vacancies. It has been reported previously that oxygen vacancies are the active site for the adsorption of CO<sub>2</sub><sup>236</sup>.

Figure 6.3c shows the TG profile of LSFCr in dry CO<sub>2</sub> held isothermally at 600 and 800 °C for 1 h, respectively. As can be seen from Figure 6.3d, LSFCr did not lose much weight under these conditions, losing only 0.01 and 0.02 % of the mass at 600 and 800 °C, respectively.

To determine the oxygen non-stoichiometry ( $\delta$ ) of LSFCr, TG analysis in air and 20% CO<sub>2</sub> (balance He) was carried out and the weight loss was converted to oxygen non-stoichiometry ( $\delta$ ) using Equation 6.4<sup>119, 236</sup>,

$$\delta = \frac{M}{15.999} \left( 1 - \frac{m}{m_0} \right) + \delta_0 \quad (6.4)$$

where  $m_0$  is the initial weight and  $m$  is the final weight after heating of the sample,  $M$  is the molar mass of the sample at room temperature,  $\delta_0$  is the oxygen nonstoichiometry of the sample

at room temperature, which has been reported to be 0.1 for LSF<sub>Cr</sub><sup>119</sup>, and 15.999 is the atomic weight of oxygen.

Figure 6.4 shows the weight loss data and the calculated oxygen non-stoichiometry ( $\delta$ ). The oxygen non-stoichiometry ( $\delta$ ) in air at 800 °C is about 0.16 and when LSF<sub>Cr</sub> was held in air at 800 °C for 1 hr, it increased to about 0.18. This value of 0.18 is in agreement with what has been previously reported in the literature for LSF<sub>Cr</sub> in air at 800 °C<sup>119</sup>. The introduction of about 20% CO<sub>2</sub> (balance He, pO<sub>2</sub> ~ 10<sup>-5</sup> atm) at 800 °C immediately leads to an increase in weight loss due to further loss of lattice oxygen from LSF<sub>Cr</sub>, as seen in Figure 6.4a. From Figure 6.4b, the oxygen non-stoichiometry ( $\delta$ ) of LSF<sub>Cr</sub> after 1 h in CO<sub>2</sub> at 800 °C is about 0.23.

The  $\delta$  value of LSF<sub>Cr</sub> in CO<sub>2</sub> is higher than in air because of the pO<sub>2</sub> differences between the two gases, as the more reducing CO<sub>2</sub> atmosphere will lead to reduction (more oxygen loss) of the LSF<sub>Cr</sub> material. As expected, re-introduction of air after CO<sub>2</sub> exposure rapidly decreased the  $\delta$  value from 0.23 to its initial value of 0.16 at 800 °C, then gradually decreasing during the cooling profile to about 0.11 at room temperature.

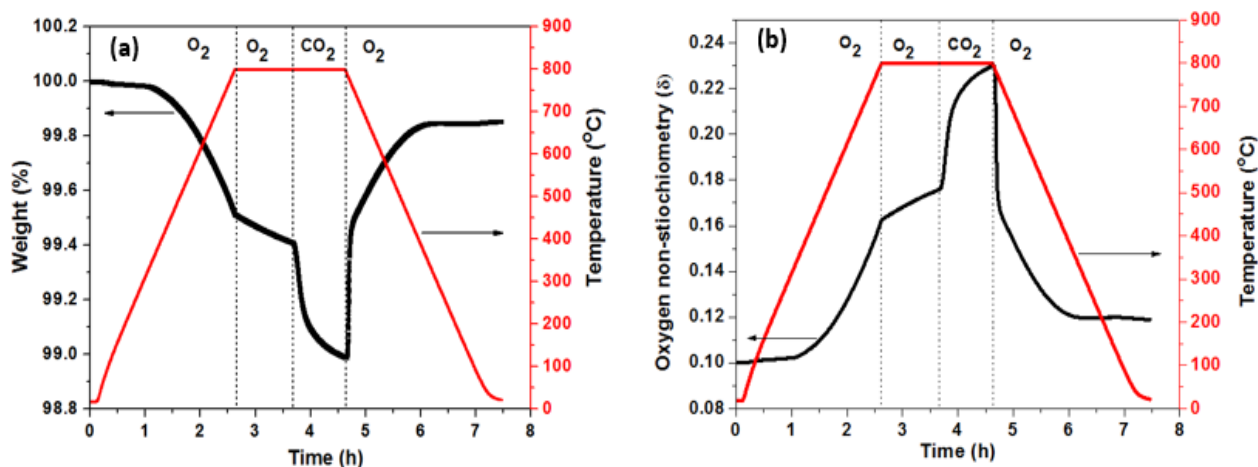


**Figure 6.4 (a) TGA profile of LSF<sub>Cr</sub> powder in 20% O<sub>2</sub> and 20% CO<sub>2</sub> (both balance He) from 30-800 °C at a 5 °C/min ramp rate and (b) plot showing oxygen non-stoichiometry ( $\delta$ ).**

To confirm whether the slight increase in sample weight (0.1%), seen in Figure 6.3b, during the TGA experiments was due to CO<sub>2</sub> adsorption on the surface of the LSF<sub>Cr</sub> or due to the minor formation of SrCO<sub>3</sub>, FTIR analysis was employed, since the XRD technique has a relatively low sensitivity and its detection limit is about 5 mol%<sup>6</sup>. FTIR analysis was employed to further confirm that no SrCO<sub>3</sub> was formed on exposure of LSF<sub>Cr</sub> to dry and 100% CO<sub>2</sub> at 800 °C. The FTIR analysis was carried out on a LSF<sub>Cr</sub> powder sample that has been exposed to dry and 100% CO<sub>2</sub> at 800 °C for 24 h.

Figure 6.5 (i) shows the FTIR spectrum for SrCO<sub>3</sub>. The band at 1471 cm<sup>-1</sup> corresponds to the asymmetric stretching mode of the C-O bond, while the sharp bands at 858 and 704 cm<sup>-1</sup> represent the in-plane and out-of-plane bending of CO<sub>3</sub><sup>2-</sup><sup>242</sup>.

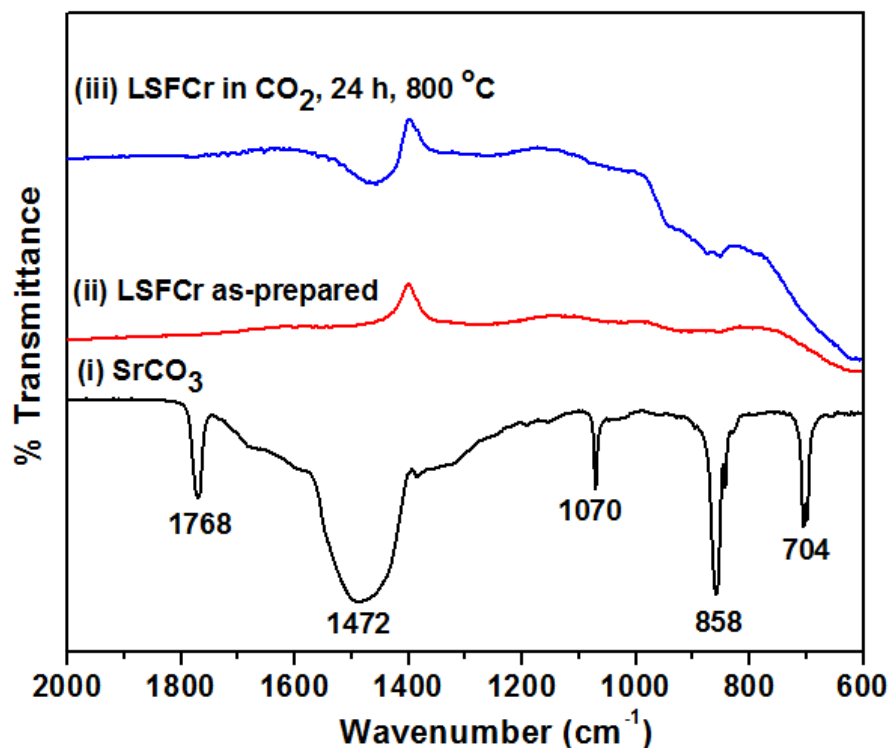


**Figure 6.5** Room temperature FTIR transmittance spectra for a homogenous mixture of dried KBr and powder samples of (i) SrCO<sub>3</sub>, (ii) as-prepared LSF<sub>Cr</sub>, and (ii) LSF<sub>Cr</sub> exposed to dry CO<sub>2</sub> from 30-800 °C with a 24 h dwell time at 800 °C. Sample (iii) was heated and cooled at a ramp rate of 5 °C/min in a dry 100 % CO<sub>2</sub> atmosphere.

From Figure 6.5, it can be seen that the bands corresponding to  $\text{SrCO}_3$  are not observed for either the as-prepared LSFCr powder or the LSFCr powder after exposure to 100%  $\text{CO}_2$  at 30-800 °C, with a 24 h dwell time at 800 °C. However, at  $1470\text{ cm}^{-1}$ , an asymmetric stretching band, corresponding to the C-O bond, is observed in Figure 6.5. This band indicates some form of interaction of LSFCr with  $\text{CO}_2$ , probably the presence of a small amount of carbonate species on the LSFCr surface.

The morphology of the LSFCr powder after exposure to pure, dry  $\text{CO}_2$  at 30-800 °C, with a 24 h dwell time at 800 °C, was also compared to the as-prepared powder. Figure 6.6 shows that the morphology of both samples is similar, with the LSFCr powder having agglomerated into bigger particles.

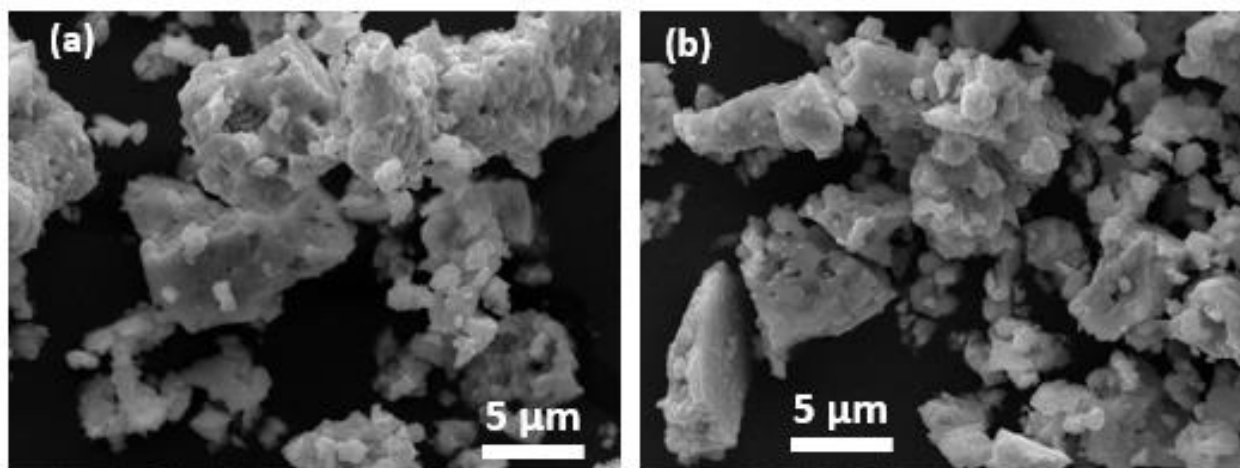


**Figure 6.6 SEM images of LSFCr powder (a) as-prepared and (b) exposed to dry  $\text{CO}_2$  from 30-800 °C with a 24 h dwell time at 800 °C. Sample (b) was heated and cooled at a ramp rate of 5 °C/min in the same gas atmosphere.**

#### 6.2.1.2 Chemical stability of LSFCr in dry $\text{CO}_2/\text{CO}$ mixtures

It has been shown that LSFCr is very stable in dry  $\text{CO}_2$  environments and remains as a single phase, with no evidence for bulk  $\text{SrCO}_3$  formation. However, the ultimate purpose of this

work is to use LSF<sub>Cr</sub> as an electrode material for both CO<sub>2</sub> reduction and CO oxidation in a RSOFC. Therefore, the stability of LSF<sub>Cr</sub> in CO<sub>2</sub>/CO mixtures is critical. To test this, the LSF<sub>Cr</sub> powder was exposed to 10 and 30 % CO (balance CO<sub>2</sub>) at 30-800 °C with a 24 h dwell time at 800 °C. The 70% CO<sub>2</sub>:30% CO mixture (pO<sub>2</sub> ~ 10<sup>-19</sup>) was investigated because its pO<sub>2</sub> is lower than 10<sup>-21</sup> atm, where LSF<sub>Cr</sub> is known to be structurally unstable<sup>46, 116</sup>.

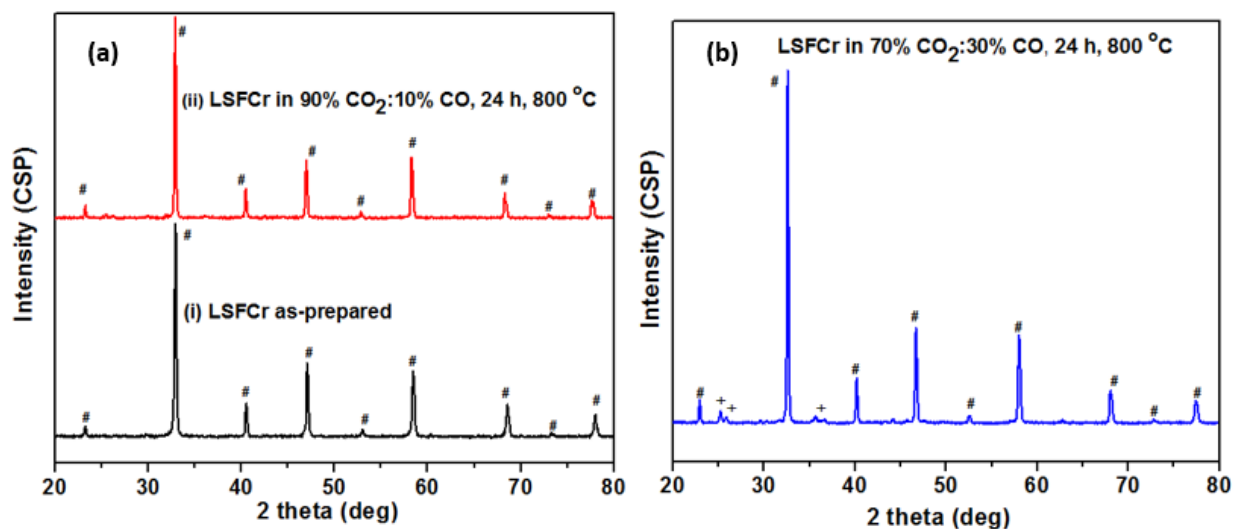


**Figure 6.7** *Ex situ* XRD patterns, showing the chemical stability of the LSF<sub>Cr</sub> powder (a) as-prepared (i), exposed to 90% CO<sub>2</sub>:10% CO<sub>2</sub> (ii), and (b) 70% CO<sub>2</sub>:30% CO atmosphere, all from 30-800 °C with a 24 h dwell time at 800 °C. All samples were heated and cooled at a ramp rate of 5 °C/min in the same gas atmosphere. The symbols used to identify the peaks are as follows: (#) LSF<sub>Cr</sub> (perovskite) and (+) SrCO<sub>3</sub>.

As shown in Figure 6.7, LSF<sub>Cr</sub> retains its perovskite phase in both 90% CO<sub>2</sub>:10% CO and 70% CO<sub>2</sub>:30% CO mixtures. However, a detailed look at Figure 6.7b, where LSF<sub>Cr</sub> was exposed to 70% CO<sub>2</sub>:30% CO, shows some extra peaks, corresponding to a SrCO<sub>3</sub>. This may indicate that LSF<sub>Cr</sub> is approaching its structural limit at pO<sub>2</sub> of 10<sup>-19</sup> atm at 800 °C. However, even though this minor impurity phase is observed to form in CO<sub>2</sub>/CO, it did not have any

negative effect on the electrochemical performance and stability of the LSFCr electrode in this gas environment, as will be shown later in this chapter.

As seen in Figure 6.8, there is very little difference in the morphology of the as-prepared powder (Figure 6.8a) and the samples exposed to 90% CO<sub>2</sub>:10% CO and 70% CO<sub>2</sub>:30% CO (Figures 6.8b and 6.8c), again indicating that no new bulk phases are formed. However, similar to what was observed in Figure 6.6, the LSFCr particles seem to have agglomerated, leading to irregular and larger particles, as can be clearly seen in Figures 6.8b and 6.8c.

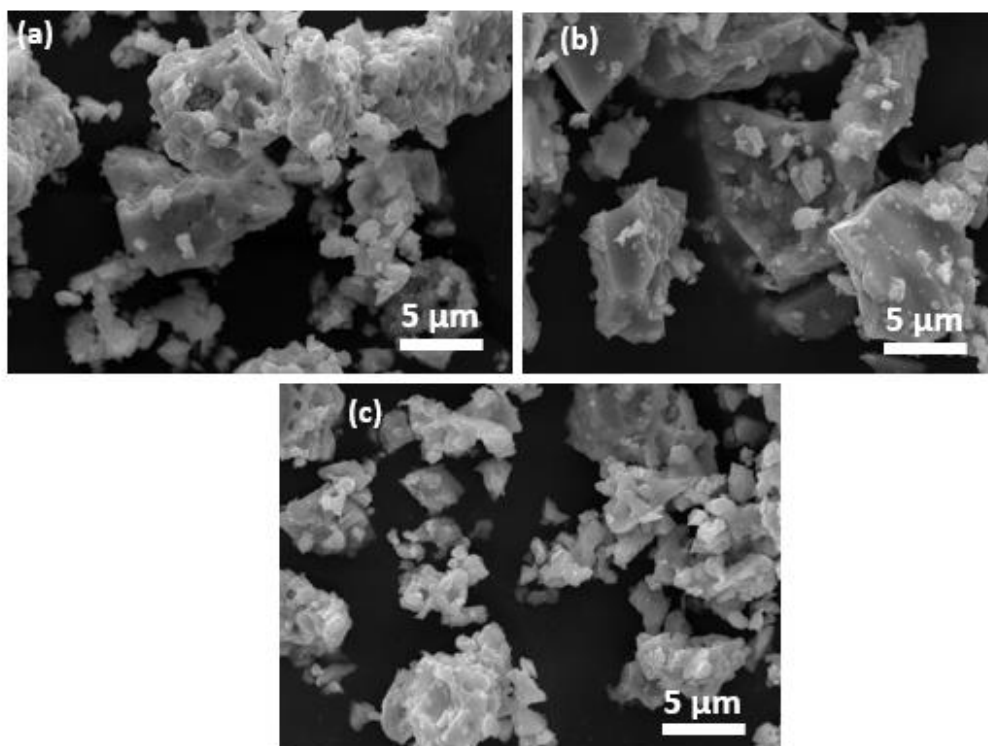


**Figure 6.8 SEM images of LSFCr powders (a) as-prepared and after exposure to (b) 10% 90% CO<sub>2</sub>:10% CO and (c) 70% CO<sub>2</sub>:30% CO, from 30-800 °C with a 24 h dwell time at 800 °C. All samples were heated and cooled at 5 °C/min in the same gas atmosphere.**

High resolution transmission electron microscopy (HRTEM) analysis was also performed on the LSFCr material and also after exposure to dry 100% CO<sub>2</sub> and 90% CO<sub>2</sub>:10% CO, all after

heating at 30-800 °C with a 24 h dwell time at 800 °C. The cation content of LSF<sub>Cr</sub>, evaluated semi-quantitatively by energy dispersive spectroscopy in more than ten single crystals, is in good agreement with the theoretical proportions of the elements in LSF<sub>Cr</sub>, indicating the high purity of the powders. High-resolution TEM micrographs, recorded along the same [001]<sub>p</sub> zone axis (Figures 6.9a-c) in the three materials, show the same microstructure, suggesting that the microstructure of LSF<sub>Cr</sub> is unaffected by CO<sub>2</sub> or CO/CO<sub>2</sub> exposure.

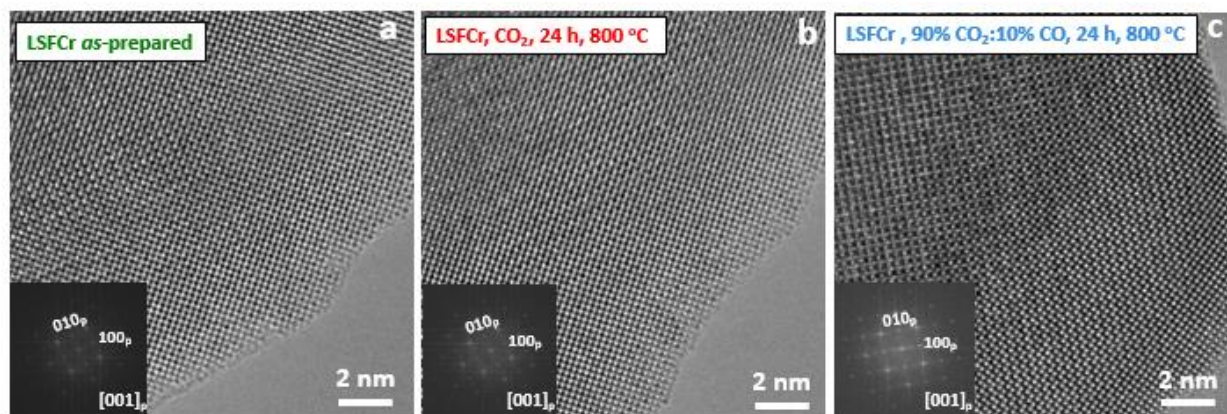


**Figure 6.9** HRTEM images recorded along [001]<sub>p</sub> zone axis (p refers to the cubic perovskite) for LSF<sub>Cr</sub> powders (a) as-prepared (b) dry and pure CO<sub>2</sub>, and (c) 90% CO<sub>2</sub>:10%CO, from 30-800 °C with a 24 h dwell time at 800 °C. All samples were heated and cooled at a ramp rate of 5 °C/min in the same gas atmosphere.

### 6.2.1.3 Chemical stability of LSF<sub>Cr</sub> in dry CO/N<sub>2</sub> mixtures

To confirm that the LSF<sub>Cr</sub> material decomposes to a LaSrFeO<sub>4</sub>-based phase (K<sub>2</sub>NiF<sub>4</sub>) and α-Fe at a pO<sub>2</sub> of  $\leq 10^{-21}$  atm, as reported in the literature when LSF<sub>Cr</sub> was exposed to dry 10% H<sub>2</sub> (balance N<sub>2</sub>) at 800 °C <sup>46</sup>, the LSF<sub>Cr</sub> powder was exposed to 10% CO and 30% CO (balance N<sub>2</sub>) at 800 °C, which corresponds to theoretical pO<sub>2</sub> values of 10<sup>-21</sup> and 10<sup>-23</sup> atm, respectively. Figures 6.10 shows that exposure of the LSF<sub>Cr</sub> powder from 30-800 °C to 10% CO:90% N<sub>2</sub>, with a 24 h holding time, and to 30% CO:70% N<sub>2</sub>, with a holding time of 6 h, all at

800 °C, partially decomposed the LSF<sub>Cr</sub> perovskite structure, forming the LaSrFeO<sub>4</sub>-based phase (K<sub>2</sub>NiF<sub>4</sub>). However, exposure of LSF<sub>Cr</sub> to 30% CO:70% N<sub>2</sub> at 800 °C for 24 h led to more conversion to the LaSrFeO<sub>4</sub>-based phase (K<sub>2</sub>NiF<sub>4</sub>) and α-Fe, as shown in Figure 6.10 (iii). The chemical stability study reported by Chen *et al.*<sup>46</sup> was performed primarily in a H<sub>2</sub>/N<sub>2</sub> atmosphere, and thus, this is the first time the stability of LSF<sub>Cr</sub> in CO (balance N<sub>2</sub>) is being reported.

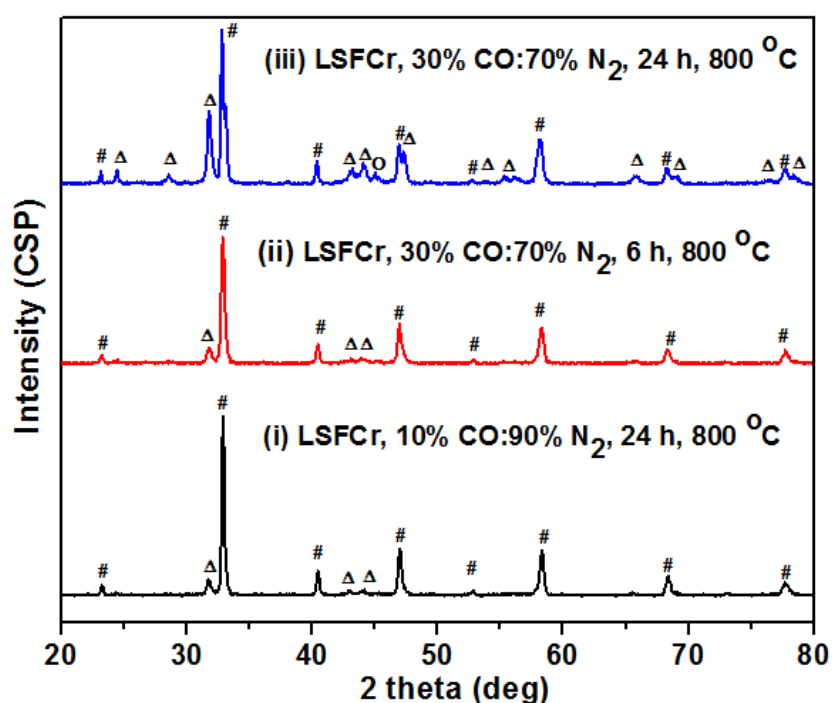


**Figure 6.10** *Ex situ* XRD patterns showing the stability of the La<sub>0.3</sub>Sr<sub>0.7</sub>Fe<sub>0.7</sub>Cr<sub>0.3</sub>O<sub>3-δ</sub> (LSF<sub>Cr</sub>) powder exposed from 30-800 °C to (i)10% CO:90% N<sub>2</sub> held for 24 h at 800 °C (ii) 30% CO:70% N<sub>2</sub> held for 6 h at 800 °C, (iii) 30% CO:70% N<sub>2</sub> held for 24 h at 800 °C. All samples were heated and cooled at a ramp rate of 5 °C/min in the same gas atmosphere. The symbols used to identify the peaks are as follows: (#) LSF<sub>Cr</sub> (perovskite); (Δ) LaSrFeO<sub>4</sub>-based phase (K<sub>2</sub>NiF<sub>4</sub>); and (O) α-Fe.

Comparing the stability of LSFCr in 30% CO:70% CO<sub>2</sub> (Figure 6.7b) and 30% CO:70% N<sub>2</sub> (Figure 6.10 (iii)) at 800 °C using a 24 h dwell time reveals that the LSFCr powder retains most of its perovskite phase in 30% CO:70% CO<sub>2</sub> (pO<sub>2</sub> ~10<sup>-19</sup> atm) atmosphere, with only minor secondary phases formed. In comparison, in 30% CO:70% N<sub>2</sub> (Figure 6.10(iii)), with a pO<sub>2</sub> of about 10<sup>-23</sup> atm at 800 °C, it decomposes to the LaSrFeO<sub>4</sub>-based phase (K<sub>2</sub>NiF<sub>4</sub>) and α-Fe.

However, Figure 6.11 shows that re-exposure of the LSFCr powder from 30-800 °C to air, with a 24 h holding time at 800 °C after the CO/N<sub>2</sub> exposure study, converts the LaSrFeO<sub>4</sub>-based phase (K<sub>2</sub>NiF<sub>4</sub>) back to the perovskite phase, with only minor impurities observed. This is in agreement with what has been reported previously for LSFCr decomposition in dry H<sub>2</sub> at 800 °C and its ability to regenerate fully in air to its initial perovskite form<sup>46</sup>.

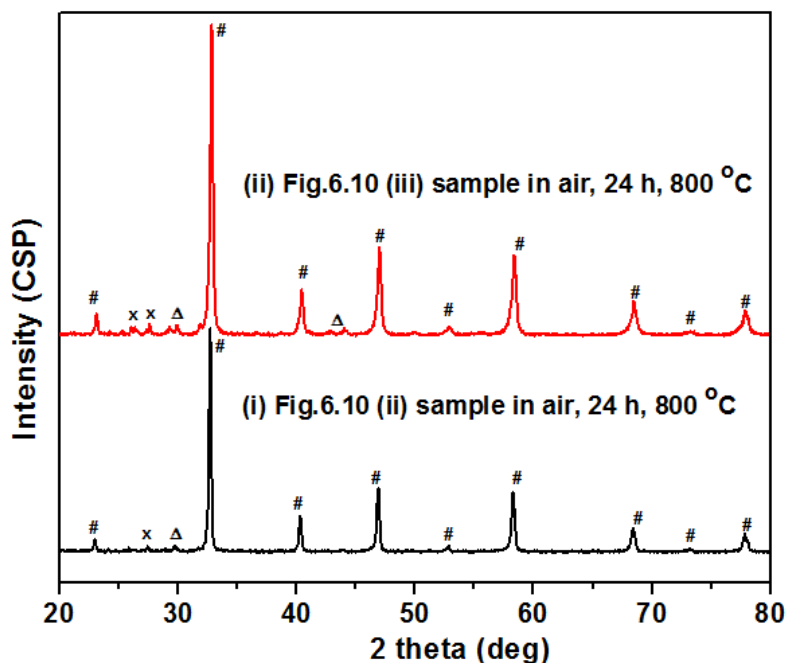


**Figure 6.11** *Ex situ* XRD patterns showing the re-exposure of decomposed (i) Fig. 6.10 (ii) and (ii) Fig.6.10 (iii) LSFCr samples to air from 30-800 °C, with 24 h holding time at 800 °C. All samples were heated and cooled at a ramp rate of 5 °C/min in the air atmosphere. The symbols used to identify the peaks are as follows: (#) LSFCr (perovskite); (Δ) LaSrFeO<sub>4</sub>-based phase (K<sub>2</sub>NiF<sub>4</sub>); and (x) impurities.

SEM-EDX analysis was carried out on the powder after exposure to CO/N<sub>2</sub> to determine if the decomposed species (LaSrFeO<sub>4</sub>-based phase and  $\alpha$ -Fe) could catalyze the Boudouard reaction ( $2\text{CO} = \text{C} + \text{CO}_2$ ), leading to the formation of carbon. The SEM images in Figure 6.12 shows a different morphology than what was seen in Figures 6.6 and 6.8. The images show that a carbon-like structure has been formed, especially on samples exposed to 30% CO:70% N<sub>2</sub> at 800 °C for at 6 h and 24 h, respectively (Figures 6.12b and 6.12c). However, as shown in Figure 6.12d, when the LSF<sub>Cr</sub> sample was exposed to air for 24 h at 800 °C, carbon is removed (as CO<sub>2</sub>) and the same morphology as seen for the as-prepared sample is observed.

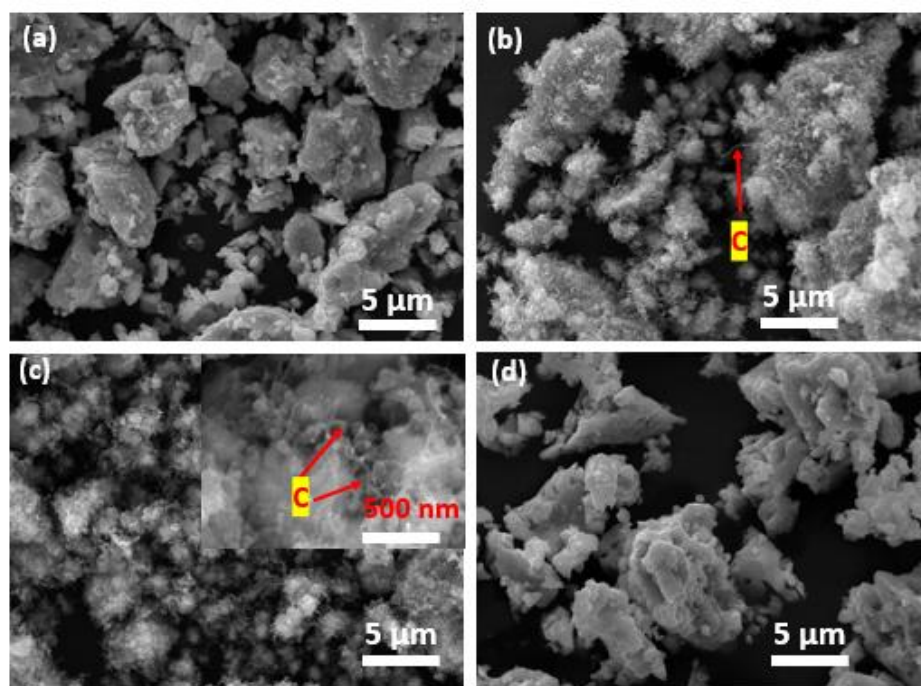


**Figure 6.12** SEM images of LSF<sub>Cr</sub> powder exposed to (a) 10% CO:90% N<sub>2</sub> for 24 h at 800 °C, (b) 30% CO:70% N<sub>2</sub> for 6 h at 800 °C, (c) 30% CO:70% N<sub>2</sub> for 24 h at 800 °C, and (d) exposure of the Fig. 6.12b sample to air for 24 h at 800 °C. All samples were heated and cooled at a ramp rate of 5 °C/min in the same gas atmosphere.

To semi-quantify the amount of coke formed, EDX analysis was carried out. Figure 6.13 shows a SEM image of the LSF<sub>Cr</sub> powder after exposure to 30% CO:70% N<sub>2</sub> for 6 h at 800 °C,

showing the regions where the EDX analyses were performed. The weight and atomic percentages of La, Sr, Fe, Cr and C obtained are shown in Table 6.1. Comparing the elemental content of LSFCr powder exposed to 30% CO:70% N<sub>2</sub> to the as-prepared LSFCr powder, it is seen from Table 6.1 that the weight percent (wt. %) and atomic (at. %) of carbon are higher in all four regions examined than seen for the as-prepared sample. The at. % of C in LSFCr after exposure to 30% CO:70% N<sub>2</sub> ranges from 75-93%, compared to 33% for the as-prepared sample. The 33 at.% carbon obtained for the as-prepared sample is probably due to contamination of the sample by adventitious carbon<sup>243</sup>.

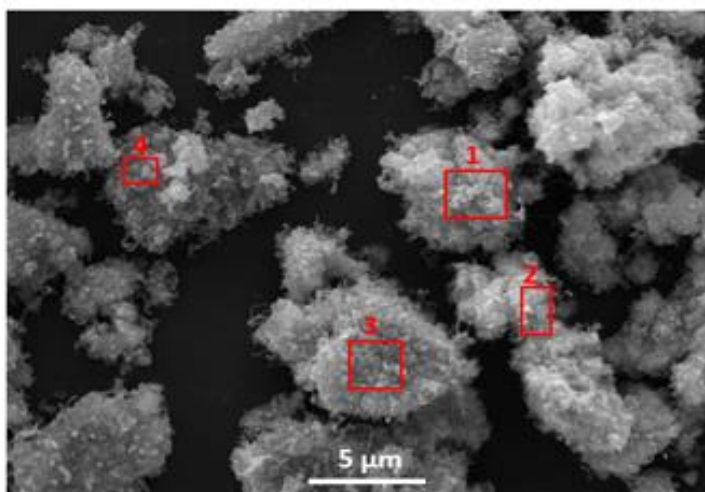


**Figure 6.13 SEM image of LSFCr powder exposed to 30% CO:70% N<sub>2</sub> held for 6 h at 800 °C showing the four regions analyzed by EDX.**

However, the high 75-93 at. % of carbon observed for the 30% CO:70% N<sub>2</sub> LSFCr samples clearly indicates that the structures seen in the SEM images (Figures 6.12 and 6.13) are likely carbon. Thermodynamically, the Boudouard reaction is only favorable at < 700 °C. However, since the samples were ramped from 30-800 °C in CO/N<sub>2</sub>, held for either 6 h or 24 h at

800 °C, and then cooled in the same atmosphere, it is likely that the observed carbon deposition is due to both gas phase and catalytic disproportionation of CO to C.

**Table 6.1 Elemental content from SEM-EDX analysis of the various regions of the SEM image in Figure 6.13 for LSF<sub>Cr</sub>, exposed to 30% CO:70% N<sub>2</sub> for 6 h at 800 °C.**

Region analyzed	La		Sr		Fe		Cr		C	
	wt. %	at. %								
1	19	3.8	24	7.8	19	9.6	6.1	3.3	32	76
2	13	1.8	16	3.7	14	4.8	4.2	1.6	53	88
3	19	3.7	24	7.6	17	8.5	5.5	2.9	34	77
4	2.5	0.30	6.5	1.2	17	4.8	2.8	0.90	71	93
As-prepared LSF <sub>Cr</sub>	30	13	31	21	24	25	9.0	10	6.4	31

There are limited studies in the literature showing the chemical stability of perovskite electrodes in CO and the possible formation of carbon. A Raman spectroscopy study by Su *et al.* showed that exposure of La<sub>0.8</sub>Sr<sub>0.2</sub>Sc<sub>0.2</sub>Mn<sub>0.8</sub>O<sub>3</sub> (LSSM) powder to CO for 5 h at 600, 850 and 900 °C did not result in any carbon deposition<sup>244</sup>. However, this study showed electrochemical degradation of a LSSM-based electrode, operated in pure CO at 850 °C. This is due to the structural instability of LSSM at such a low pO<sub>2</sub>, since the structural stability limit of LSSM is at a pO<sub>2</sub> of 10<sup>-18</sup> atm<sup>244</sup>.

### **6.2.2 Electrochemical performance of LSF<sub>Cr</sub> in CO<sub>2</sub> and CO<sub>2</sub>/CO atmospheres**

This section of Chapter 6 is focussed primarily on determining the electrochemical activity and stability of LSF<sub>Cr</sub> as a fuel electrode in various CO<sub>2</sub>/CO mixtures, using cyclic voltammetry (CV), potentiostatic/galvanostatic methods, and electrochemical impedance spectroscopy (EIS). The work was carried out using a LSF<sub>Cr</sub>/GDC/YSZ/GDC/LSF<sub>Cr</sub>

symmetrical full cell (see Section 3.2.2.1 for details of cell fabrication) during CO<sub>2</sub> reduction and CO oxidation at 600-850 °C. The fuel electrode was fed with variable CO<sub>2</sub> (10-100% CO<sub>2</sub> (balance N<sub>2</sub>)) or 50-90 % CO<sub>2</sub>:10-50% CO gas mixtures, while the oxygen electrode was fed with air.

A cross-sectional SEM image of a typical LSFCr/GDC/YSZ/GDC/LSFCr cell, used in this section of the work (see Section 3.2.2.1 for details of cell fabrication) and after electrochemical testing in CO<sub>2</sub>/CO atmospheres, is shown in Figure 6.14. The image shows that there is no sign of delamination of the electrodes from the electrolyte, with the fuel and oxygen electrodes, both LSFCr, being ca. 30 μm in thickness. As can be seen from Figure 6.14, a porous GDC buffer layer, ca. 10 μm in thickness, was used to prevent inter-diffusion between the YSZ electrolyte and the LSFCr electrodes<sup>125, 126</sup>.

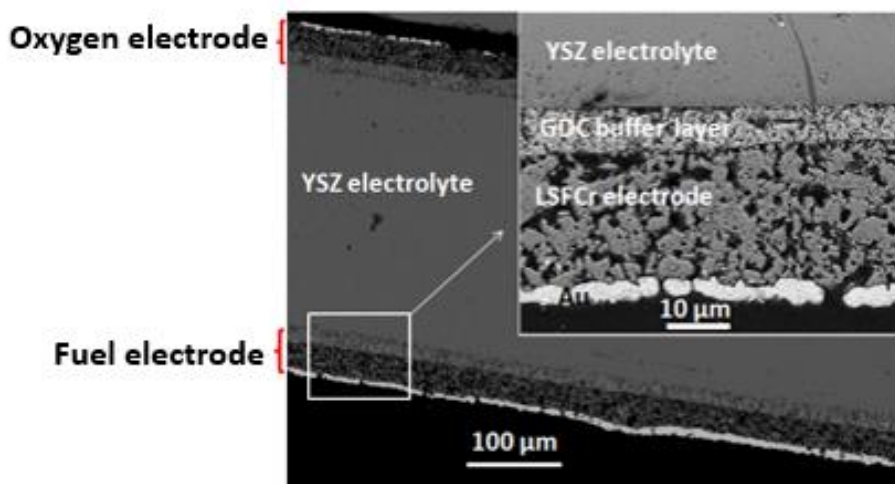


**Figure 6.14** A cross-sectional SEM image of the LSFCr/GDC/YSZ/GDC/LSFCr symmetrical RSOFC under study here, showing the fuel electrode and the oxygen electrode after electrochemical cell testing in CO<sub>2</sub>/CO atmospheres. Inset shows a higher magnification image of the fuel electrode of the cell.

It should also be noted, that in this chapter (Section 6.2.2), the cyclic voltammetry (CV) data have been plotted with potential (V) on the y axis and current density (i) on the x-axis, instead of the more conventional format used in the other chapters of this thesis and in the general electrochemical literature. However, the format used here is commonly found in the RSOFC literature and may be intended to have the appearance of standard fuel cell performance plots. Also, none of the CV data have been  $iR$  corrected in this part of the work, thus allowing a better comparison with the data reported for other cells in the literature.

Furthermore, in these full cell studies, the OCP is ca. 0.8 V to 1.0 V in the CO<sub>2</sub>/CO mixtures and roughly 0.2 V to 0.4 V in pure CO<sub>2</sub> at the fuel electrode. The convention in this chapter (Section 6.2.2), is to use negative sign as a reminder that the reactions are being studied in the non-spontaneous direction (SOEC mode). For example, when OCP is ca. 1.0, applying -0.3 V vs. the OCP (SOEC mode) implies that the cell voltage is at 1.3 V (or 0.3 V overpotential above OCP), while applying 0.3 V vs. the OCP (SOFC mode) implies that the cell voltage is at 0.7 (or 0.3 V below OCP).

#### 6.2.2.1 Performance of LSF<sub>Cr</sub>-based RSOFC cell in dry CO<sub>2</sub> (balance N<sub>2</sub>)

Figure 6.15 shows the impedance data obtained from a symmetrical LSF<sub>Cr</sub>-based full cell operated at 800 °C, with 100%, dry CO<sub>2</sub> fed to the fuel electrode and air fed to the oxygen electrode. Pure CO<sub>2</sub> without CO was evaluated first to better understand the processes associated with the fuel and oxygen electrodes. The CO<sub>2</sub> fed to the fuel electrode is expected to reduce to CO and O<sup>2-</sup> (Chapter 2, Reaction 2.3), with the O<sup>2-</sup> transported through the YSZ electrolyte to the oxygen electrode, where O<sub>2</sub> gas is released (Chapter 2, Reaction 2.1). Therefore, the measured

performance of the cell is a reflection of the combination of the reactions at both the fuel and oxygen electrodes, as discussed also in Chapter 5.

The Nyquist plot in Figure 6.15a in pure CO<sub>2</sub> shows an incomplete semi-circle at both the open circuit potential (OCP, 0.2 V) and -0.3 V vs. the OCP (at a cell voltage of 0.5 V), respectively. This is expected, as there is only a small amount of CO generated under these conditions (pure CO<sub>2</sub>, 0.5 V). As the cell is polarized more negatively away from the OCP at -0.7 V vs. the OCP (at an operating potential of the cell of 0.9 V), a complete semi-circle was observed. This is because operating the cell at 0.9 V leads to the electrolysis of CO<sub>2</sub> to CO and O<sub>2</sub>.

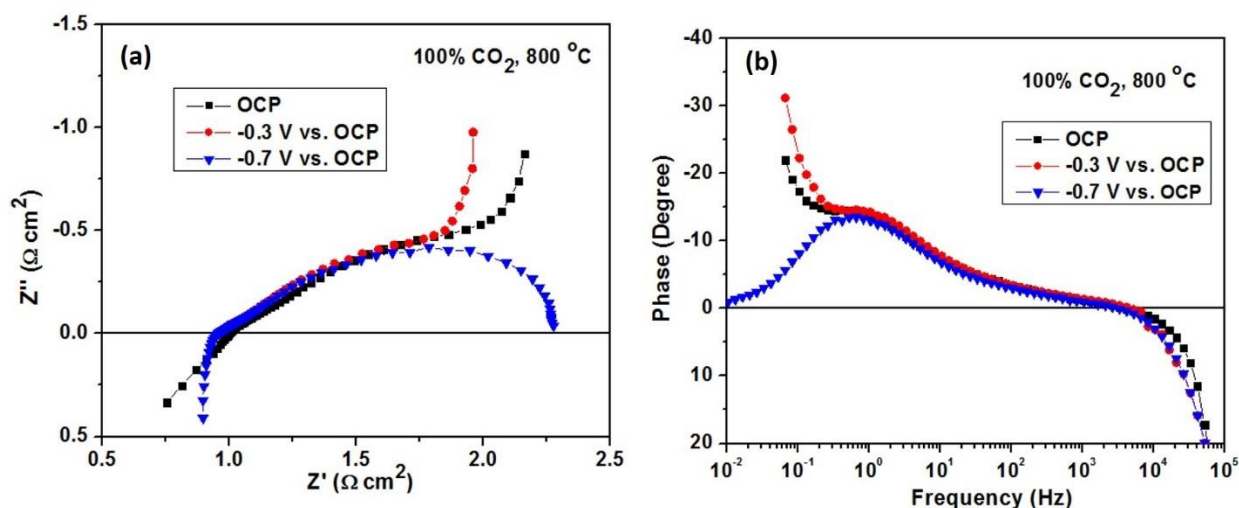


**Figure 6.15** OCP and polarized impedance data for symmetrical RSOFC with a configuration of LSFCr/GDC/YSZ/GDC/LSFCr, operated at 800 °C and showing (a) the Nyquist plot and (b) the phase angle Bode plot, in 100%, dry CO<sub>2</sub> at the fuel electrode and with air exposure at the oxygen electrode.

From Figure 6.15b, the Bode plot at -0.7 V vs. the OCP (i.e., at a cell operating potential of 0.9 V) shows that the performance of the cell is dominated by the low frequency arc, which has a ca. 1 Hz summit frequency. As discussed in Chapter 5, this low frequency arc observed for

the 2-electrode LMFCr-based full cell can be ascribed to the processes occurring at the fuel electrode (CO<sub>2</sub> reduction/CO oxidation), while the high frequency arc (at ca. 100 Hz) represents the oxygen reduction or evolution reactions occurring at the oxygen electrode.

Figure 6.16 shows the cyclic voltammograms (CV) of the LSFCr-based full cell at 850-750 °C, with varying amounts of CO<sub>2</sub> fed to the fuel electrode and air fed to the oxygen electrode. From Figure 6.16, the apparent onset potential for CO<sub>2</sub> reduction at 800 °C is ca. -0.8 V in the dry 100% CO<sub>2</sub>, 50% CO<sub>2</sub>:50% N<sub>2</sub>, and 10 % CO<sub>2</sub>:90% N<sub>2</sub> gas mixtures. At the apparent onset potential, there is enough CO generated by the cell to move the Nernst potential to a value consistent with a CO<sub>2</sub>/CO mixture.

It is seen in Figure 6.16 that, when the cell is fed with 10% CO<sub>2</sub> (balance N<sub>2</sub>) at the fuel electrode and air at the oxygen electrode, the current is reactant concentration limited (showing a plateau current) at more negative potentials. In both 50 and 100 % CO<sub>2</sub>, the cell shows a higher performance during the electrolysis phase. Thus, at 1.5 V, current densities of -0.4 A/cm<sup>2</sup> and 0.38 A/cm<sup>2</sup> were obtained in 100% and 50% CO<sub>2</sub>, respectively. The observed performance of the LSFCr full cell in Figure 6.16 is higher than has been reported for other types of perovskite-based full cells in the literature. For example, Xu *et al.*<sup>100</sup> investigated a LSCM-SDC/YSZ/LSCM-SDC cell in 100% CO<sub>2</sub> at 800 °C, giving a 0.1 A/cm<sup>2</sup> current density at 1.5 V.

Figure 6.16b shows the electrolysis of 100 % CO<sub>2</sub> when the cell was operated at 750, 800, and 850 °C. At a potential of 1.5 V, the current density increased from 0.2 A/cm<sup>2</sup> to 0.65 A/cm<sup>2</sup> as the temperature was increased from 750 to 850 °C, as expected.

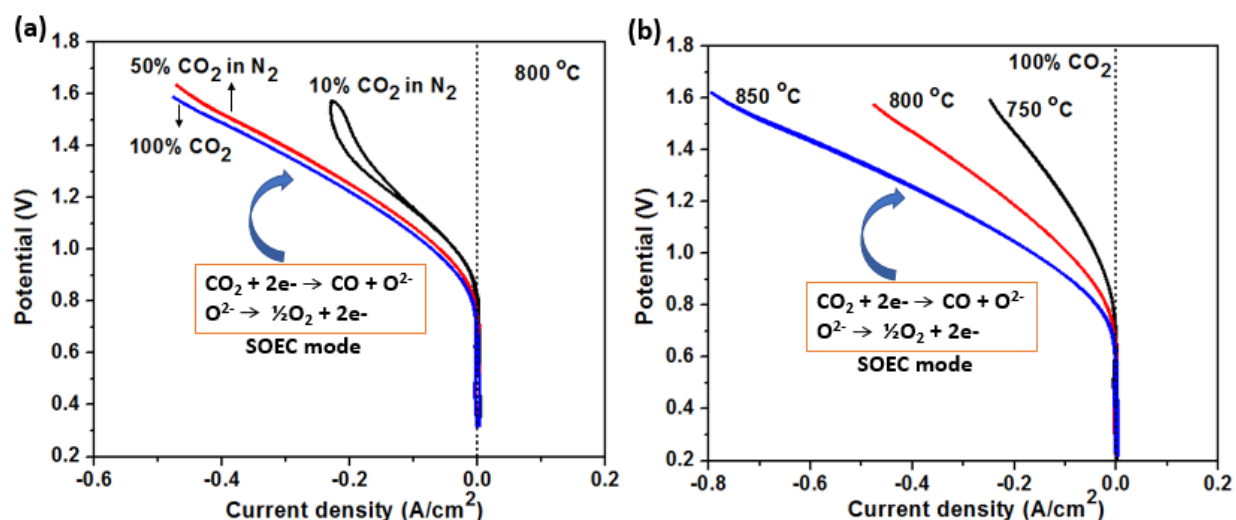


**Figure 6.16** CV of the symmetrical LSFCr/GDC/YSZ/GDC/LSFCr full cell showing (a) the response in dry 100% CO<sub>2</sub>, 50% CO<sub>2</sub>:50% N<sub>2</sub>, and 10 % CO<sub>2</sub>:90% N<sub>2</sub> gas mixtures fed to the fuel electrode and with air exposure at the oxygen electrode at 800 °C, and (b) temperature studies of 100% CO<sub>2</sub> fed to the fuel electrode at 850, 800 and 750 °C and with air exposure at the oxygen electrode.

#### 6.2.2.2 Performance of LSFCr RSOFC cell in dry CO<sub>2</sub>/CO gas mixtures

In Section 6.2.2.1, it was shown that the LSFCr-based 2-electrode full cell can be operated in only CO<sub>2</sub> environments, although the performance is quite variable as the potential at the CO<sub>2</sub>/CO electrode is not fixed (or pinned). Therefore, to investigate the electrochemical performance of the LSFCr cell when operated in both the SOEC (CO<sub>2</sub> electrolysis) and SOFC (CO oxidation) modes, CO<sub>2</sub>/CO mixtures were fed to the fuel electrode and air to the oxygen electrode all at 600-800 °C (Figure 6.17). The Nyquist plots in Figure 6.17a were fitted to the same  $R_s(R1CPE1)(R2CPE2)$  equivalent circuit model as used in Chapter 5 (Figure 5.1c) for the full cell tested in humidified H<sub>2</sub>/N<sub>2</sub> environments. An example of the good fits obtained of the EIS data to the selected equivalent circuit is shown in Figure 6.17a, giving a chi-squared value of  $< 10^{-4}$ . It should be noted that all of the fits of the impedance data shown in this chapter gave

similarly low chi-squared values. Again, the series inductor, sometimes seen at high frequencies, was excluded. Similar to the impedance data obtained for the LCFCr symmetrical full cell in Chapter 5 (Figure 5.1), the high frequency (100 Hz) arc (R1CPE1) is related primarily to the processes occurring at the oxygen electrode and the low frequency (1 Hz) arc (R2CPE2) is dominated by the processes occurring at the fuel electrode.

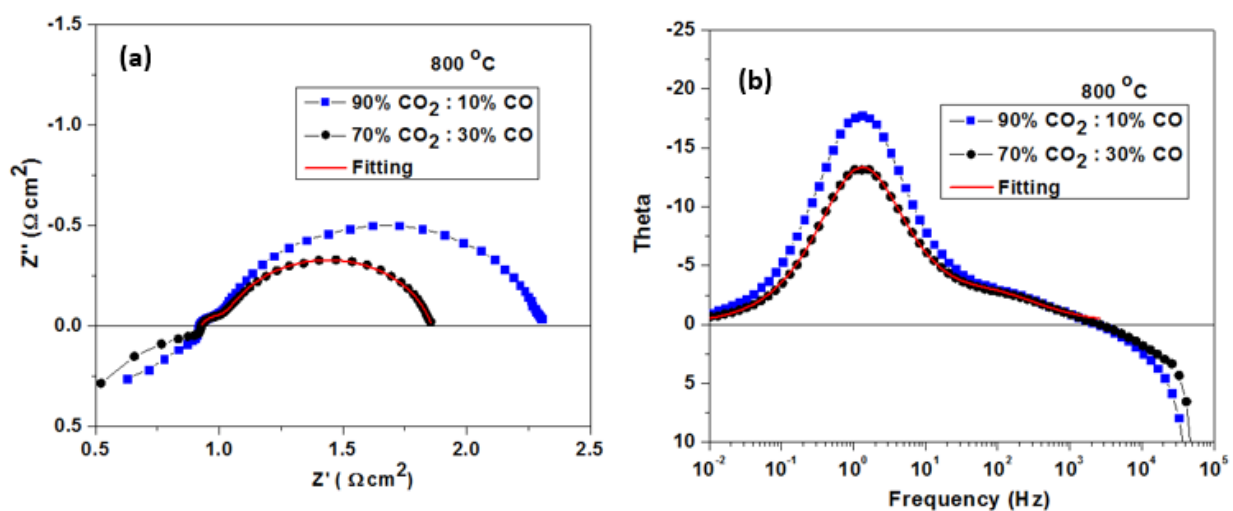


**Figure 6.17** OCP impedance data for symmetrical RSOFC with a configuration of LSFcr/GDC/YSZ/GDC/LSFcr, operated at 800 °C, and showing (a) the Nyquist and (b) the Bode plots, all in 90% CO<sub>2</sub>:10% CO and 70% CO<sub>2</sub>:30% CO gas mixtures at the fuel electrode and with air exposure at the oxygen electrode.

As seen in Figure 6.17a, the polarization resistance ( $R_p$ ), related to the reactions at both the fuel and air sides of the cell, decreases from 1.3  $\Omega \text{ cm}^2$  in 90% CO<sub>2</sub>:10% CO gas composition to 0.94  $\Omega \text{ cm}^2$  in 70% CO<sub>2</sub>:30% CO. It is important to note that these  $R_p$  values at 800 °C in the various CO/CO<sub>2</sub> gas compositions studied here are more than 100 times lower than the  $R_p$  of ca. 500  $\Omega \text{ cm}^2$  reported by Sapountzi *et al.*<sup>245</sup> for a La<sub>0.75</sub>Sr<sub>0.25</sub>Cr<sub>0.9</sub>Fe<sub>0.1</sub>O<sub>3- $\delta$</sub>  fuel electrode, operated in 90% CO:10% CO<sub>2</sub> at 800 °C. Also seen in Figure 6.17a is that the series resistance ( $R_s$ ) of 0.92  $\Omega \text{ cm}^2$  remained unchanged as the CO<sub>2</sub>/CO ratio was varied in this work, as expected. The

capacitance of the low frequency arc is usually attributed to changes in the oxygen non-stoichiometry (chemical capacitance) of mixed conducting oxides, such as LSFCr, during air perturbation<sup>246, 247</sup>.

Figure 6.18a shows the CVs of the LSFCr-based full cell operated with either 90% CO<sub>2</sub>:10% CO or 70% CO<sub>2</sub>:30% CO fed to the fuel electrode. The open circuit potential (OCP), obtained for the LSFCr-based full cell at 800 °C, was 0.85 and 0.91 V, respectively, in these two gases, corresponding to a pO<sub>2</sub> of 10<sup>-17</sup> and 10<sup>-18</sup> atm, respectively, calculated from Equation 6.3. Considering that the structural stability limit of LSFCr is at a pO<sub>2</sub> ≤ 10<sup>-21</sup> atm at 800 °C<sup>46</sup>, the LSFCr material, as shown in Figures 6.7 and 6.9, should be structurally stable in this CO<sub>2</sub>/CO atmospheres.

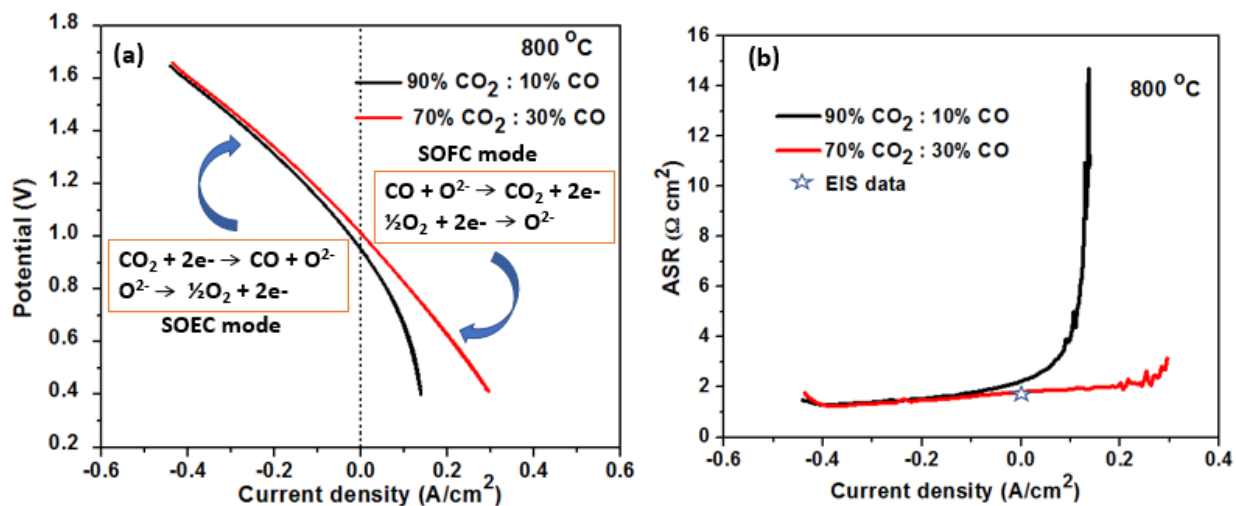


**Figure 6.18** CV data obtained from symmetrical full cell with a configuration of LSFCr/GDC/YSZ/GDC/LSFCr, operated at 800 °C, showing (a) the CV plots acquired at 1 mV/s scan rate, and (b) the ASR-i plots (derived from the CV data in (a)), all in 90% CO<sub>2</sub>:10% CO and 70% CO<sub>2</sub>:30% CO gas mixtures at the fuel electrode and with air exposure at the oxygen electrode.

In the SOEC mode, the CVs (Figure 6.18a) show that, at a cell voltage of 1.5 V, the current density for the reduction of 90% CO<sub>2</sub>:10% CO and 70% CO<sub>2</sub>:30% CO gas mixtures is -0.41 and -0.39 A/cm<sup>2</sup>, respectively. Figure 6.18a also shows that, in the SOFC mode, an increase in the CO content from 10% to 30% leads to an increase in the electrochemical performance.

It should be noted that the magnitude of the current densities observed in Figure 6.18a for this LSFcr-based cell in 90-70% CO<sub>2</sub> (balance CO) at 800 °C is very promising and better than what has been observed in other studies using mixed conducting oxide electrodes. For example, Yue *et al.*<sup>103</sup>, who examined the electrolysis of CO<sub>2</sub> at a LSCM-GDC cathode in 90% CO<sub>2</sub>:10% CO at 900 °C, obtained a current density of 0.28 A/cm<sup>2</sup> at 1.5 V. In the study reported by Yue *et al.*<sup>103</sup>, a doped-ceria phase was added to the LSCM material to improve its performance towards CO<sub>2</sub> electrolysis. However, the excellent performance of the LSFcr fuel electrode, under study here, towards the CO<sub>2</sub>/CO reactions was achieved without the addition of doped ceria phase.

To better understand the total area specific resistance (ASR) associated with the cell when operated in either the fuel cell or electrolysis mode, the CVs, shown in Figure 6.18a, were differentiated to give the ASR ( $ASR = dE/di$ ) of the cell. This also allowed a comparison between the ASR value obtained from the CV studies and EIS ( $ASR = R_s + R_p$ ) data, shown in Figure 6.17. As seen in Figure 6.18b, there is good agreement between the total ASR obtained from both techniques. Also, the ASR-i plot shows that, at higher negative current densities, there is little change in the ASR even as the amount of CO<sub>2</sub> present in the input gas stream was varied. In the SOFC mode, the ASR decreases with the introduction of CO, as expected.

The performance of the LSFcr-based full cell, operated on 70% CO<sub>2</sub>:30% CO composition at varying temperatures, was also investigated. Figure 6.19 shows that the cell performs better in both the SOEC and SOFC modes with increasing temperature, as expected.

The corresponding impedance results are shown in Figures 6.20a-c. From the Nyquist plot (Figure 6.20a-b), the series resistance ( $R_s$ ) is seen to increase with temperature because the conductivity of YSZ decreases with temperature.

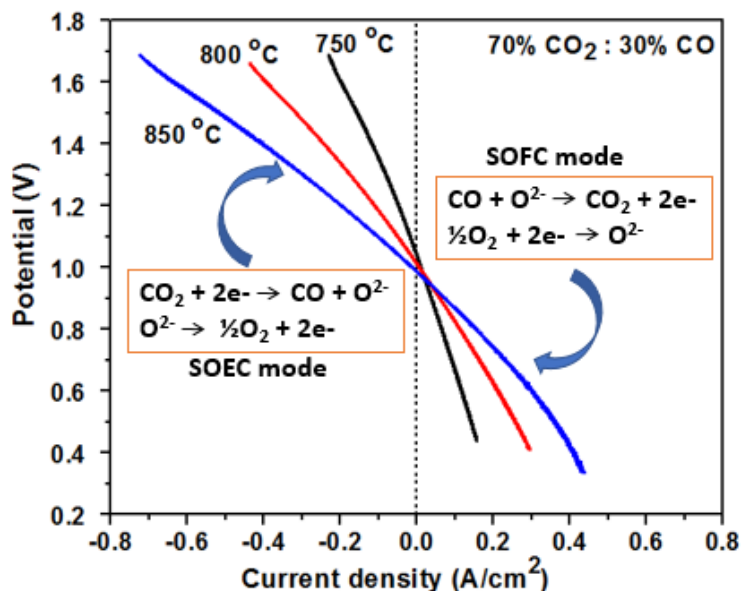


**Figure 6.19** CVs (acquired at 1 mV/s) of the symmetrical LSF-Cr full cell, showing temperature studies at 850, 800 and 750 °C for 70% CO<sub>2</sub>:30% CO fed to the fuel electrode and air exposure to the oxygen electrode.

Furthermore, Figures 6.20a and 6.20b show that  $R_p$  increases from 0.51  $\Omega \text{ cm}^2$  at 850 °C to 38  $\Omega \text{ cm}^2$  at 600 °C. Figure 6.20d shows the Arrhenius plot for the various resistances obtained from the fitting of the Nyquist plots shown in Figures 6.20a and 6.20b to a  $R_s(R1CPE1)(R2CPE2)$  equivalent circuit (Figure 5.1c). As discussed earlier and verified in Chapter 5, the high frequency arc ( $R1CPE1$ , ca. 100 Hz) is related to the processes occurring at the oxygen electrode, while the low frequency arc ( $R2CPE2$ , ca. 1 Hz) is assigned to the CO<sub>2</sub>/CO reactions at the fuel electrode.

The activation energy ( $E_a$ ) obtained for the series resistance ( $R_s$ ) is 88 kJ/mol. This value is in good agreement with the activation energy values (85-97 kJ/mol) reported for oxide ion conduction in the YSZ (yttria-stabilized zirconia) electrolyte<sup>248-250</sup>. The  $E_a$  value for the polarization resistance ( $R_p$ ) is 145 kJ/mol, which is a little higher than that reported by Yue *et al.*<sup>102</sup> in the same gas composition for a LSCM-GDC electrode. The high frequency resistance ( $R_1$ ) shows an  $E_a$  of 105 kJ/mol, while that of low frequency resistance ( $R_2$ ) is 143 kJ/mol. The low  $E_a$  value obtained for  $R_1$ , which represents the processes occurring at the oxygen electrode, confirms what has been reported by others and in Chapter 5, showing that the LSFCr material is more active as an oxygen electrode than as a fuel electrode<sup>46</sup>.

The low frequency resistance ( $R_2$ ) also exhibits a strong temperature dependence, which argues against rate limitations due to gas convection or diffusion processes, while the low frequency capacitance ( $C_2$ ) is related to changes in the oxygen non-stoichiometry of the perovskite material<sup>246, 247</sup>. The calculated low frequency capacitance ( $C_2$ ), using Equation 4.3, decreases from 0.34 F/cm<sup>2</sup> at 850 °C to 0.043 F/cm<sup>2</sup> at 600 °C. This probably reflects the changing chemical capacitance properties of LSFCr due to the formation of more oxygen vacancies at higher temperatures, compared to at 600 °C. Even though Chapter 5 did not focus on the chemical capacitance behaviour of LSFCr in humidified H<sub>2</sub> atmosphere, a similar trend is expected.

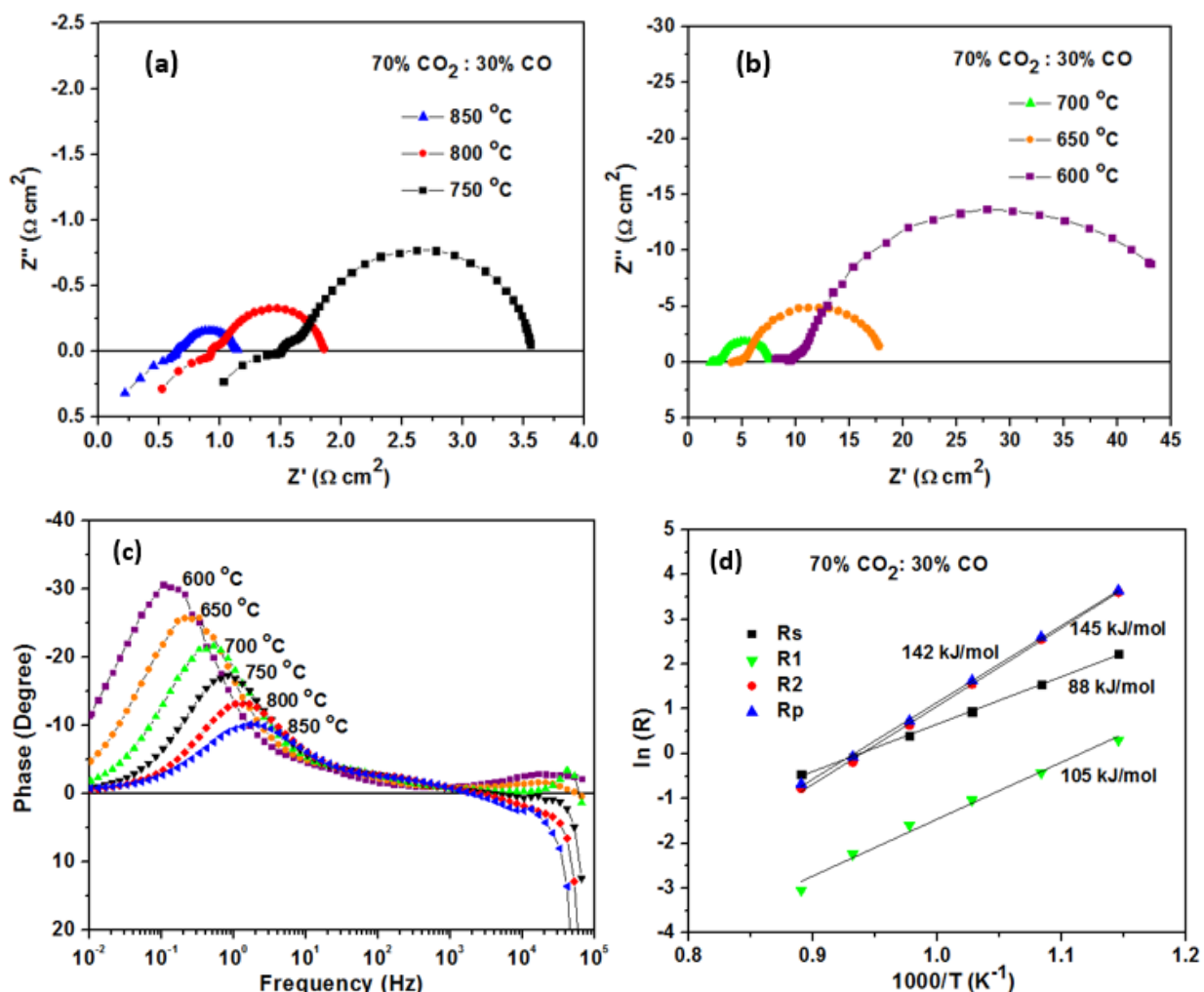


**Figure 6.20** Temperature studies of the LSFcr/GDC/YSZ/GDC/LSFCr cell operated at 600-800 °C, showing (a) OCP EIS Nyquist response at 750-850 °C (b) OCP EIS Nyquist response at 600-700 °C, (c) phase angle Bode plot, and (d) activation energy plot of the EIS determined resistances, all in 70% CO<sub>2</sub>:30% CO gas mixture at the fuel electrode and air at the oxygen electrode.

To confirm that the contribution of the oxygen reduction (ORR) and evolution (OER) reactions to the observed  $R_p$  is seen at high frequencies ( $R_1$ ) in the 2-electrode full cell experiments, a 2-electrode half cell study was carried out in air at 800 °C, with LSFcr present on both sides of the cell and with  $R_p$  thus being entirely due to the oxygen reaction. It is seen in

Figure 6.21 that the  $R_p$  of this cell, operated in air, is only  $0.25 \Omega \text{ cm}^2$  for each electrode. This further confirms that LSF<sub>Cr</sub> is more active as an air electrode than as a fuel electrode, in agreement with what has been reported previously<sup>46, 251</sup> where a symmetrical LSF<sub>Cr</sub> cell, operated at  $800 \text{ }^\circ\text{C}$  in air with either an LSGM or YSZ electrolyte, showed a  $R_p$  of 0.10 or  $0.30 \Omega \text{ cm}^2$  per electrode, respectively.

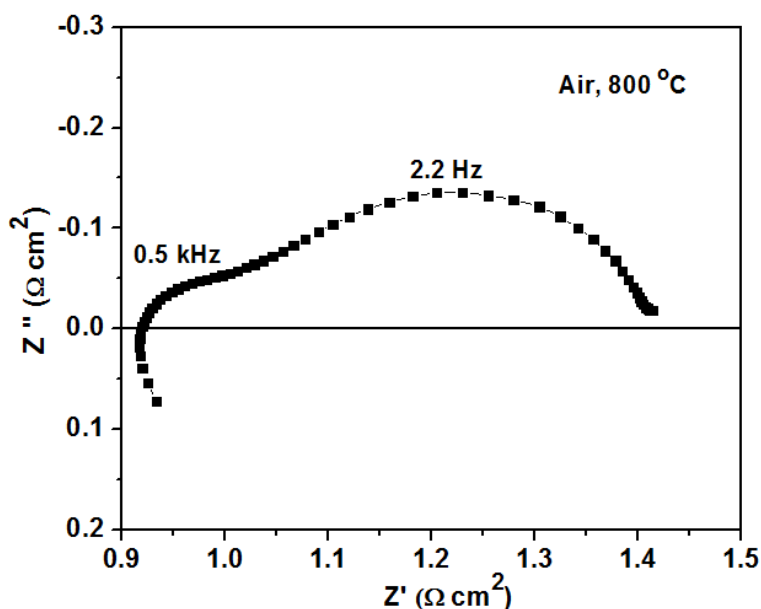


**Figure 6.21 Impedance response (at the open circuit potential) of a symmetrical LSF<sub>Cr</sub> half cell tested in air at  $800 \text{ }^\circ\text{C}$ , showing total  $R_p$  of  $0.50 \Omega \text{ cm}^2$  for both electrodes.**

It is therefore clear that the reactions occurring at the fuel electrode provide the dominant contribution to the measured  $R_p$  in Figure 6.17a, being  $1.1 \Omega \text{ cm}^2$  and  $0.69 \Omega \text{ cm}^2$  for the 90%  $\text{CO}_2$ :10%  $\text{CO}$  and 70%  $\text{CO}_2$ :30%  $\text{CO}$  gas compositions, respectively. However, as  $R_p$  of the full cell is still small relative to what has been attained from other mixed conducting oxides, such as LSCM<sup>102</sup>, the  $\text{CO}/\text{CO}_2$  reactions occurring at the LSF<sub>Cr</sub> fuel electrode can still be viewed as very active. For instance, in a 3-electrode fuel cell study using LSCM as the fuel electrode, operated in 70%  $\text{CO}_2$ :30%  $\text{CO}$  at  $800 \text{ }^\circ\text{C}$ , an  $R_p$  of  $2.4 \Omega \text{ cm}^2$  was obtained<sup>102</sup>. This is larger than the total

$R_p$  ( $0.92 \Omega \text{ cm}^2$ ) obtained for the LSFcr electrodes (both air and fuel) in the present work under the same conditions<sup>102</sup>, showing that LSFcr is more active in a CO/CO<sub>2</sub> atmosphere than is LSCM. Also,  $R_s$  in the air study (Figure 6.21) was similar to that observed in the CO/CO<sub>2</sub> studies, at around  $0.92 \Omega \text{ cm}^2$ , as expected, since  $R_s$  (dominated by the YSZ electrolyte) should be independent of the gas environment.

As LSFcr is porous, some regions of the underlying GDC could be exposed to the gas environment. Therefore, it was of interest to determine if the Gd<sub>0.1</sub>Ce<sub>0.9</sub>O<sub>2- $\delta$</sub>  (GDC) buffer layer at the fuel electrode contributes to the observed CO<sub>2</sub>/CO activity. This is because under reducing atmospheres, GDC is known to be a mixed ionic and electronic conductor<sup>252</sup> and thus has been successfully employed as an electrode for SOEC applications<sup>39, 253</sup>. For example, a GDC/YSZ/GDC cell, operated on 95% CO<sub>2</sub>:5% CO at 800 °C, showed a total polarization resistance of ca.  $8 \Omega \text{ cm}^2$  ( $4 \Omega \text{ cm}^2$  per electrode)<sup>39</sup>. In another study, a GDC electrode, infiltrated with Cu in a full cell configuration, gave an  $R_p$  value of ca.  $17 \Omega \text{ cm}^2$  at 750 °C when 90% CO<sub>2</sub>:10% CO was fed to the fuel electrode and air to the oxygen electrode<sup>253</sup>.

Thus, here, a GDC/YSZ/GDC cell was constructed and tested, all in 90% CO<sub>2</sub>:10% CO at 800 °C. Figure 6.22 reveals a polarization resistance of ca.  $50 \Omega \text{ cm}^2$  ( $25 \Omega \text{ cm}^2$  per electrode). This rather poor performance, compared to the  $1.3 \Omega \text{ cm}^2$  observed in Figure 6.17a when LSFcr is also present, clearly shows that the GDC buffer layer is not very active for the CO<sub>2</sub>/CO reaction and that the performance of the LSFcr/GDC/YSZ/GDC/LSFcr cell reported here does reflect the CO<sub>2</sub>/CO and oxygen reactions at the LSFcr catalyst material.

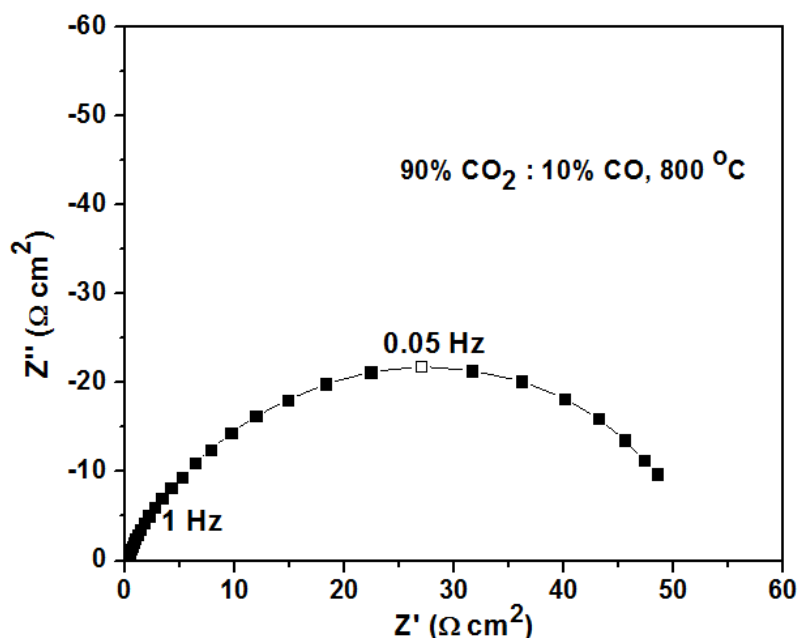


**Figure 6.22** Impedance response (at the open circuit potential) of a symmetrical GDC/YSZ/GDC cell, all in 90% CO<sub>2</sub>:10% CO at 800 °C, showing a total R<sub>p</sub> of 50 Ω cm<sup>2</sup> for both GDC electrodes.

Polarized impedance studies were also carried out to more closely examine the performance of the LSF<sub>Cr</sub>-based full cell in both the SOFC and SOEC modes. The Nyquist plots in Figure 6.23a show the polarization of the cell in both the negative (SOEC mode, -0.2 V vs. OCP) and positive (SOFC mode, 0.2 V vs. OCP) directions. Clearly, the cell performed better in the SOEC mode (CO<sub>2</sub> electrolysis) compared to in the SOFC mode (CO oxidation and O<sub>2</sub> reduction), as seen from the lower R<sub>p</sub> value observed during electrolysis.

These impedance data are in full agreement with the CV results shown in Figure 6.18a, where a better performance was also observed in the SOEC mode. From both the Nyquist (Figure 6.23a) and Bode (Figure 6.23b) plots, it is seen that the polarization affected only the low frequency arc, while the high frequency arc does not change. From Figure 6.23c, it is obvious that the resistance associated with the low frequency arc (R<sub>2</sub>), which exhibits a summit

frequency of 1 Hz, dominates the EIS response in both the SOFC (0.1 to 0.3 V vs. OCP) and SOEC (-0.1 to -0.3 V vs. OCP) modes.

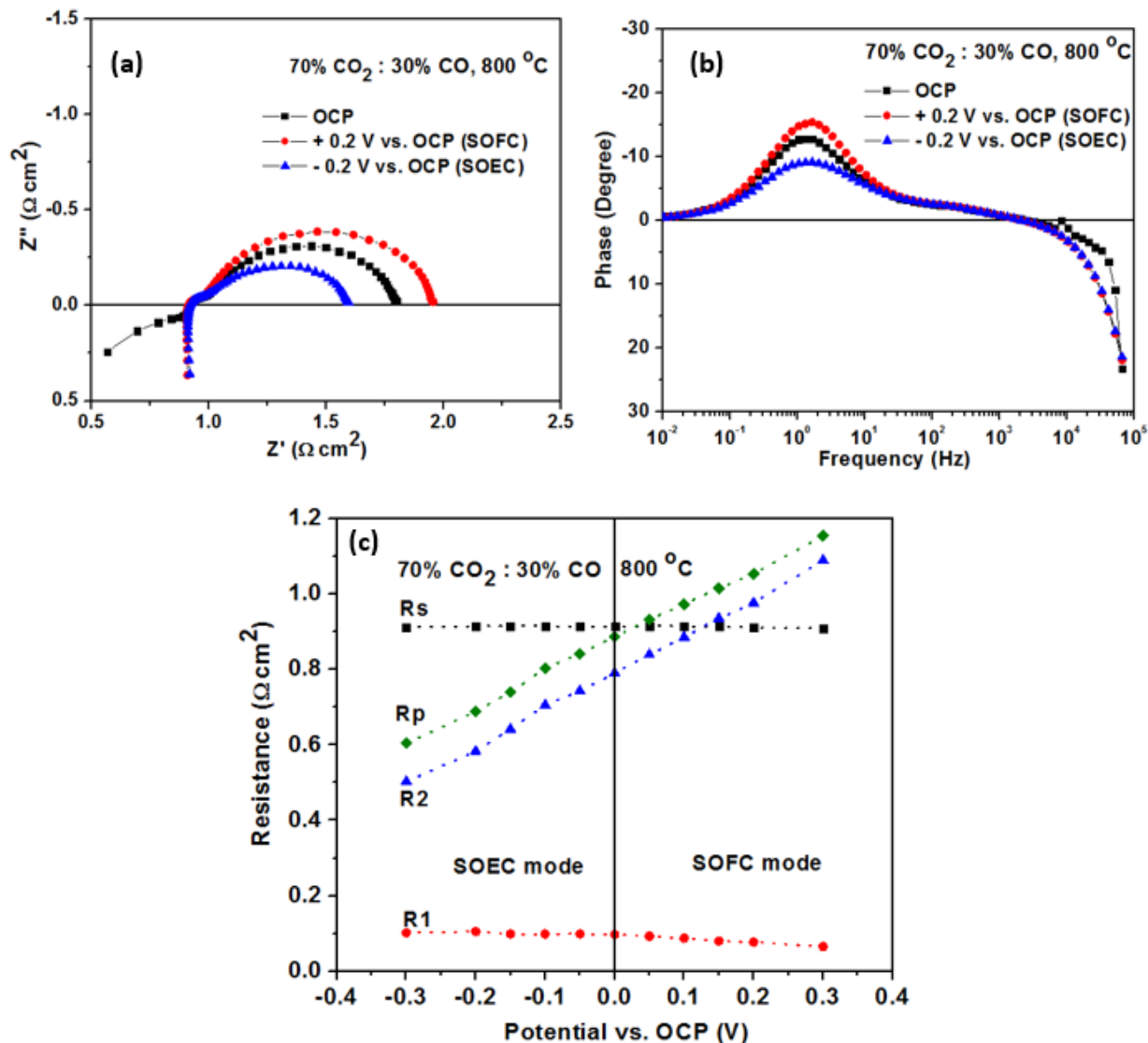


**Figure 6.23** OCP and polarized EIS response of the symmetrical LSFcr-based full cell, operated at 800 °C with 70% CO<sub>2</sub>:30% CO fed to the fuel electrode and air fed to the oxygen electrode, showing (a) the Nyquist and (b) the phase angle Bode plots (acquired at OCP, 0.2 V vs. OCP, and -0.2 V vs. OCP) and (c) the corresponding resistances obtained from the fitted Nyquist plots using the  $R_s(R_1CPE_1)(R_2CPE_2)$  equivalent circuit model.

As discussed above, the low frequency resistance exhibits a strong temperature dependence, which argues against rate limitations due to gas phase convection or diffusion processes. Therefore, it is likely related to the surfaces reactions occurring at the fuel electrode.

Figure 6.24 shows the impedance response of the LSF<sub>Cr</sub>-based full cell with various CO<sub>2</sub>/CO mixtures (90% CO<sub>2</sub>:10% CO, 70% CO<sub>2</sub>:30% CO, and 50% CO<sub>2</sub>:50% CO) fed to the fuel electrode and the oxygen electrode exposed to air at 800 °C at various potentials. As the CO content is increased, R<sub>p</sub> decreases, as discussed previously.

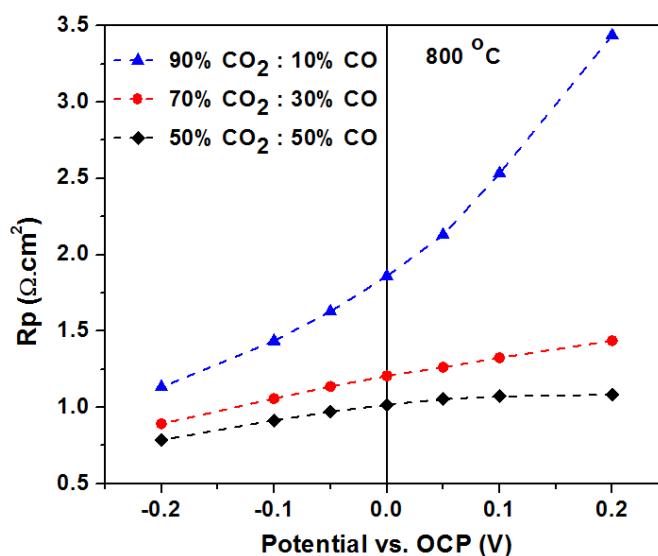


**Figure 6.24 Polarization resistance (R<sub>p</sub>) of the symmetrical LSF<sub>Cr</sub> full cell, operated at 800 °C with 90% CO<sub>2</sub>:10% CO, 70% CO<sub>2</sub>:30% CO, and 50% CO<sub>2</sub>:50% CO fed to the fuel electrode and air fed to the oxygen electrode. R<sub>p</sub> obtained at different fuel electrode potentials from the fitted Nyquist plots using the Rs(R1CPE1)(R2CPE2) equivalent circuit model.**

It can be seen that, for the three CO<sub>2</sub>/CO mixtures examined, increasing the applied negative bias (SOEC mode) causes R<sub>p</sub> to decrease, whereas an increase in the applied positive bias (SOFC mode) leads to an increase in R<sub>p</sub>. However, the rate at which R<sub>p</sub> increases with increasing positive polarization is minimal for the 50% CO<sub>2</sub>:50% CO mixture compared to in

90% CO<sub>2</sub>:10% CO. This is expected because of the increase in the CO content. It is also worth mentioning that the results of the 3-electrode half cell study of LSF<sub>Cr</sub> in a 30% CO<sub>2</sub>:30% CO atmosphere, which will be discussed in detail in Chapter 7, also show a better performance during the reduction of CO<sub>2</sub> than during CO oxidation<sup>55</sup>.

### 6.2.2.3 Stability of LSF<sub>Cr</sub>-based RSOFC cells in dry CO/CO<sub>2</sub> mixtures

To evaluate the stability of the full cell in the SOEC mode, a galvanostatic test was performed. Figure 6.25a shows the medium-term performance of the cell run in the SOEC mode after 133 h at -100 mA/cm<sup>2</sup> in a 90% CO<sub>2</sub>:10% CO mixture at the fuel electrode and air at the oxygen electrode at 800 °C. The V-t plot shows that the LSF<sub>Cr</sub> electrode is very stable during the reduction of CO<sub>2</sub> to CO at the fuel electrode and oxygen evolution at the oxygen electrode. After 133 h of operation, the rate of potential loss (degradation rate) is seen to be only 0.057 mV/h.

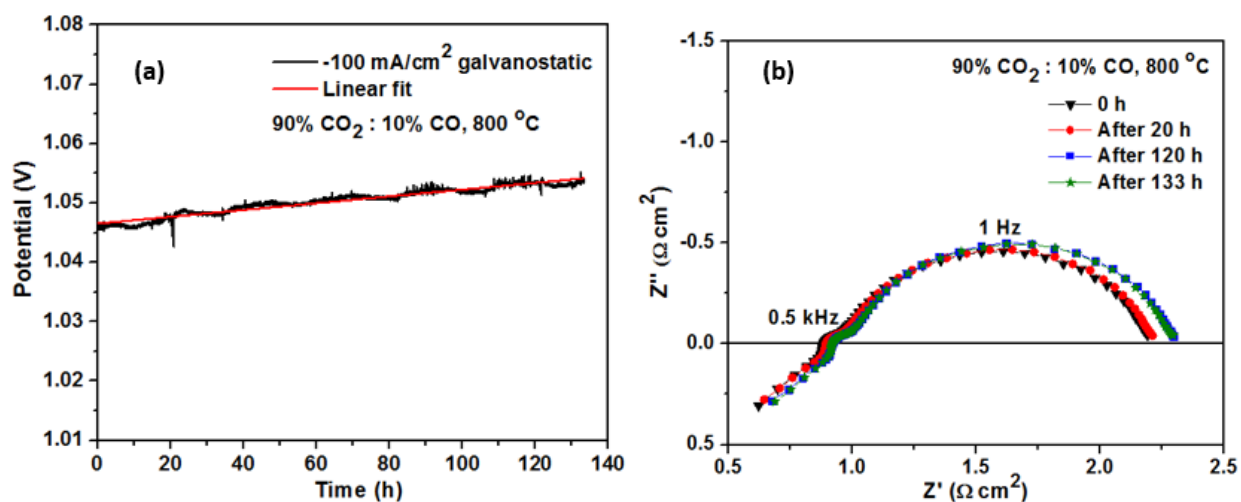


**Figure 6.25** Medium term stability study of the symmetrical LSF<sub>Cr</sub>-based RSOFC, tested for 133 h at 800 °C with 90% CO<sub>2</sub>:10% CO fed to the fuel electrode and air fed to the oxygen electrode, showing (a) the V-t plot at a -100 mA/cm<sup>2</sup> galvanostatic hold and (b) the corresponding Nyquist plots collected at the open circuit potential at 0, 20, 120 and 133 h.

A direct comparison of the degradation rate of the LSFcr fuel electrode with Ni-YSZ fuel electrodes during CO<sub>2</sub> reduction cannot easily be made, primarily because of the different experimental conditions used. Even so, some studies have shown that running Ni-YSZ cathodes on clean CO<sub>2</sub>/CO gas, free of impurities (e.g., H<sub>2</sub>S), resulted in negligible degradation rates<sup>40, 254</sup>. However, when Ni-YSZ was operated on as-received CO<sub>2</sub>/CO gas (without the use of a pre-cleaning step to remove any impurities present in the gases), significant degradation was observed<sup>40, 254</sup>. For instance, a CO<sub>2</sub> electrolysis study, carried out by Ebbesen *et al.*<sup>40</sup>, showed a degradation rate of 0.25 mV/h when a Ni-YSZ supported cell was operated on as-received 70% CO<sub>2</sub>:30% CO, containing trace amount of impurities such as H<sub>2</sub>S, for 150 h at 0.25 A/cm<sup>2</sup>, all at 850 °C<sup>40</sup>.

This degradation is not surprising because, as discussed in Chapter 4, Ni-YSZ fuel electrodes are susceptible to H<sub>2</sub>S poisoning, even at very low ppm of H<sub>2</sub>S and at these higher temperatures. Therefore, the development of sulfur tolerant electrodes for RSOFC applications is still very important. As discussed in Chapter 5, the LMFCr material is sulfur tolerant in low ppm H<sub>2</sub>S at > 750 °C. Therefore, it is a good electrocatalyst for use as the fuel electrode in RSOFC applications.

Figure 6.25b shows the corresponding OCP-EIS data acquired before the beginning of the galvanostatic experiments, and then at 20, 120 and 133 h during the constant current studies of Figure 6.25a. While R<sub>p</sub> changed by only 2.9% after 133 h of operation, R<sub>s</sub> changed only slightly over this time period, indicating no delamination of the electrodes from the YSZ electrolyte or the build-up of any resistive phases at any of the interfaces, consistent with the SEM image in Figure 6.14. This indicates that the cells fabricated and studied in this work were of high quality, with good adhesion of each layer to its neighboring phase.

Figure 6.26 shows a backscattered secondary electron (BSE) image and electron microprobe WDX elemental mapping of the cross-section of a polished LSFCr fuel electrode after several days of electrochemical testing in CO<sub>2</sub>/CO atmospheres. As can be seen, there is no interdiffusion or segregation of cations between the buffer layer (GDC) on top of the YSZ electrolyte and the electrode material (LSFCr). Taken together, the results in this Chapter have clearly shown that LSFCr is a very good electrode material for CO<sub>2</sub> reduction to CO at high temperatures, as it is very active and yet stable.

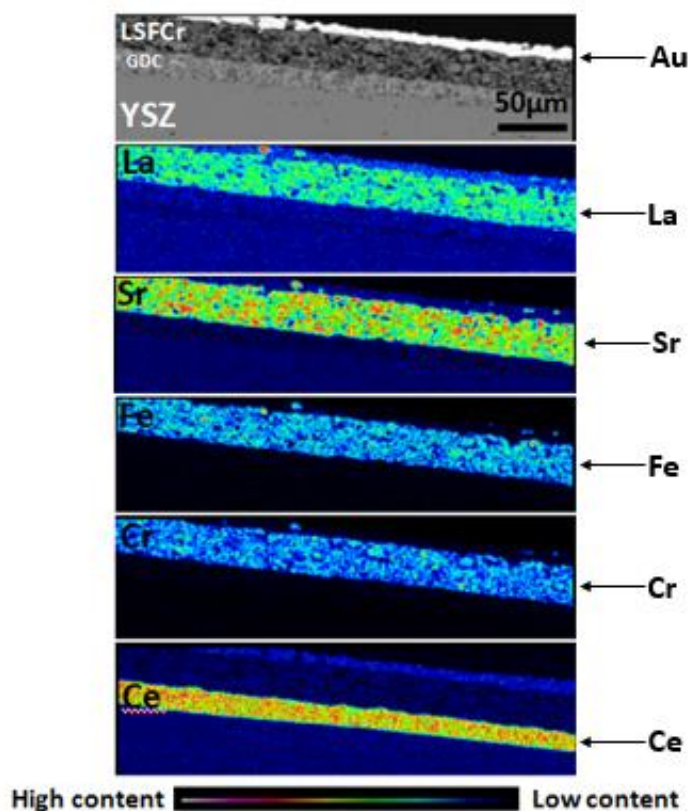


**Figure 6.26** Electron microprobe WDX elemental mapping of the polished cross-section of a LSFCr fuel electrode after several days of electrochemical testing of the cell CO<sub>2</sub>/CO atmospheres in the temperature range of 600-850 °C.

### 6.3 Summary

The structural stability of the mixed conducting  $\text{La}_{0.3}\text{Sr}_{0.7}\text{Fe}_{0.7}\text{Cr}_{0.3}\text{O}_{3-\delta}$  (LSFCr) perovskite in  $\text{CO}_2$ ,  $\text{CO}_2/\text{CO}$ , and  $\text{CO}/\text{N}_2$  atmospheres was investigated in this chapter, using X-ray diffraction (XRD), Fourier transform infrared (FTIR) spectroscopy, thermogravimetric analysis (TGA), scanning electron microscopy (SEM), high resolution transmission electron microscopy (HRTEM), and energy dispersive X-ray spectroscopy (EDX). It is shown that the exposure of LSFCr to pure  $\text{CO}_2$  ( $p\text{O}_2 \sim 10^{-7}$  atm) from 30-800 °C, with a 24 h dwell time at 800 °C, did not lead to the formation of any unwanted secondary phases, such as  $\text{SrCO}_3$ . Also, exposure of LSFCr to 90-70%  $\text{CO}_2$ :10-30%  $\text{CO}$  ( $p\text{O}_2$  of  $10^{-18}$  -  $10^{-19}$  atm) from 30-800 °C, with a 6-24 h dwell time at 800 °C, still retained its perovskite phase with only minor impurities observed.

In 10%  $\text{CO}$ :90%  $\text{N}_2$  ( $p\text{O}_2 \sim 10^{-21}$  atm at 800 °C), LSFCr decomposed slightly, forming the  $\text{LaSrFeO}_4$ -based phase ( $\text{K}_2\text{NiF}_4$ ) phase, but LSFCr in 30%  $\text{CO}$ :70%  $\text{N}_2$  ( $p\text{O}_2 \sim 10^{-23}$  atm) from 30-800 °C, with a 24 h dwell time at 800 °C, caused more  $\text{LaSrFeO}_4$ -based phase ( $\text{K}_2\text{NiF}_4$ ) to form. This confirms that, at a  $p\text{O}_2$  lower than the reported structural  $p\text{O}_2$  limit of  $10^{-21}$  atm, LSFCr starts to decompose to other phases. It was also shown that the decomposed phases of LSFCr observed in  $\text{CO}/\text{N}_2$  environments likely catalyze the Boudouard reaction, leading to the formation of carbon on LSFCr. However, re-exposure of the LSFCr sample to air, with a 24 h dwell time at 800 °C, regenerated the perovskite single phase with only minor impurities remaining.

The electrochemical performance of LSFCr in  $\text{CO}/\text{CO}_2$  atmospheres was also examined in this chapter. Specifically, it was shown that a 2-electrode, symmetrical, LSFCr/GDC/YSZ/GDC/LSFCr cell, evaluated at 600-800 °C, exhibited a very good electrochemical performance during both the reduction of  $\text{CO}_2$  (SOEC mode) and the oxidation

of CO (SOFC mode) at the fuel electrode, with oxygen evolution (OER, SOEC) and oxygen reduction (ORR, SOFC) being very active at the air electrode. This work has also shown that LSFcr is more active towards the reduction of CO<sub>2</sub> than the oxidation of CO.

The polarization resistance (R<sub>p</sub>) observed at 800 °C from the open circuit (OCP) impedance data were 1.36 and 0.94 Ω cm<sup>2</sup> in 90% CO<sub>2</sub>:10% CO and 70% CO<sub>2</sub>:30% CO, respectively. Based on the 2-electrode half cell studies of LSFcr electrodes in air at 800 °C, which gave a R<sub>p</sub> value of 0.25 Ω cm<sup>2</sup>, the contribution of the air electrode to the observed R<sub>p</sub> in the full cell studies, where CO/CO<sub>2</sub> was fed to the fuel electrode and air to the oxygen electrode, was minimal. However, as R<sub>p</sub> of the full cell is still small relative to what has been reported for other mixed conducting oxides as a CO<sub>2</sub>/CO conversion electrode, the LSFcr fuel electrode can still be considered as a very good electrocatalyst.

In terms of long-term performance, the LSFcr/GDC/YSZ/GDC/LSFcr cell showed a very stable activity towards the reduction of CO<sub>2</sub> (and evolution of oxygen) during 133 h of galvanostatic testing, exhibiting only a 0.057 mV/h degradation rate. From the SEM images, no delamination was observed at either the fuel or oxygen electrodes after these medium term studies.

Taken together, the results presented in this chapter clearly show that the LSFcr perovskite material can be employed as a stable and high performing electrode material for CO<sub>2</sub> reduction, CO oxidation, and also as a reversible oxygen electrode for use in symmetrical RSOFCs.

## Chapter Seven: **Three electrode half cell study of $\text{La}_{0.3}\text{Sr}_{0.7}\text{Fe}_{0.7}\text{Cr}_{0.3}\text{O}_{3-\delta}$ (LSFCr) electrodes in $\text{CO}_2/\text{CO}$ environments**

This chapter contains some data from a published paper (B. Molero, P. Addo, A. Buyukaksoy, and V. Birss, *Electrochemistry of  $\text{La}_{0.3}\text{Sr}_{0.7}\text{Fe}_{0.7}\text{Cr}_{0.3}\text{O}_3$  as an oxygen and fuel electrode for RSOFCs*, Faraday Discussions, 2015. **182**: p.159-175), reproduced by permission of The Royal Society of Chemistry.

### **7.1 Introduction**

In Chapter 6, the electrochemical performance and stability of symmetrical, 2-electrode, full cells, employing  $\text{La}_{0.3}\text{Sr}_{0.7}\text{Fe}_{0.7}\text{Cr}_{0.3}\text{O}_{3-\delta}$  (LSFCr) at both electrodes, was investigated, with  $\text{CO}_2/\text{CO}$  mixtures fed to the fuel electrode and air fed to the oxygen electrode. However, in 2-electrode cells, the electrochemical performance is controlled by the processes occurring at both electrodes, and yet the focus of this thesis is on the fuel side activity. Therefore, to fully understand the reaction activity and mechanism at the fuel electrode, a 3-electrode full or half cell configuration was required, as was also the case in parts of Chapter 4 during the study of  $\text{H}_2$  reactions at Ni/YSZ (yttria stabilized zirconia) anodes. Use of a 3-electrode configuration allows the identification and quantification of the various electrochemical steps, ohmic losses, and diffusion limitations occurring at the gas/working electrode and working electrode/electrolyte interfaces.

The overall  $\text{CO}_2/\text{CO}$  reaction, using the Kroger-Vink notation for mixed ionic and electronic conductor materials, such as ceria and perovskites, is shown in Reaction 7.1,



where  $V_o^{\bullet\bullet}$  is an oxygen vacancy and  $O_o^x$  represents the lattice oxygen anion. The mechanism of  $\text{CO}_2$  reduction and  $\text{CO}$  oxidation on perovskites is not well defined in the literature, although limited studies using operando ambient pressure X-ray photoelectron spectroscopy (AP-XPS) to

probe the surface reaction at a doped ceria-based electrode have been reported<sup>255-257</sup>. These AP-XPS studies showed that CO<sub>2</sub> reduction on doped-ceria, which has a mixed valence of Ce<sup>3+</sup> and Ce<sup>4+</sup>, goes through a stable carbonate intermediate step and that the coverage of carbonate is dependent on the surface concentration of Ce<sup>3+</sup><sup>255-257</sup>. Also, they showed that, during cathodic polarization (CO<sub>2</sub> reduction), the surface Ce<sup>3+</sup> concentration increased with negative overpotential while the carbonate coverage became saturated<sup>255</sup>. However, during anodic polarization (CO oxidation), both the surface Ce<sup>3+</sup> and carbonate concentration decreased with overpotential<sup>255</sup>. The general reaction can be written more specifically for a ceria electrode, as shown in Reaction 7.2<sup>255</sup>.



where Ce'\_{Ce} represents the Ce<sup>3+</sup> cations, and Ce<sup>x</sup>\_{Ce} represents the Ce<sup>4+</sup> cations. The simplified assumed reaction steps or pathways proposed by Feng *et al.*<sup>255</sup> in the CO<sub>2</sub> reduction direction are as follows:

Step 1: Bulk Ce<sup>3+</sup> and oxygen vacancy generation:



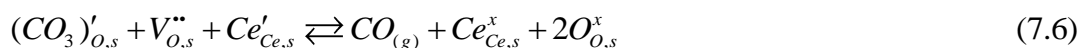
Step 2: Bulk Ce<sup>3+</sup> and oxygen vacancy migration to the surface:



Step 3: CO<sub>2</sub> adsorption and carbonate formation, and first electron transfer:



Step 4: CO formation and oxygen incorporation, and second electron transfer:



where the subscripts 'b', 's', 'M' and 'YSZ' denote the bulk and surface species of the ceria electrode, the metal current collector, and the YSZ (yttria-stabilized zirconia) electrolyte, respectively.

It was shown that the rate determining step occurs at the ceria-gas interface (Steps 3 and 4)<sup>255</sup> and that the bulk and near-surface migration of localized electrons and oxygen vacancies is not rate determining (Steps 1 and 2)<sup>255</sup>. It is assumed here that a similar series of steps will take place during CO<sub>2</sub> reduction on the mixed conducting perovskite oxide under study here, which is mainly LSFCr.

In a three electrode configuration, current flows between the counter (CE) and working (WE) electrodes and the overpotential at the WE is isolated from the potential of the entire cell by the use of a reference electrode (RE), allowing the characteristics of the WE to be obtained separately from the CE<sup>171, 172</sup>. However, there are numerous challenges associated with the use of a three electrode configuration in SOFCs and RSOFCs for the accurate measurement of the various electrochemical processes occurring at the WE<sup>171, 172, 258-261</sup>. Some of these include identifying the correct placement or position of the RE with respect to the WE and CE, and the alignment of the CE and WE versus each other<sup>171, 172, 258-261</sup>. Even so, various types of three electrode cell geometries/configurations have been investigated in recent years. These include embedding the RE into a thick electrolyte<sup>262</sup> as well as placing the RE simply on the surface of the electrolyte of a planar cell but ensuring the correct distance from the WE<sup>171, 172, 258-262</sup>.

The planar cell configuration is simple and easy to fabricate. However, it has been reported that a misalignment between the CE and WE could result in either over or under estimation of the series ( $R_s$ ) and polarization ( $R_p$ ) resistances during impedance measurements<sup>171, 172</sup>. Also, placing the RE at a location where there is a equipotential distribution leads to errors or distortions in the impedance data<sup>171, 172, 262</sup>.

As one criterion for these types of planar cells, the RE needs to be placed at a distance  $> 3x$  the thickness of the electrolyte away from the WE<sup>171, 172, 262</sup>. The effect of misalignment of the WE and CE on the errors associated with impedance measurement is less severe as the thickness of the electrolyte increases<sup>262</sup>. Thus, it has been shown that accurate impedance data can be acquired by using an electrolyte as thick as 250  $\mu\text{m}$ <sup>260</sup>. In this chapter, the thickness of the YSZ electrolyte was 300  $\mu\text{m}$ , whereas in Chapter 4, a much thicker YSZ electrolyte (1000  $\mu\text{m}$ ) was used for the three-electrode study. The reason for using a 300  $\mu\text{m}$  thick YSZ here was to allow a direct 3-electrode comparison with the  $\text{CO}_2/\text{CO}$  performance data reported for the 2-electrode full cell study in Chapter 6, where LSFCr was used at both electrodes.

LSFCr was also used in the present chapter as the WE, counter electrode (CE) and reference electrode (RE) (Figure 7.1) and then operated in a half cell mode on either pure  $\text{CO}_2$  or in mixed  $\text{CO}_2/\text{CO}$  atmospheres. Both direct current (dc) and impedance measurements were used here to understand and separate the electrochemical processes occurring at the gas/LSFCr electrode (surface processes) and the LSFCr electrode/electrolyte interfaces (Figure 7.1b) during  $\text{CO}_2$  reduction and CO oxidation.

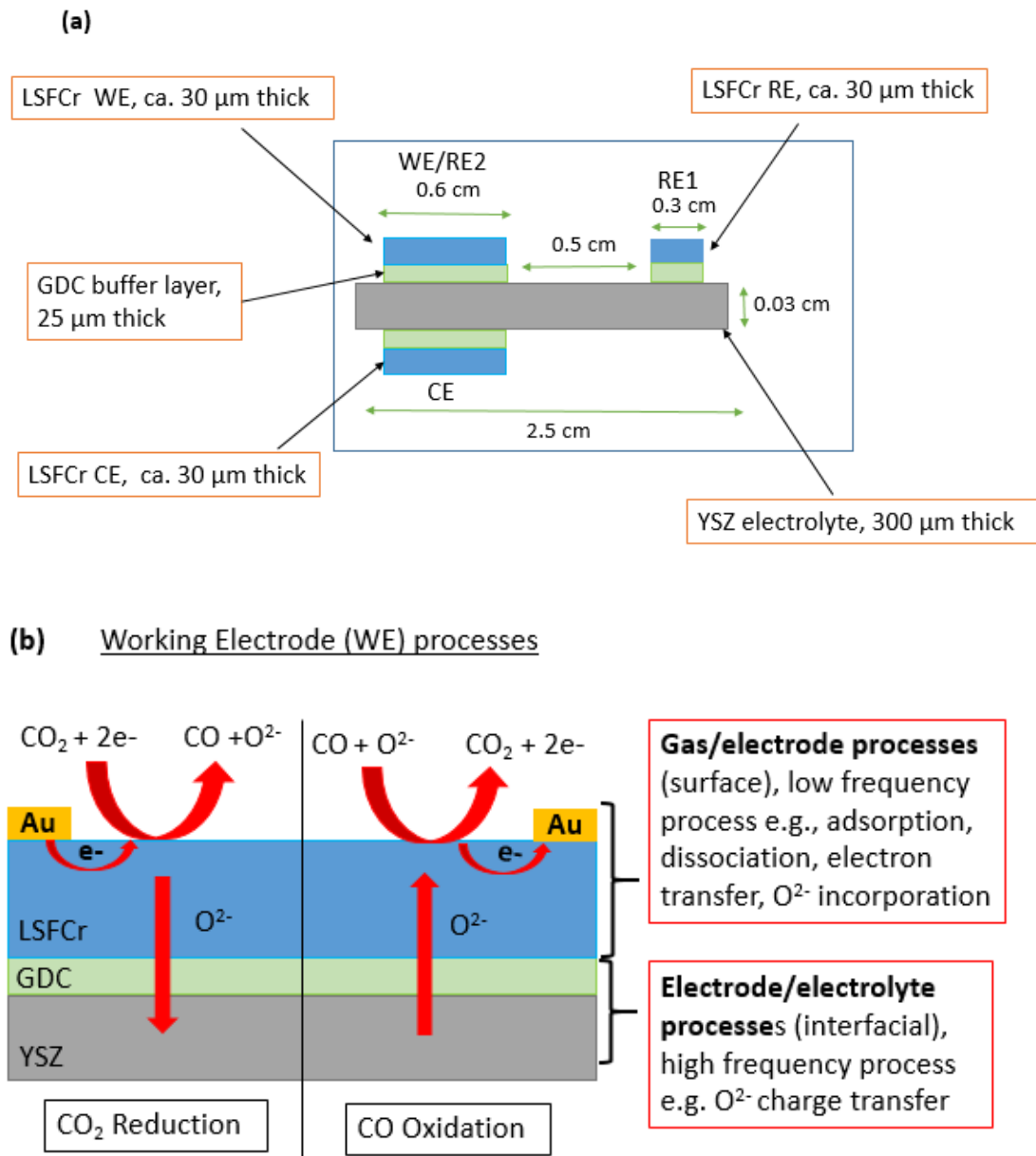


**Figure 7.1** Schematic of (a) the LSFcr 3-electrode half cell configuration used and (b) the electrochemical processes occurring at the gas/electrode/electrolyte interface during  $\text{CO}_2$  reduction and CO oxidation.

It is shown in this chapter that the LSFcr WE is more active for the reduction of  $\text{CO}_2$  than for the oxidation of CO. The low frequency resistance ( $R_2$ ), which is associated with surface processes occurring at the gas/electrode interface, such as adsorption, dissociation and

charge transfer, is found to dominate the polarization resistance, as the high frequency resistance (R1), due to ion transfer at the LSFCr/GDC interface, is quite small. Also, it is shown that comparing between the resistance values obtained from a 2- and 3-electrode half cell configuration helps to ascertain the validity and reliability of the electrochemical data collected in the 3-electrode set-up.

## **7.2 Results and Discussion**

### ***7.2.1 3-electrode half cell configurations***

Figure 7.1 shows the 3-electrode half cell configuration used to investigate the electrochemical performance of the  $\text{La}_{0.3}\text{Sr}_{0.7}\text{Fe}_{0.7}\text{Cr}_{0.3}\text{O}_{3-\delta}$  (LSFCr) material towards the reduction of  $\text{CO}_2$  and oxidation of CO. As seen in Figure 7.1a, a relatively thick YSZ electrolyte (300  $\mu\text{m}$ ) was used and coated with a 25  $\mu\text{m}$   $\text{Gd}_{0.1}\text{Ce}_{0.9}\text{O}_{2-\delta}$  (GDC) buffer layer (one attached at each electrode), giving a 350  $\mu\text{m}$  thickness in total. This should be sufficiently thick so that the 3-electrode data are reliable. It has been reported that an electrolyte thickness of  $> 250 \mu\text{m}$  and the geometry used here, with the RE placed to the side of the WE, but at a distance  $> 3x$  the thickness of the electrolyte away from the WE, should be safe<sup>260</sup>. In fact, in the present work, electrode placement was done very carefully, ensuring the symmetrical positioning and sizing of the WE and CE, both composed of LSFCr. Also, the thickness of the screen-printed CE and WE was very similar, thus achieving very similar electrochemical characteristics.

### ***7.2.2 Validation of 3-electrode half cell data***

One approach to confirm the validity of the results obtained from 3-electrode half cell testing under SOFC/SOEC conditions is to examine the measured impedance data, based on

different electrode pairs, such as WE/RE (3 electrode configuration) and WE/CE (2 electrode configuration)<sup>262</sup>. The comparison of the  $R_p$  values obtained from the impedance spectra of the WE/RE and WE/CE electrode pairs should then give an indication of the reliability of the 3-electrode setup<sup>262</sup>.

Figure 7.2a shows the impedance spectra of a 3-electrode half cell (shown in Figure 7.1a) and a 2-electrode half cell in 70% CO<sub>2</sub>:30% CO at 800 °C. For simplicity and direct comparison, the series resistance, which is due mainly to the electrolyte, was removed from the Nyquist plots, with the data then fitted to the equivalent circuit shown in Figure 7.2b in both cases. An example of the good fits obtained of the EIS data to the selected equivalent circuit is shown in Figure 7.2b, giving a chi-squared value of  $< 10^{-4}$ . It should be noted that all of the fits of the impedance data shown in this chapter gave similarly low chi-squared values.

The  $R_p$  for the WE, obtained from the 3-electrode half cell, was ca.  $0.80 \Omega \text{ cm}^2$ , while the total  $R_p$  for the 2-electrode half cell was  $1.6 \Omega \text{ cm}^2$ . This indicates that the  $R_p$  contribution of each of the WE and CE in the 2-electrode half cell is the same, being  $0.80 \Omega \text{ cm}^2$ , respectively, which is also the same as the  $R_p$  obtained for the WE alone in the 3-electrode half cell. These results argue that the RE was placed at an appropriate location (Figure 7.1a) and that the data obtained in the 3-electrode cell are reliable.

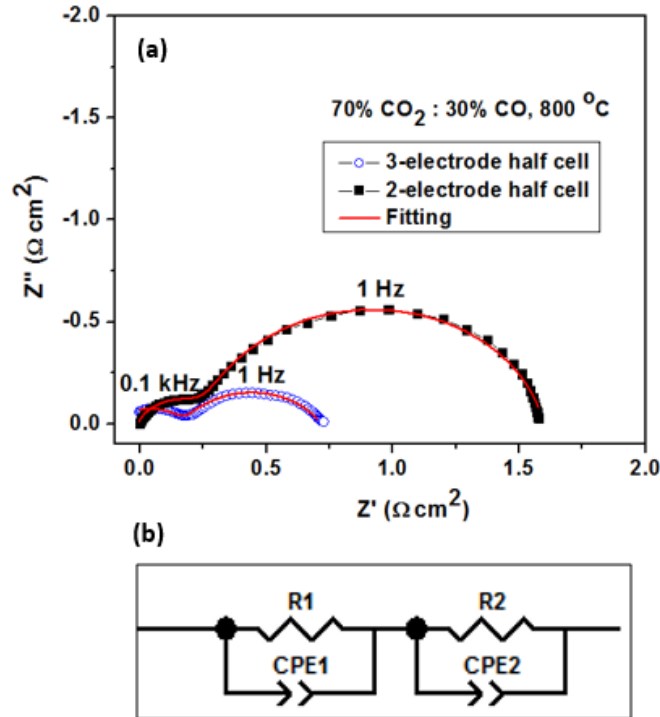


**Figure 7.2 (a) Impedance response (at the open circuit potential) of a LSFCr WE in a 3-electrode cell and the two LSFCr electrodes in the 2-electrode half cell, both tested in 70%  $\text{CO}_2$ :30%  $\text{CO}$  at 800 °C, and (b) the equivalent circuit model used to fit the data in (a).**

The  $R_p$  of  $0.80 \Omega \text{ cm}^2$ , obtained from the 3-electrode cell, was also compared to the  $R_p$  obtained in the symmetrical (2-electrodes, both LSFCr) full cells, shown in Chapter 6 (Figure 6.17). From Figure 6.17, the  $R_p$  obtained for a 2-electrode full cell in 70%  $\text{CO}_2$ :30%  $\text{CO}$  at 800 °C was ca.  $1 \Omega \text{ cm}^2$ . As shown in Figure 6.21, LSFCr is a very good oxygen electrocatalyst, giving an  $R_p$  of ca.  $0.25 \Omega \text{ cm}^2$  at 800 °C. As such, the  $R_p$  for the fuel electrode was ca.  $0.75 \Omega \text{ cm}^2$ . This again suggests that the  $R_p$  of ca.  $0.80 \Omega \text{ cm}^2$ , observed here for the WE in the 3-electrode half cell experiment in Figure 7.2, is very reasonable.

### 7.2.3 LSFcr in 100% dry CO<sub>2</sub> using 3-electrode half cell

Figure 7.3 shows both the open circuit and polarized impedance data (all at overpotentials of +100 mV and -100 mV), obtained for the LSFcr WE in a pure CO<sub>2</sub> atmosphere, showing three well-defined time constants, with one process seen at high frequencies (R1CPE1, at ca. 10 kHz) and two at lower frequencies (R2CPE2 at 1 Hz and R3CPE3 at 0.05 Hz). Notably, in the 2-electrode full cell studies of LSFcr in Chapter 6 (Figure 6.15), three time constants were also seen in pure CO<sub>2</sub>. CO<sub>2</sub> alone was investigated here, partly to compare with the results obtained with the 2-electrode full cells in Chapter 6, but also to help identify any diffusion controlled processes. This is because CO will be present in very low concentrations under these conditions, as it is generated only as the product of CO<sub>2</sub> reduction under negative polarization.

The 3-electrode half cell impedance data (Figure 7.3a), obtained both at the OCP and under polarization, were fitted to an  $R_s(R1CPE1)(R2CPE2)(R3CPE3)$  equivalent circuit (Figure 7.3c), where the CPEs were again converted to capacitance (C) using Equation 4.3. Table 7.1 shows the values of the circuit elements and the calculated capacitances under all of these conditions. From Table 7.1, the polarization resistance ( $R_p = R1+R2+R3$ ) is smaller at -100 mV during CO<sub>2</sub> reduction than at the OCP, and is the largest at +100 mV polarization in these experiments, which were carried out in the absence of CO in the gas feed stream.

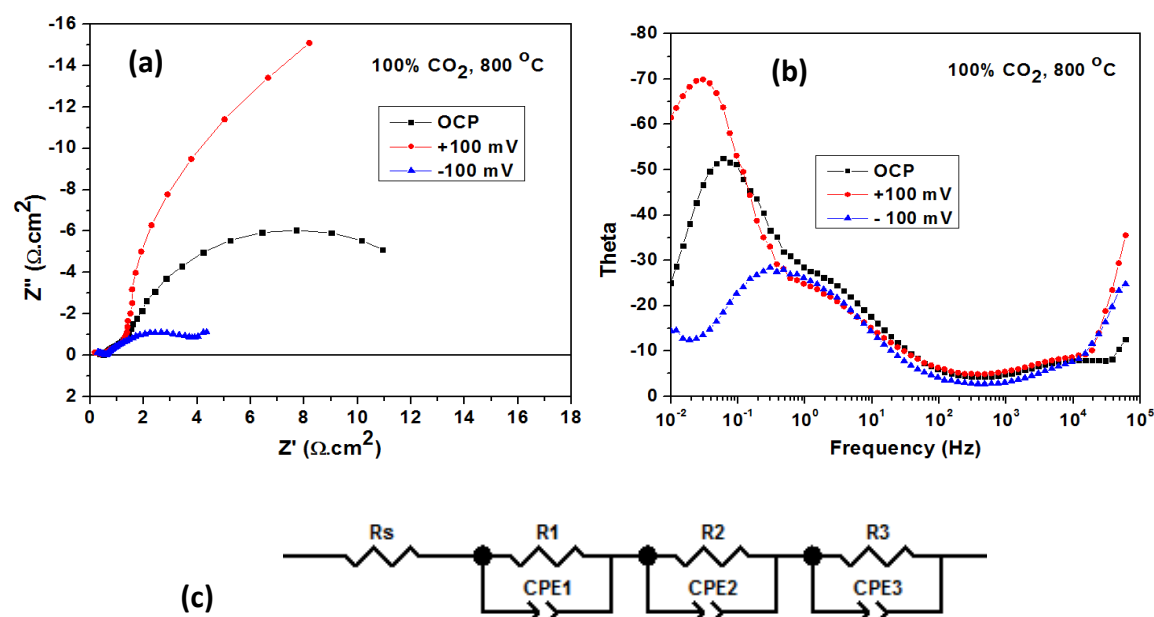


Figure 7.3 OCP and polarized (+100 mV and -100 mV) impedance response of LSFCE WE in 3-electrode half cell, operated at 800 °C in 100% CO<sub>2</sub>, showing (a) the Nyquist plots, (b) the phase angle Bode plots, and (c) the equivalent circuit model used to fit the data in (a).

Table 7.1 Fitted parameters\* from Figure 7.3a\*\* using the Rs(R1CPE1)(R2CPE2)(R3CPE3) equivalent circuit model (Figure 7.3c)

Potential (mV)	R1 (Ω cm <sup>2</sup> )	C1 <sup>#</sup> (F/cm <sup>2</sup> )	n1	R2 (Ω cm <sup>2</sup> )	C2 <sup>#</sup> (F/cm <sup>2</sup> )	n2	R3 (Ω cm <sup>2</sup> )	C3 <sup>#</sup> (F/cm <sup>2</sup> )	n3	Rp <sup>\$</sup> (Ω cm <sup>2</sup> )
OCP	0.20	8.7x10 <sup>-5</sup>	0.64	1.1	0.13	0.67	13	0.68	0.97	14
+100	0.25	6.5x10 <sup>-6</sup>	0.38	0.91	0.14	0.71	41	0.85	1.0	42
-100	0.22	8.2x10 <sup>-5</sup>	0.64	0.87	0.17	0.67	2.8	0.67	0.82	3.9

\*(R1, C1, n1) were obtained from the high frequency (10 kHz) arc, while (R2, C2, n2) and (R3, C3, n3) are from the low (1 Hz) and still lower (0.05 Hz) frequency arcs, respectively.

\*\*3-electrode LSFCE half cell, operated at 800 °C in 100% CO<sub>2</sub>.

# C1, C2 and C3 represent the high, low and lower frequency capacitors, respectively, and were calculated using Equation 4.3.

\$ Rp = R1+R2+R3. Rp values may not add up due to internal rounding.

The resistance associated with the high frequency arc (R1, at ca. 1-10 kHz) in Figure 7.3 was suggested in Chapters 5 (Section 5.2.5), and in the literature for similar MIEC oxide electrodes<sup>224, 225</sup>, to be due to oxide ion charge transfer at the electrode/electrolyte interface. This was consistent with the insensitivity of the high frequency arc characteristics to H<sub>2</sub>S exposure in Chapter 5 (Section 5.2.5). This interpretation is strengthened here by the relatively low value of the parallel capacitor (C1, 0.06- 0.9 x 10<sup>-5</sup> F/cm<sup>2</sup>) in Table 7.1, which is typical for an interfacial capacitance<sup>224, 225</sup>.

In terms of R2 and C2 (at ca. 1 Hz), C2 may be reflective of the chemical capacitance (changes in stoichiometry) of the LSFcr material, as was discussed also in Chapter 6 for the capacitance seen in this frequency range for this catalyst. The presence of a chemical capacitance is typical for mixed ionic and electronic conducting (MIEC) materials and is related to changes in stoichiometry (redox chemistry) of the MIEC during operation<sup>46, 247, 263</sup>. As seen in Table 7.1, C2 is in the range of 0.13-0.17 F/cm<sup>2</sup> and is relatively independent of polarization. The fact that C2 is the largest at -100 mV (0.17 F/cm<sup>2</sup>) vs. at the OCP and at +100 mV polarization may indicate that more oxygen vacancies are created in this potential range due to the enhanced redox chemistry of Fe<sup>4+</sup> to Fe<sup>3+</sup> in LSFcr under these conditions. R2 is only weakly dependent on overpotential (Table 7.1), but this would be expected at a 100 mV overpotential, which is in the linear (ohmic) range in 3-electrode experiments.

The low frequency arc (R3C3, at ca. 0.05 Hz) is ascribed to a gas diffusion process (likely CO oxidation), as the C3 values are very large, being in the range of 0.67-0.85 F/cm<sup>2</sup>, similar to what was reported by others for gas diffusion control<sup>196, 264</sup>, and also as they are essentially independent of overpotential. Further, the n3 values are generally close to unity<sup>196, 264</sup>, which is typical of gas diffusion rate control. R3 is much higher under anodic vs. cathodic polarization,

presumably because there is no CO in the gas stream and thus only the small quantities of CO generated during CO<sub>2</sub> reduction are available for the oxidation process to occur under anodic polarization. In contrast, under cathodic polarization, R3 is quite small, since CO<sub>2</sub> is being rapidly reduced to CO. Notably, this low frequency arc (R3C3), observed at ca. 0.05 Hz, is seen in both the 3-electrode half cell work in Figure 7.3 and was also seen in the 2-electrode full cell studies (Figure 6.15), showing good agreement between these two sets of results.

Cyclic voltammetry (CV) was also carried out to obtain further insights into the electrochemical mechanism of CO<sub>2</sub> reduction and CO oxidation at the LSFcr working electrode (WE) in pure CO<sub>2</sub> environments. The CV (5 mV/s) in Figure 7.4 shows higher current densities in the cathodic scan than in the anodic direction, which is not surprising, since there is no CO in the gas stream. This also agrees with the observed anodic limiting current density (concentration polarization) observed from 0 to +0.7 V, in full agreement with the EIS data and the discussion of Figure 7.3.

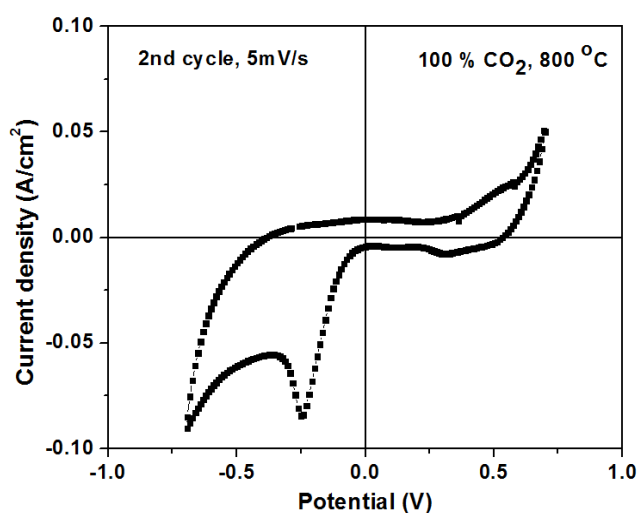


**Figure 7.4** Cyclic voltammetry data obtained for LSFcr WE in 3-electrode half cell, operated at 800 °C in pure CO<sub>2</sub> at 5 mV/s.

In the cathodic direction, Figure 7.4 shows a gradually increasing current density as CO<sub>2</sub> reduction commences, with a peak observed at ca. -0.25 V. A similar peak has been reported by Sapountzi *et al.*<sup>245</sup>, using La<sub>0.75</sub>Sr<sub>0.25</sub>Cr<sub>0.9</sub>Fe<sub>0.1</sub>O<sub>3-δ</sub> in CO/CO<sub>2</sub> atmospheres, and has been attributed to the redox chemistry of the perovskite oxide. Here, it is proposed that this peak reflects the reduction of Fe<sup>4+</sup> to Fe<sup>3+</sup> in the LSF<sub>Cr</sub> lattice, or at least its surface, with the associated formation of oxide ion vacancies, equivalent to the chemical capacitance seen in the impedance results in Figure 7.3. It is uncertain, however, why a matching anodic peak is not then observed in the positive scan, regenerating the Fe<sup>4+</sup> content.

In summary, in pure CO<sub>2</sub> environments at 800 °C, the 3-electrode work carried out in Section 7.2.3 has shown that, at the OCP, the low frequency diffusion-related resistance (R<sub>3</sub>, 0.05 Hz) dominates the polarization resistance (R<sub>p</sub>). However, under cathodic polarization (CO<sub>2</sub> reduction), R<sub>3</sub> decreases significantly (by ca. 20 times), likely as there is no shortage of CO<sub>2</sub> in the gas atmosphere, leading to an overall decrease in R<sub>p</sub>.

#### **7.2.4 LSF<sub>Cr</sub> in 30% CO<sub>2</sub>:30% CO (balance N<sub>2</sub>) in using 3-electrode half cells**

To further evaluate the performance of the LSF<sub>Cr</sub> WE towards CO<sub>2</sub> reduction and also CO oxidation in the 3-electrode cell, in comparison with the 2-electrode full cells studied in Chapter 6, a 30% CO<sub>2</sub>:30% CO ratio (1:1) was fed to the cell. Figure 7.5 shows the OCP and polarized impedance data at 800 °C, revealing that LSF<sub>Cr</sub> performs better in the cathodic mode (reduction of CO<sub>2</sub>) than in the anodic mode (CO oxidation). As this was also observed in Chapter 6, this suggests that there are some real kinetic differences between these two reactions.

Only two time constants appear under these CO<sub>2</sub>/CO conditions, similar to what was seen in the 2-electrode half cell studies (Figures 7.2a and 5.12). Thus, the Nyquist plots in Figure 7.5a

were fitted to a  $R_s(R1CPE1)(R2CPE2)$  equivalent circuit model (Figure 7.5c). The  $(R3CPE3)$  time constant, observed at very low frequencies (0.05 Hz) in the pure  $CO_2$  environment in Figure 7.3a and ascribed to gas phase diffusion limitations (likely of CO), is minimal or barely detectable in Figure 7.5a and thus it was excluded from the fitting model. Table 7.2 shows the fitted parameters, demonstrating that the polarization resistance ( $R_p$ ) at the OCP is  $0.87 \Omega \text{ cm}^2$ , while at +100 mV, it is  $1.4 \Omega \text{ cm}^2$ , and at -100 mV,  $R_p$  is  $0.67 \Omega \text{ cm}^2$ . The  $R_p$  values obtained for the cell operated on  $CO_2/CO$  gas mixtures are lower than in pure  $CO_2$  (Table 7.1) because there are no gas phase limitations in this  $CO_2/CO$  study.

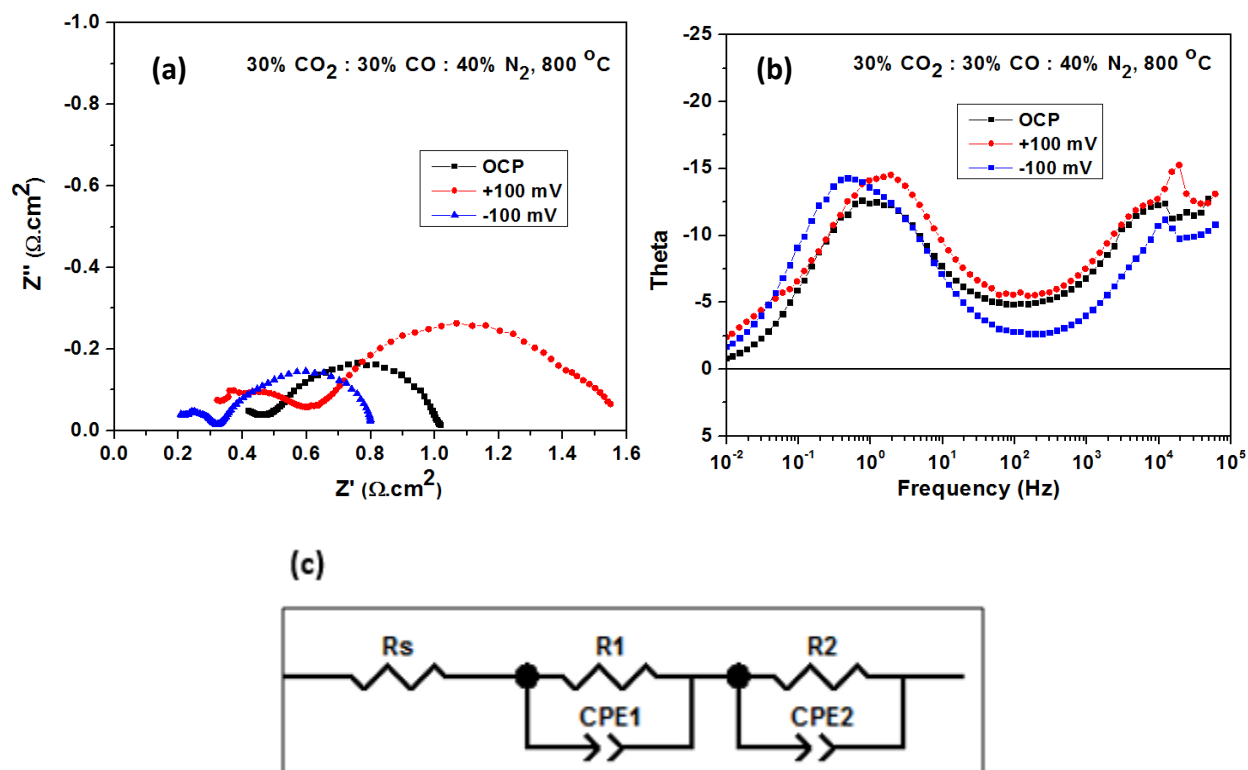


**Figure 7.5** OCP and polarized (+100 mV and -100 mV) EIS response of the LSFcr WE in 3 electrode half cell experiment at 800 °C in 30%  $CO_2$ :30% CO:40%  $N_2$ , showing (a) the Nyquist plots, (b) the phase angle Bode plots, and (c) the equivalent circuit model used to fit the data in (a).

In the CO<sub>2</sub>/CO system (Figure 7.5), the low frequency capacitance (C2) (Table 7.2) is now slightly higher in value than in 100% CO<sub>2</sub> (Table 7.1). If it still reflects the LSFcr chemical capacitance, then this is perhaps not surprising because the cell is now in a more reducing environment, which would lead to an increase in the concentration of oxygen vacancies as more of the B site cations are reduced. The n2 parameter in the CO<sub>2</sub>/CO atmosphere (Table 7.2) remains unchanged vs. the situation in pure CO<sub>2</sub> (Table 7.1), showing values of around 0.65, independent of potential. However, R2 in the CO<sub>2</sub>/CO atmosphere, assigned in the pure CO<sub>2</sub> studies to be due to the processes occurring at the gas/electrode interface (e.g., CO<sub>2</sub>/CO adsorption and dissociation), is about 50% lower than in pure CO<sub>2</sub> at both the OCP and at -100 mV. In contrast, R2 in the CO<sub>2</sub>/CO environment at +100 mV is the same as seen in pure CO<sub>2</sub>.

Again, the high frequency resistance (R1) in the CO<sub>2</sub>/CO environment is ascribed to the oxygen anion exchange at the underlying LSFcr/GDC interface, as was also the case in the 100% CO<sub>2</sub> and discussed in Chapters 5 and 6. Also, the high frequency C1 values are typical of interfacial capacitances of this kind (10<sup>-5</sup> F/cm<sup>2</sup>), as was also the case in 100% CO<sub>2</sub>.

**Table 7.2 Fitted parameters\* from Figure 7.5a\*\* using the Rs(R1CPE1)(R2CPE2) equivalent circuit model (Figure 7.5c).**

Potential (mV)	R1 (Ω cm <sup>2</sup> )	C1 <sup>#</sup> (F/cm <sup>2</sup> )	n1	R2 (Ω cm <sup>2</sup> )	C2 <sup>#</sup> (F/cm <sup>2</sup> )	n2	Rp <sup>\$</sup> (Ω cm <sup>2</sup> )
OCP	0.31	5.8x10 <sup>-5</sup>	0.52	0.57	0.47	0.65	0.87
+100	0.41	4.8x10 <sup>-5</sup>	0.53	0.94	0.26	0.63	1.4
-100	0.16	9.1x10 <sup>-5</sup>	0.65	0.51	0.86	0.66	0.67

\* (R1, C1, n1) and (R2, C2, n2) from high (10 kHz) and low (1 Hz) frequency arcs, respectively.

\*\* 3-electrode (LSFcr) half cell, operated at 800 °C in 30% CO<sub>2</sub>:30% CO:40% N<sub>2</sub>.

# C1 and C2 represent the capacitance in the high and low frequencies arcs, respectively, and were calculated using Equation 4.2.

\$ Rp = R1+R2. Rp values may not add up due to internal rounding.

Figure 7.6 shows the CV of the LSFCr WE in 30% CO<sub>2</sub>:30% CO:40% N<sub>2</sub> at 1 mV/s at 800 °C. It is interesting to note that much higher current densities are again observed in the negative scan during the reduction of CO<sub>2</sub> to CO than in the positive scan during the oxidation of CO to CO<sub>2</sub>. This shows that CO oxidation is slower than CO<sub>2</sub> reduction at LSFCr electrodes, consistent with the impedance data (Figure 7.5, Table 7.2) and perhaps suggesting that a CO adsorption step is the rate limiting step. Even so, the performance of the LSFCr electrode towards CO oxidation is quite good, comparable to what has been reported for other types of perovskites, such as La<sub>1-x</sub>Sr<sub>x</sub>Cr<sub>1-y</sub>Mn<sub>y</sub>O<sub>3-δ</sub><sup>103</sup>.

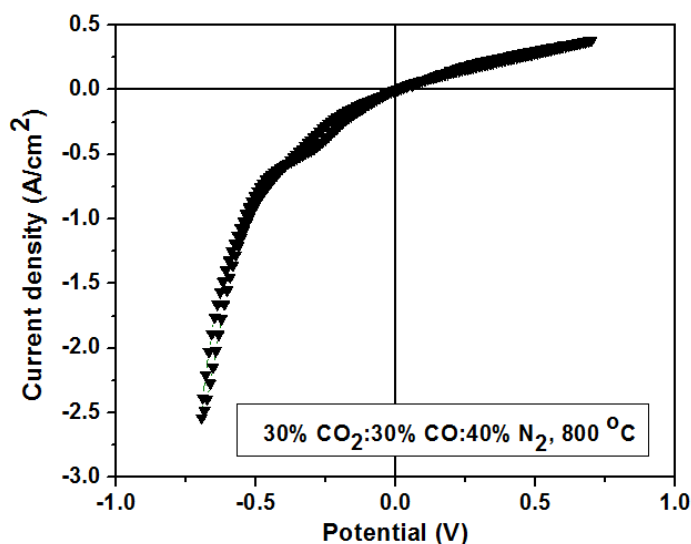


**Figure 7.6** Cyclic voltammetry (CV) data obtained for LSFCr WE in 3-electrode half cell at 800 °C in 30% CO<sub>2</sub>:30% CO:40% N<sub>2</sub> at 1 mV/s.

It is also interesting that the CO<sub>2</sub> reduction currents are roughly 10 times higher in the 30% CO<sub>2</sub>:30% CO mixture (Figure 7.6) than in 100% CO<sub>2</sub> (Figure 7.4), perhaps due to the fact that the LSFCr material (WE and RE) is in a different redox state in these two CO<sub>2</sub>-containing environments. The potential of the CO<sub>2</sub>/CO equilibrium (0 V in Figure 7.6) is ca. 670 mV more

negative (more reducing) than in pure CO<sub>2</sub>, arguing that a higher concentration of Fe<sup>3+</sup> should be present at the surface, according to Reaction 7.7.



where Fe'\_{Fe} represents the Fe<sup>3+</sup> cations and Fe<sup>x</sup>\_{Fe} represents the Fe<sup>4+</sup> cations. According to Reaction 7.7, an increase in the surface concentration of Fe<sup>3+</sup> sites and of oxygen vacancies should favour the reduction of CO<sub>2</sub>. It has been reported that near surface oxygen vacancies are energetically favourable for CO<sub>2</sub> activation<sup>255</sup>. This is in agreement with the explanation given for the magnitude of R2 and C2 in Table 7.2, where a lower R2 and higher C2 are seen at -100 mV polarization vs. at the OCP. The excellent performance in the cathodic direction during CO<sub>2</sub> reduction could potentially also be due to preferential adsorption of CO<sub>2</sub> on the active sites.

To further analyze the CV data, the low field exchange current density (*i*<sub>0</sub>) was obtained from the slope of the *i*-*V* plot (Figure 7.6) within ± 50 mV of the OCP, based on Equation 7.8:

$$i_0 = \frac{RT\nu}{nF} slope = \frac{RT\nu}{nFR_p} \quad (7.8)$$

where *i*<sub>0</sub> is the exchange current density, R is the gas constant, T is temperature, F is the Faraday constant, n is the number of electrons, ν is the number of occurrence of the rate limiting step, and R<sub>p</sub> is the polarization resistance. For the CO<sub>2</sub>/CO reduction reaction, n and ν were assumed to be 2 and 1, respectively (as the total number of electrons passed per molecule (n) of CO<sub>2</sub> reduced is 2 and the number of occurrence of the rds (ν) would probably be 1).

The *i*<sub>0</sub> values obtained from the low field CV analysis were then compared to the *i*<sub>0</sub> values obtained from the EIS-determined R<sub>p</sub> values at the OCP (using Equation 7.8) (Table 7.2), giving fairly similar values, i.e., 41 mA/cm<sup>2</sup> from CV and 53 mA/cm<sup>2</sup> from the impedance data. These high *i*<sub>0</sub> values are fully consistent with the excellent activity of the LSFCr catalyst towards

the CO/CO<sub>2</sub> redox process. Notably, the high field Butler Volmer approximation was not used here because it is questionable if Butler Volmer formalisms can be applied to electrochemical data acquired at a WE material that is changing its composition (and catalytic activity) over the potential range being analysed.

Overall, in 30% CO<sub>2</sub>:30% CO:40% N<sub>2</sub> environments at 800 °C, the 3-electrode work described in Section 7.2.4 has confirmed that, under cathodic polarization, the LSF<sub>Cr</sub> WE is more active for the reduction of CO<sub>2</sub> than the oxidation of CO under anodic polarization, giving both a lower polarization resistance and higher current density values. Because the CO<sub>2</sub> and CO partial pressures were the same in this work, this indicates that there are intrinsic differences in the reaction mechanism or in the energetics related to the interactions of these two gases at the LSF<sub>Cr</sub> surface. It is also possible that Fe and Cr are in different oxidation states at positive and negative overpotentials, thus influencing the catalyst reactivity.

### ***7.2.5 Performance of LSF<sub>Cr</sub> WE in fixed CO content (balance CO<sub>2</sub>)***

Figure 7.7 shows that open circuit potential (OCP) R<sub>p</sub> value increases slightly when the CO content was fixed but the CO<sub>2</sub> content was increased from 30 % to 70%, balance N<sub>2</sub>. The fact that only a small change is seen could make sense, as the Nernst equilibrium potential is expected to be quite similar in these two environments. Even so, it is seen that the low frequency arc resistance increases slightly when the CO<sub>2</sub> content is increased, contrary to expectations. The low frequency resistance (R<sub>2</sub>) is attributed to surfaces processes (adsorption, dissociation, electron transfer) occurring on the LSF<sub>Cr</sub> catalyst and increases slightly from 0.57 Ω cm<sup>2</sup> to 0.62 Ω cm<sup>2</sup> with an increase in CO<sub>2</sub> content. It is possible that adsorbed CO<sub>2</sub> is adsorbing fairly strongly on the surface of LSF<sub>Cr</sub>, leading to this slight decrease in performance. This is

consistent with the FTIR spectroscopy results in Chapter 6 (Figure 6.5), where a small band corresponding to the asymmetric stretching mode of the C-O bond was observed at  $1471\text{ cm}^{-1}$  when LSFCr powder was exposed to pure  $\text{CO}_2$  for 24 h at  $800\text{ }^\circ\text{C}$ .

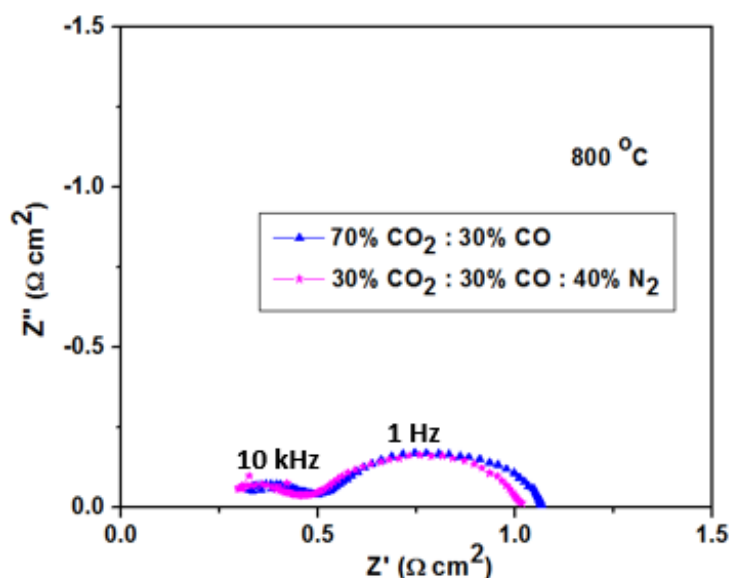


**Figure 7.7** OCP EIS response of LSFCr in 3-electrode half cell, operated at  $800\text{ }^\circ\text{C}$  in either  $70\% \text{CO}_2:30\% \text{CO}$  or  $30\% \text{CO}_2:30\% \text{CO}:40\% \text{N}_2$  environments.

### 7.2.6 Effect of more extreme cathodic polarization of LSFCr WE on $\text{CO}_2$ reduction

The effect of more extreme negative polarization on the activity of the LSFCr WE on  $\text{CO}_2$  reduction in a  $90\% \text{CO}_2:10\% \text{CO}$  gas mixture at  $800\text{ }^\circ\text{C}$  was evaluated in more detail to obtain more insight into how the high (R1CPE1) and the low frequency (R2CPE2) processes would be affected. Figure 7.8 shows the impedance data acquired at the OCP and under negative bias. From Figure 7.8a, the  $R_p$  is seen to decrease quite significantly with polarization. As expected, the negative bias affects mainly the low frequency resistance, causing R2 (related to the  $\text{CO}_2$  adsorption/dissociation/reduction process at the LSFCr surface) to decrease with increasing polarization (OCP to  $-300\text{ mV}$ , Table 7.3), while the resistance associated with the high frequency process (R1, related to the underlying GDC/LSFCr interface) remains essentially

unchanged. This behavior is clearly seen in the phase angle Bode plot (Figure 7.8b), where the low frequency process at 1 Hz changes more than does the high frequency process (10 kHz).

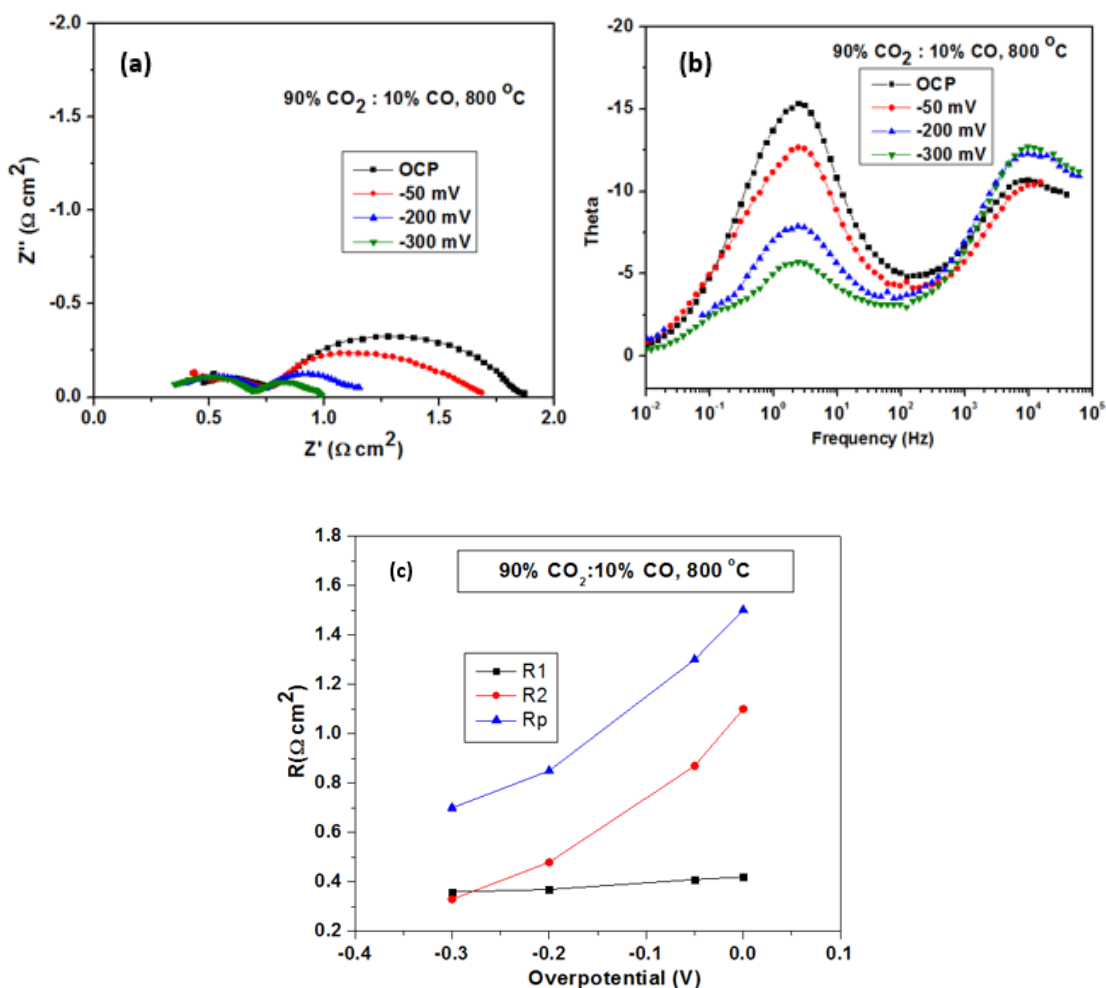


**Figure 7.8 OCP and negatively polarized EIS response of LSF-Cr WE in 3-electrode half cell, operated at 800 °C in 90% CO<sub>2</sub>:10% CO, showing (a) the Nyquist plots, (b) the phase angle Bode plots, and (c) the resistance vs. overpotential plot.**

To quantify and then better understand the trends of the various parameters ( $R$ ,  $n$  and  $C$ ) that were obtained with negative polarization, the Nyquist plots (Figure 7.8a) were fitted with the  $R_s(R_1CPE_1)(R_2CPE_2)$  equivalent circuit model (Figure 7.5c). Table 7.3 shows the fitted parameters, while Figure 7.8c shows a plot of the resistances obtained from the fitting vs.

overpotential. From Table 7.3 and Figure 7.8c, it is seen that there is a slight decrease in R1, related to the oxide ion charge transfer at the electrode/electrolyte interface, with increasing polarization. As stated earlier, C1 can be ascribed to interfacial capacitance because of its low value ( $10^{-5}$  F/cm<sup>2</sup>), as seen in Table 7.3.

From Figure 7.8c, it is seen that R<sub>p</sub> is dominated by the low frequency resistance (R2). Table 7.3 shows that R2 decreased from ca. 1.1 Ω cm<sup>2</sup> at OCP (0 mV) to 0.30 Ω cm<sup>2</sup> at -300 mV bias, while C2 increased from 0.14 F/cm<sup>2</sup> at OCP to 0.37 F/cm<sup>2</sup> at -300 mV. The increase in C2 with increasing negative bias can be attributed to an increase in the number of oxygen vacancies with polarization, as expected for chemical capacitance behavior (discussed in Section 7.2.3). Again, R2 is probably due to the adsorption/dissociation/reduction of CO<sub>2</sub> at the gas/electrode interface, as indicated earlier (Section 7.2.3) and in Figure 7.3a.

**Table 7.3 Fitted parameters\* from Figure 7.8a\*\* using the R<sub>s</sub>(R1CPE1)(R2CPE2) equivalent circuit model (Figure 7.3c).**

Potential (mV)	R1 (Ω cm <sup>2</sup> )	n1	C1 (F/cm <sup>2</sup> )	R2 (Ω cm <sup>2</sup> )	C2 (F/cm <sup>2</sup> )	n2	R <sub>p</sub> (Ω cm <sup>2</sup> )
OCP	0.42	0.56	6.4 x 10 <sup>-05</sup>	1.1	0.14	0.71	1.5
-50	0.41	0.60	4.9 x 10 <sup>-05</sup>	0.87	0.19	0.65	1.3
-200	0.37	0.59	6.0 x 10 <sup>-05</sup>	0.48	0.31	0.68	0.85
-300	0.36	0.65	6.1 x 10 <sup>-05</sup>	0.33	0.37	0.62	0.70

\*(R1, C1, n1) and (R2, C2, n2) obtained from the high (10 kHz) and low (1 Hz) frequency arcs, respectively.

\*\* 3-electrode (LSFCr) half cell, operated at 800 °C in 90% CO<sub>2</sub>:10% CO.

# C1 and C2 represent the capacitance in the high and low frequencies arcs, respectively, and were calculated using Equation 4.3.

### 7.3 Summary

In this chapter, the electrochemical performance of the mixed conducting  $\text{La}_{0.3}\text{Sr}_{0.7}\text{Fe}_{0.7}\text{Cr}_{0.3}\text{O}_{3-\delta}$  (LSFCr) perovskite has been studied in detail, both at open circuit and under polarization, in a 3-electrode half cell configuration in pure  $\text{CO}_2$  and  $\text{CO}_2/\text{CO}$  mixtures at 800 °C. The 3-electrode half cell configuration allowed for the isolation of the electrochemical processes occurring at the LSFCr working electrode (WE) during  $\text{CO}_2$  reduction and CO oxidation. It is shown, using impedance spectroscopy (EIS) and cyclic voltammetry (CV), that the performance of this material in all of these gas environments is very good. The study also showed conclusively that LSFCr is a better catalyst for  $\text{CO}_2$  reduction than for CO oxidation, indicating an overall better performance in the electrolysis vs. fuel cell mode, consistent with what was observed in Chapter 6. This may be related to the different oxidation state (density of oxygen vacancies) of the LSFCr surface under these two conditions.

The low frequency arc, now arising only from the LSFCr WE, is ascribed to surface processes occurring at the gas/LSFCr electrode interface, while the high frequency arc appears to relate to oxide ion transfer at the underlying LSFCr electrode/GDC electrolyte interface. The surface processes within R2 include the adsorption and dissociation of the  $\text{CO}_2$  and CO gas molecules and desorption of products, and electron transfer steps. As expected, it was observed that both the high (R1) and low (R2) resistances decreased with increasing cathodic overpotential. However, R2 was strongly influenced by increasing overpotential, consistent with what is expected for charge transfer reactions.

In both  $\text{CO}_2$  and  $\text{CO}/\text{CO}_2$  environments, there was good evidence for the presence of a chemical capacitance (low frequency capacitor, C2), as also seen from the significant effect of the reducing atmosphere ( $\text{CO}_2$  vs.  $\text{CO}_2/\text{CO}$ ) on the rate of the  $\text{CO}/\text{CO}_2$  redox reactions. This was

ascribed to changes in the oxidation state of the Fe component (and related changes in the oxide ion vacancy concentration) of LSF<sub>Cr</sub> in these different gas environments.

## Chapter Eight: **Conclusions and Suggested Future Work**

### **8.1 Main conclusions of this thesis work**

The main focus of this thesis was to develop high performance sulfur and coke tolerant fuel electrodes for reversible solid oxide fuel cell (RSOFC) applications. RSOFCs are single units that can run in both the solid oxide fuel cell (SOFC) and solid oxide electrolysis cell (SOEC) modes. The conventional fuel electrode for use in RSOFCs is Ni-yttria-stabilized zirconia (YSZ). However, in both SOFC and SOEC modes, they are susceptible to sulfur poisoning at operating conditions (Chapter 4). Therefore, the development of sulfur tolerant fuel electrode materials, such as  $\text{La}_{0.3}\text{M}_{0.7}\text{Fe}_{0.7}\text{Cr}_{0.3}\text{O}_{3-\delta}$  ( $\text{M} = \text{Sr}, \text{Ca}, (\text{LMFCr})$ ), is very important (Chapter 5).

In this thesis work, a key outcome has been the demonstration that both  $\text{La}_{0.3}\text{Ca}_{0.7}\text{Fe}_{0.7}\text{Cr}_{0.3}\text{O}_{3-\delta}$  (LCFCr) and  $\text{La}_{0.3}\text{Sr}_{0.7}\text{Fe}_{0.7}\text{Cr}_{0.3}\text{O}_{3-\delta}$  (LSFCr) perovskites are very good electrocatalysts for use as fuel electrodes for RSOFC applications. This was confirmed in a range of gases, including humidified  $\text{H}_2$  and in  $\text{CO}_2/\text{CO}$  mixtures. In all cases, the observed  $R_p$  values are at least as good as or better than reported for other metal oxide-based electrodes, such as  $\text{La}_{1-x}\text{Sr}_x\text{Cr}_{1-y}\text{M}_y\text{O}_{3-\delta}-\text{Gd}_x\text{Ce}_{1-x}\text{O}_{2-\delta}$  (LSCM-GDC)<sup>102</sup>

Another novel and important contribution has been in showing and understanding the unusual effects of ppm levels of  $\text{H}_2\text{S}$  on Ni-YSZ and LMFCr electrodes as a function of temperature. In Chapters 4 and 5, an extensive study was carried out to understand the effect of low ppm levels of  $\text{H}_2\text{S}$  on the electrochemical performance of Ni-YSZ and LMFCr fuel electrodes, operated on humidified  $\text{H}_2$ , with or without the addition of  $\leq 10$  ppm  $\text{H}_2\text{S}$ , over a temperature range of 500-800 °C. In Chapter 4, the electrochemical investigation of a Ni-YSZ fuel electrode, based on a 3-electrode half cell configuration, showed that at  $\leq 650$  °C, exposure

to  $\leq 10$  ppm  $\text{H}_2\text{S}$  led to an unexpected activation of the hydrogen oxidation reaction (HOR), while at temperatures  $> 650$  °C,  $\text{H}_2\text{S}$  exposure led to deactivation of the performance of the cell. This activation seen at  $\leq 650$  °C was surprising, because it has been reported that the extent of  $\text{H}_2\text{S}$  poisoning of Ni-YSZ fuel electrodes should be more severe at lower temperatures. Therefore, various surface and bulk characterization techniques and density function theory calculations (DFT) were employed to further understand this activation behaviour. Based on these analyses, it was concluded that a Ni-S species (e.g.,  $\text{Ni}_3\text{S}_2$ ) may have formed locally at the triple phase boundary (TPB) with YSZ, where the  $\text{pH}_2$  could be depleted, thus lowering the energy barrier for  $\text{H}_2$  oxidation, as shown by density functional theory calculations.

In Chapter 5, the opposite trend was observed when a  $\text{La}_{0.3}\text{Ca}_{0.7}\text{Fe}_{0.7}\text{Cr}_{0.3}\text{O}_{3-\delta}$  (LCFCr) fuel electrode was exposed to  $\leq 10$  ppm  $\text{H}_2\text{S}$ , using both symmetrical half and full cell configurations. Now, activation of the HOR was seen at  $> 700$  °C, while deactivation behavior was observed at  $\leq 700$  °C. Based primarily on XPS analysis, it was suggested that the activation was due to an increase in the density of surface terminated- $\text{FeO}_2$  species, thereby improving the HOR rate. Importantly, it was shown that the S poisoning observed at lower temperatures could be very rapidly reversed, arguing again that  $\text{H}_2\text{S}$  exposure modified only the surface of the LCFCr electrode.

Another important outcome of this thesis work is related to the rigorous and first time study of the chemical stability and electrochemical performance of  $\text{La}_{0.3}\text{Sr}_{0.7}\text{Fe}_{0.7}\text{Cr}_{0.3}\text{O}_{3-\delta}$  (LSFCr) as a fuel electrode in  $\text{CO}_2/\text{CO}$  environments, investigated in Chapters 6 and 7. The primary conclusion of Chapter 6 was that the LSFCr material is structurally stable in pure  $\text{CO}_2$ , with no formation of any carbonate species, while in 70%  $\text{CO}_2$ :30%  $\text{CO}$  environment, minor impurities were observed. However, these impurities did not have any negative effect on the

electrochemical performance of the cell. Also, it was shown that exposure of LSF<sub>Cr</sub> to CO/N<sub>2</sub> atmospheres led to the formation of secondary phases, such as a LaSrFeO<sub>4</sub>-based phase (K<sub>2</sub>NiF<sub>4</sub>), as well as carbon deposition. However, the perovskite phase could be recovered when the decomposed powder was re-exposed to air. Even so, Chapter 6 showed that a symmetrical RSOFC, based on two LSF<sub>Cr</sub> electrodes, with CO<sub>2</sub>/CO mixtures fed to the fuel electrode and the oxygen electrode exposed to air, exhibited better performance than other perovskites-based electrodes reported in the literature<sup>102</sup> (e.g., La<sub>1-x</sub>Sr<sub>x</sub>Cr<sub>1-y</sub>M<sub>y</sub>O<sub>3-δ</sub>-Gd<sub>x</sub>Ce<sub>1-x</sub>O<sub>2-δ</sub> (LSCM-GDC)).

Chapter 7 explored the reliability of using a 3-electrode half cell configuration to understand the various electrochemical processes occurring at the LSF<sub>Cr</sub> working electrode (WE). A careful comparison of the impedance data from a 2-electrode half cell and a full cell vs. the 3-electrode half cell was made, showing good agreement in the polarization resistance values. This argued that the data collected in Chapter 7 using the 3-electrode half cell configuration for the CO<sub>2</sub>/CO reactions at the LSF<sub>Cr</sub> WE were reliable. This allowed the conclusion to be reached that the LSF<sub>Cr</sub> electrocatalyst is intrinsically more active for the reduction of CO<sub>2</sub> than for CO oxidation.

Overall, this thesis has shown that, in the presence of low ppm H<sub>2</sub>S, the rate of the hydrogen oxidation reaction (HOR) is enhanced at lower temperatures ( $\leq 650$  °C) for Ni-YSZ fuel electrodes and at higher temperature ( $> 700$  °C) for the LCF<sub>Cr</sub> fuel electrodes. Also, it was shown that LSF<sub>Cr</sub>-based RSOFCs can be operated in CO<sub>2</sub>/CO mixtures in both the SOFC and SOEC modes, with a somewhat better performance observed in the SOEC mode than in the SOFC mode.

## 8.2 Suggestions for future work.

The following are some of the research ideas that could be further investigated:

- (a) Improved characterization of Ni-YSZ and  $\text{La}_{0.3}\text{M}_{0.7}\text{Fe}_{0.7}\text{Cr}_{0.3}\text{O}_{3-\delta}$  (M = Sr, Ca, (LMFCr)) fuel electrodes

Although quite a range of techniques were used in this thesis to try to understand what was causing the enhancement of the hydrogen oxidation reaction (HOR), seen for both Ni-YSZ and  $\text{La}_{0.3}\text{Ca}_{0.7}\text{Fe}_{0.7}\text{Cr}_{0.3}\text{O}_{3-\delta}$  (LCFCr), in the presence of low ppm  $\text{H}_2\text{S}$ , the use of additional approaches could be useful. This could include aberration-corrected transmission electron microscopy (TEM) with electron energy loss spectroscopy (EELS) to investigate the structural and chemical changes occurring at the Ni-YSZ interface and on the LCFCr material at the nanoscale level, with and without the presence of  $\text{H}_2\text{S}$ . Also, an *in situ* high temperature XPS analysis of Ni-YSZ and LCFCr in the presence of  $\text{H}_2\text{S}$  would be very useful. Furthermore, a comparison of the sulfur tolerance of LCFCr and LSFcr should be made. Further, density functional theory (DFT) calculations of the interaction of  $\text{H}_2\text{S}$  with LMFCr and its effect on the hydrogen oxidation reaction, at varying temperatures, should be carried out to help further understand the experimental results.

- (b) Chemical stability of LMFCr in  $\text{CO}_2$  and  $\text{CO}_2/\text{CO}$  environments

This thesis only reported the chemical stability of LSFcr in  $\text{CO}_2/\text{CO}$  atmospheres. Therefore, a study of the chemical stability of the Ca analog (LCFCr) should also be investigated in these gases. A detailed high resolution transmission electron microscopy (HRTEM) analysis for both of the LSFcr and LCFCr materials should be carried out to fully understand the structural

stability of these perovskites in CO<sub>2</sub>/CO and CO/N<sub>2</sub> atmospheres. A detailed study of the carbon deposition and the coke tolerant behaviour of LMFCr should also be carried out.

(c) In-operando atmospheric pressure (AP)-XPS analysis of LMFCr in CO<sub>2</sub>/CO

An in-operando AP-XPS analysis of the LMFCr-half cells should be carried out to better understand the reaction mechanisms during CO<sub>2</sub> reduction and CO oxidation at the LMFCr working electrode (WE), as well as the redox chemistry of the LMFCr during operation.

(d) Electrolysis of H<sub>2</sub>O and/or CO<sub>2</sub> based on LMFCr RSOFC

It was demonstrated in this work that LSFCr is a good electrocatalyst for CO<sub>2</sub> reduction and CO oxidation. However, its stability and performance in high steam contents is still lacking. Therefore, the performance and long term stability (e.g., 1000 h) of the LMFCr-based RSOFCs for the co-electrolysis of H<sub>2</sub>O/CO<sub>2</sub> to synthesis gas should be investigated. Further, a rigorous gas composition analysis of the output gas during co-electrolysis should also be performed.

(e) Improving stability of LMFCr in reducing atmospheres

It was shown in Chapter 6 that LMFCr is unstable in highly reducing atmospheres. Thus, methods to improve the stability, e.g., the addition of ceria to the electrode material, should be investigated.

## References

1. M. Asif and T. Muneer, *Renew Sust Energ Rev*, 2007, **11**, 1388-1413.
2. W. Krewitt, S. Teske, S. Simon, T. Pregger, W. Graus, E. Blomen, S. Schmid and O. Schafer, *Energ Policy*, 2009, **37**, 5764-5775.
3. J. L. Sawin and F. Sverrisso, *Renewables 2016 Global Status Report*, Renewable Energy Policy for the 21st Century (REN21), Paris, France, 2016.
4. EIA, *International Energy Outlook 2016* Washington, DC, May 2016.
5. R. K. Pachauri and Y. K. Chauhan, *Renew Sust Energ Rev*, 2015, **43**, 1301-1319.
6. H. T. A. E.-S. Handal, PhD, University of Calgary, 2015.
7. GCI, *The Global Status of CCS 2016 Summary Report*, Global CCS Institute (GCI), Docklands, Australia, 2016.
8. IEA, *Energy Technology Perspectives 2016: Towards Sustainable Urban Energy Systems*, OECD/IEA, Paris, France, 2016.
9. R. M. Cuellar-Franca and A. Azapagic, *Journal of CO<sub>2</sub> Utilization*, 2015, **9**, 82-102.
10. R. M. Cuellar-Franca and A. Azapagic, *J Co2 Util*, 2015, **9**, 82-102.
11. M. Extavour and P. Bunje, *Chem Eng Prog*, 2016, **112**, 52-59.
12. M. Azuma, K. Hashimoto, M. Hiramoto, M. Watanabe and T. Sakata, *J Electrochem Soc*, 1990, **137**, 1772-1778.
13. Y. Hori, in *Modern Aspects of Electrochemistry*, eds. C. G. Vayenas, R. E. White and M. E. Gamboa-Aldeco, Springer New York, New York, NY, 2008, pp. 89-189.
14. J. Qiao, Y. Liu, F. Hong and J. Zhang, *Chem Soc Rev*, 2014, **43**, 631-675.
15. M. A. Laguna-Bercero, *J Power Sources*, 2012, **203**, 4-16.
16. J. C. Ruiz-Morales, D. Marrero-Lopez, J. Canales-Vazquez and J. T. S. Irvine, *Rsc Adv*, 2011, **1**, 1403-1414.
17. D. M. Bierschenk, J. R. Wilson and S. A. Barnett, *Energ Environ Sci*, 2011, **4**, 944-951.
18. H. S. Spacil and C. S. Tedmon, *J Electrochem Soc*, 1969, **116**, 1618-1626.
19. W. Oser, *Electrochemical method for conversion of carbon dioxide*, USPTO 3316163 A, 1967.
20. K. R. Sridhar and R. Foerstner, *J Propul Power*, 2000, **16**, 1105-1111.
21. K. R. Sridhar, C. S. Iacomini and J. E. Finn, *J Propul Power*, 2004, **20**, 892-901.
22. K. R. Sridhar and B. T. Vaniman, *Solid State Ionics*, 1997, **93**, 321-328.
23. W. Donitz and R. Streicher, *Chem-Ing-Tech*, 1980, **52**, 436-438.
24. Y. Matsuzaki and I. Yasuda, *Solid State Ionics*, 2000, **132**, 261-269.
25. H. P. He and J. M. Hill, *Appl Catal a-Gen*, 2007, **317**, 284-292.
26. P. Tanasini, M. Cannarozzo, P. Costamagna, A. Faes, J. Van Herle, A. Hessler-Wyser and C. Comminellis, *Fuel Cells*, 2009, **9**, 740-752.
27. F. Bidrawn, G. Kim, G. Corre, J. T. S. Irvine, J. M. Vohs and R. J. Gorte, *Electrochem Solid St*, 2008, **11**, B167-B170.
28. N. Q. Minh, *Ecs Transactions*, 2011, **35**, 2897-2904.
29. S. Gamble, *Mater Sci Tech-Lond*, 2011, **27**, 1485-1497.
30. N. Q. Minh and M. B. Mogensen, *Electrochemical Society Interface*, 2013, **22**, 55-62.
31. A. B. Stambouli and E. Traversa, *Renewable and Sustainable Energy Reviews*, 2002, **6**, 433-455.
32. S. D. Ebbesen, C. Graves and M. Mogensen, *Int J Green Energy*, 2009, **6**, 646-660.

33. C. Graves, S. D. Ebbesen, M. Mogensen and K. S. Lackner, *Renew Sust Energ Rev*, 2011, **15**, 1-23.
34. H. Uchida, N. Osada and M. Watanabe, *Electrochem Solid St*, 2004, **7**, A500-A502.
35. A. Hauch, S. H. Jensen, S. Ramousse and M. Mogensen, *J Electrochem Soc*, 2006, **153**, A1741-A1747.
36. S. H. Jensen, P. H. Larsen and M. Mogensen, *Int J Hydrogen Energ*, 2007, **32**, 3253-3257.
37. F. Bidrawn, G. Kim, G. Corre, J. T. S. Irvine, J. M. Vohs and R. J. Gorte, *Electrochem Solid St*, 2008, **11**, B167-B170.
38. P. K. Addo, B. Molero-Sanchez, M. Chen, S. Paulson and V. Birss, *Fuel Cells*, 2015, **15**, 689-696.
39. R. D. Green, C. C. Liu and S. B. Adler, *Solid State Ionics*, 2008, **179**, 647-660.
40. S. D. Ebbesen and M. Mogensen, *J Power Sources*, 2009, **193**, 349-358.
41. C. M. Stoots, J. E. O'Brien, J. S. Herring and J. J. Hartvigsen, *J Fuel Cell Sci Tech*, 2009, **6**.
42. Y. H. Li, P. Li, B. B. Hu and C. R. Xia, *J Mater Chem A*, 2016, **4**, 9236-9243.
43. C. Graves, S. D. Ebbesen and M. Mogensen, *Solid State Ionics*, 2011, **192**, 398-403.
44. Z. Zhan, W. Kobsiriphat, J. R. Wilson, M. Pillai, I. Kim and S. A. Barnett, *Energ Fuel*, 2009, **23**, 3089-3096.
45. A. Wood, H. P. He, T. Joia, M. Krivy and D. Steedman, *J Electrochem Soc*, 2016, **163**, F327-F329.
46. M. Chen, S. Paulson, V. Thangadurai and V. Birss, *J Power Sources*, 2013, **236**, 68-79.
47. Q. Zhou, C. Yuan, D. Han, T. Luo, J. L. Li and Z. L. Zhan, *Electrochim Acta*, 2014, **133**, 453-458.
48. C. Su, W. Wang, M. Liu, M. O. Tadé and Z. Shao, *Adv Energy Mater*, 2015, **5**, 1500188.
49. J. Canales-Vazquez, J. C. Ruiz-Morales, D. Marrero-Lopez, J. Pena-Martinez, P. Nunez and P. Gomez-Romero, *J Power Sources*, 2007, **171**, 552-557.
50. Z. Q. Cao, B. Wei, J. P. Miao, Z. H. Wang, Z. Lu, W. Y. Li, Y. H. Zhang, X. Q. Huang, X. B. Zhu, Q. Feng and Y. Sui, *Electrochem Commun*, 2016, **69**, 80-83.
51. Y. Wang, T. Liu, S. M. Fang and F. L. Chen, *J Power Sources*, 2016, **305**, 240-248.
52. Z. H. Ma, C. W. Sun, C. Ma, H. Wu, Z. L. Zhan and L. Q. Chen, *Chinese J Catal*, 2016, **37**, 1347-1353.
53. C. M. Chanquia, A. Montenegro-Hernandez, H. E. Troiani and A. Caneiro, *J Power Sources*, 2014, **245**, 377-388.
54. T. L. Cable and S. W. Sofie, *J Power Sources*, 2007, **174**, 221-227.
55. B. Molero-Sanchez, P. Addo, A. Buyukaksoy, S. Paulson and V. Birss, *Faraday Discuss*, 2015, **182**, 159-175.
56. P. Addo, B. Molero-Sanchez, A. Buyukaksoy, S. Paulson and V. Birss, *Ecs Transactions*, 2015, **66**, 219-228.
57. B. Molero-Sanchez, J. Prado-Gonjal, D. Avila-Brande, M. Chen, E. Moran and V. Birss, *Int J Hydrogen Energ*, 2015, **40**, 1902-1910.
58. R. O'Hayre, S.-W. Cha, W. Colella and F. B. Prinz, *Fuel cell fundamentals*, John Wiley & Sons, Inc., New Jersey, 2nd edn., 2009.
59. S. Srinivasan, *Fuel cells from fundamentals to applications*, Springer, 2006.
60. S. Y. Gomez and D. Hotza, *Renew Sust Energ Rev*, 2016, **61**, 155-174.

61. C. H. Wendel, P. Kazempoor and R. J. Braun, *J Power Sources*, 2016, **301**, 93-104.
62. S. H. Jensen, C. Graves, M. Mogensen, C. Wendel, R. Braun, G. Hughes, Z. Gao and S. A. Barnett, *Energ Environ Sci*, 2015, **8**, 2471-2479.
63. S. D. Ebbesen, R. Knibbe and M. Mogensen, *J Electrochem Soc*, 2012, **159**, F482-F489.
64. S. D. Ebbesen and M. Mogensen, *ECS Transactions*, 2013, **50**, 167-182.
65. P. Mocoteguy and A. Brisse, *Int J Hydrogen Energ*, 2013, **38**, 15887-15902.
66. S. C. Singhal, *Solid State Ionics*, 2000, **135**, 305-313.
67. A. Hauch, K. Brodersen, M. Chen and M. B. Mogensen, *Solid State Ionics*, 2016, **293**, 27-36.
68. A. Hauch, A. Hagen, J. Hjelm and T. Ramos, *ECS Transactions*, 2013, **57**, 615-625.
69. A. Hauch, M. Mogensen and A. Hagen, *Solid State Ionics*, 2011, **192**, 547-551.
70. A. Hauch, P. S. Jorgensen, K. Brodersen and M. Mogensen, *J Power Sources*, 2011, **196**, 8931-8941.
71. R. Knibbe, M. L. Traulsen, A. Hauch, S. D. Ebbesen and M. Mogensen, *J Electrochem Soc*, 2010, **157**, B1209-B1217.
72. A. Hauch and M. Mogensen, *Solid State Ionics*, 2010, **181**, 745-753.
73. S. D. Ebbesen, C. Graves, A. Hauch, S. H. Jensen and M. Mogensen, *J Electrochem Soc*, 2010, **157**, B1419-B1429.
74. A. Hauch, S. H. Jensen, J. B. Bilde-Sorensen and M. Mogensen, *J Electrochem Soc*, 2007, **154**, A619-A626.
75. C. M. Kim, J. Kim and K. Park, *Powder Technol*, 2014, **254**, 425-431.
76. A. Buyukaksoy, V. Petrovsky and F. Dogan, *J Electrochem Soc*, 2013, **160**, F482-F486.
77. G. Tao, K. R. Sridhar and C. L. Chan, *Solid State Ionics*, 2004, **175**, 621-624.
78. X. Wang, K. Li, L. C. Jia, Q. Zhang, S. P. Jiang, B. Chi, J. Pu, L. Jian and D. Yan, *J Power Sources*, 2015, **277**, 474-479.
79. S. J. Wang, A. Inoishi, J. Hong, Y. Ju, H. Hagiwara, S. Ida and T. Ishihara, *J Mater Chem A*, 2013, **1**, 12455-12461.
80. Y. W. Ju, S. Ida, T. Inagaki and T. Ishihara, *J Power Sources*, 2011, **196**, 6062-6069.
81. H. C. Park and A. V. Virkar, *J Power Sources*, 2009, **186**, 133-137.
82. T. Ishihara, M. Shinagawa, A. Kawakami and H. Matsumoto, *Material Science Forum*, 2007, **539-543**, 1350-1355.
83. T. Ishihara, J. W. Yan, M. Shinagawa and H. Matsumoto, *Electrochim Acta*, 2006, **52**, 1645-1650.
84. T. Ishihara, S. Matsushita, T. Sakai and H. Matsumoto, *Solid State Ionics*, 2012, **225**, 77-80.
85. G. Tao, K. R. Sridhar and C. L. Chan, *Solid State Ionics*, 2004, **175**, 615-619.
86. J. Kim, S. Lee, K. H. Kang and H. S. Hong, *Int J Energ Res*, 2010, **34**, 438-444.
87. T. Ishihara, N. Jirathiwathanakul and H. Zhong, *Energ Environ Sci*, 2010, **3**, 665-672.
88. B. Mirfakhraei, PhD, University of Calgary, 2015.
89. R. Bernd and M. Hans-Heinrich, *Method of producing fuel cells with solid electrolytes and ceramic oxide electrode layers*, US3377203 A, 1968.
90. C. Graves, C. Chatzichristodoulou and M. B. Mogensen, *Faraday Discuss*, 2015, **182**, 75-95.
91. B. Mirfakhraei, V. Birss, V. Thangadurai, S. Paulson, K. E. Bere and F. Gitzhofer, *ECS Transactions*, 2011, **35**, 1727-1734.

92. H. T. Handal, P. Addo, A. Buyukaksoy, V. Birss and V. Thangadurai, *J Electrochem Soc*, 2016, **163**, F3091-F3098.
93. L. Zhu, R. Ran, M. Tade, W. Wang and Z. P. Shao, *Asia-Pac J Chem Eng*, 2016, **11**, 338-369.
94. J. Richter, P. Holtappels, T. Graule, T. Nakamura and L. J. Gauckler, *Monatsh Chem*, 2009, **140**, 985-999.
95. X. Z. Zhang, L. T. Ye, J. P. Hu, J. Li, W. H. Jiang, C. J. Tseng and K. Xie, *Electrochim Acta*, 2016, **212**, 32-40.
96. R. M. Xing, Y. R. Wang, Y. Q. Zhu, S. H. Liu and C. Jin, *J Power Sources*, 2015, **274**, 260-264.
97. Q. Q. Qin, C. Ruan, L. T. Ye, L. Z. Gan and K. Xie, *J Solid State Electr*, 2015, **19**, 3389-3399.
98. J. J. A. Flores, I. E. Cabrera, J. E. Valencia and A. R. Rojas, *Bol Soc Esp Ceram V*, 2015, **54**, 198-208.
99. Y. Song, Q. Zhong and W. Y. Tan, *Int J Hydrogen Energ*, 2014, **39**, 13694-13700.
100. S. S. Xu, S. S. Li, W. T. Yao, D. H. Dong and K. Xie, *J Power Sources*, 2013, **230**, 115-121.
101. Y. X. Li, Y. Gan, Y. Wang, K. Xie and Y. C. Wu, *Int J Hydrogen Energ*, 2013, **38**, 10196-10207.
102. X. L. Yue and J. T. S. Irvine, *Electrochem Solid St*, 2012, **15**, B31-B34.
103. X. L. Yue and J. T. S. Irvine, *J Electrochem Soc*, 2012, **159**, F442-F448.
104. X. L. Yue and J. T. S. Irvine, *Solid State Ionics*, 2012, **225**, 131-135.
105. J. C. Ruiz-Morales, J. Canales-Vazquez, D. Marrero-Lopez, J. T. S. Irvine and P. Nunez, *Electrochim Acta*, 2007, **52**, 7217-7225.
106. J. C. Ruiz-Morales, J. Canales-Vazquez, B. Ballesteros-Perez, J. Pena-Martinez, D. Marrero-Lopez, J. T. S. Irvine and P. Nunaz, *J Eur Ceram Soc*, 2007, **27**, 4223-4227.
107. S. W. Tao and J. T. S. Irvine, *J Electrochem Soc*, 2004, **151**, A252-A259.
108. V. Yurkiv, G. Constantin, A. Hornes, A. Gondolini, E. Mercadelli, A. Sanson, L. Dessemond and R. Costa, *J Power Sources*, 2015, **287**, 58-67.
109. X. W. Zhou, N. Yan, K. T. Chuang and J. L. Luo, *Rsc Adv*, 2014, **4**, 118-131.
110. Y. X. Li, J. E. Zhou, D. H. Dong, Y. Wang, J. Z. Jiang, H. F. Xiang and K. Xie, *Phys Chem Chem Phys*, 2012, **14**, 15547-15553.
111. S. S. Li, Y. X. Li, Y. Gan, K. Xie and G. Y. Meng, *J Power Sources*, 2012, **218**, 244-249.
112. K. B. Yoo and G. M. Choi, *Solid State Ionics*, 2009, **180**, 867-871.
113. S. Lee, G. Kim, J. M. Vohs and R. J. Gorte, *J Electrochem Soc*, 2008, **155**, B1179-B1183.
114. D. E. Fowler, J. M. Haag, C. Boland, D. M. Bierschenk, S. A. Barnett and K. R. Poeppelmeier, *Chem Mater*, 2014, **26**, 3113-3120.
115. D. M. Bierschenk, J. M. Haag, K. R. Poeppelmeier and S. A. Barnett, *J Electrochem Soc*, 2013, **160**, F90-F93.
116. J. M. Haag, D. M. Bierschenk, S. A. Barnett and K. R. Poeppelmeier, *Solid State Ionics*, 2012, **212**, 1-5.
117. M. Y. Gong, D. Bierschenk, J. Haag, K. R. Poeppelmeier, S. A. Barnett, C. C. Xu, J. W. Zondlo and X. B. Liu, *J Power Sources*, 2010, **195**, 4013-4021.

118. J. M. Haag, B. D. Madsen, S. A. Barnett and K. R. Poeppelmeier, *Electrochem Solid St*, 2008, **11**, B51-B53.
119. M. Chen, S. Paulson, W. H. Kan, V. Thangadurai and V. Birss, *J Mater Chem A*, 2015, **3**, 22614-22626.
120. B. Molero-Sanchez, J. Prado-Gonjal, D. Avila-Brande, V. Birss and E. Moran, *Ceram Int*, 2015, **41**, 8411-8416.
121. L. Kindermann, D. Das, D. Bahadur, R. Weiss, H. Nickel and K. Hilpert, *J Am Ceram Soc*, 1997, **80**, 909-914.
122. L. Kindermann, D. Das and H. Nickel, *Solid State Ionics*, 1996, **89**, 215-220.
123. L. Kindermann, D. Das, H. Nickel, K. Hilpert, C. C. Appel and F. W. Poulson, *J Electrochem Soc*, 1997, **144**, 717-720.
124. M. Gazda, P. Plonczak, S. Molin, B. Kusz and P. Jasinski, *Acta Phys Pol A*, 2008, **114**, 135-141.
125. A. Mai, V. A. C. Haanappel, F. Tietz and D. Stover, *Solid State Ionics*, 2006, **177**, 2103-2107.
126. N. Jordan, W. Assenmacher, S. Uhlenbruck, V. A. C. Haanappel, H. P. Buchkremer, D. Stover and W. Mader, *Solid State Ionics*, 2008, **179**, 919-923.
127. J. Kim, H. I. Ji, H. P. Dasari, D. Shin, H. Song, J. H. Lee, B. K. Kim, H. J. Je, H. W. Lee and K. J. Yoon, *Int J Hydrogen Energ*, 2013, **38**, 1225-1235.
128. H. Q. Wang, K. J. Yakal-Kremiski, T. Yeh, G. M. Rupp, A. Limbeck, J. Fleig and S. A. Barnett, *J Electrochem Soc*, 2016, **163**, F581-F585.
129. F. Y. Shen and K. Lu, *Electrochim Acta*, 2016, **211**, 445-452.
130. T. Matsui, M. Komoto, H. Muroyama, K. Kishida, H. Inui and K. Eguchi, *J Power Sources*, 2016, **312**, 80-85.
131. Z. B. Wang, R. R. Peng, W. H. Zhang, X. J. Wu, C. R. Xia and Y. L. Lu, *J Mater Chem A*, 2013, **1**, 12932-12940.
132. P. Ried, P. Holtappels, A. Wichser, A. Ulrich and T. Graule, *J Electrochem Soc*, 2008, **155**, B1029-B1035.
133. I. A. Raj, A. S. Nesaraj, M. Kumar, F. Tietz, H. P. Buchkremer and D. Stoever, *J New Mat Electr Sys*, 2004, **7**, 145-151.
134. L. Qiu, T. Ichikawa, A. Hirano, N. Imanishi and Y. Takeda, *Solid State Ionics*, 2003, **158**, 55-65.
135. S. P. Jiang, *Solid State Ionics*, 2002, **146**, 1-22.
136. B. C. H. Steele and J. M. Bae, *Solid State Ionics*, 1998, **106**, 255-261.
137. S. Vazquez, S. Davyt, J. E. Basbus, A. L. Soldati, A. Amaya, A. Serquis, R. Faccio and L. Suescun, *J Solid State Chem*, 2015, **228**, 208-213.
138. F. Zurlo, E. Di Bartolomeo, A. D'Epifanio, V. Felice, I. N. Sora, L. Tortora and S. Licoccia, *J Power Sources*, 2014, **271**, 187-194.
139. Q. J. Zhou, L. Xu, Y. J. Guo, D. Jia, Y. Li and W. C. J. Wei, *Int J Hydrogen Energ*, 2012, **37**, 11963-11968.
140. C. Jin, C. H. Yang, F. Zhao, D. Cui and F. L. Chen, *Int J Hydrogen Energ*, 2011, **36**, 3340-3346.
141. G. Cinti, A. Baldinelli, A. Di Michele and U. Desideri, *Appl Energ*, 2016, **162**, 308-320.
142. N. Khandan, M. Kazemeini and M. Aghaziarati, *Applied Petrochemical Research*, 2012, **1**, 21-27.

143. J. Hartvigsen, S. Elangovan, L. Frost, A. Nickens, C. Stoots, J. O'Brien and J. S. Herring, *ECS Transactions*, 2008, **12**, 625-637.
144. W. L. Becker, R. J. Braun, M. Penev and M. Melaina, *Energy*, 2012, **47**, 99-115.
145. W. Y. Li, Y. X. Shi, Y. Luo and N. S. Cai, *J Power Sources*, 2013, **243**, 118-130.
146. X. Sun, M. Chen, P. Hjalmarsson, S. D. Ebbesen, S. H. Jensen, M. Mogensen and P. V. Hendriksen, *ECS Transactions*, 2012, **41**, 77-85.
147. Y. K. Tao, S. D. Ebbesen and M. B. Mogensen, *J Power Sources*, 2016, **328**, 452-462.
148. J. E. O'Brien, M. G. McKellar, E. A. Harvego and C. M. Stoots, *Int J Hydrogen Energ*, 2010, **35**, 4808-4819.
149. P. Kim-Lohsoontorn and J. Bae, *J Power Sources*, 2011, **196**, 7161-7168.
150. S. W. Kim, M. Park, H. Kim, K. J. Yoon, J. W. Son, J. H. Lee, B. K. Kim, J. H. Lee and J. Hong, *Appl Catal B-Environ*, 2017, **200**, 265-273.
151. X. F. Sun, M. Chen, S. H. Jensen, S. D. Ebbesen, C. Graves and M. Mogensen, *Int J Hydrogen Energ*, 2012, **37**, 17101-17110.
152. Y. Luo, W. Li, Y. Shi, T. Cao, X. Ye, S. Wang and N. Cai, *J Electrochem Soc*, 2015, **162**, F1129-F1134.
153. Y. M. Choi, C. Compson, M. C. Lin and M. L. Liu, *Chem Phys Lett*, 2006, **421**, 179-183.
154. J. H. Wang and M. L. Liu, *Electrochem Commun*, 2007, **9**, 2212-2217.
155. S. W. Zha, Z. Cheng and M. L. Liu, *J Electrochem Soc*, 2007, **154**, B201-B206.
156. L. Deleebeeck, M. Shishkin, P. Addo, S. Paulson, H. Molero, T. Ziegler and V. Birss, *Phys Chem Chem Phys*, 2014, **16**, 9383-9393.
157. D. G. Ivey, E. Brightman and N. Brandon, *J Power Sources*, 2010, **195**, 6301-6311.
158. H. H. M. Thi, B. Saubat, N. Sergent and T. Pagnier, *Solid State Ionics*, 2015, **272**, 84-90.
159. Z. Cheng, J. H. Wang, Y. M. Choi, L. Yang, M. C. Lin and M. L. Liu, *Energ Environ Sci*, 2011, **4**, 4380-4409.
160. O. A. Marina, C. A. Coyle, M. H. Engelhard and L. R. Pederson, *J Electrochem Soc*, 2011, **158**, B424-B429.
161. K. Sasaki, K. Susuki, A. Iyoshi, M. Uchimura, N. Imamura, H. Kusaba, Y. Teraoka, H. Fuchino, K. Tsujimoto, Y. Uchida and N. Jingo, *J Electrochem Soc*, 2006, **153**, A2023-A2029.
162. R. Mukundan, E. L. Brosha and F. H. Garzon, *Electrochem Solid St*, 2004, **7**, A5-A7.
163. G. Tsekouras and J. T. S. Irvine, *J Mater Chem*, 2011, **21**, 9367-9376.
164. B. Wetenhall, J. M. Race and M. J. Downie, *Int J Greenh Gas Con*, 2014, **30**, 197-211.
165. A. Faes, A. Hessler-Wyser, D. Presvytes, C. G. Vayenas and J. Van Herle, *Fuel Cells*, 2009, **9**, 841-851.
166. O. M. Pecho, A. Mai, B. Munch, T. Hocker, R. J. Flatt and L. Holzer, *Materials*, 2015, **8**, 7129-7144.
167. J. W. Kim, A. V. Virkar, K. Z. Fung, K. Mehta and S. C. Singhal, *J Electrochem Soc*, 1999, **146**, 69-78.
168. V. M. Janardhanan, V. Heuveline and O. Deutschmann, *J Power Sources*, 2008, **178**, 368-372.
169. J. Kim, W. Y. Seo, J. Shin, M. L. Liu and G. Kim, *J Mater Chem A*, 2013, **1**, 515-519.
170. E. Barsoukov and J. R. Macdonald, *Impedance Spectroscopy-Theory Experiment and Application*, John Wiley & Sons, New York, 2005.
171. M. Cimenti, V. I. Birss and J. M. Hill, *Fuel Cells*, 2007, **7**, 377-391.

172. M. Cimenti, A. C. Co, V. I. Birss and J. M. Hill, *Fuel Cells*, 2007, **7**, 364-376.
173. S. C. Singhal and K. Kendall, eds., *High-Temperature Solid Oxide Fuel Cells: Fundamentals, Design and Applications*, Elsevier, Amsterdam, 2003.
174. J. R. Macdonald, *Ann Biomed Eng*, 1992, **20**, 289-305.
175. J. R. Macdonald, *Electrochim Acta*, 1993, **38**, 1883-1890.
176. Q. A. Huang, R. Hui, B. W. Wang and H. J. Zhang, *Electrochim Acta*, 2007, **52**, 8144-8164.
177. T. Smith, PhD, University of Calgary, 2007.
178. J. B. Jorcin, M. E. Orazem, N. Pebere and B. Tribollet, *Electrochim Acta*, 2006, **51**, 1473-1479.
179. C. V. Cushman, P. Bruner, J. Zakel, G. H. Major, B. M. Lunt, N. J. Smith, T. Grehl and M. R. Linford, *Analytical Methods*, 2016, **8**, 3419-3439.
180. B. Molero-Sánchez, P. K. Addo, A. Buyukaksoy and V. Birss, *Ecs Transactions*, 2015, **66**, 185-193.
181. A. Cavallaro, G. F. Harrington, S. J. Skinner and J. A. Kilner, *Nanoscale*, 2014, **6**, 7263-7273.
182. P. Keyvanfar, PhD, University of Calgary, 2017.
183. S. J. Xia, Birss, V., presented in part at the The 9th International Symposium on SOFCs, The Electrochemistry Society Proceeding Series, 1275–1283
- 2005.
184. Y. Matsuzaki and I. Yasuda, *Solid State Ionics*, 2000, **132**, 261-269.
185. S. Zha, Z. Cheng and M. Liu, *J Electrochem Soc*, 2007, **154**, B201-B206.
186. J. B. Hansen, *Electrochem Solid St*, 2008, **11**, B178-B180.
187. C. H. Bartholomew and R. B. Pannell, *Appl Catal*, 1982, **2**, 39-49.
188. D. S. Monder and K. Karan, *J Phys Chem C*, 2010, **114**, 22597-22602.
189. J. F. B. Rasmussen and A. Hagen, *J Power Sources*, 2009, **191**, 534-541.
190. V. Birss, L. Deleebeeck, S. Paulson and T. Smith, *ECS Transactions*, 2011, **35**, 1445-1454.
191. M. S. Khan, S. B. Lee, R. H. Song, J. W. Lee, T. H. Lim and S. J. Park, *Ceram Int*, 2016, **42**, 35-48.
192. E. D. Wachsman and K. T. Lee, *Science*, 2011, **334**, 935-939.
193. E. Wachsman, T. Ishihara and J. Kilner, *Mrs Bull*, 2014, **39**, 773-782.
194. N. M. Galea, E. S. Kadantsev and T. Ziegler, *J Phys Chem C*, 2007, **111**, 14457-14468.
195. M. J. Escudero, A. Aguadero, J. A. Alonso and L. Daza, *Journal of Electroanalytical Chemistry*, 2007, **611**, 107-116.
196. S. Primdahl and M. Mogensen, *J Electrochem Soc*, 1998, **145**, 2431-2438.
197. P. G. Keech, PhD, University of Calgary, 2005.
198. B. d. Boer, PhD, Twente Univesity, 1998.
199. C. M. Grgicak, R. G. Green and J. B. Giorgi, *J Power Sources*, 2008, **179**, 317-328.
200. C. M. Grgicak and J. B. Giorgi, *J Phys Chem C*, 2007, **111**, 15446-15455.
201. J.-H. Wang and M. Liu, *Electrochem Commun*, 2007, **9**, 2212-2217.
202. G. J. Offer, J. Mermelstein, E. Brightman and N. P. Brandon, *J Am Ceram Soc*, 2009, **92**, 763-780.
203. P. Lohsoontorn, D. J. L. Brett and N. P. Brandon, *J Power Sources*, 2008, **175**, 60-67.
204. T. Ogura, K. Nakao, T. Ishimoto and M. Koyama, *ECS Transactions*, 2011, **35**, 853-858.

205. R. Lohsoontorn, D. J. L. Brett and N. P. Brandon, *J Power Sources*, 2008, **183**, 232-239.
206. Z. Cheng, PhD, Georgia Institute of Technology, 2008.
207. Z. Cheng and M. L. Liu, *Solid State Ionics*, 2007, **178**, 925-935.
208. R. V. Siriwardane, J. A. Poston Jr and E. P. Fisher, *Appl Surf Sci*, 2005, **243**, 40-54.
209. H. H. Brongersma, M. de Ridder, A. Gildenpfennig and M. M. Viitanen, *J Eur Ceram Soc*, 2003, **23**, 2761-2767.
210. M. de Ridder, R. G. van Welzenis, A. W. D. van der Gon, H. H. Brongersma, S. Wulff, W. F. Chu and W. Weppner, *J Appl Phys*, 2002, **92**, 3056-3064.
211. H. Tellez, J. Druce, J. A. Kilner and T. Ishihara, *Faraday Discuss*, 2015, **182**, 145-157.
212. J. Druce, J. A. Kilner and T. Ishihara, *ECS Transactions*, 2013, **57**, 3269-3276.
213. S. W. Tao and J. T. S. Irvine, *Nat Mater*, 2003, **2**, 320-323.
214. S. W. Zha, P. Tsang, Z. Cheng and M. L. Liu, *J Solid State Chem*, 2005, **178**, 1844-1850.
215. L. Aguilar, S. W. Zha, S. W. Li, J. Winnick and M. Liu, *Electrochem Solid St*, 2004, **7**, A324-A326.
216. S. M. Bukhari, W. D. Penwell and J. B. Giorgi, *ECS Transactions*, 2013, **57**, 1507-1515.
217. Y. F. Bu, Q. Zhong, D. D. Xu, X. L. Zhao and W. Y. Tan, *J Power Sources*, 2014, **250**, 143-151.
218. H. Hayashi, M. Kanoh, C. J. Quan, H. Inaba, S. R. Wang, M. Dokiya and H. Tagawa, *Solid State Ionics*, 2000, **132**, 227-233.
219. V. P. Kumar, Y. S. Reddy, P. Kistaiah, G. Prasad and C. V. Reddy, *Mater Chem Phys*, 2008, **112**, 711-718.
220. Y. Jiang and A. V. Virkar, *J Electrochem Soc*, 2003, **150**, A942-A951.
221. A. Leonide, PhD, Karlsruhe Institute of Technology, 2010.
222. J. C. Ruiz-Morales, H. Lincke, D. Marrero-Lopez, J. Canales-Vazquez and P. Nunez, *Bol Soc Esp Ceram V*, 2007, **46**, 218-223.
223. L. DeLeebeeck, MSc, University of Calgary, 2010.
224. F. S. Baumann, J. Fleig, H. U. Habermeier and J. Maier, *Solid State Ionics*, 2006, **177**, 1071-1081.
225. F. S. Baumann, J. Maier and J. Fleig, *Solid State Ionics*, 2008, **179**, 1198-1204.
226. C. J. Zhang, Y. Yu, M. E. Grass, C. Dejoie, W. C. Ding, K. Gaskell, N. Jabeen, Y. P. Hong, A. Shayorskiy, H. Bluhm, W. X. Li, G. S. Jackson, Z. Hussain, Z. Liu and B. W. Eichhorn, *J Am Chem Soc*, 2013, **135**, 11572-11579.
227. E. Walker, S. C. Ammal, S. Suthirakun, F. L. Chen, G. A. Terejanu and A. Heyden, *J Phys Chem C*, 2014, **118**, 23545-23552.
228. Y. J. Zhou, Z. Lu, B. Wei, X. B. Zhu, Q. Y. Xie, Y. Q. Li and W. H. Su, *Fuel Cells*, 2013, **13**, 1040-1047.
229. J. M. Haag, S. A. Barnett, J. W. Richardson and K. R. Poepfelmeier, *Chem Mater*, 2010, **22**, 3283-3289.
230. M. Chen, S. Paulson, V. Thangadurai and V. Birss, *ECS Transactions*, 2012, **45**, 343-348.
231. Z. Zhao, L. Liu, X. Zhang, B. Tu, D. Ou and M. Cheng, *Int J Hydrogen Energ*, 2012, **37**, 19036-19044.
232. Z. Zhao, L. Liu, X. M. Zhang, W. M. Wu, B. F. Tu, D. A. Cui, D. R. Ou and M. J. Cheng, *Int J Hydrogen Energ*, 2013, **38**, 15361-15370.

233. P. Holtappels, L. G. J. De Haart, U. Stimming, I. C. Vinke and M. Mogensen, *J Appl Electrochem*, 1999, **29**, 561-568.
234. X. Tan, N. Liu, B. Meng, J. Sunarso, K. Zhang and S. Liu, *J Membrane Sci*, 2012, **389**, 216-222.
235. S. J. Benson, D. Waller and J. A. Kilner, *J Electrochem Soc*, 1999, **146**, 1305-1309.
236. Y. Zhang, G. M. Yang, G. Chen, R. Ran, W. Zhou and Z. P. Shao, *Acs Appl Mater Inter*, 2016, **8**, 3003-3011.
237. J. Yi, M. Schroeder, T. Weirich and J. Mayer, *Chem Mater*, 2010, **22**, 6246-6253.
238. M. D. Carvalho, T. Ramos, L. P. Ferreira and A. Wattiaux, *Solid State Sci*, 2010, **12**, 476-481.
239. K. Nomura, Y. Ujihira, T. Hayakawa and K. Takehira, *Applied Catalysis A: General*, 1996, **137**, 25-36.
240. K. Singh, PhD, University of Calgary, 2016.
241. G. Juhász, Z. Homonnay, K. Nomura, T. Hayakawa, S. Hamakawa and A. Vértes, *Solid State Ionics*, 2001, **139**, 219-231.
242. B. Sreedhar, C. S. Vani, D. K. Devi, V. Sreeram and M. V. B. Rao, *American Journal of Materials Science 2012*, 2(5): 142-146, 2012, **2**, 142-146.
243. A. Yan, V. Maragou, A. Arico, M. Cheng and P. Tsiakaras, *Applied Catalysis B: Environmental*, 2007, **76**, 320-327.
244. C. Su, Y. Z. Wu, W. Wang, Y. Zheng, R. Ran and Z. P. Shao, *J Power Sources*, 2010, **195**, 1333-1343.
245. F. M. Sapountzi, S. Brosda, K. M. Papazisi, S. P. Balomenou and D. Tsiplakides, *J Appl Electrochem*, 2012, **42**, 727-735.
246. S. B. Adler, *Chem Rev*, 2004, **104**, 4791-4843.
247. P. Hjalmarsson, M. Søgaaard and M. Mogensen, *Solid State Ionics*, 2009, **180**, 1395-1405.
248. J. Nielsen and J. Hjelm, *Electrochim Acta*, 2014, **115**, 31-45.
249. M. Ghatee, M. H. Shariat and J. T. S. Irvine, *Solid State Ionics*, 2009, **180**, 57-62.
250. O. Yamamoto, Y. Takeda, R. Kanno, K. Kohno and T. Kamiharai, *J Mater Sci Lett*, 1989, **8**, 198-200.
251. Q. Zhou, C. Yuan, D. Han, T. Luo, J. Li and Z. Zhan, *Electrochim Acta*, 2014, **133**, 453-458.
252. J. Liu and W. Weppner, *Ionics*, 1999, **5**, 115-121.
253. C. Y. Cheng, G. H. Kelsall and L. Kleiminger, *J Appl Electrochem*, 2013, **43**, 1131-1144.
254. S. D. Ebbesen and M. Mogensen, *Electrochem Solid St*, 2010, **13**, D106-D108.
255. Z. L. A. Feng, M. L. Machala and W. C. Chueh, *Phys Chem Chem Phys*, 2015, **17**, 12273-12281.
256. Y. Yu, B. H. Mao, A. Geller, R. Chang, K. Gaskell, Z. Liu and B. W. Eichhorn, *Phys Chem Chem Phys*, 2014, **16**, 11633-11639.
257. Y. Yu, A. Geller, B. Mao, R. Chang, Z. Liu and B. W. Eichhorn, *ECS Transactions*, 2013, **57**, 3119-3126.
258. S. B. Adler, *J Electrochem Soc*, 2002, **149**, E166-E172.
259. G. J. Offer, P. Shearing, J. I. Golbert, D. J. L. Brett, A. Atkinson and N. P. Brandon, *Electrochim Acta*, 2008, **53**, 7614-7621.
260. S. P. Jiang, *J Appl Electrochem*, 2004, **34**, 1045-1055.

261. J. Winkler, P. V. Hendriksen, N. Bonanos and M. Mogensen, *J Electrochem Soc*, 1998, **145**, 1184-1192.
262. G. Inzelt, A. Lewenstam and F. Scholz, eds., *Handbook of reference electrodes*, Springer-Verlag, Beilin Heidelberg, 2013.
263. S. B. Adler, *Chem Rev*, 2004, **104**, 4791-4844.
264. S. Primdahl and M. Mogensen, *J Electrochem Soc*, 1999, **146**, 2827-2833.

## Appendix

The following are the copyright permissions granted for the figures shown in Chapters 1-2 and the re-use of published papers shown in Chapters 4-7.

### 1. Permission for Figure 1.1

#### Re: Copyright Permission Request

Fri 2/17/2017 12:32 PM

Sent Items

To: REN21 Secretariat <secretariat@ren21.net>;

Hello,

Thank you for the permission.

Paul

---

**From:** REN21 Secretariat <secretariat@ren21.net>  
**Sent:** Wednesday, February 15, 2017 1:35:00 AM  
**To:** Paul Addo  
**Subject:** Re: Copyright Permission Request

Dear Paul,

thank you for your email and your interest in the work of REN21. We herewith grant you permission to use the two figures for your PhD Thesis. Please make sure that the sources are referenced correctly .

We would also appreciate if you could let us know the exact details and maybe send us a copy or link to the online version of the final article (if possible), so we can use it for our statistics.

Best regards and happy writing,

On 14 February 2017 at 19:57, Paul Addo

Hello Sir/Madam,

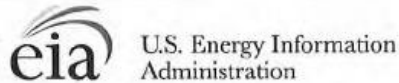
Please I will like to seek your written permission to use some figures in the RENEWABLES 2016 GLOBAL STATUS REPORT for my PhD thesis (University of Calgary, Canada)  
[secretariat@ren21.net](mailto:secretariat@ren21.net)

Read more at: <http://www.ren21.net/contact/secretariat@ren21.net>

Read more at: <http://www.ren21.net/contact/>

Thank you  
Paul Addo

## 2. Permission for Figure 1.2



### About EIA Copyrights and Reuse

#### Public domain and use of EIA content

U.S. government publications are in the public domain and are not subject to copyright protection. You may use and/or distribute any of our data, files, databases, reports, graphs, charts, and other information products that are on our website or that you receive through our email distribution service. However, if you use or reproduce any of our information products, you should use an acknowledgment, which includes the publication date, such as: "Source: U.S. Energy Information Administration (Oct 2008)."

#### Quoting EIA content and translations

When quoting EIA text, the acknowledgment should clearly indicate which text is EIA content and which is not. When translating EIA content into another language, please indicate the organization responsible for the translation and provide a link back to the original EIA web page in the acknowledgment.

#### Protected materials

You may see on our website documents, illustrations, photographs, or other information resources contributed or licensed by private individuals, companies, or organizations that may be protected by U.S. and foreign copyright laws. Transmission or reproduction of protected items beyond that allowed by fair use as defined in the copyright laws requires the written permission of the copyright owners.



The EIA logo is a registered trademark (Registration Number 4019501) of the U.S. Department of Energy and may not be used without the expressed consent of the U.S. Energy Information Administration. The mark consists of the acronym "EIA" with an associated design element of three curved lines above the literal element that extend to its right. For

more information, please contact Dale Sweetnam at [dale.sweetnam@eia.gov](mailto:dale.sweetnam@eia.gov).



Please note that our "Energy Ant" (seen on our Energy Kids website at <http://www.eia.gov/kids/>) is a registered servicemark of the U.S. Department of Energy. For more information about use restrictions of this graphic item, please contact [InfoCtr@eia.gov](mailto:InfoCtr@eia.gov).

The photographs on our website are protected by private licensing agreements and may not be reproduced without EIA's and/or the licensor's prior written consent. Contact Us if you have any questions regarding the reproduction of any illustrations, photographs, or other protected information. For background material on other copyright issues, see Copyright Basics from the U.S. Copyright Office.

### 3. Permission for Figure 2.1

#### ELSEVIER LICENSE TERMS AND CONDITIONS

Mar 20, 2017

This Agreement between Paul Addo ("You") and Elsevier ("Elsevier") consists of your license details and the terms and conditions provided by Elsevier and Copyright Clearance Center.

License Number	4073270081137
License date	Mar 20, 2017
Licensed Content Publisher	Elsevier
Licensed Content Publication	Renewable and Sustainable Energy Reviews
Licensed Content Title	Sustainable hydrocarbon fuels by recycling CO2 and H2O with renewable or nuclear energy
Licensed Content Author	Christopher Graves,Sune D. Ebbesen,Mogens Mogensen,Klaus S. Lackner
Licensed Content Date	January 2011
Licensed Content Volume	15
Licensed Content Issue	1
Licensed Content Pages	23
Start Page	1
End Page	23
Type of Use	reuse in a thesis/dissertation
Portion	figures/tables/illustrations
Number of figures/tables/illustrations	1
Format	both print and electronic
Are you the author of this Elsevier article?	No
Will you be translating?	No
Order reference number	
Original figure numbers	Figure 5
Title of your thesis/dissertation	Development of Fuel Electrodes for Reversible Solid Oxide Fuel Cell Applications
Expected completion date	Mar 2017
Estimated size (number of pages)	200
Elsevier VAT number	GB 494 6272 12
Requestor Location	Paul Addo

4. Permission for Figure 2.2

**Request for Permission to Reproduce or Re-Publish ECS Material**

Please fax this form to: The Electrochemical Society (ECS), Attn: Permissions Requests, 1.609.730.0629.  
You may also e-mail your request to: [copyright@electrochem.org](mailto:copyright@electrochem.org). Include all the information as required on this form. Please allow 3-7 days for your request to be processed.

I am preparing a (choose one):  paper  chapter  book  thesis

entitled: Development of Fuel Electrodes for Reversible Solid Oxide Fuel Cell

to be published-by: Application → published by University of Calgary

in an upcoming publication entitled: \_\_\_\_\_

I request permission to use the following material in the publication noted above, and request nonexclusive rights for all subsequent editions and in all foreign language translations for distribution throughout the world.

**Description of material to be used**—Indicate what material you wish to use (figures, tables, text, etc.) and give the full bibliographic reference for the source publication. You may attach a separate list, organized by ECS title.

✓ Figure 1 from N.P.Minh and M.B.Mojensen, The Electrochemical Society Interface, 2013, 22, 55-62

Signature: \_\_\_\_\_ Date: 03/21/2017

Name: Paul Agbo

Address: \_\_\_\_\_

Telephone: \_\_\_\_\_ Fax: \_\_\_\_\_

E-mail: \_\_\_\_\_

Permission is granted to reproduce the above-referenced material. Please acknowledge the author(s) and publication data of the original material, and include the words: "Reproduced by permission of The Electrochemical Society."

MAR 22 2017 \_\_\_\_\_  
Date Ann F. Goedkoop, ECS Associate Director of Publications

## 5. Permission for Figure 2.3

### ELSEVIER LICENSE TERMS AND CONDITIONS

Mar 20, 2017

This Agreement between Paul Addo ("You") and Elsevier ("Elsevier") consists of your license details and the terms and conditions provided by Elsevier and Copyright Clearance Center.

License Number	4073270582637
License date	
Licensed Content Publisher	Elsevier
Licensed Content Publication	Renewable and Sustainable Energy Reviews
Licensed Content Title	Current developments in reversible solid oxide fuel cells -
Licensed Content Author	Sergio Yesid Gómez,Dachamir Hotza
Licensed Content Date	August 2016
Licensed Content Volume	61
Licensed Content Issue	n/a
Licensed Content Pages	20
Start Page	155
End Page	174
Type of Use	reuse in a thesis/dissertation
Intended publisher of new work	other
Portion	figures/tables/illustrations
Number of figures/tables/illustrations	1
Format	both print and electronic
Are you the author of this Elsevier article?	No
Will you be translating?	No
Order reference number	
Original figure numbers	Figure 2
Title of your thesis/dissertation	Development of Fuel Electrodes for Reversible Solid Oxide Fuel Cell Applications
Expected completion date	Mar 2017
Estimated size (number of pages)	200
Elsevier VAT number	GB 494 6272 12
Requestor Location	Paul Addo



## 6. Permission for Figure 2.4

### ELSEVIER LICENSE TERMS AND CONDITIONS

Mar 20, 2017

This Agreement between Paul Addo ("You") and Elsevier ("Elsevier") consists of your license details and the terms and conditions provided by Elsevier and Copyright Clearance Center.

License Number	4073271461673
License date	Mar 20, 2017
Licensed Content Publisher	Elsevier
Licensed Content Publication	Journal of Power Sources
Licensed Content Title	A thermodynamic approach for selecting operating conditions in the design of reversible solid oxide cell energy systems
Licensed Content Author	Christopher H. Wendel, Pejman Kazempoor, Robert J. Braun
Licensed Content Date	1 January 2016
Licensed Content Volume	301
Licensed Content Issue	n/a
Licensed Content Pages	12
Start Page	93
End Page	104
Type of Use	reuse in a thesis/dissertation
Intended publisher of new work	other
Portion	figures/tables/illustrations
Number of figures/tables/illustrations	1
Format	both print and electronic
Are you the author of this Elsevier article?	No
Will you be translating?	No
Order reference number	
Original figure numbers	Figure 2
Title of your thesis/dissertation	Development of Fuel Electrodes for Reversible Solid Oxide Fuel Cell Applications
Expected completion date	Mar 2017
Estimated size (number of pages)	200
Elsevier VAT number	GB 494 6272 12
Requestor Location	Paul Addo

## 7. Permission for Figure 2.5

### ROYAL SOCIETY OF CHEMISTRY LICENSING TERMS AND CONDITIONS

Mar 20, 2017

This Agreement between Paul Addo ("You") and Royal Society of Chemistry ("Royal Society of Chemistry") consists of your license details and the terms and conditions provided by Royal Society of Chemistry and Copyright Clearance Center.

License Number	4073301069048
License date	Mar 20, 2017
Licensed Content Publisher	Royal Society of Chemistry
Licensed Content Publication	Energy & Environmental Science
Licensed Content Title	Large-scale electricity storage utilizing reversible solid oxide cells combined with underground storage of CO <sub>2</sub> and CH <sub>4</sub>
Licensed Content Author	S. H. Jensen, C. Graves, M. Mogensen, C. Wendel, R. Braun, G. Hughes, Z. Gao, S. A. Barnett
Licensed Content Date	Jul 6, 2015
Licensed Content Volume	8
Licensed Content Issue	8
Type of Use	Thesis/Dissertation
Requestor type	academic/educational
Portion	figures/tables/images
Number of figures/tables /images	1
Format	print and electronic
Distribution quantity	1000
Will you be translating?	no
Order reference number	
Title of the thesis/dissertation	Development of Fuel Electrodes for Reversible Solid Oxide Fuel Cell Applications
Expected completion date	Mar 2017
Estimated size	200
Requestor Location	Paul Addo

## 8. Permission for Figure 2.6

### ROYAL SOCIETY OF CHEMISTRY LICENSE TERMS AND CONDITIONS

Mar 20, 2017

---

This Agreement between Paul Addo ("You") and Royal Society of Chemistry ("Royal Society of Chemistry") consists of your license details and the terms and conditions provided by Royal Society of Chemistry and Copyright Clearance Center.

License Number	4073410766217
License date	Mar 20, 2017
Licensed Content Publisher	Royal Society of Chemistry
Licensed Content Publication	Energy & Environmental Science
Licensed Content Title	From Ni-YSZ to sulfur-tolerant anode materials for SOFCs: electrochemical behavior, in situ characterization, modeling, and future perspectives
Licensed Content Author	Zhe Cheng, Jeng-Han Wang, YongMan Choi, Lei Yang, M. C. Lin, Meilin Liu
Licensed Content Date	Aug 26, 2011
Licensed Content Volume	4
Licensed Content Issue	11
Type of Use	Thesis/Dissertation
Requestor type	academic/educational
Portion	figures/tables/images
Number of figures/tables /images	1
Format	print and electronic
Distribution quantity	1000
Will you be translating?	no
Order reference number	
Title of the thesis/dissertation	Development of Fuel Electrodes for Reversible Solid Oxide Fuel Cell Applications
Expected completion date	Mar 2017
Estimated size	200
Requestor Location	Paul Addo



9. Permission to re-use published articles shown in Chapters 4 and 7

RE: Formally request permission

CONTRACTS-COPYRIGHT (shared) <Contracts-Copyright@rsc.org>

Thu 3/9/2017 7:47 AM

Inbox

To: Paul Addo <

Dear Paul

The Royal Society of Chemistry (RSC) hereby grants permission for the use of your paper(s) specified below in the printed and microfilm version of your thesis. You may also make available the PDF version of your paper(s) that the RSC sent to the corresponding author(s) of your paper(s) upon publication of the paper(s) in the following ways: in your thesis via any website that your university may have for the deposition of theses, via your university's Intranet or via your own personal website. We are however unable to grant you permission to include the PDF version of the paper(s) on its own in your institutional repository. The Royal Society of Chemistry is a signatory to the STM Guidelines on Permissions (available on request).

Please note that if the material specified below or any part of it appears with credit or acknowledgement to a third party then you must also secure permission from that third party before reproducing that material.

Please ensure that the thesis states the following:

For the article from *Faraday* Discussions - Reproduced by permission of The Royal Society of Chemistry; and

For the article from *PCCP* – Reproduced by permission the PCCP Owner Societies and include a link to the paper on the Royal Society of Chemistry's website.

Please ensure that your co-authors are aware that you are including the paper in your thesis.

Regards

Gill Cockhead

Publishing Contracts & Copyright Executive

Follow the Royal Society of Chemistry:  
[www.rsc.org/follow](http://www.rsc.org/follow)

Winner of The Queen's Award for Enterprise, International Trade 2013

---

**From:** Paul Addo <

**Sent:** 28 February 2017 05:20

**To:** CONTRACTS-COPYRIGHT (shared) <Contracts-Copyright@rsc.org>

**Subject:** Formally request permission

Hello,

I am a co-author of the two articles below and will like to formally request permission to re-use them for my PhD thesis entitle "Development of Fuel Electrodes for Reversible Solid Oxide Fuel Cell Application"

***Faraday Discuss.*, 2015,182, 159-175**

DOI: 10.1039/C5FD00029G

***Phys. Chem. Chem. Phys.*16, 9383-9393**

DOI: 10.1039/C3CP53377H

Thank you for your assistance and please let me know if you need further information.

Sincerely,  
Paul Addo

This communication is from The Royal Society of Chemistry, a company incorporated in England by Royal Charter (registered number RC000524) and a charity registered in England and Wales (charity number 207890). Registered office: Burlington House, Piccadilly, London W1J 0BA. Telephone: 0207 4378 6556, Facsimile: 0207 4490 3393 (Head Office). This communication (including any attachments) may contain confidential, privileged or copyright material. It may not be relied upon or disclosed to any person other than the intended recipient(s) without the consent of The Royal Society of Chemistry. If you are not the intended recipient(s), please (1) notify us immediately by replying to this email and delete all copies from your system and (2) note that disclosure, distribution, copying or use of this communication is strictly prohibited. Any advice given by The Royal Society of Chemistry has been carefully formulated but is necessarily based on the information available, and The Royal Society of Chemistry cannot be held responsible for accuracy or completeness. In this respect, any views or opinions presented in this email are solely those of the author and may not represent those of The Royal Society of Chemistry.

The Royal Society of Chemistry owes no duty of care and shall not be liable for any resulting damage or loss as a result of the use of this email and/or attachments. The Royal Society of Chemistry acknowledges that a disclaimer cannot restrict liability at law for personal injury or death arising through a finding of negligence. The Royal Society of Chemistry does not warrant that its emails or attachments are Virus-free: Please rely on your own screening.

## 10. Permission to re-use published article shown in Chapter 5

### RE: URGENT-Formal Copyright Request

Copyright <copyright@electrochem.org>

Tue 3/21/2017 6:05 AM

To: Paul Addo [REDACTED]

Dear Paul Addo,

Thank you for your permission request. Since you are the author of the articles, as per the ECS Transfer of Copyright Agreement, you have the right to reproduce your own work. Please see part "C" of the "Rights of Authors" section on the agreement:

<http://www.electrochem.org/dl/support/assets/crtf.pdf>

Please let me know if you have any questions, or if there is anything additional I can do to assist.

Sincerely,  
Logan Streu

Ms. Logan Streu | Publications Discoverability Manager

500 The Electrochemical Society

#### Early bird registration!

231st ECS Meeting

May 28-June 1 in New Orleans

[Learn more](#)

---

**From:** Paul Addo [REDACTED]

**Sent:** Monday, March 20, 2017 4:59 PM

**To:** Copyright <copyright@electrochem.org>

**Subject:** URGENT-Formal Copyright Request

Hello,

Please I am a co-author of this article (P. Addo, B. Molero-Sanchez, A. Buyukaksoy, S. Paulson and V. Birss, Ecs Transactions, 2015, 66, 219-228) and would like to seek your formal permission to

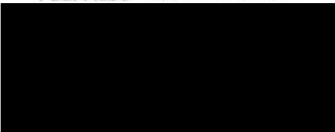
## 11. Permission to re-use published article shown in Chapter 6

### JOHN WILEY AND SONS LICENSE TERMS AND CONDITIONS

Feb 28, 2017

---

This Agreement between Paul Addo ("You") and John Wiley and Sons ("John Wiley and Sons") consists of your license details and the terms and conditions provided by John Wiley and Sons and Copyright Clearance Center.

License Number	4057440371244
License date	Feb 28, 2017
Licensed Content Publisher	John Wiley and Sons
Licensed Content Publication	Fuel Cells
Licensed Content Title	CO/CO <sub>2</sub> Study of High Performance La <sub>0.3</sub> Sr <sub>0.7</sub> Fe <sub>0.7</sub> Cr <sub>0.3</sub> O <sub>3-δ</sub> Reversible SOFC Electrodes
Licensed Content Author	P. K. Addo, B. Molero-Sanchez, M. Chen, S. Paulson, V. Birss
Licensed Content Date	Sep 21, 2015
Licensed Content Pages	8
Type of use	Dissertation/Thesis
Requestor type	Author of this Wiley article
Format	Print and electronic
Portion	Full article
Will you be translating?	No
Title of your thesis / dissertation	Development of Fuel Electrodes for Reversible Solid Oxide Fuel Cell Applications
Expected completion date	Mar 2017
Expected size (number of pages)	200
Requestor Location	Paul Addo 
Publisher Tax ID	EU826007151
Billing Type	Invoice